

INFORMATION TO USERS

This manuscript has been reproduced from the microfilm master. UMI films the text directly from the original or copy submitted. Thus, some thesis and dissertation copies are in typewriter face, while others may be from any type of computer printer.

The quality of this reproduction is dependent upon the quality of the copy submitted. Broken or indistinct print, colored or poor quality illustrations and photographs, print bleedthrough, substandard margins, and improper alignment can adversely affect reproduction.

In the unlikely event that the author did not send UMI a complete manuscript and there are missing pages, these will be noted. Also, if unauthorized copyright material had to be removed, a note will indicate the deletion.

Oversize materials (e.g., maps, drawings, charts) are reproduced by sectioning the original, beginning at the upper left-hand corner and continuing from left to right in equal sections with small overlaps. Each original is also photographed in one exposure and is included in reduced form at the back of the book.

Photographs included in the original manuscript have been reproduced xerographically in this copy. Higher quality 6" x 9" black and white photographic prints are available for any photographs or illustrations appearing in this copy for an additional charge. Contact UMI directly to order.

UMI

A Bell & Howell Information Company
300 North Zeeb Road, Ann Arbor MI 48106-1346 USA
313/761-4700 800/521-0600

The Pennsylvania State University

The Graduate School

Eberly College of Science

**LOW-ENERGY ELECTRON DIFFRACTION STUDY OF
ALKALI METALS ADSORBED ON SILVER (111),
AND THEIR COADSORPTION WITH RARE GASES**

A Thesis in

Physics

by

Gerald S. Leatherman

**Submitted in Partial Fulfillment
of the Requirements
for the Degree of**

Doctor of Philosophy

December 1996

UMI Number: 9716252

UMI Microform 9716252
Copyright 1997, by UMI Company. All rights reserved.

**This microform edition is protected against unauthorized
copying under Title 17, United States Code.**

UMI
300 North Zeeb Road
Ann Arbor, MI 48103

We approve the thesis of Gerald S. Leatherman

Date of Signature

Renee D. Diehl
Renee D. Diehl
Associate Professor of Physics
Thesis Adviser
Chair of Committee

July 22, 1996

David L. Allara
David L. Allara
Professor of Chemistry

July 22, 1996

Kristen A. Fichthorn
Kristen A. Fichthorn
Associate Professor of Chemical Engineering and Physics

July 22, 1996

Nitin Samarth
Nitin Samarth
Assistant Professor of Physics

July 22, 1996

Howard Grotch
Howard Grotch
Professor of Physics
Head of the Department of Physics

July 22, 1996

Abstract

The adsorption of Cs, Rb, or K on Ag(111) has been investigated using Low-Energy Electron Diffraction (LEED). The overlayer lattice parameter was found to decrease with the inverse square root of the coverage over the entire submonolayer coverage range, indicating repulsive adsorbates which compress uniformly. At low temperatures over most of the coverage range the overlayer exists as a triangular lattice which is incommensurate with the substrate. However at coverages of exactly 1/12, 1/9, 1/7, 1/4 and 1/3 commensurate overlayers with primitive unit cell periodicities of $(2\sqrt{3}\times 2\sqrt{3})R30^\circ$, (3×3) , $(\sqrt{7}\times \sqrt{7})R19.1^\circ$, (2×2) , and $(\sqrt{3}\times \sqrt{3})R30^\circ$ are formed, respectively, for each of the three alkali species. Two higher-order commensurate phases are observed: a $(\sqrt{21}\times \sqrt{21})R10.9^\circ$ phase at a coverage of 4/21 for Rb and K, and a (5×5) phase at a coverage of 9/25 for Rb only. The incommensurate and low-order commensurate phases undergo a transition to a fluid phase at temperatures which increase with alkali coverage. The transition temperatures vary from 35 K for potassium at a coverage of 0.11 to 250 K at a coverage of 0.33, with somewhat higher temperatures for Rb and Cs. Over certain coverage ranges the overlayer lattice is rotated at a non-symmetry angle with respect to the substrate. This angle varies with changing misfit, and also changes by a relatively large amount with temperature. The results at low temperature are compared with various models of epitaxial rotation, and some of the temperature-dependent results are shown to be consistent with a mean-field theory describing rotational epitaxy.

Dynamical LEED structural determinations have been completed for three of these commensurate phases: the (3×3) , (2×2) , and $(\sqrt{3}\times \sqrt{3})R30^\circ$. The results indicate that for the (2×2) and (3×3) phases the adatom resides in the FCC hollow site, while for the $(\sqrt{3}\times \sqrt{3})R30^\circ$ phases it occupies the HCP hollow site. The (2×2) and (3×3) phases exhibit significant substrate rumpling, which has the effect of pushing the adsorbate atoms into the surface. The chemisorption bondlength does not change significantly as a function of coverage for any of the alkalis.

Rare gas (Xe, Kr, or Ar) coadsorption with submonolayer amounts of K or Cs on Ag(111) was also investigated. Rare gas dosed onto a submonolayer of K or Cs results in a binary monolayer in which rare gas and alkali atoms coexist. For K coadsorption the interaction of the rare gas with the alkali is repulsive, leading to a segregation of phases and a decreased desorption temperature for the rare gas from the surface. For Cs coadsorption however, at least at low coverages, the interaction is attractive and results in mixing and an increase in the rare gas desorption temperature. For the K and rare gas coadsorption system, desorption data were analyzed to determine the spreading pressure in the alkali layer. From the behavior of the alkali monolayer coexisting with rare gas, it was deduced that the energy per K adatom of the K $p(2\times 2)$ commensurate phase is 11 meV lower than that of the incommensurate

phase at a nearby coverage, and that the corresponding number for the $(\sqrt{7}\times\sqrt{7})R19.1^\circ$ commensurate phase is 5 meV.

Coadsorption of rare gas with amounts of K as small as 0.04 ML results in a rare gas overlayer which is rotated with respect to the substrate rather than aligned, as seen for rare gases on clean Ag(111). The rotation is attributed to an increased surface corrugation experienced by the rare gas, due to the presence of the alkali. The rotation angles do not agree with the Novaco-McTague predictions, but are closer to the prediction of a Bohr-Grey trajectory. A similar effect, but with different rotation angles, is observed for adsorption of rare gases on an Ag(111) surface pretreated with CO.

Table of Contents

List of Figures	viii
List of Tables	xiii
Acknowledgments	xiv
 Chapter One. Introduction.....	 1
 Chapter Two. Theory	 6
2.1. Low-Energy Electron Diffraction.....	6
2.1.1. Kinematical Theory	6
2.1.2. Dynamical Theory	10
2.2. Alkali Metal Adsorption	16
2.3. Rotational Epitaxy	21
2.3.1. Bohr-Grey Model.....	23
2.3.2. Coincidence Lattice Model	23
2.3.3. Novaco-McTague Theory.....	27
2.3.4. Shiba Theory	29
2.4. References	30
 Chapter Three. Experimental Apparatus.....	 32
3.1. UHV Chamber.....	32
3.2. Sample	34
3.2.1. Preparation.....	34
3.2.2. Mounting.....	36
3.2.3. Heating & Cooling.....	37
3.2.4. Deposition of Materials.....	39
3.3. Auger Electron Spectroscopy (AES)	41
3.4. Kelvin Probe.....	41
3.5. Low-Energy Electron Diffraction (LEED).....	44
3.5.1. Electron Optics.....	44
3.5.2. Video Data Acquisition.....	46
3.5.3. Video Data Processing.....	48
3.5.3.1 LEED I(E) Processing.....	49
3.5.3.2 Kinematical Data Processing	52
3.5.4. Determination of Uncertainties	53
3.5.4.1 LEED Transfer Width	53
3.5.4.2 Uncertainties in Video Processing.....	57
3.6. References	66
 Chapter Four. Characterization of the Clean Ag(111) Surface	 67
4.1. Introduction and Historical Summary	67
4.2. Results.....	68
4.3. Discussion	72
4.4. References	74
 Chapter Five. Alkali Metals Adsorbed on Ag(111)	 75
5.1. Introduction.....	75
5.2. Historical Summary	75
5.2.1. General.....	75

5.2.2. Alkali Metals on Ag(111)	76
5.2.2.1 Cesium	76
5.2.2.2 Rubidium	77
5.2.2.3 Potassium	78
5.2.2.4 Sodium	78
5.2.2.5 Lithium	79
5.2.3. Summary and Discussion	79
5.3. Experimental Phase Diagrams	81
5.3.1. Commensurate and Incommensurate Phases	81
5.3.2. Disorder Transitions	90
5.3.3. Higher Order Commensurate Phases	99
5.3.4. Alkali Bilayers	105
5.3.5. Sodium or Lithium on Ag(111)	106
5.4. Site Determinations	109
5.4.1. Procedure	109
5.4.2. Results	110
5.4.3. Discussion	121
5.5. Rotational Epitaxy	127
5.5.1. Results	127
5.5.2. Discussion	131
5.6. References	134
Chapter Six. Rare Gas Coadsorption with Alkali Metals or CO on Ag(111)	137
6.1. Introduction and Historical Summary	137
6.2. Procedure	141
6.3. Rare Gases on Clean Ag(111)	142
6.4. Rare gases coadsorbed with K on Ag(111)	144
6.4.1. Rare Gas Rotation Angle	144
6.4.2. Segregation of Rare Gas and Potassium	148
6.4.3. Alkali Spreading Pressure Determination	152
6.4.3.1 Non-equilibrium Method	156
6.4.3.2 Equilibrium Method	160
6.4.4. Energy of Alkali Commensurate Phases	162
6.5. Rare Gases Coadsorbed with Cs on Ag(111)	164
6.6. Work Function Results for Rare Gases Coadsorbed with K or Cs on Ag(111)	170
6.7. Xe Adsorbed on an Alkali Monolayer	171
6.8. Rare Gases Coadsorbed with Carbon Monoxide on Ag(111)	174
6.9. References	182
Chapter Seven. Summary and Conclusion	184
7.1. The Ag(111) Surface	184
7.2. Alkali Metals Adsorbed on Ag(111)	184
7.3. Rare Gases Coadsorbed with Alkali Metals or CO on Ag(111)	187
Appendix A. LEED I(E) Spectra for Commensurate Phases	190
Appendix B. Documentation of Video-LEED Data Acquisition Program	200
B.1. Introduction	200
B.2. Lvideo Program Description	201
B.2.1. File Formats	203
B.2.2. Specific Video Frame Acquisition and Analysis Functions	203

Appendix C. Documentation of Video-LEED Data Analysis Programs.....	218
C.1. LEED I(E) Analysis.....	218
C.2. Intensity Integration at a Single Energy	225
C.3. Extraction of One-Dimensional Intensity Profiles	228

List of Figures

Figure 1.1.	Calculation of the mean free path for an electron in a solid, as a function of the kinetic energy of the electron	2
Figure 2.1.	Scattering of a plane wave from an array of atoms	7
Figure 2.2.	Ewald sphere construction for diffraction in three dimensions	8
Figure 2.3.	Ewald sphere construction for two-dimensional diffraction compared to the geometry used in a LEED experiment.	10
Figure 2.4.	An electron scattered from an ion core potential well.....	12
Figure 2.5.	Muffin tin model of a solid	13
Figure 2.6.	Classical model of alkali metal adsorption on a metal surface	17
Figure 2.7.	Work function behavior for alkali metal adsorption	18
Figure 2.8.	Gurney model of alkali metal adsorption on a metal surface	20
Figure 2.9.	Charge density contours for Na on Al(111) calculated using the LDA method	22
Figure 2.10.	Moiré interference fringes between two incommensurate lattices	24
Figure 2.11.	Bohr-Grey trajectories for rotational epitaxy	25
Figure 2.12.	Predictions of three additional models for rotational epitaxy	26
Figure 2.13.	Diagram showing the method of calculating higher order commensurate points	26
Figure 2.14.	Energy of rotation calculated by the Novaco-McTague theory, as a function of overlayer rotation angle, for an overlayer with a misfit of 0.1 with respect to the commensurate (2x2)	28
Figure 3.1.	UHV chamber, pumped by turbo and titanium sublimation pumps.....	33
Figure 3.2.	Experimental apparatus available in the UHV chamber	35
Figure 3.3.	Diagram of Laue X-ray diffraction apparatus, used for orienting the Ag(111) sample.....	38
Figure 3.4.	Sample holder	38
Figure 3.5.	Source for alkali metal deposition.....	40
Figure 3.6.	Auger spectra from the Ag(111) surface	42
Figure 3.7.	Schematic diagram of Kelvin Probe apparatus	43

Figure 3.8.	LEED apparatus	45
Figure 3.9.	Block diagram of the Data Translation video frame grabber and processor boards	47
Figure 3.10.	Correction to LEED I(E) curve due to saturated camera intensity at the center of the spot.....	50
Figure 3.11.	Line intensity profile through a diffraction spot from a video frame of a LEED pattern.....	54
Figure 3.12.	Correction to made to a diffraction pattern due to the flat-plate distortion.....	54
Figure 3.13.	Computer corrections performed on a diffraction pattern	55
Figure 3.14.	LEED transfer width as a function of beam energy	58
Figure 3.15.	Analysis of LEED detector fluctuations with time.....	59
Figure 3.16.	A slightly non-normal angle of incidence, which causes an error in measured reciprocal lattice positions	63
Figure 3.17.	Diagram showing the error caused by the flat plate correction when the screen center is not known exactly.....	63
Figure 3.18.	Error in diffraction position due to parabolic electron trajectory between grid and channel plate	64
Figure 3.19.	Analysis of the error in position caused by the suppresser voltage.....	65
Figure 4.1.	Diffraction pattern from the clean Ag(111) surface.....	69
Figure 4.2.	LEED I(E) spectra for clean Ag(111), compared with best-fit calculated spectra.....	71
Figure 4.3.	Variation of the R factor with the first Ag(111) layer spacing.....	73
Figure 5.1.	Work function curves for Cs/Ag(111) and K/Ag(111).....	80
Figure 5.2.	Monolayer phase diagram for K/Ag(111).....	82
Figure 5.3.	Monolayer phase diagram for Rb/Ag(111)	83
Figure 5.4.	Monolayer phase diagram for Cs/Ag(111)	84
Figure 5.5.	Alkali lattice parameter and density as a function of coverage	85
Figure 5.6.	LEED patterns for Cs/Ag(111).	87
Figure 5.7.	Real space structures for commensurate phases.....	88
Figure 5.8.	Annealing out of frozen-in disorder in Rb/Ag(111) overlayer at a coverage of 0.30.....	91
Figure 5.9.	LEED patterns showing melting of the $(\sqrt{7} \times \sqrt{7})R19.1^\circ$ commensurate phase.....	92

Figure 5.10. Melting of the K p(2x2) phase	93
Figure 5.11. Melting of the K ($\sqrt{7} \times \sqrt{7}$)R19.1° phase	94
Figure 5.12. Diagram showing the possible fine detail of a phase diagram in the vicinity of a commensurate phase	95
Figure 5.13. LEED patterns showing the melting of the K/Ag(111) incommensurate phase at a coverage of 0.201	97
Figure 5.14. Various melting curves for K/Ag(111), as a function of coverage	98
Figure 5.15. LEED patterns of higher-order commensurate phases	100
Figure 5.16. K/Ag(111), two coexisting phases at a coverage of 0.19: HOC (higher order commensurate) and incommensurate	102
Figure 5.17. Proposed structures for higher-order commensurate phases	103
Figure 5.18. Results of a structure factor calculation for the ($\sqrt{21} \times \sqrt{21}$) R10.8° HOC phase	104
Figure 5.19. ($\sqrt{13} \times \sqrt{13}$)R13.9° diffraction pattern from Li/Ag(111)	108
Figure 5.20. Schematic phase diagram for Li/Ag(111)	108
Figure 5.21. Diagram of an FCC(111) surface, showing the difference between HCP and FCC hollow sites	111
Figure 5.22. Structure of the alkali p(3x3) phase on Ag(111), with adsorption in the FCC hollow site	112
Figure 5.23. Structure of the alkali p(2x2) phase on Ag(111), with adsorption in the FCC hollow site	113
Figure 5.24. Structure of the ($\sqrt{3} \times \sqrt{3}$)R30° phase, with adsorption in the HCP hollow site	114
Figure 5.25. Chemisorption bondlength and anisotropic vibrational amplitudes for alkalis on Ag(111)	116
Figure 5.26. Variation of the Pendry R factor near the minimum with the structural parameters, for the K p(3x3) / Ag(111) phase	118
Figure 5.27. Comparison of K p(2x2)/Ag(111) for an overlayer deposited at 35 K and not annealed to an overlayer deposited at 35 K, annealed to room temperature, and then cooled again for data collection	119
Figure 5.28. Comparison of equivalent LEED beams of solved structures to low-coverage unsolved structures	120

Figure 5.29.	Alkali chemisorption bondlength as a function of coverage, for K, Rb, and Cs on Ag(111).....	122
Figure 5.30.	Bulk moduli of various substrates, shown together with alkali phase which form on them.....	125
Figure 5.31.	Rotational behavior of Cs, Rb, or K on Ag(111), compared with various theoretical models.....	128
Figure 5.32.	Rotational behavior of Rb/Ag(111) as a function of temperature	129
Figure 5.33.	Rotation angle as a function of temperature for K or Cs on Ag(111)	130
Figure 5.34.	Comparison of the temperature dependent Rb/Ag(111) data at two coverages to a power law having the exponent 0.5.....	133
Figure 6.1.	Energy level diagram showing the binding energy of an adsorbed rare gas atom.....	139
Figure 6.2.	Diagram showing the expected work function variation across a surface when alkali atoms are adsorbed.....	139
Figure 6.3.	Isobars and phase diagrams for Ar / Ag(111).....	143
Figure 6.4.	LEED patterns for Xe on Ag(111), precovered with a small amount of K	145
Figure 6.5.	Rare gas rotation angle as a function of misfit with respect to the $(\sqrt{3}\times\sqrt{3})R30^\circ$ phase, for a rare gas monolayer on potassium-precovered Ag(111)	146
Figure 6.6.	LEED patterns for Kr adsorption on Ag(111) predosed with 0.13 ML potassium	149
Figure 6.7.	Rotation angle of a potassium lattice coadsorbed with Kr, compared with the behavior of the rotated K / Ag(111) phase.....	150
Figure 6.8.	LEED intensities for the $p(2\times 2)$ phase of K coadsorbed with Kr, compared with the $p(2\times 2)$ phase of K alone on Ag(111).....	151
Figure 6.9.	Zero-pressure desorption curves for Kr coadsorption with various precoverages of K on Ag(111)	153
Figure 6.10.	Zero-pressure desorption curves for Xe coadsorption with various precoverages of K on Ag(111)	154
Figure 6.11.	Isobars at 1.9×10^{-6} mbar for Kr coadsorption with K on Ag(111)	155
Figure 6.12.	Potassium spreading pressure determination using coadsorbed rare gas	158
Figure 6.13.	Rare gas spreading pressure as a function of three-dimensional pressure and temperature, obtained from equilibrium experiments reported in previous work.....	161
Figure 6.14.	Commensurate sticking behavior of a K monolayer being compressed by rare gas	163

Figure 6.15. LEED patterns for Kr / Ag(111) precovered with 0.11 ML Cs	165
Figure 6.16. Data for the new phase which appears upon adsorption of Kr onto a Cs precovered Ag(111) surface.....	166
Figure 6.17. LEED patterns for Kr adsorption on Ag(111), precovered with 0.14 ML Cs	167
Figure 6.18. Temperature at which all Kr coadsorbed with Cs on Ag(111) has desorbed, as a function of Cs precoverage	169
Figure 6.19. Work function change due to the adsorption of Kr on Ag(111), precovered with Cs or K.....	172
Figure 6.20. Schematics of the LEED patterns seen for Xe adsorbed on a monolayer of Rb on Ag(111).....	175
Figure 6.21. LEED patterns showing CO coadsorption with Ar on Ag(111)	177
Figure 6.22. Lattice parameter of the ($\sqrt{7} \times \sqrt{7}$)R19.1° Ar + CO / Ag(111) phase as a function of temperature	178
Figure 6.23. Behavior of the Ar overlayer adsorbed on Ag(111) pretreated with CO, as a function of annealing temperature	179
Figure 6.24. Overlayer rotation angle for rare gases coadsorbed with CO on Ag(111).....	180
Figure A.1. LEED I(E) spectra for the K p(3x3) phase on Ag(111).	191
Figure A.2. LEED I(E) spectra for the Rb p(3x3) phase on Ag(111).....	192
Figure A.3. LEED I(E) spectra for the Cs p(3x3) phase on Ag(111).	193
Figure A.4. LEED I(E) spectra for the K p(2x2) phase on Ag(111).	194
Figure A.5. LEED I(E) spectra for the Rb p(2x2) phase on Ag(111).....	195
Figure A.6. LEED I(E) spectra for the Cs p(2x2) phase on Ag(111).	196
Figure A.7. LEED I(E) spectra for the K ($\sqrt{3} \times \sqrt{3}$)R30° phase on Ag(111).	197
Figure A.8. LEED I(E) spectra for the Rb ($\sqrt{3} \times \sqrt{3}$)R30° phase on Ag(111).....	198
Figure A.9. LEED I(E) spectra for the Cs ($\sqrt{3} \times \sqrt{3}$)R30° phase on Ag(111).	199

List of Tables

Table 3.1.	Error in fitted lorentzian parameters due to random errors in pixel intensities representative of a typical experiment.....	61
Table 4.1.	Equivalent beam sets for an FCC (111) surface.....	70
Table 5.1.	Commensurate phases for Cs, Rb, or K on Ag(111).....	86
Table 5.2.	Saturation coverage for alkalis, compared with the ionic and covalent alkali radii	89
Table 5.3.	Critical exponents for disordering of the K p(2x2) phase on Ag(111), compared to lattice-gas model predictions	90
Table 5.4.	Spacing and Rotation Angles for Second Layer Alkalis on Ag(111).....	106
Table 5.5.	Structural parameters of alkali phases on Ag(111), determined by LEED I(E) analysis	115
Table 6.1.	Heats of adsorption for rare gases on Ag(111), measured using LEED isobar experiments.....	144

Acknowledgments

I would like to express appreciation to a number of individuals who contributed to the work presented in this thesis. I wish to thank Michael Strauss for preparing single crystals for use in the experiments. I thank Heather Boylan, Heidi Sonick, and Karen Menuz for help in data analysis and figure preparation. I would like to thank Dr. Milton Cole, Dr. Gianfranco Vidali, and Dr. Louis Bruch for useful discussions. I especially wish to thank my advisor, Dr. Renee Diehl, for her excellent guidance and creative insights. Finally, I express heartfelt thanks to my wife Evangeline for her support throughout this endeavor.

The work presented in this thesis was supported by NSF grant DMR-9022681.

Chapter One

Introduction

While the study of solid matter has perhaps been the most intensely studied fields of physics, the study of the surfaces of matter and the interfaces between a solid and another phase has been much more difficult. X-ray diffraction techniques, which made possible the study of bulk solids, have until recently not been well suited for the study of surfaces. The reason for this is that because x-rays interact relatively weakly with matter, they penetrate far into a solid and therefore return information which is overwhelmingly determined by properties in the bulk rather than near the surface. The study of surfaces on an atomic level did not begin until the discovery in 1927 that electrons can be made to diffract from matter.¹

Figure 1.1 illustrates why electrons are so useful in the study of surfaces.² Because they interact strongly with matter, electrons have a mean-free-path in an average solid that is less than 20 Å for electrons with energies between 10 and 1000 eV. Because of this, low energy electrons scattered or ejected from a solid have the potential to provide information specific to the surface region of the material. Low Energy Electron Diffraction (LEED) is an electron scattering technique in which elastically scattered electrons are measured and their directional distribution is analyzed to provide structural information about the surface. If the surface consists of an array of atoms which is ordered over large regions, the electrons coherently scatter producing strong peaks, or “beams” in particular directions. The positions of these beams, measured as they strike a screen, are used to determine the periodicity of the surface. In addition, by analyzing the dependence of the intensity of these beams on the incident electron energy, the exact atomic structure of the region near the surface may be determined.

Even after the discovery of electron diffraction in 1927, surface science did not begin to blossom until many years later. The main reason for this is because conditions at a surface are very difficult to control. In order to performed an experiment it is desirable to remove all extraneous influences from the system, leaving only the ones which are under investigation. This becomes very difficult when studying behavior of surfaces at an atomic level because it means removing all of the gas-phase material, or atmosphere, around the sample. Technology capable of doing this to the level required for a reproducible experiment started to become available only in the late 1950s and early 1960s. Even then it was not until the development of the Auger Electron Spectroscopy (AES), a technique used in measuring the composition of a surface, that surface science truly became feasible. This spectroscopy technique, in which inelastically scattered electrons are measured, provides elemental identification of the material in

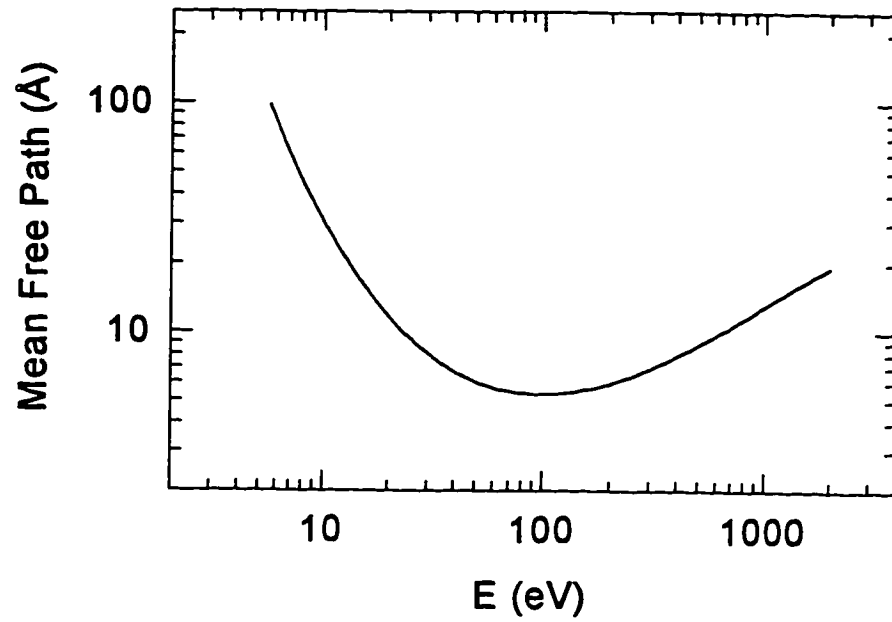


Figure 1.1. Calculation of the mean free path for an electron in a solid, as a function of the kinetic energy of the electron.² This is the mean distance an electron travels before undergoing a scattering event.

the first few atomic layers. In the last twenty years, LEED, AES, and UHV (Ultra-High Vacuum) equipment have finally become commercially available, and there has been an explosion of research on the behavior of surfaces. These have mainly included studies of the physical structure of surfaces, their vibrational qualities, and their electronic structure.

Why are surfaces of interest? First of all, they are of interest for purely scientific reasons. Many of the properties of matter are derived from the translational symmetry that a crystalline material has. At the surface the translational symmetry in one dimension is suddenly broken. It is interesting to study the results of this reduced symmetry at the surface. A single layer of atoms or molecules introduced onto a surface of another material can sometimes be thought of as existing in a two-dimensional space, making possible the study of what can be thought of as two-dimensional matter.

Surfaces are also important for technological reasons. Probably the most important of these is for the understanding of catalytic chemical reactions. In these reactions, a small amount of some material (the catalyst) added to the reactants has the effect of reducing an energy barrier to the reaction, causing it to proceed more quickly or at a lower temperature. The physical process that occurs is that one or more of the reacting species adsorb onto the surface of the catalyst, which causes the nature of its chemical bonds to change in such a way that it can more easily react with the other species to form the desired product. Traditional catalysis has been an empirical science; the physical processes involved have not usually been understood. Surface science, by characterizing surfaces at the atomic level and seeking to understand the interactions of atoms and molecules with or on a surface, has begun to provide important insights into catalytic processes. Much of surface science has in fact proceeded with the goal of improving catalytic processes or designing better catalysts.

If an atom or molecule in the gas phase comes close enough to a surface, it may stick to the surface, or be adsorbed, due to forces between the particle and the surface. Depending on the specific identity of the particle and the surface, the electronic configuration of either may be relatively unperturbed or it may become altered more dramatically. Particles which undergo little change in their electronic structure upon adsorption are said to be physisorbed. These adsorbates interact with the surface and with each other primarily through Van der Waals interactions, and have binding energies to the surface of less than 0.5 eV. Atoms or molecules which experience a larger change in their electronic configuration upon adsorption are said to be chemisorbed. These species can be thought of as chemically bound to the surface, and have binding energies of 0.5 to 15 eV.

Much of the behavior of an array of adsorbates on a surface will be governed by two factors. The first is the potential due to the substrate that the adsorbate experiences as it moves around on the surface. This potential will be corrugated in the substrate periodicity, and has the effect of pushing the adsorbates toward preferred sites. The other factor is the interaction between the adsorbates. This may be an

attractive or repulsive interaction, and has the effect of causing the adsorbates to order into an array at some equilibrium spacing. In most cases this will not be the spacing of the substrate lattice, so there will be competition between these two factors.

The simplest physisorbed and chemisorbed species are considered to be rare gases and alkali metals, respectively. Because rare gases have only filled electron shells, they are very chemically inert and therefore are considered to be the simplest physisorbates. Since they interact with each other by Van der Waals interactions, rare gas atoms on a surface usually condense into islands with a spacing about equal or slightly larger than their bulk equilibrium spacing. This spacing is fairly well defined, and so rare gas overlayers are often incommensurate, especially on close-packed substrates.

An alkali metal atom can in essence be thought of as a rare gas with one valence electron; therefore alkalis should be one of the simplest chemisorbed species. In the classical picture of alkali adsorption (to be discussed in Chapter Two) the valence electron is transferred to the substrate, creating a dipole for each adsorbate. The interaction between adsorbates is thus a strong repulsive one, causing them to spread out on the surface and making them also likely to form incommensurate structures.

Amounts of material adsorbed on a surface are measured in monolayers (ML). By convention, a monolayer corresponds to having the same number of overlayer particles as there are in the first atomic layer. One monolayer of particles therefore does not necessarily correspond to the saturation coverage for the first layer.

The experiments presented in this thesis involve the adsorption of alkali metals and of rare gases on Ag(111), and their coadsorption. Chapter Two will provide some theoretical background for the work. This will include a brief description of LEED theory, a historical review of the theory of alkali metal adsorption, and a description of theories describing rotational epitaxy, a phenomenon which results from the competition of the substrate corrugation and inter-adsorbate forces mentioned above. Chapter Three will describe the experimental apparatus in detail, discuss some of the methods of data collection and analysis used, and will present an analysis of uncertainties present in the LEED measurements. Chapter Four will report on experiments performed on the clean Ag(111) surface. These were done primarily as a prerequisite to the adsorption experiments of Chapters Five and Six. Chapter Five will present the results of a detailed study of alkali metals adsorbed on Ag(111). This will include coverage-temperature phase diagrams, descriptions of various disordering transitions, and the results of structural determinations done for the commensurate phases. Chapter Six will report on a variety of experiments in which Ar, Kr, or Xe were coadsorbed with various submonolayer and monolayer amounts of alkali metal. The goal of these experiments is to understand the interactions between the two species. Each of the chapters presenting experimental results will also present a summary of previous work relevant to the experiment. Finally Chapter Seven will summarize the results.

References

¹ C. J. Davisson and L. H. Germer, Phys. Rev. 30, 705 (1927).

² A. Zangwill, *Physics at Surfaces*, Cambridge University Press, New York (1988).

Chapter Two

Theory

2.1. Low-Energy Electron Diffraction

As a surface science technique, LEED is most often used in a qualitative way. The diffraction pattern is monitored visually during sample preparation to determine the degree of order of the surface, and during experiments to qualitatively identify overlayer structures. However, since the 1960's LEED has also been used extensively to quantitatively determine structural properties of surfaces.

The theory for quantitative analysis of LEED patterns can be divided into two categories: kinematical and dynamical. Kinematical theory has its origin in x-ray kinematical theory, and makes the approximation that each electron undergoes only one scattering event. It is useful for determining the periodicity of the overlayer as well as the lateral morphology of the surface, including features such as the amount of order, step and island distributions, and domains. However, since electrons interact so strongly with matter, the single scattering approximation breaks down, preventing the determination of exact atomic positions by kinematical theory. Dynamical LEED theory accomplishes this by explicitly calculating the scattering from the atoms in the surface region, incorporating multiple scattering effects. This makes dynamical LEED a very calculation intensive process, which has limited its use. However several advances in techniques used for these calculations have been developed in the last decade which, along with the ever-increasing speed of computers, allow calculations to be done more easily than previously.

The experiments reported in this thesis make use of both kinematical and dynamical LEED theory. This section will give an overview of kinematical and dynamical LEED theory. Most of the dynamical theory calculations were done by collaborators (named in Chapter Five), so the dynamical theory section will not present much detail. Additional information may be found in references 1, 2 and 3.

2.1.2. Kinematical Theory

Consider a plane wave with wave vector \mathbf{k}_0 incident on the surface of a crystal, as shown in Figure 2.1. The amplitude of the wave at the position of an atom \mathbf{r}_n is

$$\exp(i\mathbf{r}_n \cdot \mathbf{k}_0) \quad (2.1)$$

If the wave is scattered by the atom with an amplitude f_n , then the scattered amplitude at a detector far from the crystal at a position r_d will be

$$J = \exp(i\mathbf{r}_n \cdot \mathbf{k}_0) f_n \exp[-i(\mathbf{r}_n - \mathbf{r}_d) \cdot \mathbf{k}] \quad (2.2)$$

Since diffraction implies elastic scattering, the magnitudes of \mathbf{k}_0 and \mathbf{k} must be equal. Adding up the scattered wave from atom in the crystal and (for now) neglecting attenuation of the beam as it travels through the material, we obtain

$$J = \exp(i\mathbf{r}_d \cdot \mathbf{k}) \sum_n f_n \exp(i\mathbf{r}_n \cdot \Delta\mathbf{k}) \quad (2.3)$$

where $\Delta\mathbf{k} = \mathbf{k} - \mathbf{k}_0$. Since the measurable quantity is the square of this value, we will drop the constant phase factor in front. If the atoms in the solid are in a perfect crystalline array, then the position of an atom can be expressed as

$$\mathbf{r}_n = \mathbf{r}_{m_1, m_2, m_3, j} = \mathbf{r}_j + m_1 \mathbf{a}_1 + m_2 \mathbf{a}_2 + m_3 \mathbf{a}_3 \quad (2.4)$$

where \mathbf{a}_i represent the basis vectors of the unit cell, m_i are integers, and \mathbf{r}_j is the position of the j^{th} atom within the unit cell. The scattered wave function will then be

$$J(\Delta\mathbf{k}) = \left[\sum_j f_j \exp(i\Delta\mathbf{k} \cdot \mathbf{r}_j) \right] \cdot \left[\sum_{m_1, m_2, m_3}^N f_n \exp[(m_1 \mathbf{a}_1 + m_2 \mathbf{a}_2 + m_3 \mathbf{a}_3) \Delta\mathbf{k}] \right] \quad (2.5)$$

where N is the number of atoms in the crystal. The measured electron intensity, also called the kinematic

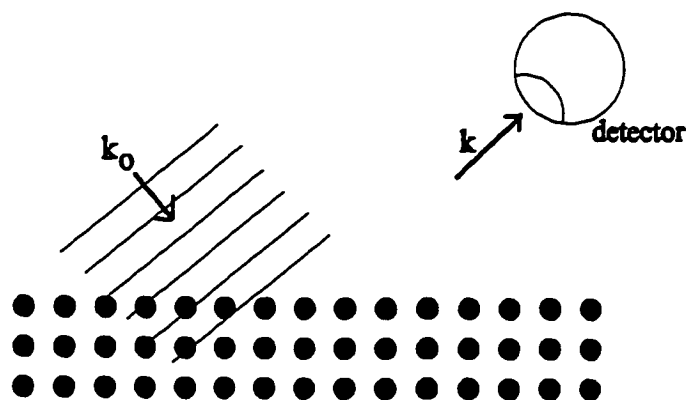


Figure 2.1. Scattering of a plane wave from an array of atoms.

structure factor, is equal to the square of the wave function:

$$I(\Delta\mathbf{k}) = |J(\Delta\mathbf{k})|^2 \quad (2.6)$$

If there are one or only a few atoms in the unit cell, then the first factor in Equation 2.5 will be either constant or slowly varying in $\Delta\mathbf{k}$. For very large N , the second factor becomes a delta function with peaks given by the condition

$$\Delta\mathbf{k} \cdot (m_1\mathbf{a}_1 + m_2\mathbf{a}_2 + m_3\mathbf{a}_3) = 2\pi n \quad (2.7)$$

where n is an integer. This can be equivalently expressed as

$$\Delta\mathbf{k} = \mathbf{g}_{hkl} = h\mathbf{g}_1 + k\mathbf{g}_2 + l\mathbf{g}_3 \quad (2.8)$$

where h , k , and l are integers and \mathbf{g}_i are the reciprocal lattice vectors for the lattice and are defined such that

$$\mathbf{g}_i \cdot \mathbf{a}_j = 2\pi\delta_{i,j} \quad (2.9)$$

where n is an integer. The integers h , k , and l are the Miller indices and Equation 2.9 is the Bragg condition. The points (h,k,l) can be thought of as forming a lattice in what is called reciprocal space. Then the Bragg condition can be represented using vectors in this space, as shown in Figure 2.2. If the initial wave vector \mathbf{k}_0 is drawn with its tip at the $(0,0,0)$ point and the scattered wave vector is placed as shown, then the Bragg condition is fulfilled when the sphere swept out by rotating \mathbf{k} intersects with a reciprocal lattice point. This is called the Ewald Sphere construction, and is a convenient way of

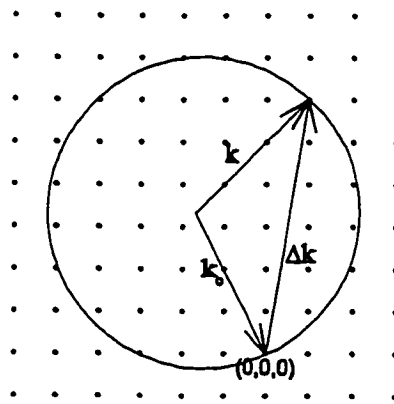


Figure 2.2. Ewald Sphere construction for diffraction in three dimensions. Diffraction occurs when $\Delta\mathbf{k}$ equals a reciprocal lattice vector.

determining when the Bragg condition will be satisfied. Changing the energy of the incident beam changes the magnitude of the k vectors, which changes the radius of the sphere so that different points are intersected.

The fact that electrons interact so strongly with matter causes two effects which are difficult to deal with theoretically: strong multiple scattering and attenuation of the wave as it travels through the material. Multiple scattering is completely ignored in kinematical theory. The effect of attenuation is to allow the detector to record scattering mainly from just the first few atomic layers. Thus the long-range periodicity which causes the Bragg diffraction delta function exists only in the x - y plane, and not in the z direction. This effectively causes the reciprocal space shown in Figure 2.2 to be two-dimensional rather than three, and the diffraction condition becomes

$$\Delta k_{\parallel} = g_{\parallel} \quad (2.10)$$

The reciprocal lattice points can then be thought of as rods in the 3-dimensional reciprocal space, since there is no condition in the z direction necessary for diffraction. Figure 2.3a shows the Ewald Sphere construction in this case. The diffraction condition has become much less stringent, and diffraction of one or more beams occurs for any incident wave vector larger than half the reciprocal lattice spacing.

Figure 2.3b shows the geometry for a typical normal incidence LEED experiment. By comparing Figures 2.3a and b it is evident that the diffraction beams seen on the LEED screen represent a direct projection of reciprocal space onto the screen. Thus the lateral surface symmetry and periodicity as well as any overlayer lattice parameter and orientation can be directly determined from the positions of the diffraction beams.

Changing the energy of the incident electron beam changes the radius of the Ewald sphere shown in Figure 2.3a, or equivalently, changes the scaling of reciprocal space with respect to the screen in Figure 2.3b. The effect on the diffraction pattern is to change the positions of the diffracted beams with energy.

In addition to changing their position, the relative intensities of the beams also change with energy. This can be thought of as a modulation in the intensity of the reciprocal space rod with changing Δk_{\parallel} . This is caused by the fact that the scattering is not from atoms in a single plane, but over a small z range in real space. (If the depth from which scattered electrons could be detected were increased, these "modulated" rods would change to rods with sharp peaks in them, eventually going to the case of 3-D diffraction.) The modulation in the rod intensity contains information about the first factor in Equation 2.5, and in fact if the kinematic approximation were valid then the atomic positions within the unit cell could be directly obtained from the reciprocal space modulation. However because of reasons which will be discussed in the next section, the atomic positions cannot be directly determined from the spectra.

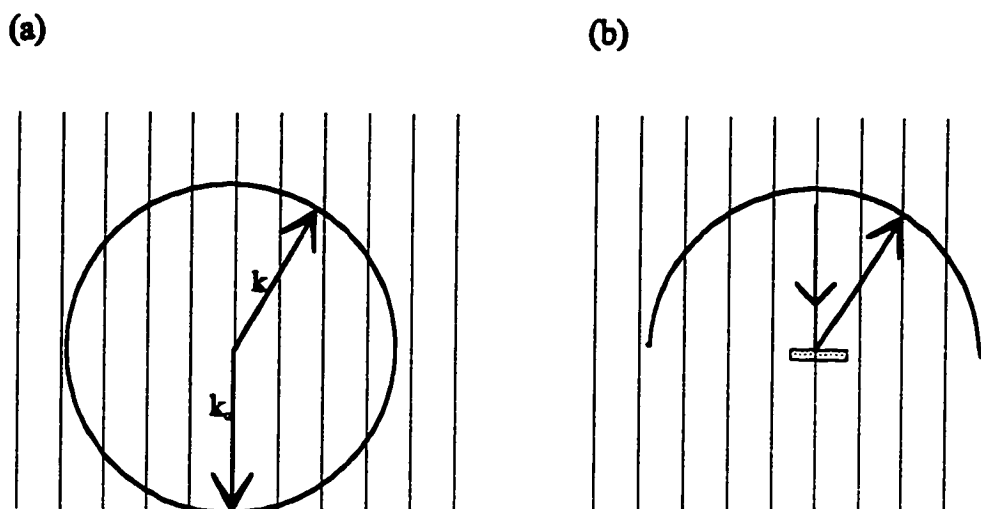


Figure 2.3. Ewald sphere construction for two-dimensional diffraction compared to the geometry used in a LEED experiment. (a) Ewald sphere construction for two-dimensional diffraction. (b) Simplified LEED experiment. A LEED experiment yields a projection of the reciprocal space rods onto the screen.

For a crystal of infinite extent and a perfect LEED instrument, the diffraction beams will be true delta functions – they will be infinitely sharp and narrow. The finite length over which there are correlations between the positions of the atoms will make N finite, broadening the peaks. This broadening can be used to determine the type and amount of disorder in a surface.

2.2. Dynamical Theory

In cases where kinematic scattering provides a good approximation, Equation 2.5 can be reverse-transformed to provide the exact positions of the scatterers. This is true for x-ray and neutron diffraction, since the probability of multiple scattering events is very low. However, because of a number of reasons which will be discussed below, electron diffraction is more complicated and the scattered intensities cannot be transformed directly to yield exact atomic positions. Instead, a number of trial structures must be considered, and the diffraction beam intensities calculated for each one. Each of these scattering spectra are compared to the experimental data (usually called $I(E)$ spectra) and the best fit spectra is selected. The structural parameters are then refined to determine the exact atomic positions, comparing the calculated spectra to the experimental data on each iteration.

There are several reasons why electron scattering is more difficult than most other kinds of scattering. First of all, electrons have a much higher scattering cross section and so multiple scattering events dominate. The multiple scattering can be incorporated into f_a , the atomic scattering factors by summing up the contributions of all scattering paths ending with that atom.

Another aspect of electron diffraction which makes it more difficult is that the scattering of electrons with the atomic cores is more complicated than the point-source scattering assumed in kinematic theory. An electron traveling through a region of lower potential around an ion core will experience an increase in wavelength or “speeding up” as it traverses the region, causing the phase of the scattered wave to be shifted by some amount from the phase of the incident wave. The scattering is then approximated as scattering from a point source, but the wave is discontinuously shifted by the amount of the calculated phase shift, as shown in Figure 2.4. This can equivalently be thought of as introducing an imaginary component to the f_a values in Equation 2.5.

An additional aspect, which was ignored in the kinematic section, is the potential step at the surface caused by the surface dipole. In effect this causes the entire region inside the solid to be offset by some negative potential, V_o , called the inner potential. Since all the scattering takes place inside the solid, the only effect of this is to offset the energies of the features in the $I(E)$ curves by the amount V_o . The value of V_o may be weakly dependent on energy.

The final aspect which makes electron diffraction difficult is attenuation. Attenuation is caused by inelastic scattering of the electrons. Mathematically this is handled by introducing an imaginary part to the inner potential, so that the inner potential is given by

$$V = V_o + iV_{oi} \quad (2.11)$$

This causes the amplitude of any wave solution to the Schrödinger equation to decay exponentially with distance.

Due to these complications, calculation of the diffracted intensities is rather demanding computationally, and several different methods have been developed to perform the calculation in as efficient a manner as possible. The method used in our case is that of Van Hove and Tong.² This method will be briefly described in the remainder of this section.

The calculation itself can be divided into three steps: (a) calculation of the scattering from individual ion cores (also called calculating the phase shifts), (b) calculation of scattering from coplanar layers of atoms (including multiple scattering within the layer), and (c) calculation of scattering (and multiple scattering) from and between layers.

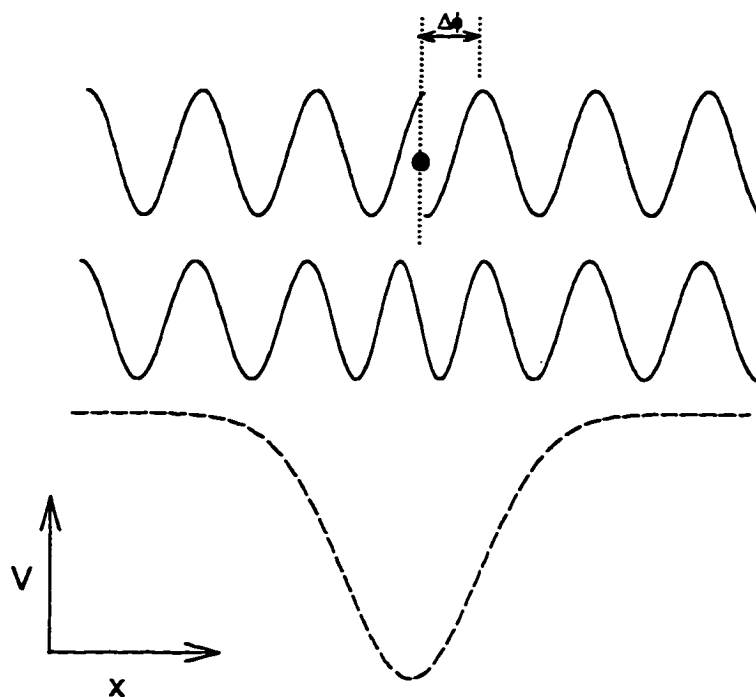


Figure 2.4. An electron scattered from an ion core potential well. The dotted curve represents the well, and the lower solid curve represents the electron wave function. As the wave propagates through the well, its frequency changes, resulting in a shift of the phase of the scattered wave function. The Scattering is approximated by the top curve, where the electron scatters from a point source but undergoes a phase shift of $\Delta\phi$.

The calculation of phase shifts begins by assuming spherically symmetric potentials for the ion cores. For each chemically inequivalent atom a self-consistent Hartree-Fock calculation of the atomic orbitals is done, and the result is used to compute the charge density as function of radius. A guess is made to the structure of the surface, and the charge densities are superimposed on each other in this configuration. (The atomic scattering is not strongly dependent on the exact positions of the atoms, so the exact arrangement does not have to be known.) The potential inside spherical regions, called “muffin tins”, around each ion core is then calculated from the charge density. The muffin tin radius is usually set so that they just touch, as shown in Figure 2.5. Between the muffin tin regions the potential is set to the constant inner potential value, and the spherical potentials around the ion cores are offset to make the potential continuous at the muffin boundary. Finally, for each inequivalent atom the magnitude of the phase shift for a wave scattered from the potential well is calculated. These phase shifts must be calculated as a function of electron energy. Since the wave is usually expanded in spherical harmonics, the phase shift is calculated for each harmonic up to some cutoff at which electron propagation becomes insignificant. In the succeeding steps the scattering from an atom can then be obtained simply by shifting the phase of the wave by the phase shift which has been previously calculated.

For the next step it is necessary to divide the atoms into layers of periodically arrayed atoms which are coplanar, and the scattering from each layer is calculated. To do this, all possible scattering paths within the layer must be summed. This intralayer scattering calculation is done by expanding the

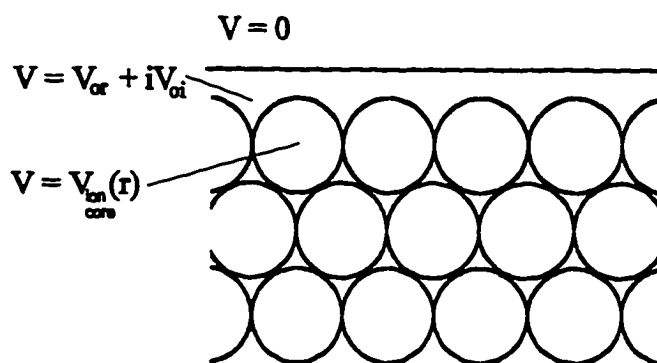


Figure 2.5. Muffin tin model of a solid. The potential around the ion cores is approximated as being spherically symmetric. The regions in between the ion cores are at a constant potential $V_0 + V_{0i}$. There is a potential step at the surface where the potential goes discontinuously to zero.

wave in spherical harmonics, and using the phase shifts for each atom which have been previously calculated. The spherical harmonic expansion is terminated after some order l_{max} , usually 9 or 10.

Finally, the interplanar scattering is calculated. In our case this was done by a method called layer doubling.¹ In this scheme the layers are divided up into pairs, and the scattering from each pair of layers is calculated. This includes all multiple scattering paths between the two layers which result in a non-negligible intensity. Next the pairs themselves are grouped as pairs, and the same procedure is followed. This is done until layers have been included deep enough that the electron wave function has dropped to negligible values. For the interlayer scattering, it is more efficient to expand the wave function in plane waves rather than spherical harmonics. The plane waves used are just the k vectors corresponding to the diffraction beams g_{hk} expected for the structure being solved.

One problem encountered in this procedure is that if the inter-layer spacing is too small (less than about one Ångström), the plane wave representation does not converge well. For many adsorbate structures, for example a buckled substrate, this can be a problem. The solution is to combine several layers into one composite layer, and do the entire composite layer in spherical harmonics before switching to the plane wave expansion.

The scattering calculation also includes temperature effects. This is done by simply including a Debye-Waller factor into the scattering amplitudes from each atom or layer. One problem presented by this approach is that it treats each atom as if it were vibrating completely independently from all the atoms surrounding it. A second problem is that it only allows for the possibility of isotropic vibrations. It is quite likely that the vibrations of atoms at the surface of a solid will be rather anisotropic. Anisotropic vibrations can be included after a fashion by using a different Debye temperature for scattering between the layers than what was used for the intralayer scattering. This is the standard method used with the Van Hove calculation package,⁴ and was used in the calculations for the data presented in this thesis.

A more accurate method of including anisotropic vibrations is the split positions method developed by Over.⁵ In this method, instead of summing the scattering for an atom from a single atomic position, two or more positions representing the distribution of positions occupied by the atom as it vibrates are used. Effectively the one atom is treated as several, each with fractional scattering power. The only difference is that multiple scattering between the split positions is suppressed. This method, while potentially more accurate, is effectively equivalent with the Van Hove method to the extent that intralayer scattering in the adsorbate layer can be neglected. Fortunately, this has been shown to be the case for single alkali metal overlayers.⁶

The result of the calculations described in the preceding paragraphs is a set of $I(E)$ diffraction intensities for a particular structure. In order to compare these with the experimental spectra, some means of evaluating the quality of agreement is necessary. In order to do this, a number of Reliability factors

(referred to commonly as R factors) have been developed. A simple R factor might just calculate the sum of the differences squared between the two sets of spectra. However, since the information is mostly contained in the positions of peaks in the spectra rather than the relative intensities between the beams, it is better to use an R factor which puts more weight on the peak positions. The Pendry R factor does just this, by using the logarithmic derivative of the intensity rather than the intensity itself. The Pendry R factor⁷ is given by

$$R_P = \frac{\int (Y_{\text{exp}} - Y_{\text{calc}})^2 dE}{\int (Y_{\text{exp}}^2 + Y_{\text{calc}}^2) dE} \quad \text{where } Y = \frac{L}{1 + V_{\text{oi}}^2 L^2} \text{ and } L = \frac{dI/dE}{I} \quad (2.12)$$

V_{oi} in this expression is the imaginary value of the inner potential. Using this R factor, two identical spectra would yield an R factor of zero, while spectra which are completely uncorrelated should yield a value of one. The calculations for the experiments in this thesis were done using the Pendry R factor.

The use of a standard R factor to objectively evaluate the level of agreement between experiment and calculation becomes very important for the next stage of the structure determination. One or more of the structural (i.e. atomic positions) or non-structural parameters (such as the value of the inner potential, Debye temperature and anisotropic vibration enhancement factors) are changed, and the entire calculation is repeated. The level of agreement is again evaluated, and the process is repeated until the minimum R factor is found.

A variation on this method, called Tensor LEED,⁸ has recently been developed to increase the efficiency of the search for the optimum structure. In this method, the full dynamical calculation is first done as described in the previous paragraphs. Then a perturbation theory is used which calculates the changes in the spectra due to small changes in the structural parameters. The structural parameters are varied by a computer program using an automatic search algorithm until the minimum R factor is found. Of course if the parameters need to be moved too far (more than about 0.5 Å) from the positions at which the dynamical calculation was originally done, the full calculation must be repeated. The perturbation calculation requires is much less computer intensive than the full dynamical calculation, so a large savings in time is gained by using this method. In fact since the development of Tensor LEED it has become feasible for the first time to perform these calculations on personal computers. Although most of the calculations for the experiments in this thesis were done in the former way, some of the simpler ones were done using Tensor LEED on a Pentium personal computer.

It has been shown that LEED $I(E)$ spectra contain primarily information from the local atomic structure at the surface, while the positions of the beams in reciprocal space (i.e. the kinematic structure factor) contains information about the long-range order and periodicity.⁹ Because of this, $I(E)$ curves from structures which have different long-range periodicity but the same local geometry will usually look

very similar if the beams being compared are from similar positions of reciprocal space. Thus in some cases it is possible to identify the adsorption site for system simply by comparing the spectra to those of another structure which has already been solved. This technique, called LEED Fingerprinting, has been discussed in detail in reference 10.

A consequence of the way that LEED calculations are done is that the technique is only applicable to commensurate phases. The reason for this is that in order to calculate the multiple scattering between all of the atoms in the structure it is necessary to have a finite unit cell over which the entire structure repeats itself. This is not true for incommensurate phases, since the overlayer periodicity does not correspond to a superlattice of the substrate. In principle incommensurate structures could be dealt with by constructing a very large unit cell, effectively changing the problem into that of a very high order commensurate phase. The problem that arises however is that the computational resources needed are strongly dependent on the size of the unit cell, so that for even moderately large unit cells the requirements become prohibitive. Ways to get around these problems have been explored,¹¹ but they have not yet been accepted into standard practice for LEED structure determinations. For this reason the calculations for the experiments reported in this thesis are restricted to commensurate phases.

2.2. Alkali Metal Adsorption

Alkali metals, having only one valence electron, have long been considered one of the simplest metals. The single valence electron is not tightly bound and therefore relatively free to interact with other species, while the next electron shell is completely filled making the remaining ion very chemically inert. Since chemisorption of an atom at a surface is considered to be a rather complicated problem, naturally theorists started by considering what appeared to be a simple system – alkali metal adsorption. As work was done over the years however it became apparent that even this simplest of systems displays a surprising degree of complexity.

In the classical model of alkali metal adsorption, an alkali metal atom becomes ionized and its s electron is transferred to the metal. The positively charged ion above the metal surface sees a negative image charge "beneath" the surface, forming a surface dipole as shown in Figure 2.6. Because of the repulsive dipole interaction, at low coverages the adsorbed alkali layer will spread uniformly across the surface. As more alkali metal is deposited the layer will compress. As the dipoles are forced closer together, they will start to depolarize each other and the overlayer will eventually become metallic.

This model, although simple, was good enough to qualitatively explain the characteristic work function signature seen in alkali metal adsorption, an example of which is shown in Figure 2.7. Upon initial alkali deposition, the work function decreases linearly with alkali density due to the dipole of the alkali atom, which is opposite of the dipole created by the electron spill-out of the clean metal surface. From the slope of the initial decrease, the initial alkali metal dipole moment per adatom in Debye can be calculated:

$$p = \frac{10^{16}}{3} \cdot \frac{\Delta\phi}{4\pi n} \quad (2.13)$$

where $\Delta\phi$ is the change in the work function in eV and n is the adsorbate density per square centimeter. As the atoms become more closely packed the dipoles begin to depolarize each other, causing a slowing in the work function decrease. By assuming a polarizability α for the adcomplex, the effect of the depolarization on the work function change can be modeled using the Topping equation:¹²

$$-\Delta\phi = \frac{eNp}{\epsilon(1 + 9\alpha N^{3/2})} \quad (2.14)$$

where p is the initial dipole moment, N is the surface atomic density, e is the charge of an electron, and ϵ is the permittivity of vacuum. A fit using this equation is shown in Figure 2.7. Finally at about 1 monolayer the overlayer becomes metallic and the work function approaches a value close to that of the bulk alkali. In this coverage region the Topping equation does not provide as good a fit, because it does not take into account the formation of metallic bonds between the adatoms.

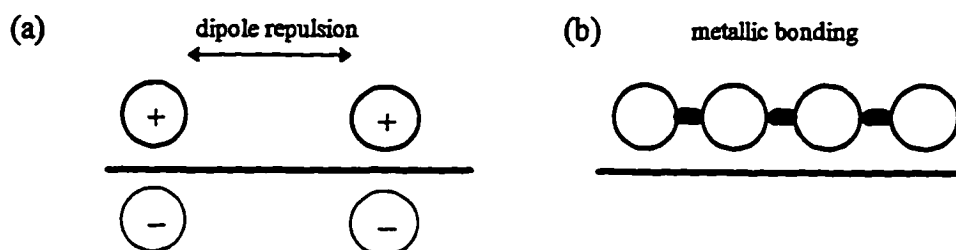


Figure 2.6. Classical model of alkali metal adsorption on a metal surface. (a) Low coverage: valence electron is transferred to the substrate and alkali atom forms a dipole with an image charge in the metal. (b) At higher coverages, the alkali atoms are forced closer together. The dipoles depolarize and metallic bonds form within the layer.

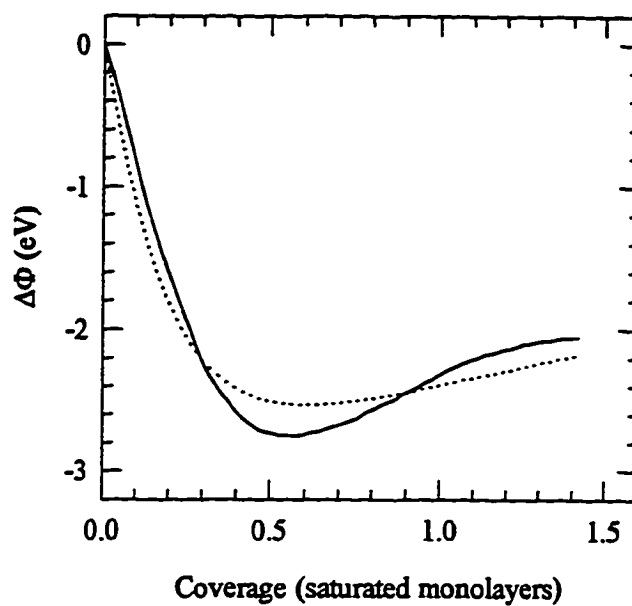


Figure 2.7. Work function behavior for alkali metal adsorption. The solid curve represent data is for K / Ag(111).¹⁵ The dotted curve is a fit based on Equation 2.14.

This simple model to explain alkali adsorption was expanded by Gurney.¹⁴ As the adatom approaches the surface, the s valence level becomes broadened into a band which will be partly occupied up to the Fermi level, as shown in Figure 2.8. Interaction with the surface causes the band to shift upward, and since alkali ionization energies are usually of the same order of magnitude as metal work functions, the midpoint of the resonance will end up above the Fermi level so that the band is mostly unoccupied. (This corresponds to the ionization of the alkali atom in the classical picture.) As the field at the surface due to the dipoles increases with increasing coverage, the level shifts downward in energy and becomes more fully occupied as charge is back donated into the level. Density functional calculations by Lang in 1971 for alkali adsorbates on jellium supported this picture and yielded work function curves which agreed qualitatively with experiment, although quantitative agreement was not obtained.¹⁵

It was widely believed that this change in electron distribution could be thought of as a change in the chemical nature of the chemisorption bond. It was thought that at low coverage when charge is transferred from the adsorbate to substrate, the adsorbate could be pictured as being ionically bound to the surface. The back-donation of charge at higher coverages then causes a change to a more covalent chemisorption bond. Since in general the effective radius of an ionically bound atom is lower than that of the same atom bound covalently, it was assumed that an increase in chemisorption bondlength would accompany the supposed change from ionic to covalent bonding.

In 1990 Ishida published a study which expanded on Lang's density functional work for alkali on jellium.¹⁶ However, the results indicated that very little if any charge was transferred to the substrate at any coverage. Instead the s level of the adatom becomes hybridized with the substrate states and the bond becomes strongly polarized toward the substrate. This charge polarization, rather than charge transfer, causes the work function behavior. The study concluded that alkali adsorbates are covalently bonded to the substrate at all coverages, contradicting previous notions.

This controversy prompted a new interest in alkali metal adsorption systems. Subsequent studies found a number of surprising results, including unexpected adsorption sites, surface alloying, and condensation transitions, none of which could be explained adequately by previous theories. (These experimental observations will be discussed further in the chapter on alkali metal adsorption.) One particular system which stands out is the alkali / Al(111) system. This would have previously been considered a prototypical simple adsorption system because Al is such a simple metal; however it was found to exhibit all three of the surprising phenomena mentioned above. At low temperatures the adatoms reside in the top sites rather than the previously assumed three-fold hollows, and at higher temperatures the adatoms occupy substitutional sites in the top substrate layer. In addition, the overlayer was found to undergo a condensation transition from a dispersed phase to a dense metallic phase at a particular coverage.

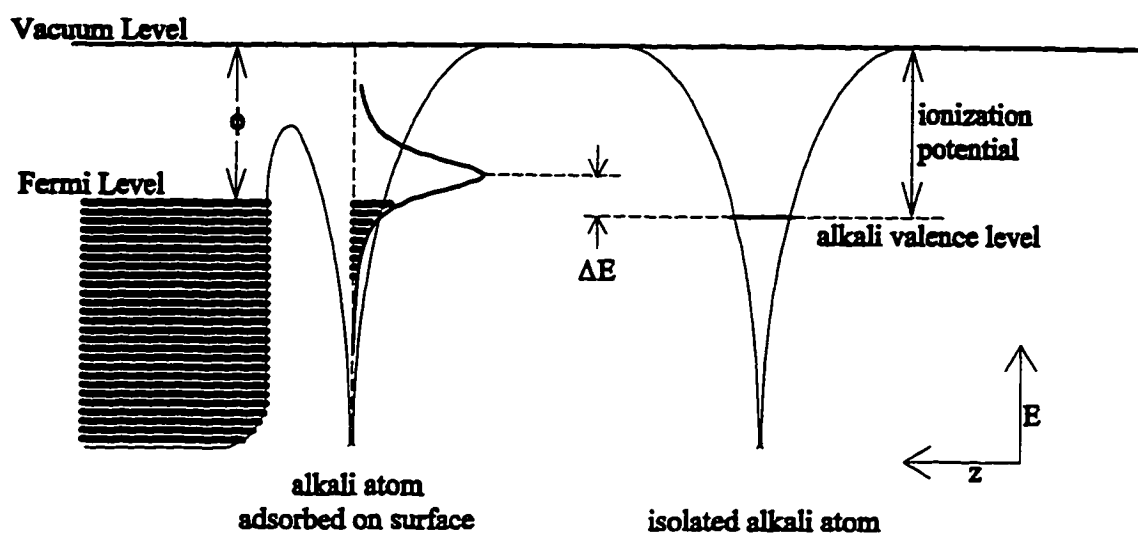


Figure 2.8. Gurney model of alkali metal adsorption on a metal surface. The s valence level shifts upward by an amount ΔE (due to interaction with an image charge) and broadens into a band as the alkali atom approaches the surface. When it gets close enough charge transfers from the level to the substrate and the level is fractionally occupied up to the Fermi level. Depolarization of the adatoms upon increasing coverage causes the level to shift downward and a back donation of charge to the level.

These new experimental results in turn prompted new theory calculations. In particular, density functional theory calculations were done by Scheffler et al. for alkali adsorbates on Al(111).^{17,18} Instead of using jellium for a substrate, they used discrete atoms; this enabled them to calculate the relative energies for adsorption into different sites. Their results turned out to be consistent with experiment, reproducing both the island condensation and the top-site adsorption. The island condensation was found to be driven by a metallization of the adsorbate-adsorbate bond at a critical coverage. The substitutional site adsorption was found to be possible because the Al(111) surface has an unusually low energy of vacancy formation for vacancies in the periodicity of the overlayer in this case, a $(\sqrt{3} \times \sqrt{3})R30^\circ$. In addition, they found that the top site was favored over the three-fold hollow sites, but that the large substrate rumpling that accompanies top site adsorption was a necessary component for it to occur.

Figure 2.9 shows a contour plot of the charge distribution obtained by Scheffler for the low coverage and the high coverage case. It is evident that there is charge redistribution as a function of coverage, which caused Scheffler to argue that the old model of an ionic-to-covalent transition was not entirely inappropriate, seemingly contradicting Ishida's conclusion. However, the charge distribution shown in Figure 2.9 was in fact similar qualitatively to that obtained by the calculations of Ishida. Therefore it is now thought that much of the ionic-or-covalent controversy was a matter of semantics, and that the concepts of ionic or covalent bonding are not applicable for an adsorbate chemisorbed to a surface.

2.3. Rotational Epitaxy

Rotational epitaxy, the alignment of an incommensurate overlayer at a non-symmetry angle with respect to the substrate, is a general phenomenon which has been observed for diverse systems including rare gases on graphite, metal overlayers, and clean reconstructed metal substrates. It occurs for incommensurate overlayers which are either elastically deformable or of finite size. If the overlayer lattice were infinite and completely rigid, its energy would be the same for all orientations and it would have no preferred orientation angle. However if the atoms are able to relax slightly toward the bottoms of the substrate potential wells then the degeneracy is broken and there will be one or more angles that correspond to an energy minimum. The fact that the overlayer extends over a finite area can also cause the energy to be dependent on rotation angle. A number of models have been developed to deal with rotational epitaxy. Some of these are based solely on geometrical arguments, while others also include information about the elastic properties of the overlayer.

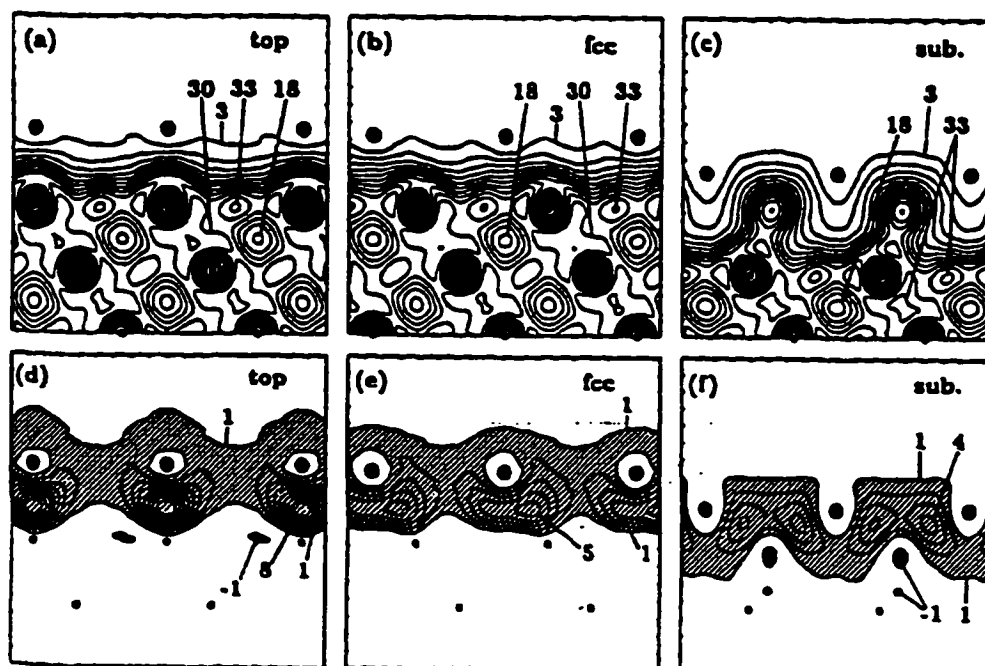


Figure 2.9. Charge density contours calculated for Na / Al(111) using the LDA method.¹⁷ (a) - (c) show the charge density contours in a plane perpendicular to the surface for three different adsorption sites: top, FCC hollow, and substitutional. The large dots represent the positions of the Na ion cores. (d) - (f) show the difference in charge densities between the case of Na adsorption and the clean surface. It can be seen that a substantial amount of charge has flowed into the region between the overlayer and the substrate, for the top and FCC site calculations.

2.3.1. Bohr-Grey Model

One geometrical model was introduced by Bohr and Grey.¹⁹ When an incommensurate lattice is placed on top of a substrate lattice, it will form periodically spaced regions (domains) where the overlayer atoms are closer to the commensurate positions. The spatial arrangement of these domains is just the Moiré interference pattern between the two lattices, and is completely determined by the misfit and orientation angle. This can be seen in Figure 2.10. The Bohr-Grey model proposes that the rotation angle will be such that these domains align themselves with a high symmetry direction of either the substrate or the overlayer. For a hexagonal lattice, this requirement can be expressed by the equation

$$\cos \varphi = r_{AS} \sin^2 \Psi_S + \cos \Psi_S \sqrt{1 - r_{AS}^2 \sin^2 \Psi_S} \quad (2.15)$$

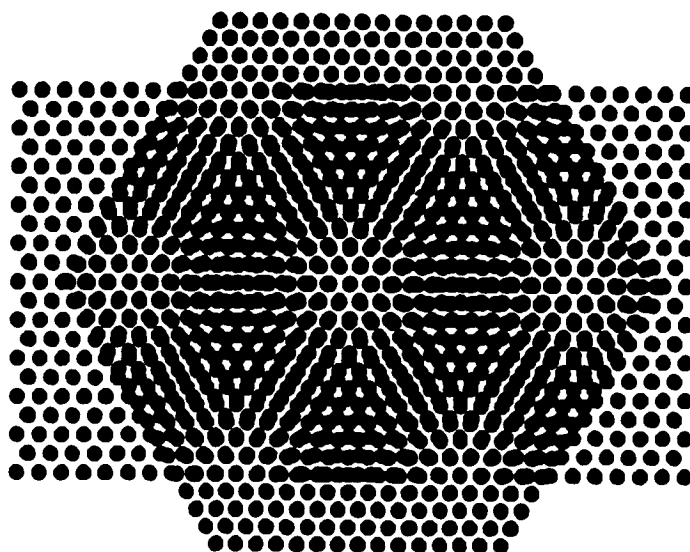
where r_{AS} is the ratio of adsorbate to substrate lattice spacing and Ψ_S is a high-symmetry angle with respect to the substrate. For the case of alignment of the domains with a high symmetry angle of the overlayer, r_{AS} is exchanged for $1/r_{AS}$ and Ψ_A is used instead of Ψ_S . The trajectories described by Equation 2.15 are shown in Figure 2.11, for Ψ_S and Ψ_A values of 30° and 60° . Misfit is defined with respect to the commensurate $p(2 \times 2)$ structure: $m = (d - 2d_S)/d_S$, where d is the overlayer lattice spacing and d_S is the substrate lattice spacing.

The Bohr-Grey model for rotational epitaxy is especially attractive because it consists of a simple geometrical principle which is generally applicable to diverse systems irrespective of their details. However, there is no obvious physical reason why it should hold. In order to provide some physical basis for the agreement of this model to experimental systems, Bohr and Grey have published a more recent study in which they performed energy calculations for a rotated hexagonal overlayer on a rigid hexagonal substrate.²⁰ The overlayer was held completely rigid, which for an infinite lattice would cause degeneracy in the energy with respect to rotation angle. However, they investigated the effects of using an overlayer lattice of finite size, and found that a finite overlayer broke the degeneracy and caused trajectories of minimum energy which coincided exactly with the results of Equation 2.15. They concluded that in most cases rotational epitaxy was determined by finite size effects during overlayer nucleation, rather than the static lattice distortions.

2.3.2. Coincidence Lattice Model

A second geometrical model, suggested by Fuselier²¹ and applied successfully to some alkali overlayers,²² proposes that the overlayer rotational behavior will be determined by coincidence lattices, or higher order commensurate periodicities. These are particular misfit and angle values where the overlayer

(a)



(b)

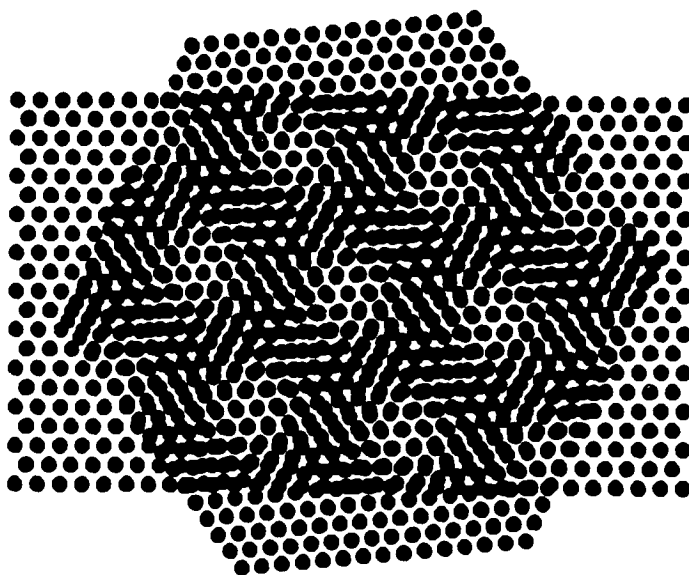


Figure 2.10 Moiré interference fringes between two incommensurate lattices. The rectangular patch represents the substrate, and the hexagonal patch represents a rotated incommensurate overlayer. Large-lengthscale domains will form in the periodicity of the light and dark areas seen in the overlapping region. The periodicity of the domains depends on the misfit and orientation angle between the two lattices.

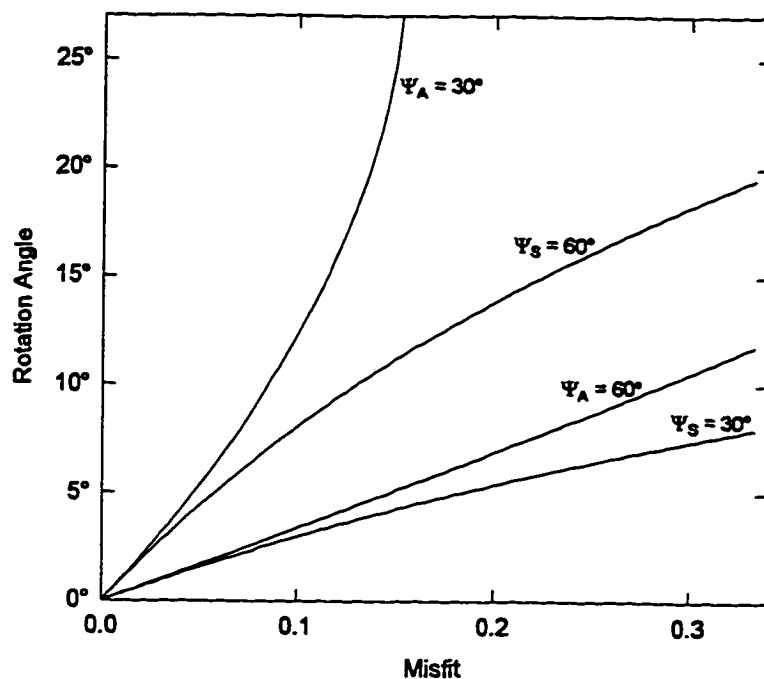


Figure 2.11 . Bohr-Grey trajectories for rotational epitaxy. The trajectories were calculated using Equation 2.15.

and substrate lattices coincide with some superlattice periodicity. Plotted on an angle versus misfit graph, these coincidence lattice points lie along branches. It seems reasonable that an overlayer might follow one of these branches quasi-continuously as the misfit changes. Coincidence lattice points calculated for a hexagonal overlayer on a hexagonal substrate are shown in Figure 2.12. Figure 2.13 shows the method used to calculate these points. Consider a hexagonal substrate with unit lattice parameter and an overlayer with a lattice parameter of a_o which is rotated by some angle ϕ . Substrate lattice positions can be expressed as $\mathbf{r}_s = m_1 \mathbf{b}_1 + m_2 \mathbf{b}_2$, and overlayer positions as $\mathbf{r}_a = n_1 \mathbf{a}_1 + n_2 \mathbf{a}_2$, where n_1 , n_2 , m_1 , and m_2 are integers. The overlayer is in a higher order commensurate structure if a superlattice unit cell of the substrate can be found where each corner also corresponds to an overlayer lattice position. We wish to find all pairs of (a, ϕ) for which this condition holds, up to some maximum superlattice unit cell length. The two lattices always coincide at the origin, so the coincidence must be checked at two additional corners. This is done by taking some substrate lattice point $m_1 \mathbf{b}_1 + m_2 \mathbf{b}_2$ and forcing it to coincide with an overlayer point $n_1 \mathbf{a}_1$ ($n_2 = 0$), by fixing ϕ and choosing integers n_1 to yield values of a_o within a range of interest. For each a_o value, vectors $n_2 \mathbf{a}_2$ ($n_1 = 0$) are generated for a range of n_2 values up to a maximum superlattice unit cell size, and each is checked to see if it lies within 1% of any substrate lattice position.

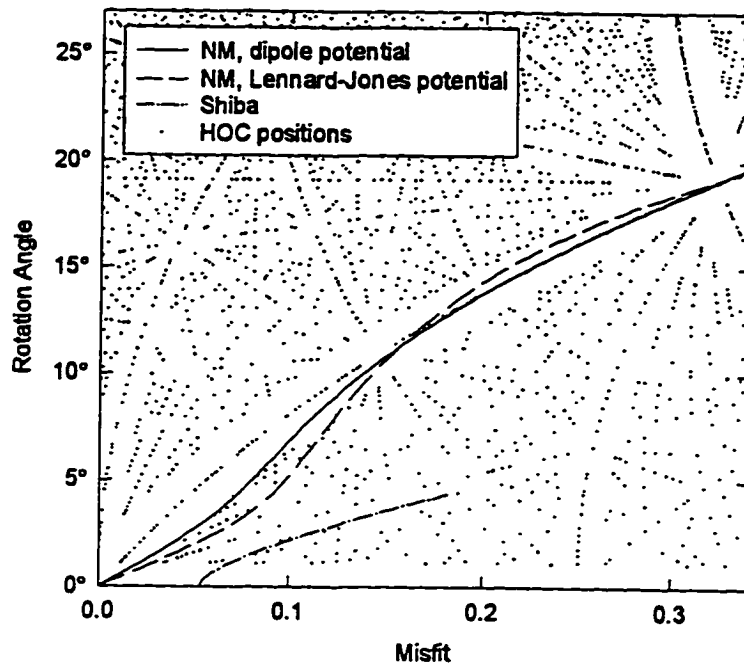


Figure 2.12 . Predictions of three additional models for rotational epitaxy. For reference, the Bohr-Grey $\Psi_A=30^\circ$ and $\Psi_A=60^\circ$ trajectories coincide with main branches of the HOC structures.

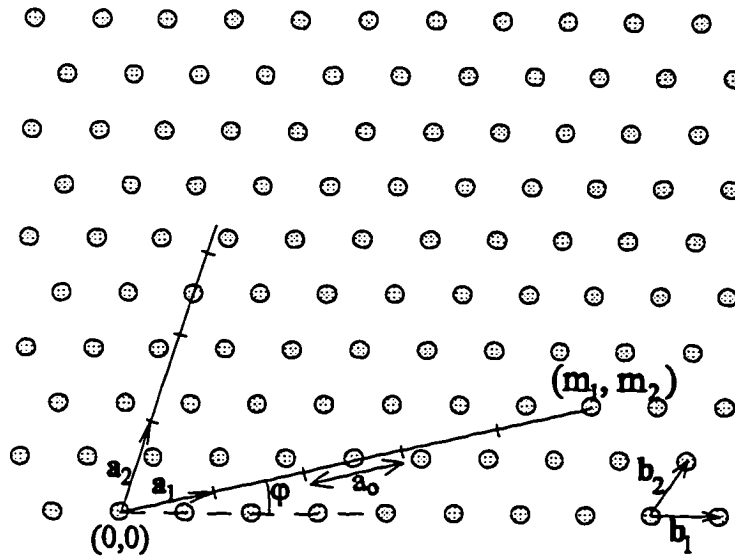


Figure 2.13 Diagram showing the method of calculating higher order commensurate points.

If it does, the (a, ϕ) pair is recorded. This whole process is repeated for all the substrate positions $m_1b_1 + m_2b_2$ within the specified maximum size. Since this process may yield the same (a, ϕ) pair multiple times, each new pair is checked against the list already obtained before being added to the list.

2.3.3. Novaco-McTague Theory

A model which takes into account the elastic interactions between adsorbates has been developed by Novaco and McTague.^{23,24} In their theory, the adsorbates are allowed to relax an infinitesimal amount toward the bottoms of the substrate potential wells. This creates static mass displacement waves in the overlayer which have the same periodicity as the Moiré pattern shown in Figure 2.10. For an unrotated monolayer this distortion will be in the form of static longitudinal waves. However if there is a finite rotation then the distortion will also have a transverse component, with larger rotations favoring a larger transverse part of the distortion. Since transverse and longitudinal distortions cost different amounts of energy, the total energy of the distorted lattice will vary with rotation angle for a certain lattice mismatch. In general there will be one or more angles that correspond to a minimum in the energy.

The Novaco-McTague energy of rotation is calculated by summing the energy cost of producing a distortion wave of a particular amplitude and wave vector and the energy gained by relaxation of the atoms in the substrate potential wells. This expression is then minimized with respect to the amplitude of the distortion wave, and the total energy gain per adatom is equal to

$$E = -\frac{1}{2} \sum_{\mathbf{G}} \frac{V_{\mathbf{G}}^2 [\mathbf{G} \cdot \mathbf{u}_l(\mathbf{q})]^2}{M \omega_l^2(\mathbf{q})} \quad (2.16)$$

where the \mathbf{G} vectors are substrate reciprocal lattice vectors, $V_{\mathbf{G}}$ are the Fourier components of the substrate corrugation potential, $\mathbf{u}_l(\mathbf{q})$ and $\omega_l(\mathbf{q})$ are the l^{th} normal mode vector and eigenfrequency of the overlayer at a wave vector \mathbf{q} corresponding to the periodicity of the Moiré interference fringes shown in Figure 2.10. The index l is summed over the transverse and longitudinal and longitudinal modes, yielding two competing terms. The dot product causes the transverse term to be zero at zero rotation, while with a nonzero rotation the transverse term will become non-zero and the magnitude of the longitudinal term will decrease. Since transverse modes are generally softer (ω_l smaller) the overlayer lattice can usually decrease its energy by rotating away from alignment with the substrate, so the transverse modes can contribute.

Calculations of the Novaco-McTague energy of rotation were done using a computer program adapted from a program written by Bruch.²⁵ The calculation is done by first scanning over all angles in steps of 0.5° , calculating the energy for each using Equation 2.16. The normal mode frequencies are

obtained by calculating the derivatives of the elastic overlayer energy with respect to position, using pair potentials, for an atom in an undistorted lattice. The result is an energy-rotation angle curve which has one or more minima. For each minimum the exact angle of minimum energy is then found using the Newton root-finding method.

The angle of minimum energy is shown as a function of misfit in Figure 2.12. Figure 2.14 shows the dependence of the total energy on rotation angle for an interadsorbate dipole-dipole repulsion and for a Lennard-Jones potential having a natural interadsorbate spacing 2.5 times the substrate spacing and a misfit of 0.1 with respect to the substrate $p(2 \times 2)$ periodicity. Since elastic properties depend on the details of the adatom-adatom interaction, one might expect different rotation angles for different adatom-adatom potentials. However, the two trajectories are actually quite close together. Changing the parameters in the potentials or using other potentials in general only changes the trajectories by small amounts. It should be noted that since the Novaco-McTague calculation is a first order approximation, the magnitude of the substrate corrugation potential, V_0 , only affects the scale of the curve shown in Figure 2.14 and not the position of the minimum. Therefore it yields a rotational behavior which is independent of the size of the substrate corrugation.

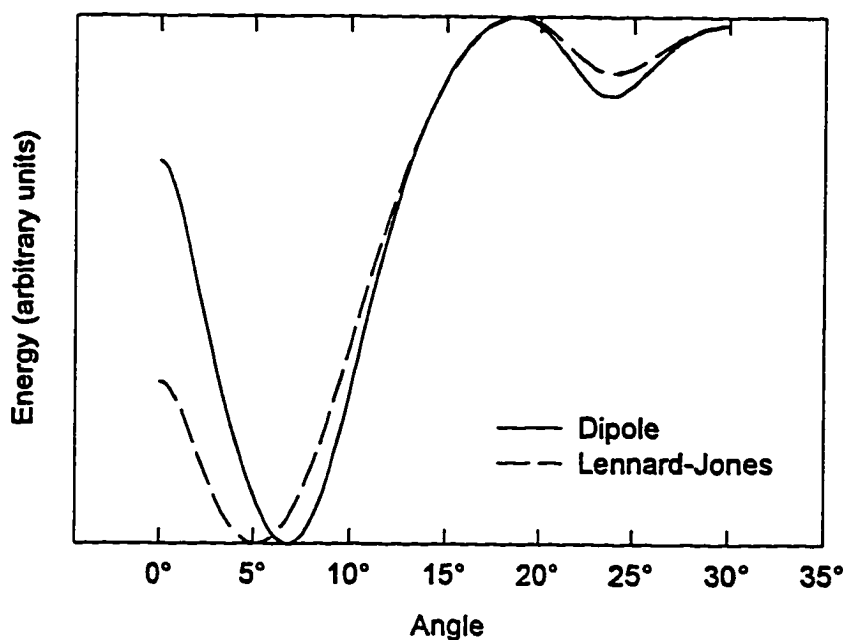


Figure 2.14. Energy of rotation calculated by the Novaco-McTague theory, as a function of overlayer rotation angle, for an overlayer with a misfit of 0.1 with respect to the commensurate (2×2) . The solid line is for a dipole potential and the dashed line is for a Lennard-Jones potential with equilibrium spacing two times that of the substrate spacing.

A second observation which can be made about Figure 2.12 is that the NM trajectory is very close to trajectories predicted by the geometrical models. The reason for this correspondence between the geometrical models and the harmonic NM model is not completely obvious. In essence however it appears that the HOC and domain-wall alignment models also pick out low-energy trajectories. The NM theory in addition is able to select the lowest-energy trajectory for a given interadsorbate interaction. In fact in many cases the Novaco-McTague energy curves often have more than one minimum, and if the angle of the other (local) minimum is plotted as a function of misfit it coincides with other branches predicted by the geometrical models. The fact that the equilibrium rotation angle is, in this case at least, not very sensitive to the exact form of the interadsorbate interaction is what causes certain geometrical trajectories to be so close to the NM prediction.

2.3.4. Shiba Theory

When the overlayer is very close to a commensurate structure, the Novaco-McTague theory breaks down. The reason for this is that the NM theory neglects an energy term, the commensurate energy, which goes to infinity as the lattice mismatch goes to zero. In practice what happens at a misfit close to zero is that there will be large regions of the surface which are effectively in a commensurate phase, with sharp domain walls between them.

A domain-wall theory was developed by Shiba which predicts that close to a commensurate structure where domain walls in the overlayer are relatively sharp, the overlayer (and the domain walls) will remain aligned along a substrate direction until a certain critical misfit is reached.^{26,27} The critical misfit occurs at a point where the domain walls become too weak for the overlayer to sustain the alignment. At this point the overlayer crosses over from a "domain wall" to a "modulated" regime, and the equilibrium angle of the rotation moves toward that predicted by the MN theory. The Shiba theory has two parameters which enter the calculation of the rotation angles as a function of misfit: the ratio of the transverse to longitudinal elastic constants and l_0 , a parameter which sets the size of the domains at critical misfit. Figure 2.12 shows the Shiba prediction for a Cauchy solid (ratio of transverse to longitudinal elastic constants being $\sqrt{3}$) and $l_0=18$.

2.4. References

- ¹ M. A. Van Hove, W. H. Weinberg, C. M. Chan, Low Energy Electron Diffraction, Springer Verlag (1986).
- ² M. A. Van Hove, S. Y. Tong, Surface Crystallography by LEED, Springer Verlag (1979).
- ³ J. B. Pendry, Low Energy Electron Diffraction, Academic Press, London (1974).
- ⁴ A. Barbieri and M. A. Van Hove (private communication).
- ⁵ H. Over, W. Moritz and G. Ertl, Phys. Rev. Lett. **70**, 315 (1993).
- ⁶ H. Over, M. Gierer, H. Bludau and G. Ertl, Phys. Rev. B **52**, 16812 (1995).
- ⁷ J. B. Pendry, J. Phys. C: Solid St. Phys. **13**, 937 (1980).
- ⁸ P. J. Rous, J. B. Pendry, D. K. Saldin, K. Heinz, K. Müller and N. Bickel, Phys. Rev. Lett. **57**, 2951 (1986).
- ⁹ P. Hu, C. J. Barnes and D. A. King, Phys. Rev. B **45**, 13595 (1992).
- ¹⁰ H. Over, M. Gierer, H. Bludau, G. Ertl and S. Y. Tong, Surface Science **314**, 243 (1994).
- ¹¹ N. Stoner, M. A. Van Hove, S. Y. Tong and M. B. Webb, Phys. Rev. Lett. **40**, 243 (1978).
- ¹² E. V. Albano, Appl. Surface Sci. **14**, 183 (1982).
- ¹³ C. Argile and G. E. Rhead, Surface Science **203**, 175 (1988).
- ¹⁴ R. W. Gurney, Phys. Rev. **47**, 479 (1935).
- ¹⁵ N. D. Lang, Phys. Rev. B **4**, 4234 (1971).
- ¹⁶ H. Ishida, Phys. Rev. B **39**, 5492 (1989).
- ¹⁷ J. Neugebauer and M. Scheffler, Phys. Rev. B **46**, 16067 (1992).
- ¹⁸ C. Stampfl, J. Neugebauer and M. Scheffler, Surface Science **307**, 8 (1994).
- ¹⁹ F. Grey and J. Bohr in Phase Transitions in Surface Films 2, eds. H. Taub, G. Torzo, H. J. Lauter and S. C. Fain, Plenum Press, New York, pp. 83-96 (1990).
- ²⁰ F. Grey and J. Bohr, Europhys. Lett. **18**, 717 (1992).
- ²¹ C. R. Fuselier, J. C. Reich and N. S. Gillis, Surface Science **667** (1980).
- ²² D. L. Doering and S. Semancik, Surface Science **175**, L730 (1986).
- ²³ A. D. Novaco and J. P. McTague, Phys. Rev. Lett. **38**, 1286 (1977).

²⁴ J. P. McTague and A. D. Novaco, *Phys. Rev. B* **19**, 5299 (1979).

²⁵ Louis Bruch (private communication).

²⁶ H. Shiba, *J. Phys. Soc. Japan*, **46**, 1852 (1979).

²⁷ H. Shiba, *J. Phys. Soc. Japan*, **48**, 211 (1980).

Chapter Three

Experimental Apparatus

Surface experiments are not easy. Because of interactions between surface atoms and the medium in which the experiment is done, it can be very difficult to keep experimental conditions controlled at the surface. The obvious answer to this problem is to remove all the atoms in the containing medium – to do the experiment in a vacuum. However, even at a pressure of 10^{-6} mbar, there will be roughly one collision of a gas phase atom with the surface per second for each surface atom. If each gas phase atom modifies the surface in some way, in a matter of seconds it will become completely contaminated at this pressure. In many cases the probability for a single collision to result in a modified surface is small, so the conditions are not as stringent. However, for reactive adsorbates such as alkali metals, it is not uncommon for nearly every gas phase atom which strikes the surface to stick. Modern ultra-high vacuum equipment, which has only become technologically possible in the last few decades, allows pressures on the order of 10^{-10} to 10^{-11} mbar to be obtained. With these capabilities about an hour is available to complete an experiment before the amount of contamination becomes significant.

In addition, since the atoms on the surface of a solid generally only comprise about one in 10^8 of the total number of atoms in the solid, it can be difficult to sort out information about the surface from information about the bulk material. A solution to this problem is to use low energy electron scattering as a probe. Electrons in the energy range of 30 to 500 eV have a mean free path of only a few atomic layers in a typical solid, so the scattered electrons provide a way to measure only characteristics of the region very close to the surface.

The experiments reported in this thesis were done in an ultra high vacuum chamber, primarily using electron scattering probes. This chapter will describe the apparatus in detail.

3.1. UHV Chamber

The experiments were done in an ultra-high vacuum chamber, shown in Figure 3.1, custom built by Vacuum Generators. The system is pumped by turbo and titanium sublimation pumps, and has a base pressure of 3×10^{-11} mbar after baking at 120°C for 24 hours. The chamber is also equipped with a liquid Nitrogen cold trap, which is filled immediately before an experiment to quickly pump away residual Ar from sputtering and to ensure base pressure during the experiment. The upper part of the chamber is lined with a μ -metal shell which provides shielding from magnetic fields.

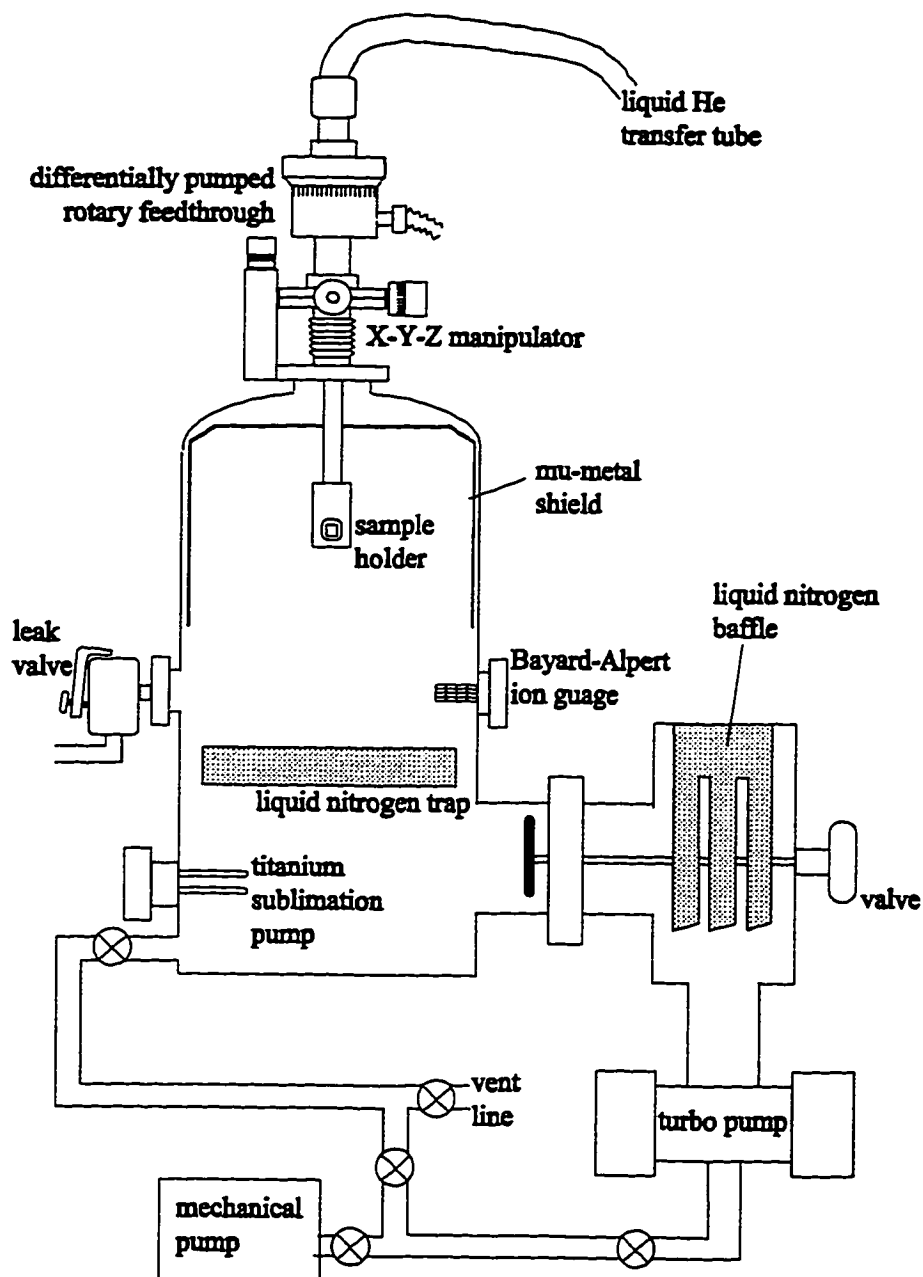


Figure 3.1. UHV chamber, pumped by turbo and titanium sublimation pumps. The instruments around the sample are shown in Figure 3.2.

The instruments available are shown in Figure 3.2 and include a flat-screen LEED (Low Energy Electron Diffraction), a cylindrical mirror electron analyzer for use in AES (Auger Electron Spectroscopy), a quadrupole mass spectrometer, and a Kelvin Probe. LEED is used as the main technique of surface characterization. AES is used primarily to monitor the surface composition and to measure overlayer coverages. The mass spectrometer is used check for leaks and to monitor the purity of gases being adsorbed. The Kelvin probe is used to measure work function changes during adsorption.

3.2. Sample

The sample used in these experiments is a Ag(111) single crystal. For surface science experiments it is desirable to have large atomically flat terraces oriented to a certain crystallographic direction. Procedures for obtaining these large terraces have been developed by researchers over the years, in large part by trial and error. This section will detail the particular procedure used in the preparation of the Ag(111) crystal.

After preparing the substrate, many experiments require the deposition of very small (submonolayer) controlled amounts of other materials onto this surface. Measurements are then done on the surface to determine various physical properties. For many of the experiments it was necessary to control the temperature of the sample during the measurements. This section will explain in detail how each of these things was accomplished.

3.2.1. Preparation

The sample was prepared from a high purity single crystal Ag rod. First the orientation of the rod was determined using Laue X-ray Diffraction as shown in Figure 3.3. The x-ray beam, generated by a Mo target, strikes the sample and is back-scattered and detected by Polaroid film. The positions of diffraction spots on the film are measured and compared to a Greninger chart. Alignment to the (111) planes was achieved after several iterations of measurement and changing the sample orientation. After orienting the crystal, the rod was cut using a wire saw from South Bay Technology. A plain stainless steel blade was used with a liquid abrasive solution of silicon carbide, water, and glycerin. Next the sample was affixed with mounting wax to a goniometer that could be mounted either in a polishing bell or on a track for laser or x-ray alignment. In this way the surface could be polished while preserving orientational alignment of the physical surface (measured by reflecting a laser beam) to the crystallographic planes

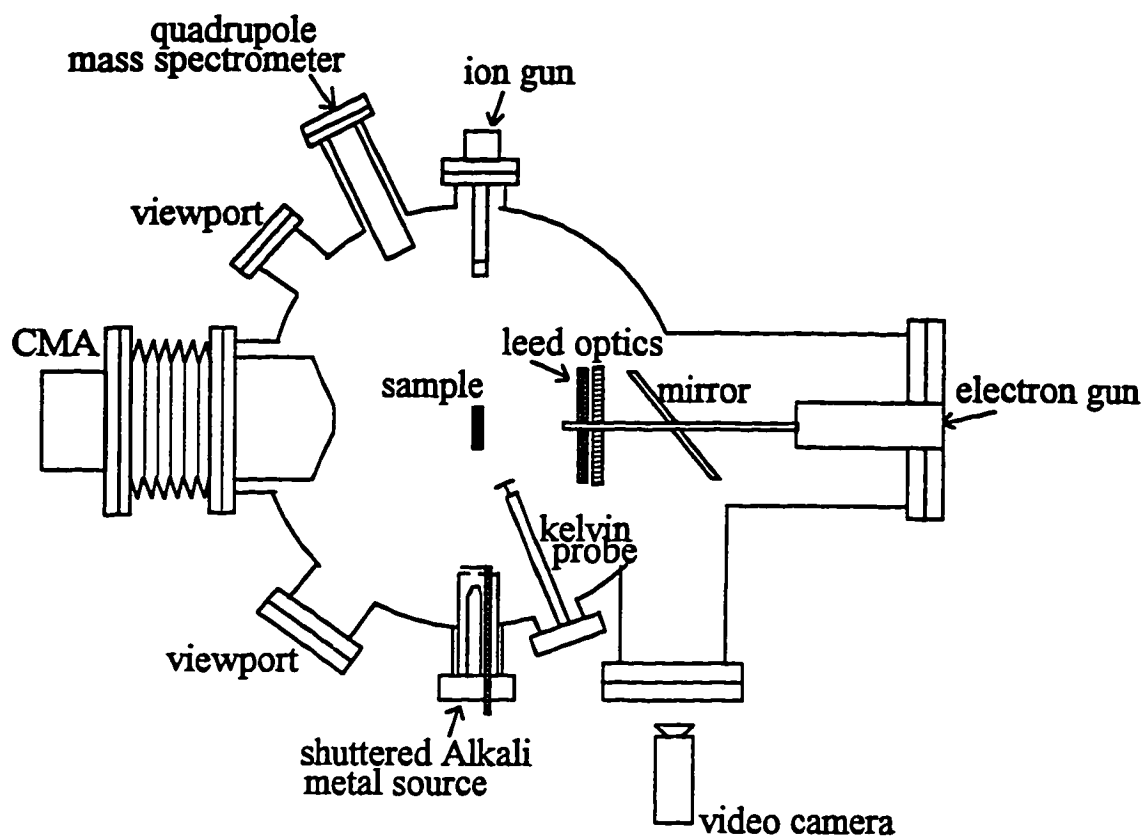


Figure 3.2. Experimental apparatus available in the UHV chamber.

(measured by Laue Diffraction). The crystal was then polished on a rotary polishing wheel, using Tex-Met polishing cloths with first silicon carbide and then a diamond paste abrasive. The crystal was polished using successively finer abrasives, beginning with 40μ particle size and ending with 0.25μ . Between each grade, the crystal was inspected carefully for non-uniform scratches with an optical microscope, and then subjected to a short chemical polish by rubbing the crystal for a few seconds on a clean polishing cloth wettened with a (10:1) mixture of CrO_3 and HCl . This step is necessary since the mechanical polishing leaves a damaged surface region approximately as deep as the abrasive particle size. While it does not improve the flatness of the surface, the chemical polish removes this damaged surface layer and has been found to be very important in the preparation of a high quality surface.¹ Carefully following these procedures enabled the production of an optical quality surface with alignment of the (111) planes to within 0.25° of the surface normal.

After mounting in the UHV chamber, the crystal was further cleaned *in situ* by bombardment of Ar^+ ions (0.5 keV and a sample current of about $10 \mu\text{A} / \text{cm}^2$) and annealing in UHV to 770-820 K. Ion sputtering times varied from several hours to about twenty minutes, and the annealing time used was 2 to 8 minutes. The initial cleaning of the sample required long sputtering and annealing cycles. However after the sample had been cleaned once, short cycles were used in order to obtain as ordered a surface as possible. Sputtering and annealing cycles were repeated until no impurities could be detected in the Auger spectrum and sharp LEED spots could be seen.

Between each experiment, the sample was cleaned by first annealing to 770 C remove the adsorbates, and then two cycles of Ar^+ ion bombardment and annealing to 770 K. The next experiment was started as soon as the residual Argon in the chamber was pumped away and the sample was cooled to the required temperature.

3.2.2. Mounting

A number of important considerations went into the sample mounting. First of all, it was necessary to be able to turn the sample in different directions to face the different instruments and to be able to translate it small amounts to put it into position for analysis. For LEED I(E) experiments normal incidence is required, so it was necessary to have a second tilt axis available. While preserving motion capability, the sample had to be in good thermal contact with the liquid helium cryostat for cooling. However it was also necessary to heat the sample to about 850 K for cleaning. LEED beam current calibration required the capability of the sample being isolated from ground while being grounded for all

other operations. Finally, we needed the ability to accurately and quickly measure the sample temperature.

The sample holder, shown in Figure 3.4, is mounted on an APD Helitran Cryostat, which can be used for either liquid helium or liquid nitrogen cooling. The cryostat is mounted on a differentially pumped rotary feedthrough (shown in Figure 3.1) which allows 360° of rotation. The rotary feedthrough in turn is mounted on a VG Omniax HPT 040 sample manipulator, which provides x-y-z translational motion for the sample.

The sample is mounted on two 0.25 mm diameter tantalum wires which pass through slits on the sides of the sample and hold the sample against an alumina plate. The mounting wires are clamped under insulating washers against the plate, so the sample is completely isolated from ground. Alumina was chosen as the insulating material because it has an extremely high electrical resistivity, but at low temperatures it has a very high thermal conductivity. To facilitate good thermal contact the back of the sample was polished and a piece of gold foil was sandwiched between the sample and the ceramic plate. The ceramic plate is mounted on a copper plate, onto which is welded a copper braid for heat conduction away from the sample. The other end of the braid is welded to another copper plate which is clamped against the coldfinger. All mating surfaces were polished and sandwiched with gold foil to facilitate sample cooling. A copper radiation shield, cooled by the returning liquid helium flow, surrounds the sample and limits the ambient radiation incident on the sample.

Adjustment of the vertical sample tilt is achieved using the spring and screw mechanism shown in Figure 3.4. The copper plate that holds the sample assembly pivots on two sharpened bolts, and is held against an adjustment screw by a stainless steel spring. The screw can be adjusted from outside the chamber using a screwdriver mounted on a bellows and rotary feedthrough.

3.2.3. Heating and Cooling

The sample is heated by passing a current through the tantalum wires. Although the current passes through the sample, heating is not achieved by Joule heating of the sample but by conduction of the Joule heat generated in the mounting wires. This method of heating presents a problem for sample cooling: the heating wires present a path for heat conduction to the sample, even when no current is being passed through the wires. This effect is minimized by using a stainless steel link (rods about 6 inches long) in the heating current leads, as shown in Figure 3.4. Since stainless steel has a very low thermal conductivity at low temperatures, this acts as an insulating wall. Stainless steel was not used for the entire current path because of its high electrical resistivity. The stainless steel rods are thermally connected (by clamping with alumina slabs) to the return helium flow, which acts as a sink for heat

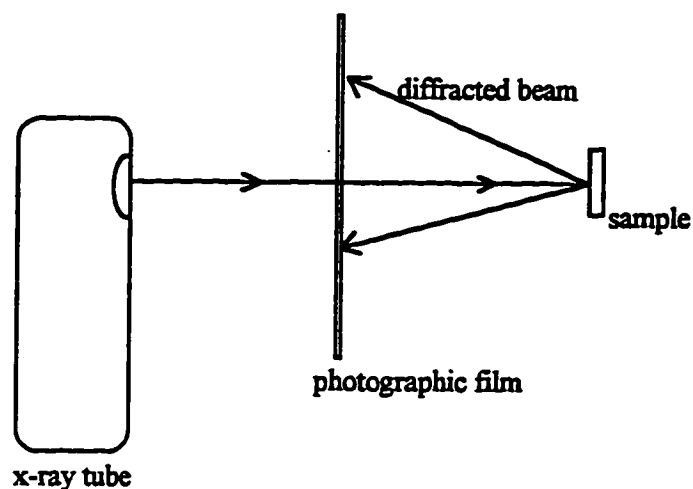


Figure 3.3. Diagram of Laue X-ray diffraction apparatus, used for orienting the Ag(111) sample.

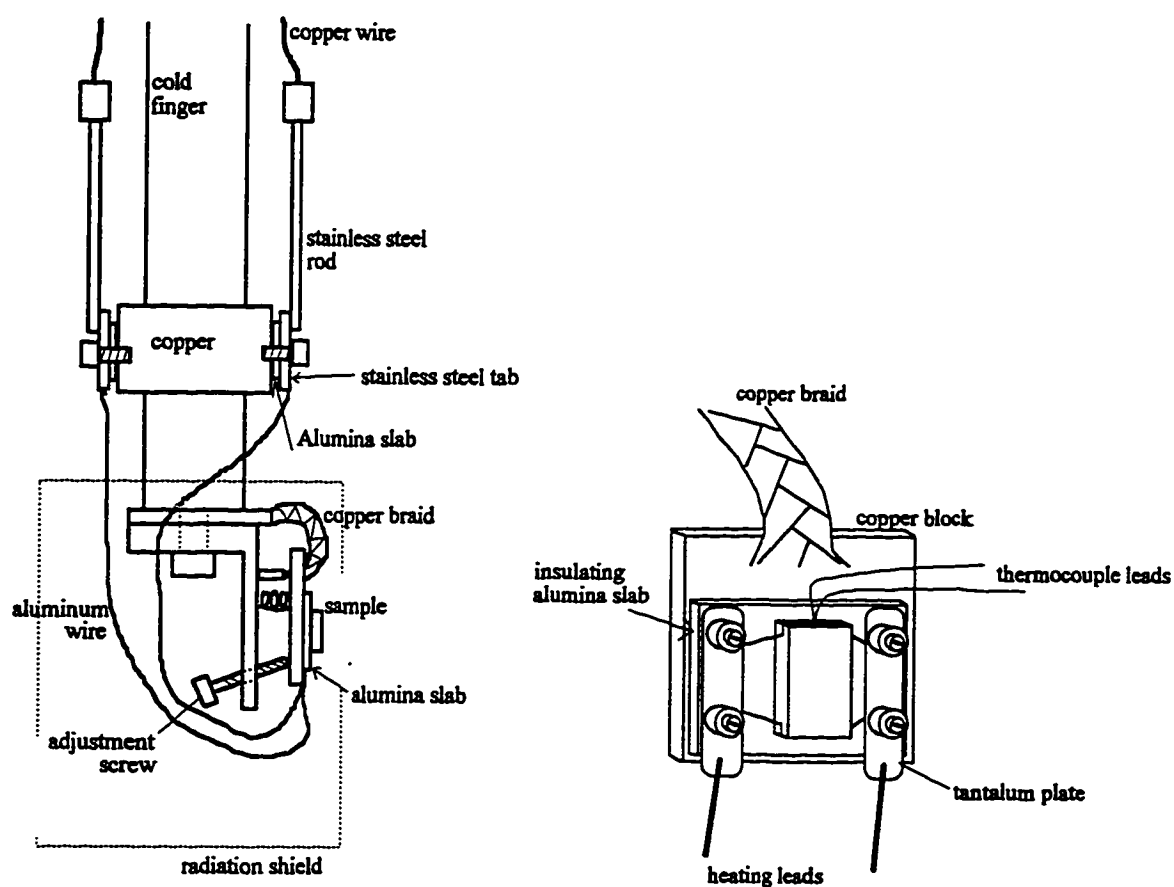


Figure 3.4. Sample holder. Thermal contact is made from the sample through the alumina slab to a copper block, which is connected to the coldfinger by a copper braid. This allowed sample cooling down to about 30 K. Heating is done by passing current through the sample mounting wires.

conducted into the system through the leads. Aluminum wire, which has a high electrical conductivity but a thermal conductivity at low temperatures about half that of copper, was used for the link between the stainless steel rods and tantalum heating wires.

Heating of the sample by electrical current presents a problem for LEED experiments. The current produces a field which deflects electrons, causing the LEED pattern to be distorted while the sample is being heated. This problem is overcome by chopping the heating current and suppressor voltage on the LEED optics out of phase with each other. The chopping is done so that when current is flowing through the sample, the suppressor voltage drops to the negative value of the beam voltage so that all electrons are repelled from the screen. The chopping frequency and duty cycle are adjustable; usually a frequency of about 20 Hz is used.

The sample temperature is measured using a chromel-alumel (type K) thermocouple, which is inserted into the slot on the side of the sample. A liquid nitrogen reference junction is used, and the output of the thermocouple is fed into an isolation amplifier, the output of which is read by the computer using a 12-bit digital-analog-converter. The isolation amplifier is necessary because while heating, the sample itself will not be exactly at ground potential.

3.2.4. Deposition of Materials

In these experiments we are interested in two kinds of monolayer deposition: alkali metal and inert gases. Alkali metal deposition is done using alkali metal sources commercially manufactured by SAES Getters.^{2,3} Figure 3.5 shows a diagram of an alkali metal source. The material is contained inside a small stainless steel canister, in the form of an alkali metal chromate (Me_2CrO_4 , where Me signifies the alkali) and a reducing agent (Zr 84% - Al 16%). The canister is heated resistively, causing a reduction reaction in which the alkali atom is liberated and vapor-deposited onto the sample through a slit in the canister. The entire source is contained in a shuttered enclosure with a small aperture to prevent alkali metal contamination of other parts of the apparatus. Before use the alkali metal sources must be carefully degassed, usually over a period of several days at a pressure close to the system base pressure. By taking these precautions, alkali metal films pure to within a half percent (as measured by AES) can be formed. After dosing alkali metal onto the surface, the surface becomes extremely reactive. Because of this the pressure in the chamber must be kept as low as possible and the experiment done as quickly as possible to avoid contamination. Assuming a sticking coefficient of one, at a pressure of 7×10^{-11} (the system base pressure attainable during an experiment) a surface will be completely covered in approximately four hours. For many of these experiments it was found that contamination levels of more than approximately

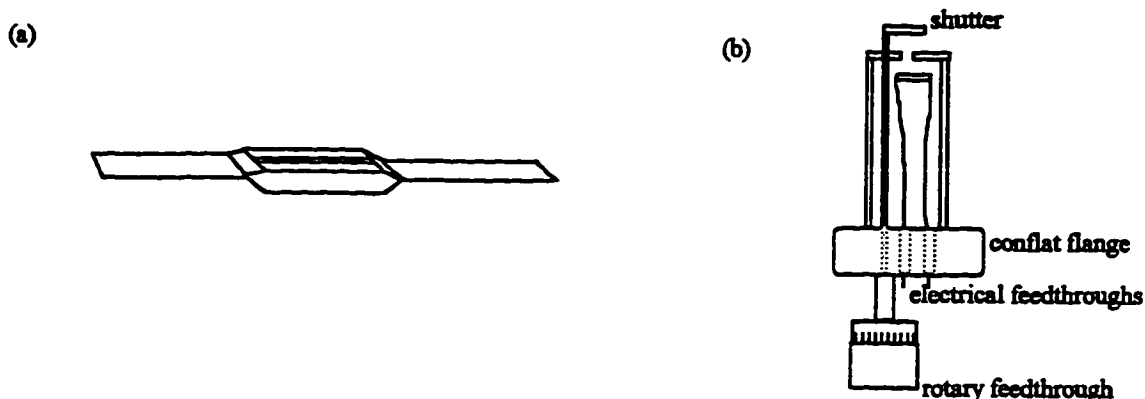


Figure 3.5. Source for alkali metal deposition. (a) Alkali metal dispenser made by SAES Getters. (b) Alkali metal source. The rotary feedthrough controls a shutter which allows accurate doses to be made.

one percent of a monolayer was sufficient to affect the reproducibility of the results. Assuming a sticking coefficient of one, the experiment must therefore be done in approximately 24 minutes to keep contamination to desired levels. Fortunately the sticking coefficient is usually less than one, so slightly longer times were often acceptable.

In practice, the experiment was usually completed 30 to 50 minutes after initial alkali deposition. The amount of time between the last sample cleaning and alkali metal deposition was not nearly as critical, since the sticking coefficient of residual gases on bare silver is very low. After each experiment an Auger scan was done to check the contamination level. The main contaminants were found to be oxygen and carbon, and the contaminant level after finishing an experiment was approximately one percent or less.

Deposition of gases (either noble gases and carbon monoxide in these experiments) is done by backfilling the entire chamber with rare gas to a pressure of 10^{-9} to 10^{-4} mbar, depending on the experiment. Since these gases are relatively inert, they can easily be pumped out of the chamber after dosing.

3.3. Auger Electron Spectroscopy (AES)

AES is done using a standard single pass cylindrical mirror analyzer (CMA) made by Perkin Elmer. The details of this system can be found in the Perkin Elmer documentation. This particular AES system had been previously used in derivative mode using a chart recorder for output. In order to handle data more efficiently, the system was interfaced with a PC-compatible computer. An analog output from a 12-bit digital-to-analog converter board in the computer was connected to the analog input terminal on the analyzer control electronics. The output, which comes from a lock-in amplifier, was fed into the a 12-bit analog-to-digital input on the same computer board mentioned earlier.

Data were acquired by computer by scanning the analyzer voltage in steps of one or two eV, measuring the output from the lock-in amplifier at each step. This was done using software written by the author for this particular purpose.

AES is used primarily to monitor surface cleanliness and to measure alkali coverage. Figure 3.6 shows a spectrum from the Ag crystal after the initial polishing (but before *in situ* cleaning), a spectrum from the clean Ag surface, and one with a partial monolayer of K. The main contaminants on the surface were C, O, and S, and initially Cr and Cl residue from the surface etch.

Alkali coverage was measured by taking the ratio of the peak-to-peak intensities of the alkali peak to the largest Ag peak. These coverage values were then calibrated for a coverage of 0.25 at the commensurate $p(2 \times 2)$ phase. Although this worked well for Cs, it was slightly more difficult for K, where the position of the major peak coincides with a minor Ag peak, as can be seen in the bottom spectrum of Figure 3.6. In order to obtain the ratio of peak intensities in this case, the clean Ag spectrum was subtracted from the one shown in the figure, and the peak intensity was measured on the difference spectrum. Measurement of Rb coverages presented more of a problem, because AES is approximately 30 times less sensitive to Rb than to Ag. Because of this it was impossible to accurately measure amounts of Rb at the relatively low coverages used in many of the experiments. Rb coverage was measured by dosing time, a method which was not quite as good since the dosing rate is not constant from source to source and changes with time as the source becomes depleted.

3.4. Kelvin Probe

Work function measurements are carried out using a Kelvin Probe S manufactured by Besocke Delta Phi. Figure 3.7 shows the schematic of the instrument. A small flat grid, mounted parallel to the sample face, is caused to vibrate by a piezo driver. As the grid vibrates, the capacitance between grid and

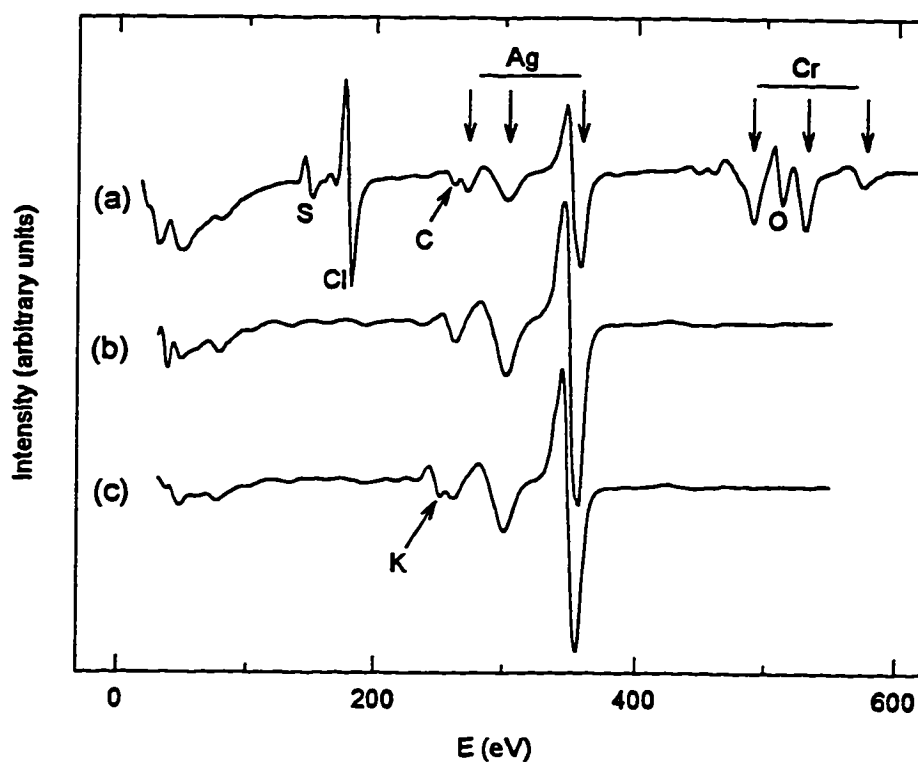


Figure 3.6. Auger spectra from the Ag(111) surface. (a) Ag(111) surface after polishing. Common contaminants (S, C, and O) are present as well as residue from the chemical polish (Cl and Cr). (b) Clean Ag(111) surface, after many sputter and anneal cycles. (c) Ag(111) surface with a partial monolayer of K. Spectra are offset for clarity.

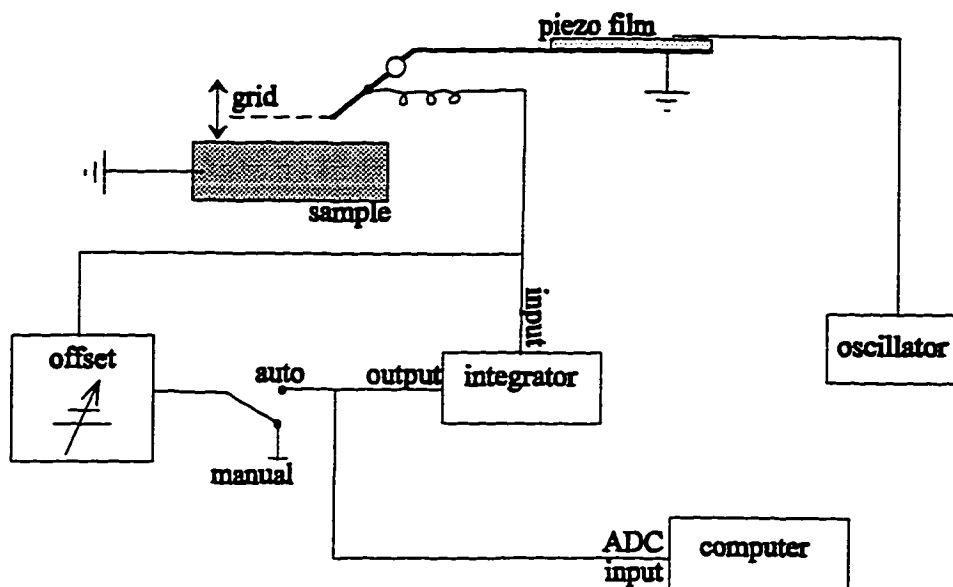


Figure 3.7. Schematic diagram of Kelvin Probe apparatus.

sample changes. If there is a non-zero voltage across the capacitor, this changing capacitance will cause a change in the charge on the capacitor, resulting in a measurable current between the grid and ground. The voltage on the sample side of this capacitor is equal to the vacuum level offset by the work function of the surface, so by biasing the grid to a potential where no current is measured the work function of the surface can be determined.

The Kelvin probe electronics contains circuitry to operate the probe in automatic mode in which the grid voltage is adjusted automatically to keep the current at zero. The grid voltage is then recorded by the computer using the same 12-bit analog-to-digital converter card used in acquiring AES data.

3.5. Low-Energy Electron Diffraction (LEED)

Figure 3.8 shows the LEED instrument, which was custom built at the University of Liverpool. A commercially made electron gun generates a beam which strikes the sample. Backscattered electrons enter the electron detection optics, where most of the inelastically scattered electrons are filtered out. The remaining electrons are amplified by a channel plate and strike a phosphor screen, producing a visible image. The image is recorded by a computer-interfaced video camera.

A conventional LEED experiment requires an electron beam of several μA to produce visible spots on a fluorescent screen. However, some physisorbed adsorbates are sensitive enough that they can be desorbed or disordered by an electron beam of several hundred eV. To solve this problem we use an electron beam of a few nA, so that the adsorbed layer is not significantly perturbed during the duration of an experiment. To detect the low intensity diffraction pattern we use a channel electron multiplier which amplifies the current of electrons hitting the phosphor screen.⁴ The flat geometry of the grids and screen introduces some complications, which will be discussed below.

3.5.1. Electron Optics

The electron beam is generated by an Apex Electronics 401W electron gun. The schematic for the gun is shown in Figure 3.8. A tungsten filament is heated resistively by a DC current, and the electrons are extracted by a bias voltage on G1. Since the filament is held at a potential of $-E$, the electrons are accelerated toward G2, which also acts as the first focusing potential. The beam passes through a series of focusing rings (G2 and G4), the potential of which can be varied between 0 and $-E$. To limit the beam current to nanoamp values a limiting aperture of 0.002 inch is used on the G2 electrode of the gun. Finally the beam passes between two sets of parallel plates used for deflecting, and emerges from the gun with a kinetic energy of $-E$. The beam voltage is controlled either by the computer using a 12-bit analog-to-digital converter, or manually by a potentiometer. Computer control of the beam voltage makes possible automated collection of LEED $I(E)$ data.

After leaving the gun and traversing a grounded drift tube, the beam strikes the sample. Elastically back-scattered electrons are then detected by the LEED optics, also shown in Figure 3.8. A grounded grid keeps the region between the sample and detection apparatus field free, so the electrons travel in straight paths. In order to suppress inelastically scattered electrons, a retarding voltage, equal to about 70% of the incident beam voltage, is applied to the front of the channel plate.

After entering the channel plate, the electrons are accelerated by a voltage of approximately 0.8 keV applied to the back of the channel plate. The channel plate, a Galileo MCP-75/32, consists of a thin glass plate with regularly spaced channels perpendicular to the surface, spaced 25 microns apart. Electrons accelerated inside one of these channels undergo collisions with the channel walls, causing additional electrons to be liberated. Each additional electron is accelerated in turn and liberates more electrons, causing the channel plate to act as an electron multiplier with a gain of about 10^3 . After leaving the channel plate, the electrons are further accelerated by a voltage of ~ 3.5 kV applied to the front of a fiber optic plate which is coated with phosphor. The electrons hitting the phosphor cause visible fluorescence which can be seen with the eye or recorded with a camera.

The use of a flat LEED optics has some advantages and some disadvantages. As was already mentioned, the channel plate enables us to use a much lower electron beam current. In addition, since only one grid is used (as opposed to three or more with a conventional LEED optics) a higher conductance of electrons through the optics is obtained. The use of a single grid also eliminates the "grid lines" or Moiré interference fringes on the diffraction pattern, which greatly enhances the quality of line intensity profiles extracted from the pattern.

One disadvantage of the flat plate is a distortion of the image due to the flat (rather than hemispherical) screen. This problem however can easily be corrected by software, and will be discussed further in the video processing section below. A second problem introduced by the flat screen is non-uniform suppression of inelastically scattered electrons. Since the repelling voltage is applied to a flat rather than hemispherical surface, the retarding force on the electrons will not always be in a direction parallel to their motion. The effect of this is that electrons are repelled from the plate if the energy of their perpendicular motion (rather than their total kinetic energy) is less than the repelling voltage. This causes more suppression of the electrons scattered at higher angles, and the result is a bright region of diffuse intensity in the center of the screen. Processing necessary to compensate for this will be discussed below as well.

3.5.2. Video Data Acquisition

A Sony XC-75 CCD camera is mounted outside the UHV chamber and focused on the image of the phosphor screen. The video camera is interfaced to a PC compatible computer via a Data Translation DT2851 frame grabber and DT2858 auxiliary frame processing board. A block diagram of these boards is shown in Figure 3.9. The video signal is digitized in real time and stored in one of two $512 \times 480 \times 8$ bit

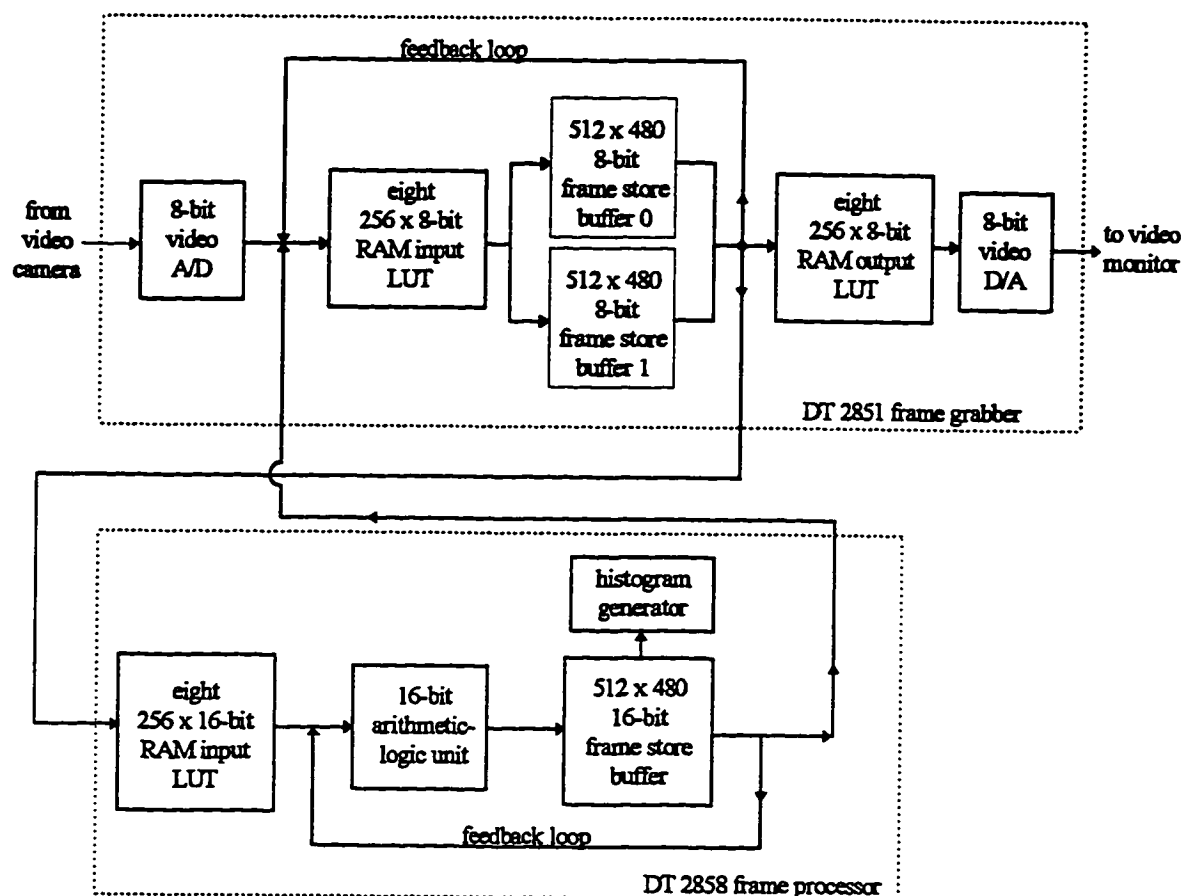


Figure 3.9. Block diagram of the Data Translation video frame grabber and processor boards. The boards were mounted inside a PC compatible computer.

on-board frame buffers. This on-board memory can be accessed directly by the computer for saving, loading, and extracting information from video frames. Using the auxiliary processing board, video frames can be averaged to increase the signal-to-noise ratio. This is done by repetitively acquiring 8-bit video frames and adding them to the 16-bit buffer on the 2858 frame processing board. After acquiring the desired number of frames, the data in the 16-bit buffer is normalized to 8 bits and sent back to the 8-bit buffer, where it can be viewed or stored. In this way approximately 7 frames can be averaged per second. Normalization and saving take an additional 0.5 second.

The frame grabber/processor combination has several additional features which are used in data visualization and analysis. Intensity histograms of entire video frames can be generated quickly using built in circuitry. Video frames can be added and subtracted from one another, or their intensity values can be offset and scaled to make certain features more visible. Lookup tables can be used to map the intensity scale arbitrarily to another scale. Finally, the frame grabber board contains display circuitry so that live or stored images may be viewed on a separate monitor.

For the acquisition of single LEED patterns, usually 15 to 50 frames are averaged to increase the signal to noise ratio. When LEED $I(E)$ spectra are to be measured, there are two ways the experiment may be done: (1) the intensities may be measured directly by the computer as the beam energy is ramped and saved as 1-d scans, or (2) a series of diffraction patterns may be acquired at increments of beam energy, the entire image saved for each one, and the $I(E)$ spectra extracted later. The section on $I(E)$ processing will discuss these two methods.

All video data acquisition and processing were performed using software written in Borland Pascal by the author. Software documentation will be presented in Appendices B and C.

3.5.3. Video Data Processing

Processing of video LEED data falls into two main categories: kinematical processing and $I(E)$ processing. In kinematical processing, diffraction spot positions, intensities, and widths are measured and kinematic diffraction theory is used to extract information about the overlayer periodicities and morphology. With $I(E)$ processing, the goal is to measure the integrated intensities of diffraction spots as a function of incident beam energy. Previously or concurrently with these operations, the data must be corrected for the flat screen distortion. This is only necessary however for kinematical processing (or for cosmetic reasons), so the flat plate correction will be discussed in the section on kinematic processing.

3.5.3.1. LEED I(E) Processing

In LEED I(E) processing, the goal is to measure the integrated intensity of each spot as a function of incident beam energy. While this would seem to be an easy task, this has been done in different ways in the past, and there are several subtle issues involved.⁵ This section will discuss the methods used in these experiments to collect the I(E) intensities.

The collection of I(E) intensities is most easily done by integrating all the pixels inside a window centered on the spot. The difficulty arises in that a diffraction spot moves as the energy is changed, so the integration window must be moved as the energy changes. This should preferably be done automatically, because only a limited amount of time is available to do the experiment before the surface becomes contaminated. One way to do this is to calculate the positions of the diffraction spots for each energy.

If the angle of incidence is known, the spot positions can be calculated from the lattice parameter and the beam energy. This provides a much better means of tracking diffraction spots than conventional spot-tracking methods. Since normal incidence is almost always used for LEED I(E) experiments, the geometry is simplified considerably. A number of spots which are symmetric around the specular beam are chosen, and the positions of these spots are measured for two different energies. From this data the scaling constants and the position of the specular beam can be calculated, so that the point on the screen corresponding to any position in reciprocal space can be calculated for any energy. This method can be used either for acquiring the I(E) data from the “live” LEED pattern in real time, or for acquiring the data from a series of frames which have been saved to disk.

Another difficulty arises because video frames can only be acquired with 8-bit resolution. This presents problems because the intensity of a diffraction spot can vary by several orders of magnitude as the energy is varied. Thus at some energies the camera pixels in the center of the diffraction spot will be saturated, leading to erroneously flat measured peaks. This can be remedied in part by additional processing. A line profile can be extracted through the center of the spot and then fit to a functional form, excluding the saturated pixels. The “missing” volume of the peak can then be calculated and added to the integrated intensity. Because of time considerations, it is not practical to perform this operation when acquiring I(E) curves “live”. However, it can be incorporated into automatic analysis of LEED patterns that have been acquired previously to disk or video tape. Figure 3.10 shows an I(E) curve with and without this correction.

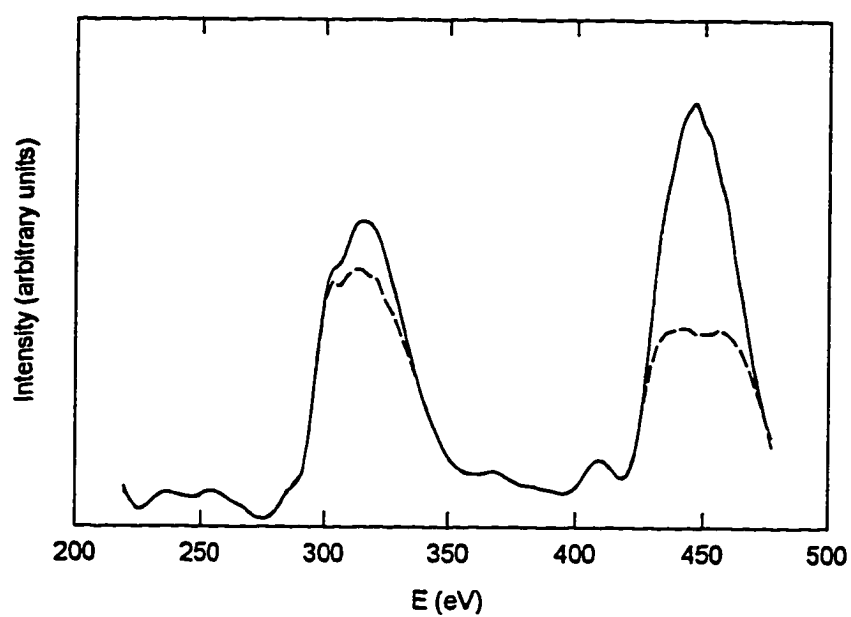


Figure 3.10. Correction to LEED $I(E)$ curve due to saturated camera intensity at the center of the spot. Dotted line is original curve; solid line is corrected curve.

In some cases even the correction described in the previous paragraph is not adequate. Overlayer spots are often less intense than the substrate spots by an order of magnitude or more. In addition, since our flat screen causes non-uniform suppression of the inelastically scattered electrons, the area at the center of the screen will often be completely saturated at a gain necessary for good measurement of the spots at the edge. Because of this it is usually necessary to acquire two sets of video frames over the same energy range to ensure good quality $I(E)$ curves for all the beams.

Another correction which must be done to the $I(E)$ data is background subtraction. This is especially important in our case because of the higher diffuse intensity due to non-uniform inelastic suppression. The background subtraction is done by fitting a planar background to the pixel intensities at the perimeter of the window. In practice this means simply finding the average perimeter pixel intensity, and subtracting that value times the number of pixels contained in the window. This method still leads to some inaccuracy since the diffuse background varies in a non-linear manner with position on the screen. However the additional errors are kept small by keeping the integration window as small as possible around the spot and by using a round integration window instead of a rectangular one, which has been the standard practice.

A number of other corrections are performed on the $I(E)$ data before analysis. As the energy is changed, the size of the integration window is also varied so that the window covers a constant area in reciprocal space. This however introduces the problem that as the size of the window decreases, the number of pixels in the integration will also decrease. So the intensity values are then divided by the number of pixels in the window. In addition, the intensity values are also normalized to the electron beam current. Thirdly, intensities must be corrected for the changing gain of the channel plate as the angle of the diffracted beam incidence onto the channel plate changes. This is done by calculating the angle of incidence from the position of the spot on the screen and looking up the gain as a function of the angle from known channel plate data.^{6,7}

For $I(E)$ data analysis is important to know the angle of incidence very precisely. The difficulty in measuring the angle of incidence is usually avoided by using normal incidence. Since $I(E)$ curves are extremely sensitive to angle of incidence when the angle is close to normal incidence, measuring $I(E)$ curves and comparing beams which should be equivalent under normal incidence provides a way to establish normal incidence to within a tenth of a degree. This alignment is most easily done if $I(E)$ curves can be acquired and displayed quickly while adjustments are being made. Since most of the previously mentioned corrections are unimportant for simply comparing one curve to another, they are turned off while acquiring $I(E)$ curves from the live LEED pattern for alignment purposes. A set of three $I(E)$ curves can be acquired over an energy range of about 200 eV and compared using the Pendry R factor in about 4 seconds, allowing convenient trial-and-error alignment of the sample.

After normal incidence is established, the experimental $I(E)$ data are acquired. This can be done either in "live" mode, or the entire video frames can be acquired and saved for later analysis. The first method is used if only a small number of very intense beams are to be acquired, for example an experiment on a clean high-symmetry surface. The second mode is used in cases where there are a large number of beams or the beams are of very low intensity. For these cases twenty to thirty video frames are averaged at each energy to increase signal to noise ratio. In most cases energy increments of three eV were used, which proved fine enough to adequately resolve all $I(E)$ features. In this way the alignment, acquisition and saving of data over a 300 to 400 eV range can be done in 20 to 30 minutes. (It could be done more quickly if the video frames were saved to video tape rather than digitized and written to disk. However this would involve either the necessity of a very high-quality VCR or a loss of spatial resolution and possibly an increase in noise from an additional digital-analog-digital conversion.) After the video frames are acquired, the $I(E)$ curves are extracted using all the previously mentioned corrections. Since the entire video frames have been acquired, this step may be repeated in different ways to determine the best parameters for the analysis. Any remaining background can be subtracted by visually inspecting the LEED patterns to determine where the intensities should go to zero, and then subtracting a low order polynomial fit to these points.

3.5.3.2. Kinematical LEED Processing

In addition to integrated intensities, it is also necessary to measure widths, peak intensities, and positions of diffraction spots. This is done by extracting one-dimensional intensity profiles through the two-dimensional image and fitting them to functional forms. In addition to line profiles, arc profiles are also used. Since the aspect ratio of the camera is not one, a correction depending on the slope of the profile must be applied to the x spacing of the resulting intensity-position curve.

Line profiles are extracted in the following way: starting at the first endpoint, steps are taken toward the other endpoint in increments spaced apart an amount equal to the distance between pixels. In order to accommodate profiles several pixels wide, at each point pixel intensities are averaged at one-pixel increments along a line perpendicular to the direction of the profile. Since in general these positions will not have integer coordinates (that is will fall in between rather than on top of a video pixel), the interpolated intensity value between pixels is calculated using a planar fit to the four neighboring pixels. Extraction of arc profiles is done in the same manner, except that the positions are chosen along the perimeter of an ellipse.

As with measurement of integrated intensities, the diffuse background must be removed when fitting intensity profiles to peaks. One way of removing the background is to extract an additional profile at a position on the screen close to the desired profile but not going through any diffraction spot, and to subtract this from the desired profile. However this introduces additional error into the data since the subtracted background contains experimental error. Since the non-uniform background varies slowly with screen position, better results are obtained by fitting the uncorrected profile to a spectral function plus a low order polynomial background and limiting the fit to the region close to the peak. Figure 3.11 shows a typical intensity profile through a diffraction spot fit to a lorentzian plus a linear background.

As was mentioned earlier, the use of a flat rather than hemispherical screen introduces a distortion into the image. Using normal incidence a conventional hemispherical screen produces a diffraction pattern which is a direct projection of reciprocal space; the flat plate correction is necessary to restore this feature. This correction, which is done by computer on the digitized image, is shown in Figure 3.12. In the diagram r' is measured radius of a feature in the diffraction pattern and r is the corrected radius. Figure 3.13 shows a sample diffraction pattern before and after the correction.

Since the flat plate correction is slowly varying in position on the screen, it is only important for measuring long distances in reciprocal space. Fits to intensity profiles through diffraction spots (which do not span large values of reciprocal space) may be done successfully without the correction. Since the flat-plate correction is a calculation-intensive process, in measuring distances between peaks it is often more efficient to perform the correction after extracting the profiles and fitting the peaks. The other error introduced by the flat screen, non-uniform suppression of inelastically scattered electrons, is also a slowly varying feature and may be compensated by using a polynomial background in the fitting of intensity profiles. For purely cosmetic purposes this diffuse background can also be removed from the image by computer by fitting it to a two-dimensional gaussian function and subtracting it from the image. Figure 3.13 shows a diffraction pattern before and after this subtraction.

3.5.4. Determination of Uncertainties

3.5.4.1. LEED Transfer Width

As with any experimental technique, a LEED experiment is limited by the resolving power of the instrument. In LEED the effect of this is to broaden diffraction spots, introducing a limit in the distance over which correlations can be measured.⁸ If $I(S_p)$ is the scattered intensity that would result from an ideally collimated monochromatic beam of infinite extent, then the actual scattering obtained, $J(S_p)$, will

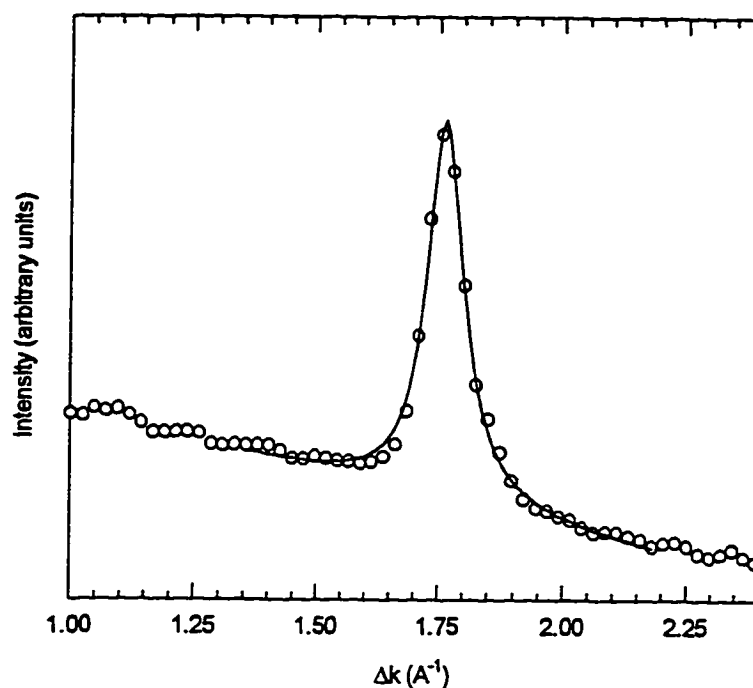


Figure 3.11. Line intensity profile through a diffraction spot from a video frame of a LEED pattern. The diffraction spot is fit to a lorentzian function plus a linear background.

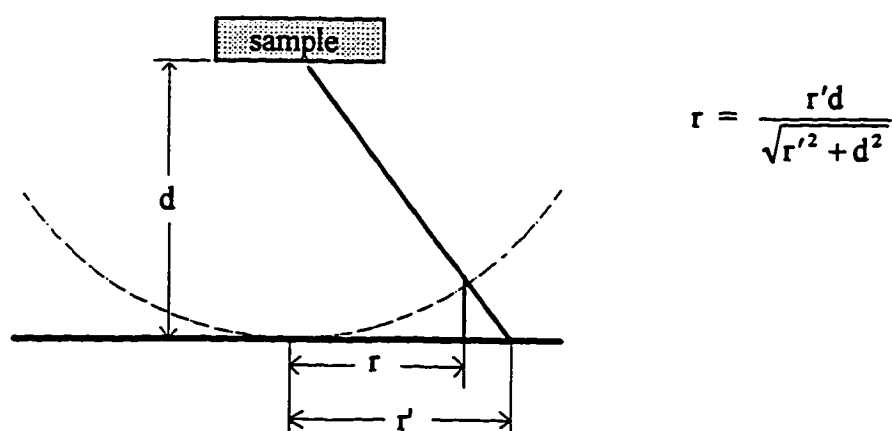


Figure 3.12. Correction to made to a diffraction pattern due to the flat-plate distortion.

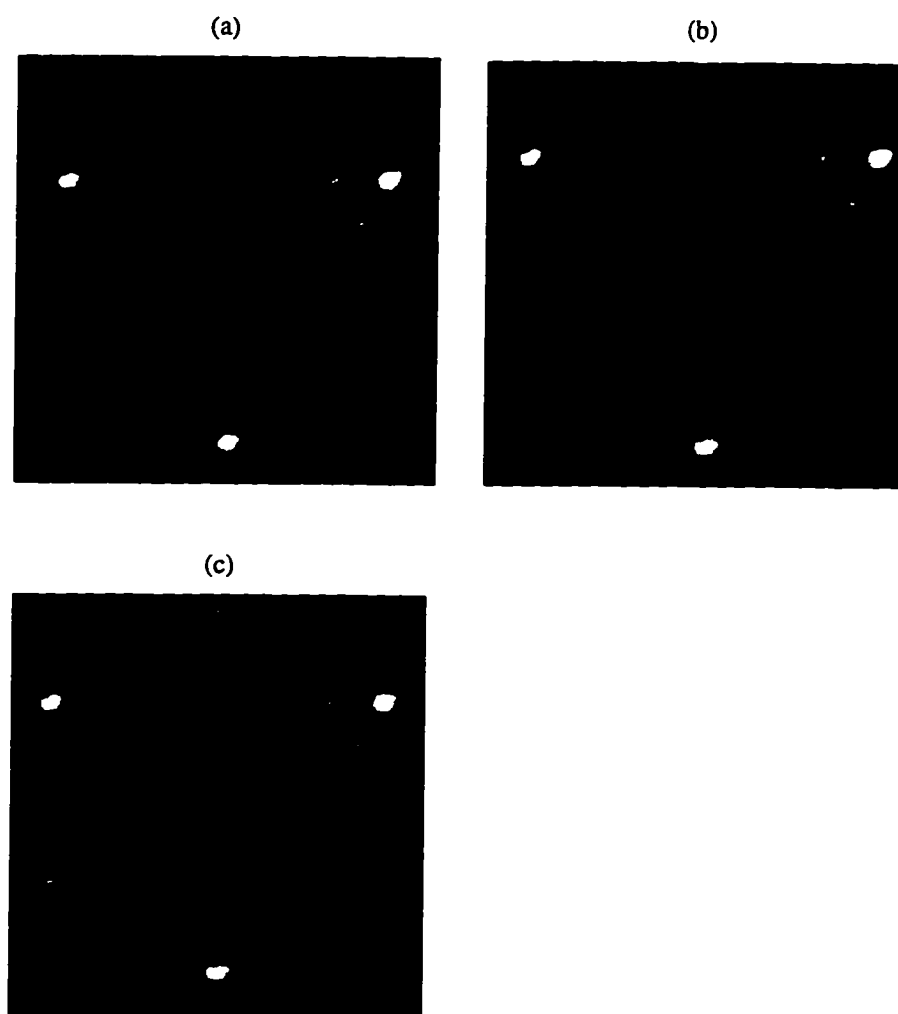


Figure 3.13. Computer corrections performed on a diffraction pattern ($Cs (2\sqrt{3} \times 2\sqrt{3})R30^\circ$). (a) Original image. (b) Same image after flat plate correction, and (c) after subtraction of diffuse inelastic intensities. Note that after flat plate correction the diffraction spots lie along straight lines as they should for an undistorted reciprocal space image.

be given by the convolution of $I(S_{\parallel})$ and the instrument response function, $T(S_{\parallel})$:

$$J(S_{\parallel}) = T(S_{\parallel}) \otimes I(S_{\parallel})$$

where \otimes denotes a convolution. If the sample is an ordered crystalline lattice, then the effect of $T(S_{\parallel})$ will be to broaden the Bragg diffraction peaks. If $T(S_{\parallel})$ is known, the measured spectra can be deconvoluted to obtain $I(S_{\parallel})$. However, $T(S_{\parallel})$ is usually not known exactly. This effectively makes it difficult to measure any periodicities which have a reciprocal lattice spacing smaller than the width of $T(S_{\parallel})$. The Fourier transform of $T(S_{\parallel})$ yields what is known as the transfer function $t(S_{\parallel})$. The full width of this function is called the transfer width, and is the distance in real space over which it becomes difficult to measure correlations on the surface if the transfer function is not known.

Although the transfer function is not known exactly, it can be estimated. It is usually assumed that $T(S_{\parallel})$ can be approximated by a gaussian function, and then various instrumental factors contributing to the width of the gaussian are evaluated. There are four important factors which must be considered: (1) the energy spread of the incident electron beam, (2) the finite size of the electron source, which leads to uncertainty in the angle of incidence, (3) finite width of the beam striking the sample, which leads to uncertainty in the angle of scattering, and (4) finite size aperture of the detector. Each of these factors will be evaluated for the instrument used in these experiments.

The energy spread of the incident beam, ΔE , causes an uncertainty in the measured parallel momentum transfer, $|\Delta S_{\parallel}|$, of

$$|\Delta S_{\parallel}| = k \frac{\Delta E}{E} |\sin \theta - \sin \theta_0|$$

where k is the magnitude of the wave vector, E is the energy, θ_0 is the angle of incidence, and θ is the scattering angle. A non-zero value of ΔE is caused by the Boltzmann temperature distribution of the tungsten filament, which is about 0.25 eV. For first order diffraction from the Ag(111) surface at normal incidence and with $E=150$ eV, this results in a $|\Delta S_{\parallel}|$ value of about 0.004 \AA^{-1} .

The finite size of the electron source causes a contribution to the uncertainty in S_{\parallel} of

$$|\Delta S_{\parallel}| = k \gamma \cos \theta_0$$

where γ is the angle subtended by the electron source at the sample. In our case γ is about 2×10^{-3} radians, so normal incidence and $E=150$ eV yield about 0.015 \AA^{-1} of uncertainty in the reciprocal space position.

The width of the beam at the sample causes a contribution of

$$|\Delta S_{\parallel}| = k \left(\frac{D}{R} \right) \frac{\cos^2 \theta}{\cos \theta_0}$$

where D is the width of the beam and R is the distance from sample to detector. At energies greater than 150 eV, the beam size is considerably smaller than a millimeter. Using normal incidence and 300 eV, assuming a beam size of 0.3 mm, yields a $|\Delta S_1|$ value of 0.025 \AA^{-1} . However at lower beam voltages the spot size is considerably larger, being as large as 1 mm below about 80 eV. Using this value and 80 eV, the uncertainty increases to 0.035 \AA^{-1} .

Finally, the finite aperture of the detector results in a contribution of

$$|\Delta S_1| = k \left(\frac{d}{R} \right) \cos \theta$$

where d is the detector aperture. In our case two different “apertures” have to be considered: the channel plate pore spacing and the finite pixel size of the video camera. The pore spacing of 25μ yields about 2500 effective apertures across the screen while there are only approximately 400 video lines across the screen, causing the video resolution to be the limiting factor. At 150 eV, this yields a ΔS_1 value of 0.015 \AA^{-1} .

Figure 3.14 shows the value of $|\Delta S_1|$ as a function of energy calculated by adding these four values in quadrature, using the specific parameters for our LEED apparatus and the value of θ appropriate for integer order diffraction beams on Ag(111), using normal incidence. Also shown are transfer width values calculated from the widths of Ag(111) integer order beams, using a clean well-ordered sample. This assumes that the sample is perfectly ordered, which of course is not the case. The oscillating behavior is caused by surface steps, and will be discussed in chapter four. The maxima in the oscillations represents the measured transfer width. Thus the measured transfer width is slightly higher than the calculated.

3.5.4.2. Uncertainties in Video Processing

There are a number of other uncertainties in the measurements which can yield errors in the measured values. The intensity measured at a particular position will fluctuate with time due to fluctuations in the electron current reaching the channel plate, noise from the control electronics, or a host of other factors. This fluctuation can be measured by monitoring the intensity of one video pixel as a function of time. Figure 3.15a shows a histogram of intensities from one pixel in the LEED image, using typical experimental parameters for the detection apparatus. The statistical distribution width is proportional to the standard $1/\sqrt{I_0}$, as shown in Figure 3.15b, with the exception of data below an intensity value of

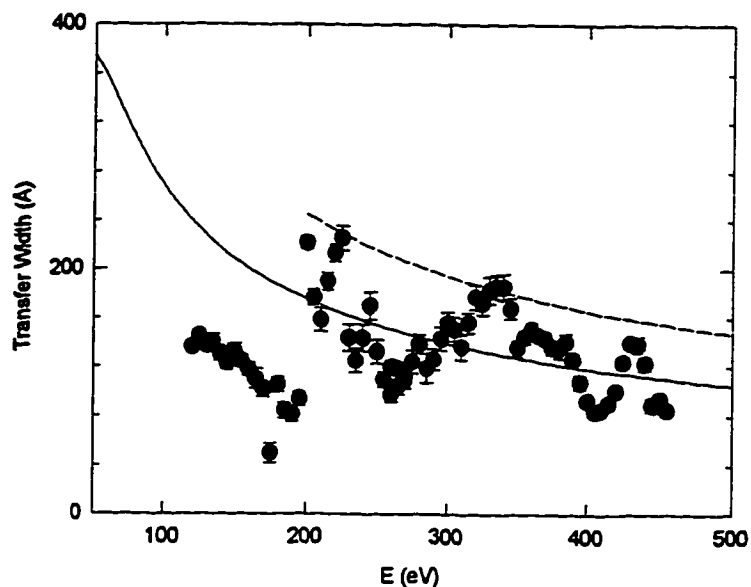


Figure 3.14. LEED transfer width as a function of beam energy. The solid line is calculated based on the specifics of the instrument, and the data points are calculated from the widths of Ag(111) diffraction spots from a clean well-ordered sample. Oscillations are due to the presence of surface steps. The dashed line represents the actual transfer width, and is a fit based on the maxima of the oscillations.

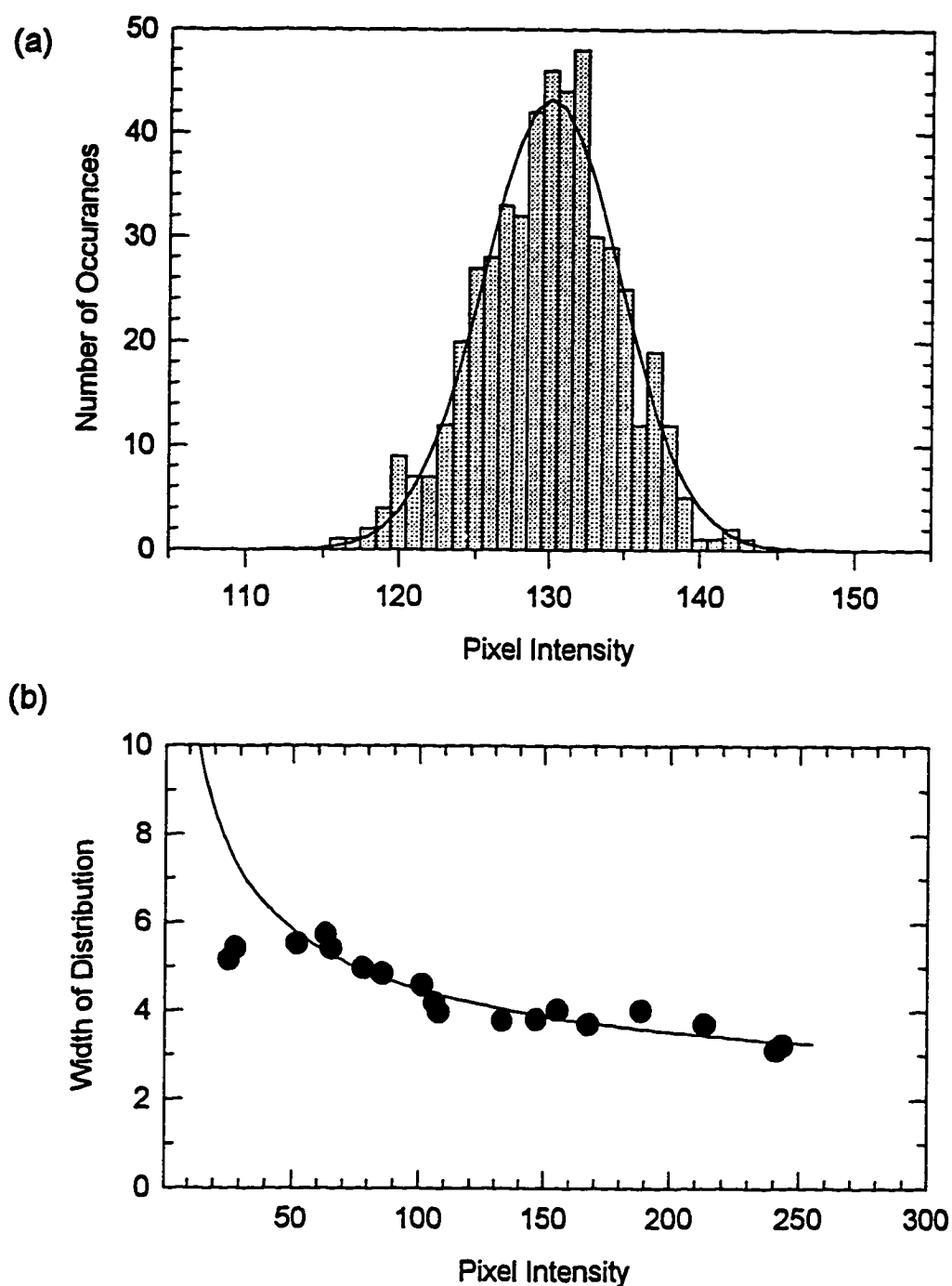


Figure 3.15. Analysis of LEED detector fluctuations with time. (a) Statistical distribution of single pixel intensities taken as a function of time, using typical experimental settings. Solid line is a gaussian fit. (b) Width of the gaussian fit as a function of mean pixel intensity. The solid line is a $1/\sqrt{I}$ fit.

about 50. The standard deviation from the mean is equal to approximately 4.5 for typical experimental intensities. (Intensity units are 8-bit gray-scale units, yielding a range of 0 to 255 from completely dark to camera saturation.) Usually about 25 frames are averaged for each LEED pattern, so the uncertainty in the intensity value of a pixel due to fluctuations with time will be $\sqrt{1/25}$ of the standard deviation, or about 0.9. Another source of error will be variations in detector efficiency with position. These could be caused by non-uniformities in the channel plate, phosphor screen, or video camera CCD element. In order to evaluate these factors, several line profiles were taken of a diffraction pattern through regions of reciprocal space which contained no sharp diffraction features. The diffraction pattern used was one which had been acquired as an average of 255 video frames, to ensure that time fluctuations did not play an important part in the fluctuations in the image. Then the intensity profiles were fit to slowly varying functions, and a histogram of deviations from the fitted function was generated. The standard deviation of the distribution is approximately 1.1, and was found to be fairly independent of the total level of illumination of the camera. This represents the uncertainty of a pixel intensity due to small-lengthscale spatial variations in the detector sensitivity. Large lengthscale variations, such as the variation of the channel plate gain as a function of incident angle which is known to exist, are not as important because they do not affect the fitting of sharp diffraction features. These large lengthscale variations do however present some problems with LEED I(E) analysis.

The two sources of uncertainty discussed in the previous two paragraphs (uncertainty in diffraction intensity due to spatial and to temporal variations) can be lumped together conveniently for our purposes. The intensities of pixels along an extracted profile will contain both of these kinds of fluctuations. In order to investigate the effect of this uncertainty on fitted diffraction peak parameters, lorentzian functions were generated (using parameters to make them look similar to a line profile through a typical diffraction spot), and each y value was offset by a random amount. The random offsets were generated using two components: first a gaussian distribution with a width that depended upon the intensity of the point (with the same distribution as that seen in Figure 3.15b), and secondly a gaussian distribution of width 1.1, independent of the intensity. These functions were then least-squares fitted to lorentzian functions. This was repeated 200 times in order to determine the distribution in the error of the fitted parameters. Table 3.1 shows the results. The standard deviation of each parameter can be viewed as the expected experimental error for that parameter due to the two kinds of fluctuations which were just discussed. For most purposes the magnitudes of these errors are insignificant.

The previous paragraphs have discussed uncertainty in measured intensities and have determined the effect of these uncertainties on fitted parameters through diffraction spots. There will also be sources of experimental error which will affect the position in reciprocal space of recorded intensities. These

Table 3.1. Error in fitted lorentzian parameters due to random errors in pixel intensities representative of a typical experiment. See text for further explanation.

	amplitude	position (\AA^{-1})	half-width (\AA^{-1})
typical parameters	0.3	0.001	0.002
worst case	1.2	0.002	0.006

errors may include angles of incidence slightly off normal, inaccuracies in the flat-plate correction, and a number of other effects which distort the reciprocal space image obtained.

We will now investigate the effect of slightly off-normal incidence on a measurement of the lattice parameter, which is done by measuring the distance between two diffraction spots which are opposite each other (i.e. their positions in reciprocal space are negatives of each other). Figure 3.16 shows a side view of two diffracted beams striking the screen. The distance of interest in measuring an overlayer lattice parameter is $a/2$. After flat-plate correction this distance is equal to

$$d \sin \theta \cos \theta_0$$

So the relative magnitude of the error is equal to $(1 - \cos \theta_0)$. Since the angle of incidence can easily be aligned to within 2° by eye (without recording equivalent $I(E)$ curves), so this gives a maximum error to measurements of reciprocal space distances of less than 0.06%. In practice, the lattice parameter is usually determined by averaging the results of two profiles in different directions. If the second profile is in a direction perpendicular to the direction of the misalignment, the distance measured becomes

$$d \frac{\sin \theta}{\cos \theta_0}$$

So the total error is equal to

$$1 - \frac{1}{2} \left(\cos \theta_0 + \frac{1}{\cos \theta_0} \right)$$

For a 2° error, this yields a reciprocal space error of $\sim 10^{-7}$, which can be safely ignored.

Another way in which errors can enter the measurement of a lattice parameter is through the flat-plate correction. In order to do the flat plate correction, the exact position of the screen center must be known. An error in this position will cause an error in the flat-plate correction, leading to errors in measured reciprocal space positions, as shown in Figure 3.17. If the screen center were known exactly, a distance of r would be measured between the spots after flat-plate correction. Because of the error in screen center, a distance of r_{err} is measured instead. The magnitude of the error, to second order in Δr , is equal to

$$\frac{|r_{\text{err}} - r|}{r} = -\frac{1}{2} \cos^2 \theta \left(\frac{\Delta r_x}{d} \right)^2 - \frac{3}{2} \cos^4 \theta \left(\frac{\Delta r_y}{d} \right)$$

where θ is the angle between the normal and the scattered beam. In a worst-case scenario, $\left| \frac{\Delta r}{d} \right|$ may be as

high as 0.04. In nearly all cases where reciprocal space distances are being measured, θ will be less than 30°, which yields a worst-case error of 0.14%. Unfortunately since the errors due to Δr_x and Δr_y have the same sign, they cannot be canceled by averaging results from profiles in perpendicular directions.

However, although an error of 0.14% in the reciprocal space distance is bordering on being significant, the error in the measured lattice parameter will be significantly smaller since the lattice parameter is obtained from a ratio of two distances, each of which are affected by the error in screen center. The error will be largest when the ratio of the distances measured is very different from one, that is when overlayer lattice parameter is far from that of the substrate. Assuming the overlayer lattice is greater than three times that of the substrate and using typical experimental parameters, the magnitude of the error will be less than about 0.3 times the quantity previously stated, which is small enough to be insignificant.

Another error introduced by the flat plate has to do with the trajectories of electrons between the grounded grid and the channel plate. Since the force due to the retarding field is not acting in the same direction as the electron's direction of motion, the electron will travel in a parabolic trajectory causing some error in the measured position, as shown in Figure 3.18. The error in the measured position divided by the radius of the (flat-plate corrected) position is equal to

$$\frac{\Delta}{r} = \frac{2\delta}{Sd} \left(\cos \theta - \sqrt{\cos^2 \theta - S} - \frac{S}{2 \cos \theta} \right)$$

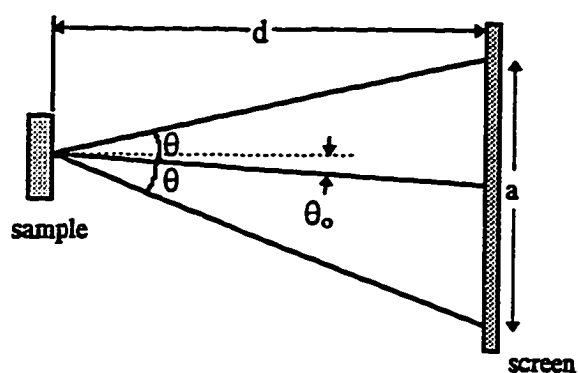


Figure 3.16. A slightly non-normal angle of incidence, which causes an error in measured reciprocal lattice positions.

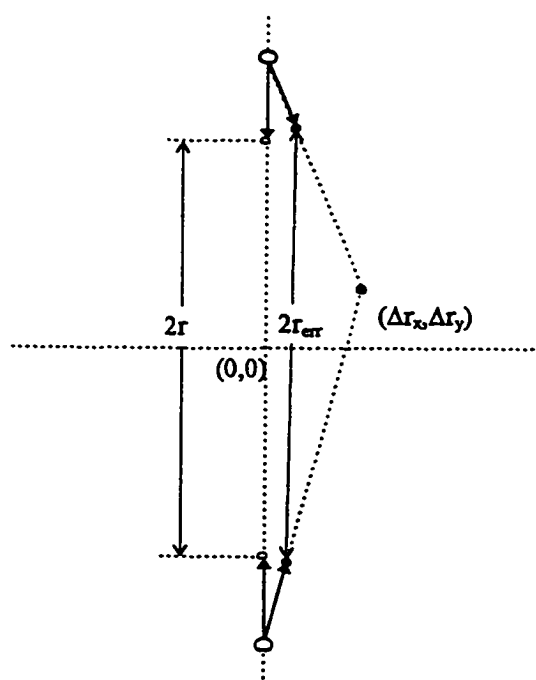


Figure 3.17. Diagram showing the error caused by the flat plate correction when the screen center is not known exactly. The open circles represent the measured positions of two diffraction spots on the flat screen, the gray circles represent the corrected positions using the actual screen center, and the solid circles represent the corrected positions using a screen center offset by $(\Delta r_x, \Delta r_y)$. $2r$ is the corrected distance between spots, and $2r_{err}$ is the corrected distance using the erroneous screen center.

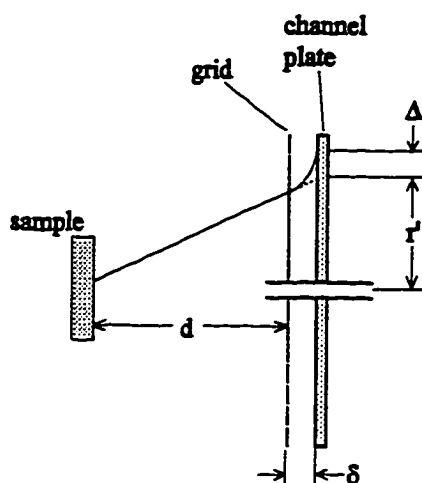


Figure 3.18. Error in diffraction position due to parabolic electron trajectory between grid and channel plate.

where S , a number between zero and one, is the ratio of the suppressor voltage to beam voltage. This correction has the same direction as the flat-plate correction, and thus could easily be incorporated into the same step. However, the expression for this correction is much more complicated mathematically than that for the flat-plate correction and would make the already computationally intense flat plate correction take much longer, and so it is desirable to find a way to get around it. Since both this correction and the flat-plate correction have the same sign, direction, and monotonic increase with r , this additional correction can be approximated by adjusting the value of d used in the flat-plate correction slightly from its actual value. In practice this was done by taking a LEED pattern of a (2×2) commensurate phase and determining the exact value of d necessary to shift the half-order spots as close as possible to exactly the half-order position. Figure 3.19a shows the magnitude of the actual correction (including both flat-plate and parabolic trajectory), compared with the flat-plate correction alone (dotted line) and a flat-plate correction using a suitably adjusted d value (dashed line). Figure 3.19b shows the error that would result in a lattice parameter measurement based on a measurement of diffraction spots at the half-order positions of an Ag(111) diffraction pattern, using the adjusted flat-plate correction. For most of the experiments that will be reported here, these errors are small enough to be insignificant. However for some of the more precise lattice parameter measurements they do become significant, and in these experiments the full correction will be used.

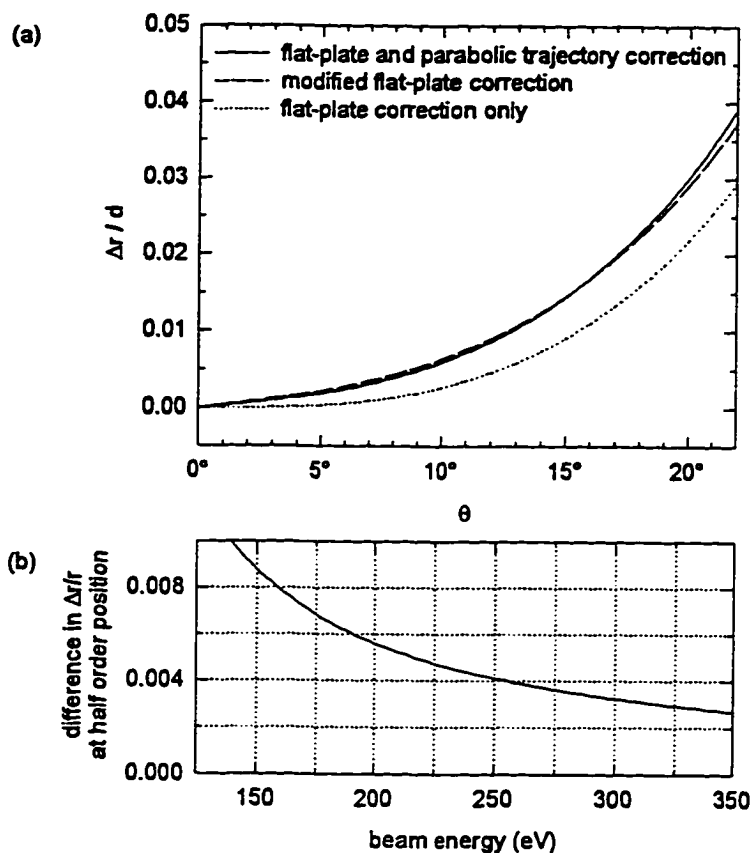


Figure 3.19. Analysis of the error in position caused by the suppressor voltage. (a) Ratio of the correction to the diffraction position to the distance between screen and sample, as a function of scattering angle. Solid line includes flat-plate and parabolic trajectory corrections, dashed line is the modified flat-plate correction (see text), and dotted line is the flat-plate correction only. (b) Worst-case relative error in a calculated lattice parameter using only modified flat-plate correction, as a function of incident beam energy. Actual error is usually significantly less, depending on experimental parameters.

3.6. References

- ¹ R. G. Musket, W. McLean, C. A. Colmenares, D. M. Makowiecki, W. J. Siekhaus, *Appl. Surf. Sci.* **10**, 143 (1982).
- ² SAES Getters, Alkali Metal Dispensers (technical brochure).
- ³ M. Succi, R. Canino and B. Ferrario, *Vacuum* **35**, 579. (1985).
- ⁴ R. D. Diehl and S. Chandavarkar, *J. Phys. E: Sci. Instrum.* **22**, 651 (1989).
- ⁵ S. K. Kim, F. Jona and J. A. Strozier, *Phys. Rev. B* **51**, 13837 (1995).
- ⁶ M. Galanti, R. Gott, J. F. Renaud, *Rev. Sci. Instrum.* **42**, 1818 (1971).
- ⁷ G. W. Fraser, *Nucl. Instrum. Meth.*, **206**, 445 (1983).
- ⁸ M. A. Van Hove, W. H. Weinberg, C. M. Chan, Low Energy Electron Diffraction, Springer Verlag (1986).

Chapter Four

Characterization of the Clean Ag(111) Surface

4.1. Introduction and Historical Summary

Most of the first systems to be investigated using LEED were clean metal surfaces. This was partly because LEED was (and still is, for the most part) restricted to conducting materials, and clean surfaces represented the simplest systems in terms of interpretation and analysis. Since then the clean surface structures of the high-index faces of nearly all of the metal surfaces have been determined. Most of these have been done by LEED.

The atoms at the surface of a material experience a very different environment from those in the bulk. Because of this top few layers of atoms may arrange themselves in a different structure from the atoms in the bulk phase. Transition metals often experience dramatic reconstructions at the surface. These occur because of the partially-filled d state, which gives rise to localized covalent bonds. At the surface truncation these become dangling bonds, and so the optimal atomic configuration often becomes different at the surface than in the bulk. An example of this is the W (001) system, where a top-layer reconstruction with $(\sqrt{2} \times \sqrt{2})R45^\circ$ symmetry occurs.¹

For metals with a filled d shell, called “noble metals”, the surface reconstruction on low index faces is usually small or nonexistent. Sometimes the spacing between the top few layers may change by a few percent, but with a few exceptions there is no dramatic change in structure. These small changes in perpendicular lattice parameter at the surface are called relaxations. While the direction of a relaxation will depend on the particular system, contractions of the first layer are more common (at least at low temperatures) than expansions. This phenomenon can be explained intuitively by the Smoluchowski smoothing which takes place at a surface.² The electron density at the surface will rearrange somewhat to minimize the corrugation of charge extending into the vacuum. This has the effect of slightly moving the center of mass of the surface charge density away from the vacuum. This in turn causes an electrostatic force on the first layer of ion cores, so that they too are displaced slightly toward the surface. This effect should be larger for more highly corrugated faces such as the FCC (110) face, and small for the close packed surfaces like FCC (111). It has been predicted that relaxations in succeeding layers should be oscillatory, with a smaller expansion in the second and an even smaller contraction in the third, etc.³ A summary of reconstructions and relaxations found on various metal surfaces can be found in reference 4.

Silver has a filled d shell and therefore is considered a noble metal. Thus its low index faces are not expected to exhibit any complicated reconstructions at the surface. Early studies in fact showed no

reconstruction or surface relaxation, to the precision of the measurement, at room temperature and 140 K.^{5,6} One of these was a LEED study in which only the Ag(111) specular beam was measured, and the other was a high-energy ion scattering study. In both studies, the uncertainty in the measurement was given as 0.1 Å. A more recent study, done by medium energy ion scattering, showed a first-layer contraction of about 2.5% at room temperature.⁷ At higher temperatures however, the first layer spacing increased dramatically, becoming expanded for temperatures above about 800 K, finally being expanded by about 10% at 1150 K. This experimental result was supported by a theoretical prediction which showed a large temperature-dependent expansion, due to softening of in-plane phonon frequencies.⁸

4.2. Experimental Results

The Ag(111) sample was repetitively cleaned by Ar⁺ ion bombarding and annealing, as described in Chapter Two, until no impurities could be seen in the Auger spectrum and the LEED spots became sharp and intense. Figure 4.1 shows a LEED pattern of the clean Ag(111) surface, taken at normal incidence. The diffraction pattern consists of a hexagonal array of beams, with no fractional order beams and a low intensity background. The positions of the beams in reciprocal space correspond to the expected in-plane spacing of atoms in a bulk-truncated FCC(111) crystal with an in-plane lattice spacing equal to that of bulk silver. From the widths of the diffraction beams it was determined that the average terrace size of the surface is at least 250 Å.⁹ This is consistent with other results in which large terraces have been formed on Ag(111) using sputter-and-anneal treatment.¹⁰

While the normal-incidence diffraction pattern has six-fold rotational symmetry when only the positions of the beams are considered, if the intensities are considered as a function of energy the symmetry is reduced to three-fold. This can be in Figure 4.1: three of the order beams are of one intensity and the other three have a different intensity. The reason for this is that while the top layer of the FCC(111) crystal has six-fold symmetry, when considered with the underlying layers its symmetry is reduced to three-fold.

In a LEED I(E) experiment, the diffraction beams must be indexed and labeled in order to identify them and compare them with calculated spectra. A coordinate system must be defined and the beams must be divided into groups which are equivalent through rotation and mirror symmetries. The I(E) spectra of equivalent beams are then averaged before comparing with the calculations. Figure 4.1b shows the coordinate system used in this case. The beams used in this experiment are labeled and the grouping of equivalent beams is shown in Table 4.1. They are divided into groups of equivalent beams using the 3-fold rotational and mirror symmetry of the FCC (111) surface.

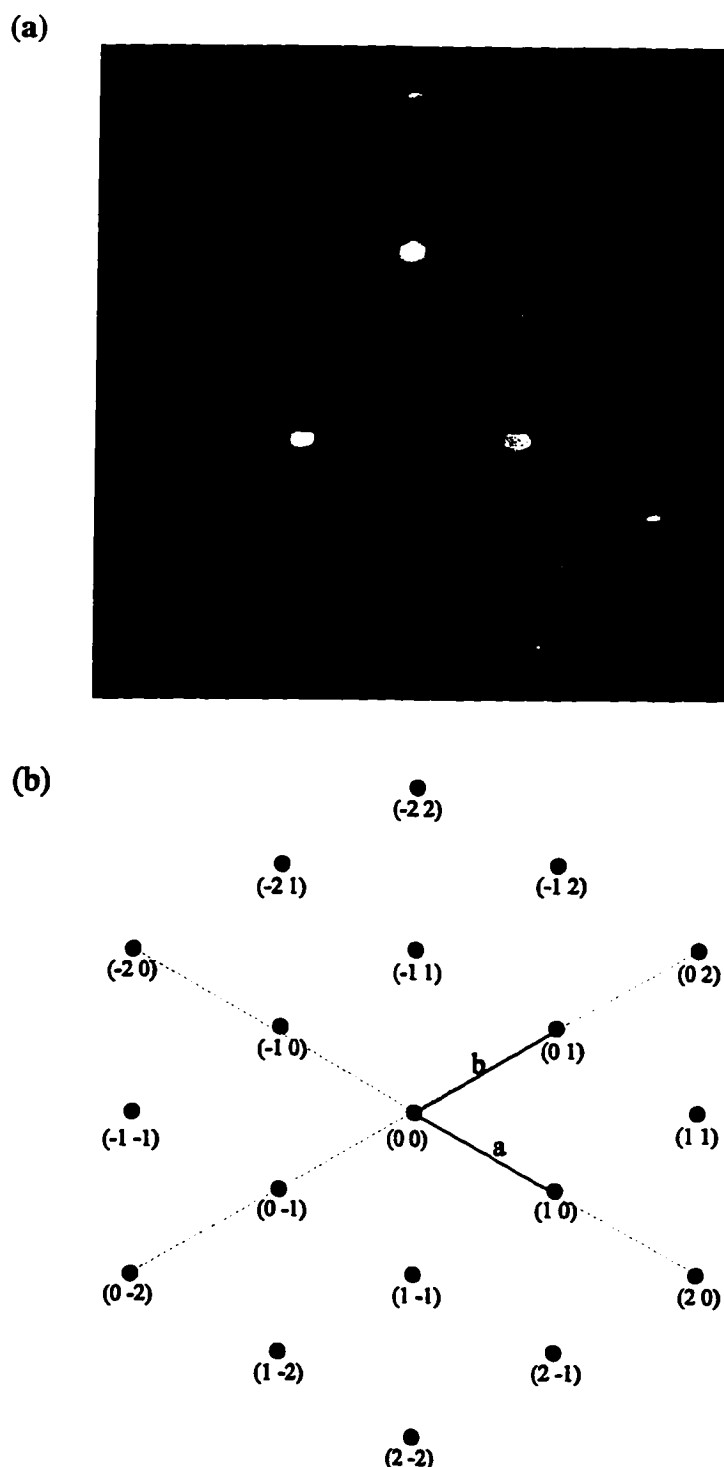


Figure 4.1. Diffraction pattern from the clean Ag(111) surface. (a) Shows the actual diffraction pattern, at an energy of 246 eV, and (b) shows the coordinate system used to index the beams. The lines a and b denote the reciprocal lattice basis vectors. Table 4.1 shows the grouping of equivalent beams. The light lines show the planes of mirror symmetry.

Table 4.1. Equivalent beam sets for an FCC (111) surface.

(0 1) set	(1 0) set	(1 1) set	(0 2) set	(2 0) set
(0 1)	(1 0)	(1 1)	(0 2)	(2 0)
(-1 0)	(-1 1)	(-1 2)	(-2 0)	(-2 2)
(1 -1)	(0 -1)	(-2 1)	(2 -2)	(0 -2)
		(-1 -1)		
		(1 -2)		
		(2 -1)		

Because the surface has three-fold symmetry rather than six-fold, there are two inequivalent directions which cannot be distinguished from each other by a qualitative look at the LEED pattern. In order to solve the structure using LEED I(E) analysis it must be determined which direction is which, i.e. which set of three inequivalent first order diffraction spots are the (1 0) spots and which are the (0 1) spots. This is often done by trying the LEED structural fitting both ways, and choosing the one which yields the best agreement. An alternative way to obtain this information is to calculate the kinematic positions of the diffraction peaks and compare them to the major peaks seen in the spectrum. While the positions will not correspond exactly because of multiple scattering and the effect of the inner potential, there should be enough correspondence in order to establish which direction is which. Figure 4.2 shows the measured spectra with the expected positions of the kinematic peaks marked with vertical lines. (Also shown are best-fit calculated spectra, reported in the following paragraph.) It is evident that there is better agreement between the kinematic positions and the measured peaks than if the indices of the measured spectra were interchanged.

LEED I(E) intensities were measured for the clean surface over a 400 eV energy range, at a sample temperature of 120 K. The structure determination was done using the Tensor LEED method described in Chapter Two. Nine phase shifts were used, and a value of -5.0 eV was used for the imaginary part of the inner potential. In the structure determination, the top layer was allowed to relax in the perpendicular direction, but all the rest of the layers were held at the bulk spacing. The Debye temperature was also varied to find the best fit. The Pendry R factor was used to compare measured and calculated spectra. Figure 4.2 shows the best-fit spectra compared with the measured spectra. The best-fit

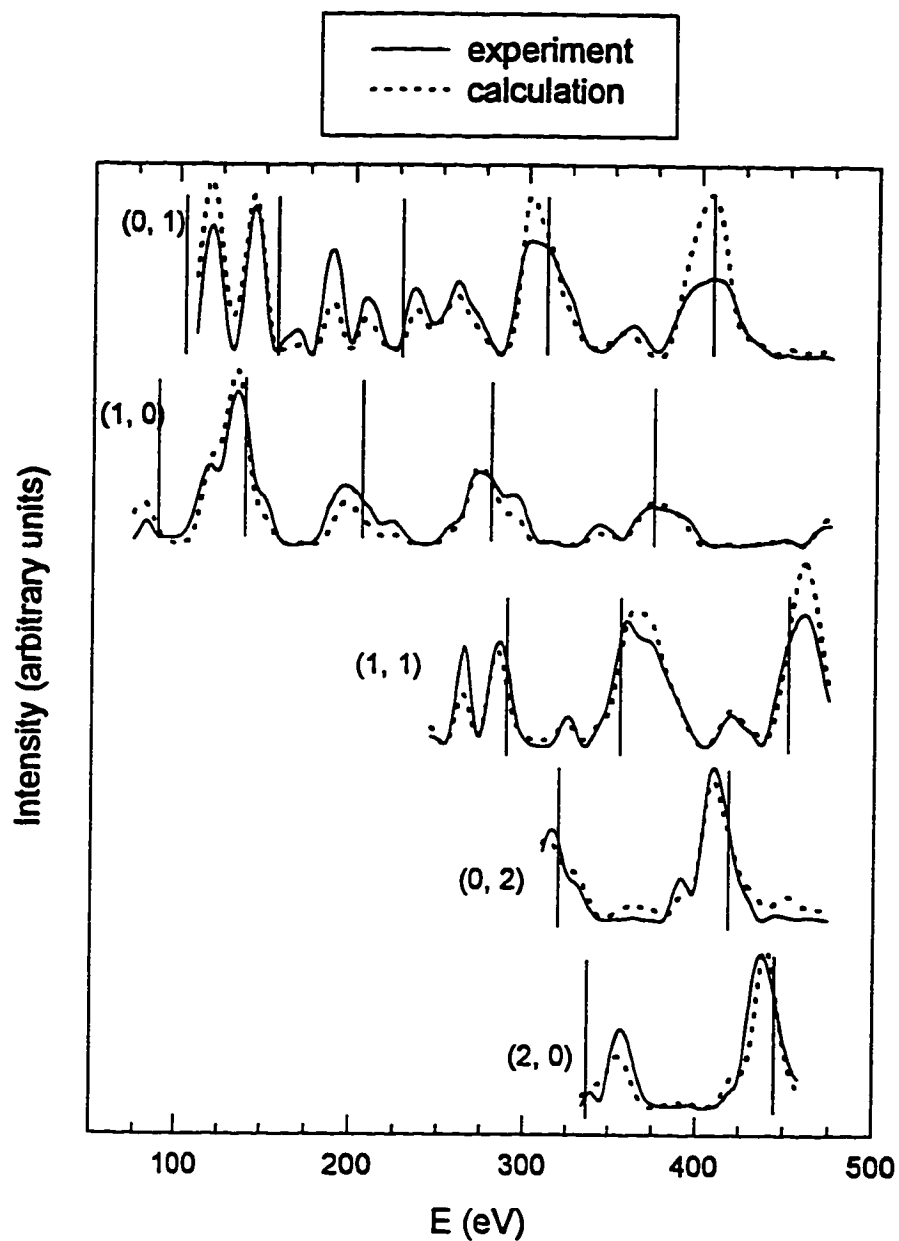


Figure 4.2. LEED $I(E)$ spectra for clean Ag(111), compared with best-fit calculated spectra. The experimental data is represented by solid lines and the calculation by dotted lines. The Pendry R factor is 0.117. The vertical lines represent the expected kinematic peak positions.

R factor is 0.117, and this corresponds to a relaxation of the top layer of $0.00 \pm 0.01 \text{ \AA}$ and a silver Debye temperature of 220 K. The real part of the inner potential was varied to achieve the best fit, resulting in a value of $8.9 \pm 0.2 \text{ eV}$. Figure 4.3 shows the variation in the R factor with a changing top layer spacing. The uncertainty in the parameter was determined from the curvature of the R factor close to the minimum.¹¹

4.3. Discussion

The results presented in this chapter are in fairly good agreement with the older work, in that no relaxation is measured at low temperature. However they appear not to be consistent with the ion-scattering results which show a contraction of 2.5% in the first layer at room temperature. The experiment described here was done at a lower temperature than this previous study; however it is highly unlikely that the top layer spacing contracts between 120 K and room temperature. The source of this discrepancy is not understood, although it is not uncommon for different surface science techniques to yield answers which disagree by a few percent.

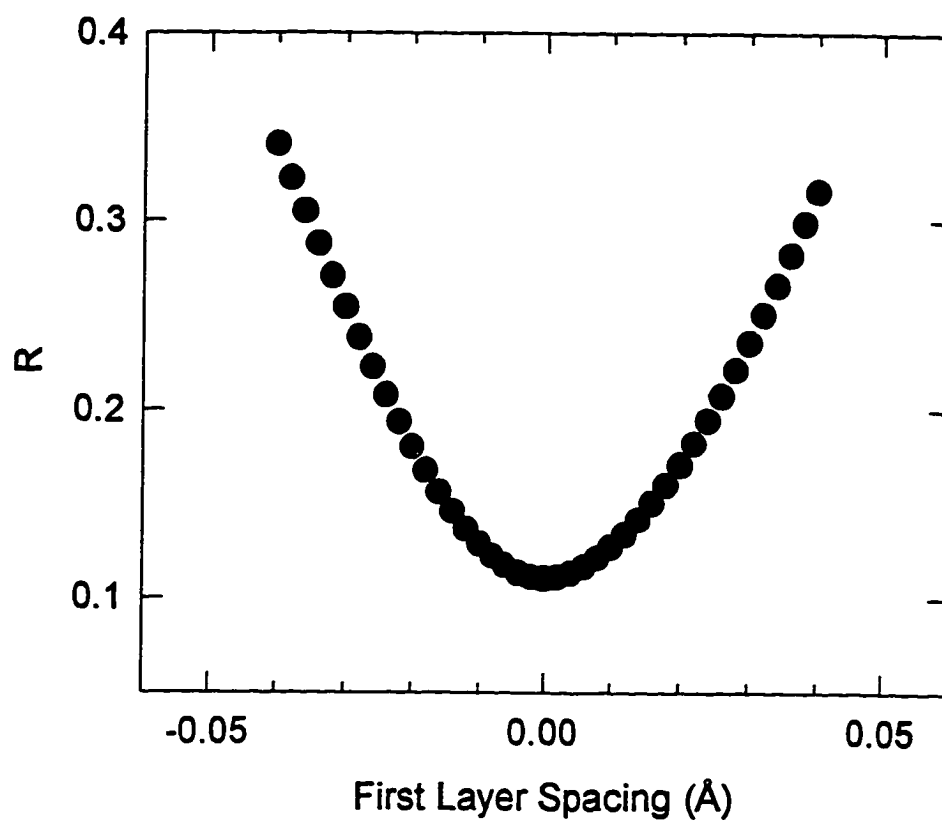


Figure 4.3. Variation of the R factor with the first Ag(111) layer spacing.

4.4 References

- ¹ J. A. Walker, M. K. Debe and D. A. King, *Surface Science* **104**, 405 (1981).
- ² M. W. Finnis and V. Heine, *J. Phys. F: Metal Phys.* **4**, L37 (1974).
- ³ U. Landman, R. N. Hill and M. Mostoller, *Phys. Rev. B* **21** 448 (1980).
- ⁴ J. E. Inglesfield, *Progress in Surface Science* **20**, 105 (1985).
- ⁵ F. Soria, J. L. Sacedon, P. M. Echenique and D. Titterington, *Surface Science* **68**, 448 (1977).
- ⁶ R. J. Culbertson, L. C. Feldman, P. J. Silverman and H. Boehm, *Phys. Rev. Lett.* **47**, 657 (1981).
- ⁷ P. Statiris, H. C. Lu and T. Gustafsson, *Phys. Rev. Lett.* **72**, 3574 (1994).
- ⁸ S. Narasimhan and M. Scheffler, *Phys. Rev. Lett.*, to be published.
- ⁹ M. Henzler, *Surface Science* **73**, 240 (1978).
- ¹⁰ P. F. Miceli, private communication.
- ¹¹ J. B. Pendry, *J. Phys. C: Solid St. Phys.* **13**, 937 (1980).

Chapter Five

Alkali Metals Adsorbed on Ag(111)

5.1. Introduction

Alkali metal adsorption systems have long been of considerable interest scientifically. Since alkali atoms have only one valence electron, they represent one of the simplest adsorbates, and therefore should be the easiest to understand. In particular alkali metal adsorption on metal surfaces such as Ag or Al were thought to be the ideal adsorption systems since these substrates do not reconstruct and usually exhibit bulk-like termination. Nevertheless, studies of these supposedly simple systems have exposed a surprising variety of interesting behavior.

This chapter will first provide a brief summary of recent discoveries in alkali metal adsorption with a view to providing motivation for the experiments reported in this thesis, and then present the experimental results for alkali adsorption on Ag(111).

5.2. Historical Summary

5.2.1. General

Because of the simplicity of alkali adsorption systems, it was assumed that the adatoms would reside in the high-coordination hollow sites. This view prevailed until a few years ago, in spite of an early structural study which found that Cs/Cu(111) reside not in the hollow site but in the top site.¹ This top site result in fact was not widely accepted until the publication of a recent study, corroborated by several techniques, showed that K/Ni(111) also resides in the top site.^{2,3}

This unexpected top site geometry prompted additional interest in alkali adsorption systems. A large number of structural determinations were produced in the ensuing years, and it was found that top-site adsorption was quite common for the large alkalis on close packed metal substrates. A comprehensive summary of these results can be found in reference 4.

Several other surprising results were found for certain systems. One particular system stands out because it provides an example of nearly all of the unexpected features seen: K on Al(111).⁵ At very low coverages a dispersed phase exhibiting dipole-dipole repulsion forms, but at a critical coverage a transition occurs and the overlayer condenses into dense metallic islands. When adsorbed at low temperatures (below about 200 K) the adatoms in these islands reside in the top site; however by

annealing a temperature-activated substitutional phase is formed. This substitutional phase, which was previously thought to be very unlikely because of the low miscibility of alkalis in bulk aluminum, is formed by ejecting a substrate atom in the top layer and replacing it with an alkali atom. Similar features were found for the other alkali metals on Al(111)^{6,7,8}, as well as for a few other select systems.

Nearly all the site determinations which have been done were done at coverages close to monolayer saturation. The reason for this is that at temperatures accessible in most experiments alkali monolayers tend to be disordered at low coverages, making structural determinations by conventional techniques such as LEED difficult. This raises the question of whether top-site adsorption is a phenomenon peculiar to high-density alkali phases, or whether it was a direct result of the interaction between the adsorbate and surface. Top site adsorption found in the high-density phases is always accompanied by a substrate rumpling, the purpose of which seems to be to provide screening between the adsorbates. Since this rumpling was found theoretically to be a necessary component of top-site adsorption for one particular case⁹, it was unclear whether to expect top-site adsorption for low-density alkali phases. For this reason it has been considered important to extend structural determinations to lower coverages.

5.2.2. Alkali Metals on Ag(111)

5.2.2.1. Cesium

Early studies of Cs adsorption on Ag(111) focused primarily on the role of Cs in surface catalytic reactions. In one early study it was found that by doping the Ag(111) surface with a small amount of Cs the reactivity and selectivity of the surface catalyst could be enhanced for oxidation reactions of ethylene.^{10,11} Naturally in the process of these studies some information was also obtained about the behavior of the unperturbed Cs / Ag(111) surface. The experiment was done at room temperature, and no ordered phases were observed by LEED. Cs was found to grow in a layer-by-layer mode as measured by AES. A lower bound to the coverage of monolayer saturation of 0.13 was obtained by measuring current from Cs desorbed as positive ions. Thermal desorption spectra showed a series of three broad features at approximately 550, 450, and 350 K which were interpreted as multilayer desorption. It was found that Cs did not penetrate the Ag lattice significantly, in contrast to the behavior of some of the smaller alkalis.

A similar study, done independently but concurrently with the previous one, found some additional information.¹² In this study LEED patterns were recorded for a Cs monolayer at 100 K. At low coverages rings were seen and were interpreted as a rotationally disordered solid. At a higher coverage a

(2x2) pattern was seen; this phase was assumed to be a p(2x2) with a coverage of 0.25. The coverage scale was then calibrated using this point, and a first layer saturation coverage of 0.3 was obtained. At coverages other than 0.25 LEED patterns with "a strong (2x2) component" but with split overlayer spots were observed. Thermal desorption spectra with features similar to the previously mentioned study were measured, but based on the coverage calibration the structure in the spectra was interpreted as being due to submonolayer desorption. In addition, multilayers could be grown and desorbed at approximately 330 K, just below the onset of first layer desorption.

Work function measurements were done on the Cs/Ag(111) system by Argile et al.¹³ The results exhibit the standard behavior for work function behavior with alkali metal adsorbates, as described in Chapter Two. At the work function minimum a decrease of 3.0 eV was measured.

In 1985 a SEXAFS study was done on the Cs / Ag(111) system by Lamble et al.¹⁴ This study, done at 120 K, found a change in the chemisorption bondlength as a function of coverage. At a coverage of 0.15 the bondlength was found to be 3.20 ± 0.03 , while for a coverage of 0.30 it was 3.50 ± 0.03 . This increase in bondlength at a higher coverage was attributed to a change in the nature of the bond from ionic to covalent with coverage. Unfortunately no LEED observations were presented and no bond-orientation or adsorption-site information was obtained. To date this study is one of only a handful which have measured the bondlength of an alkali adsorbate as a function of coverage. However it has been cited frequently in the debate about whether an ionic to covalent transition occurs.¹⁵

5.2.2.2. Rubidium

The only previous study of Rb/Ag(111) was an early thermal desorption and LEED study.¹⁶ By dosing and annealing to various temperatures a number of LEED patterns were found. These include one identified as a (9x9), a (3x3), and a "ring" pattern, all of which were taken at room temperature and were of rather poor quality. All of the ordered structures were interpreted as multilayer structures based on a Rb dosing rate which had been calibrated by comparison of the desorption spectra to previous Na desorption studies. The (9x9) pattern, which was obtained by dosing Rb at room temperature, was interpreted as a Rb FCC stacking multilayer structure. The ring pattern was obtained by annealing the (9x9) to 450 K, and was interpreted as a BCC (100) surface. Since the (9x9) pattern could be formed again by further annealing and desorption of more Rb, it was concluded that the FCC film was a metastable structure which underwent a phase transition to BCC at a critical thickness. The (3x3) pattern was only obtainable by annealing to higher temperatures and was attributed to impurities. The thermal desorption spectra showed a series of broad features, interpreted as multilayer desorption, occurring

between 400 and 900 K. Tails above 900 K on TDS spectra were interpreted as the desorption of a small amount of Rb which had diffused into the bulk.

5.2.2.3. Potassium

The first K/Ag(111) study was a room-temperature experiment using LEED, EELS (Electron Energy Loss Spectroscopy), and ellipsometry.¹⁷ They found that the monolayer saturated at a coverage of 0.33, at which a LEED pattern corresponding to two coexisting orientations (not specified) of a triangular lattice were seen. At lower coverages the LEED pattern was diffuse. The EELS and optical absorption experiments measured some fairly dramatic new features which grew in with K adsorption, between a coverage of 0.25 and 0.33. These were attributed to the presence of overlayer conduction electrons due to the metallization of the overlayer at high coverages. Work functions were also measured, and a work function change of 2.9 eV at the minimum was obtained.

A second study,¹³ already mentioned in the Cs section above, was done by Argile et al. This was a work function experiment in which both Cs and K as well as coadsorption of the two were studied. As with Cs, the K work function curve exhibits the standard behavior. The total work function change at the minimum was 2.75 eV.

A third study used EELS, UPS (Ultra-violet Photon Spectroscopy), and TDS (Thermal Desorption Spectroscopy) to measure K/Ag(111).¹⁸ The work function curve, although similar in form to those obtained in the previous two studies, showed a larger change of 3.5 eV at the minimum. The work function was modeled using the Topping equation, yielding an initial alkali dipole of 7.94 D and an adatom polarizability of 37.1 \AA^3 . The TDS spectra showed a broad featureless peak extending from ~350 K to 800 K for monolayer desorption, with multilayers desorbing at about 320 K. As with the ellipsometry study above, the spectroscopy measurements showed clear changes with coverage inside the monolayer region. These were interpreted as supporting the classical picture of an ionic-to-metallic transition.

5.2.2.3. Sodium

Na/Ag(111) was studied by Goddard et al. using LEED and TDS.¹⁹ The experiment was done at room temperature, and no ordered LEED patterns were observed for coverages less than 1.5 ML. At coverages between 1.5 and 3.0 ML, a $(\sqrt{7} \times \sqrt{7})R19.1^\circ$ pattern was observed. The LEED results were taken

as indication that the first layer grows in registry with the Ag(111) surface, with the second layer growing in a less-dense ($\sqrt{7} \times \sqrt{7}$)R19.1° phase with nine atoms per unit cell and a nearest-neighbor distance of 3.82 Å. TDS spectra showed several broad features, interpreted as multilayer desorption, between 600 and 900 K. In addition, the TDS spectra showed high temperature “tails” which were interpreted as the desorption of Na which had entered the bulk. The amount of Na entering the bulk was found to be up to 100 times larger than that for Rb, and was greater for a surface which had been damaged by light sputtering prior to Na dosing.

5.2.2.4. Lithium

In 1985 a study was done on Li / Ag(111) by Parker using AES and work function measurements.²⁰ At the work function minimum a change of 1.8 eV was measured. The evolution of auger spectra with time suggested that Li diffuses readily into the Ag bulk at room temperature, and that this diffusion was greatly enhanced for Li coverages larger than one monolayer. No ordered LEED patterns were observed due to Li adsorption. All measurements were done at room temperature.

5.2.3. Summary and Discussion

The work done on alkali metal adsorption on Ag(111) up to this point has been largely consistent with the classical ideas of alkali adsorption. Work function curves, shown in Figure 5.1, display the standard behavior discussed in Chapter Two. Thermal desorption spectra show monolayers desorbing over wide temperature ranges, consistent with an ionic chemisorption bond which is gradually depolarized with increasing coverage. Electron and optical spectroscopies indicate an overlayer which becomes metallic around the completion of the monolayer. For Cs, a change in the chemisorption bondlength was measured with coverage, providing additional evidence of a change in the nature of the bond with coverage. To date this has been one of only a few, and certainly the most dramatic such change measured for an alkali adsorption system.

Despite all of these studies, there is still a lack of structural information regarding alkalis on Ag(111). Although ordered LEED patterns were seen for the three larger alkalis at near monolayer saturation, no structural determinations were done. LEED patterns from lower coverages were usually diffuse, indicating that the layer was disordered. This is not surprising however, since most of the experiments were done at room temperature and none were done below 100 K.

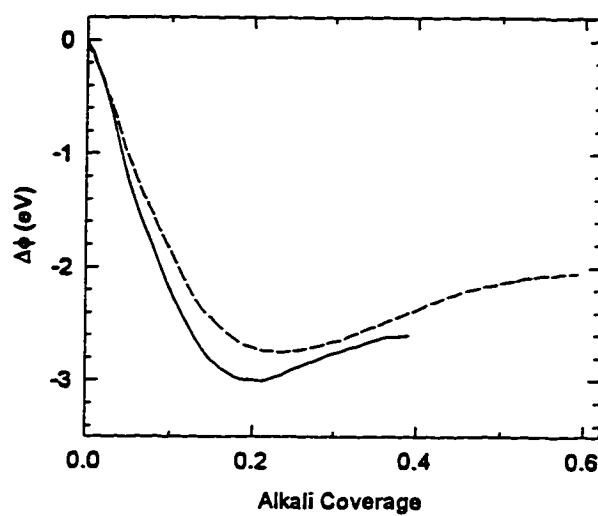


Figure 5.1. Work function curves for Cs/Ag(111) and K/Ag(111).¹⁵ The solid line represents the Cs data and the dotted line represents the K. Coverage is defined as the ratio of overlayer atoms to top-layer substrate atoms.

The lack of structural determinations is particularly unfortunate in view of the Cs bondlength change result. This result has been widely cited as evidence for an ionic-to-neutral change in the chemisorption bond. However, such changes in bondlength may also be caused by a change in the adsorption site. A change from a high-coordination site to a low-coordination one has been demonstrated to result in an increased bondlength for the Cs/Ru(0001)²¹ and Cs/Rh(111)²² systems. Since the adsorption sites for Cs/Ag(111) are completely unknown, it is difficult to draw conclusions from the measured change in bondlength.

In light of this ambiguity and the lack of structural knowledge, the additional studies of alkali adsorption on Ag(111) presented in this thesis are warranted. The remainder of this chapter will present results from these studies.

5.3. Experimental Phase Diagrams

This section will present the results of a detailed study of the phase diagrams of Cs, Rb, and K on Ag(111). Additional experiments which were not as extensive were performed on Na and Li on Ag(111), and they will be presented in the last part of this section.

5.3.1. Commensurate and Incommensurate Phases

Figures 5.2 to 5.4 show the temperature-density phase diagrams for K, Rb, and Cs monolayers on Ag(111). In general the overlayer forms a triangular lattice which is incommensurate with the substrate. For all three alkalis, the lattice parameter decreases as the inverse square of the coverage over the entire monolayer coverage range. This is shown in Figure 5.5 for Cs; also shown are the density as a function of coverage, calculated from the lattice parameter, for all three alkalis. The coverage is obtained for Cs and K by taking the ratio of the intensities of the overlayer to substrate Auger peak, and calibrating at the (2x2) commensurate phase to a coverage of 0.25, and for Rb by using dosing time rather than Auger intensity. The fact that the density increases linearly with coverage indicates that the alkali atoms are distributed uniformly across the surface, as would be expected from a layer of dipoles.

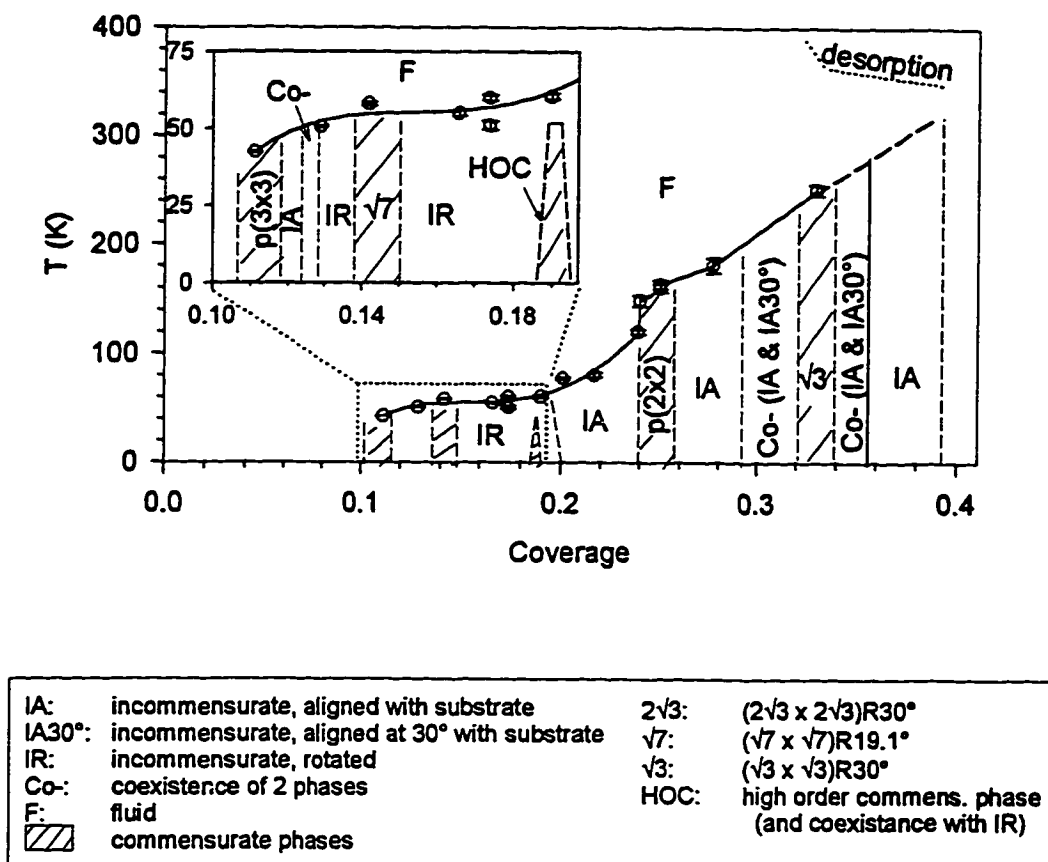
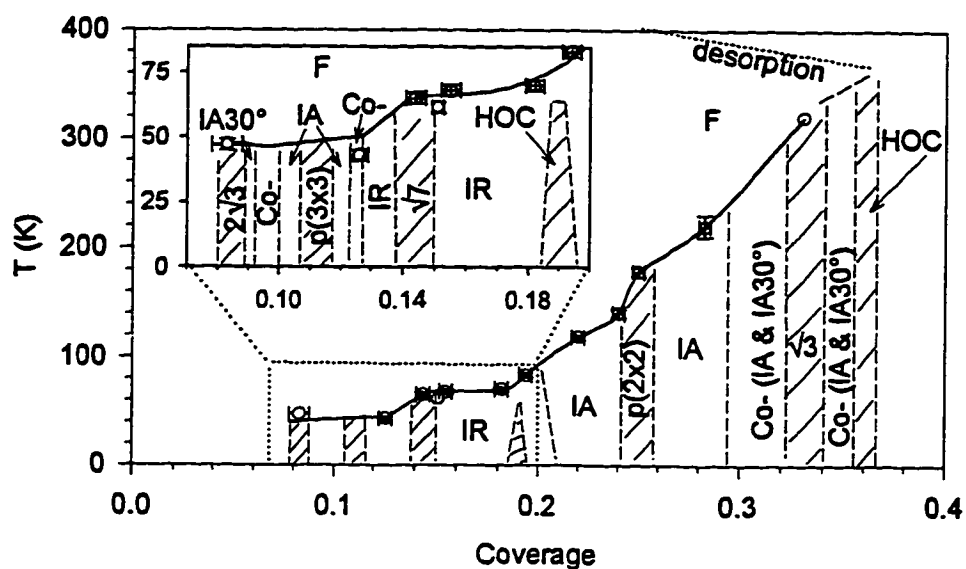


Figure 5.2. Monolayer phase diagram for K/Ag(111).




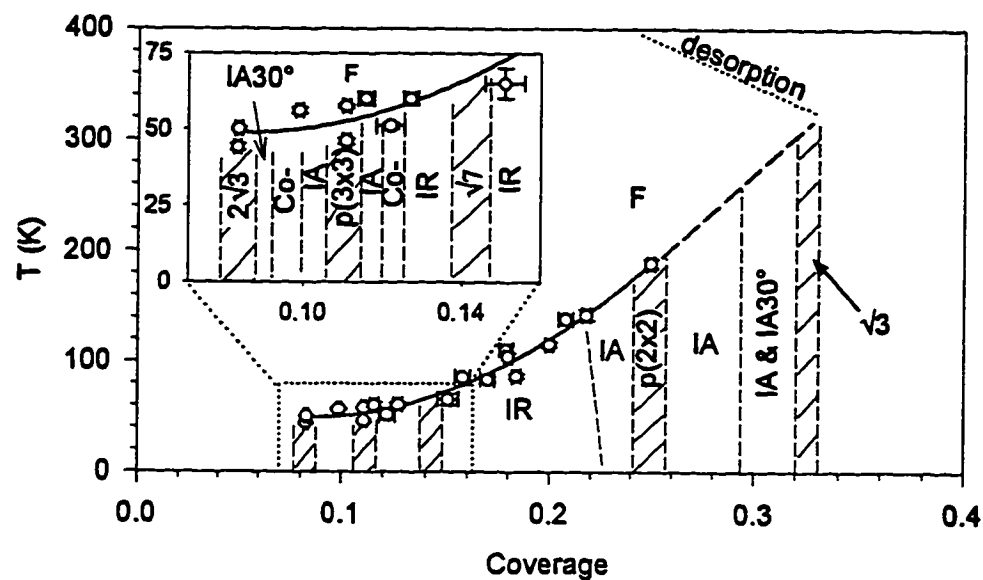
IA:	incommensurate, aligned with substrate	$2\sqrt{3}$:	$(2\sqrt{3} \times 2\sqrt{3})R30^\circ$
IA30°:	incommensurate, aligned at 30° with substrate	$\sqrt{7}$:	$(\sqrt{7} \times \sqrt{7})R19.1^\circ$
IR:	incommensurate, rotated	$\sqrt{3}$:	$(\sqrt{3} \times \sqrt{3})R30^\circ$
Co-:	coexistence of 2 phases	HOC:	high order commens. phase
F:	fluid		
	commensurate phases		

Figure 5.3. Monolayer phase diagram for Rb/Ag(111).




IA:	incommensurate, aligned with substrate	2√3:	(2√3 × 2√3)R30°
IA30°:	incommensurate, aligned at 30° with substrate	√7:	(√7 × √7)R19.1°
IR:	incommensurate, rotated	√3:	(√3 × √3)R30°
Co-:	coexistence of 2 phases	HOC:	high order commens. phase
F:	fluid		
	commensurate phases		

Figure 5.4. Monolayer phase diagram for Cs/Ag(111).

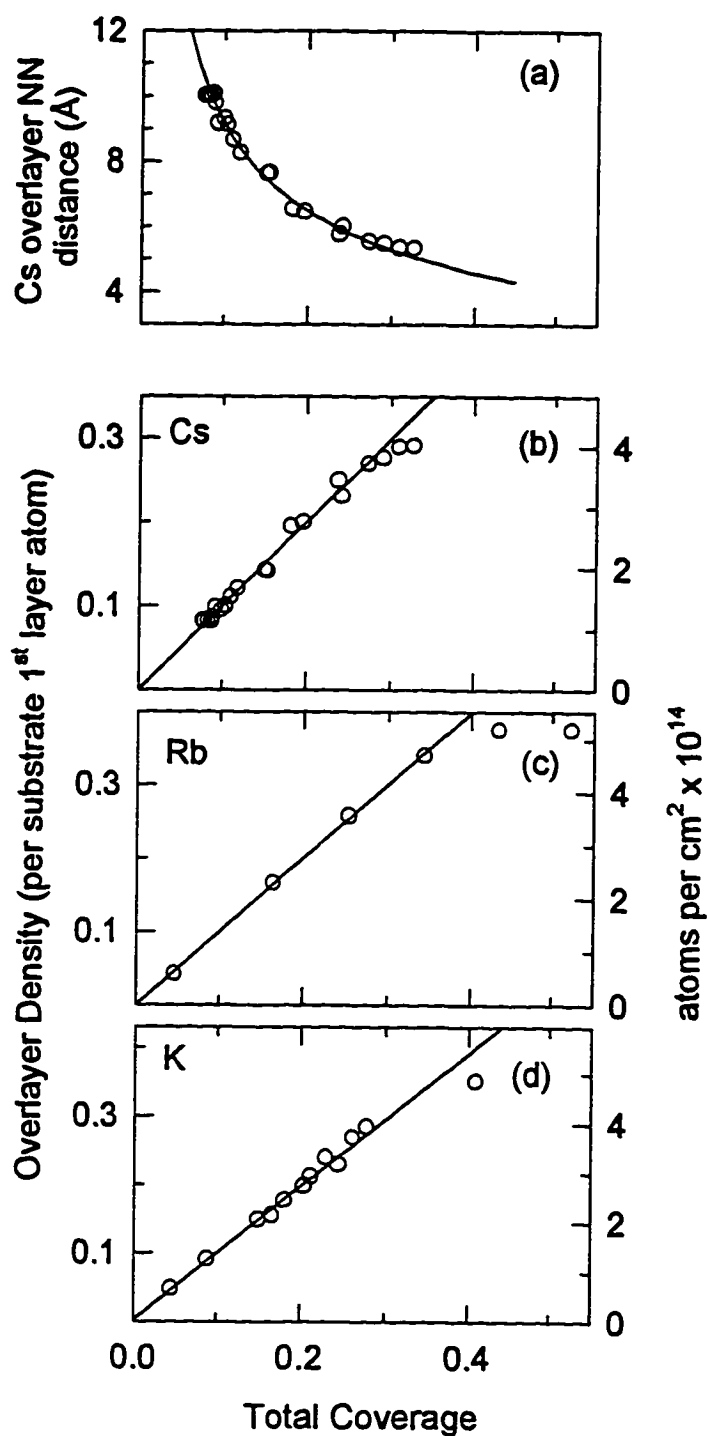


Figure 5.5. Alkali lattice parameter and density as a function of coverage. (a) Nearest neighbor distance (measured from LEED pattern) for Cs/Ag(111), as a function of coverage. The curve represents the $1/\sqrt{\theta}$ which should be seen for uniform compression. (b)-(d) Overlayer density, also measured from the LEED pattern, as a function of total coverage for Cs, Rb, or K on Ag(111).

At certain coverages, where the overlayer lattice corresponds to a superlattice of the substrate and when the temperature is low enough, the alkali overlayer becomes commensurate. The commensurate phases are listed in Table 5.1. Figure 5.6 shows the LEED patterns from each commensurate phase and Figure 5.7 shows a real space diagram of each. In each case the phase is commensurate only over a rather narrow coverage range, going incommensurate at coverages just above or below the commensurate coverage. The commensurate phases were identified by a marked increase in the sharpness of the diffraction spot over the commensurate range. The widths of the beams in the commensurate regions are approximately the same as the widths of the substrate spots, indicating an overlayer which is truly locked into the substrate periodicity.

In most cases the incommensurate phase between two commensurate phases exists as two phases of the same density, one oriented at the angle of the commensurate phase and the other at a different angle. This is shown in the phase diagrams as the regions labeled "Co-". For example, between the $(2\sqrt{3}\times 2\sqrt{3})R30^\circ$ phase at a coverage of $1/12$ and the (3×3) phase at a coverage of $1/9$, two sets of incommensurate diffraction spots can be seen, one aligned at 30° and the other at 0° . As the coverage is increased, the lattice parameter of both incommensurate phases changes continuously and the amount of overlayer at one orientation angle decreases while the other increases until, only one orientation is left, at some coverage still below the next commensurate phase. The main exception to this behavior is for coverages between 0.13 and 0.25, in which the angle changes continuously from the direction of one commensurate phase to that of another commensurate phase. This behavior will be discussed in section 5.5.

Table 5.1. Commensurate phases for Cs, Rb, or K on Ag(111).

commensurate phase	coverage (ML)	atoms per unit cell	Cs	Rb	K
$(2\sqrt{3}\times 2\sqrt{3})R30^\circ$	$1/12$	1	X	X	
$p(3\times 3)$	$1/9$	1	X	X	X
$(\sqrt{7}\times \sqrt{7})R19.1^\circ$	$1/7$	1	X	X	X
$(\sqrt{21}\times \sqrt{21})R10.8^\circ$	$4/21$	4		X	X
$p(2\times 2)$	$1/4$	1	X	X	X
$(\sqrt{3}\times \sqrt{3})R30^\circ$	$1/3$	1	X	X	X
(5×5)	$9/25$	9		X	

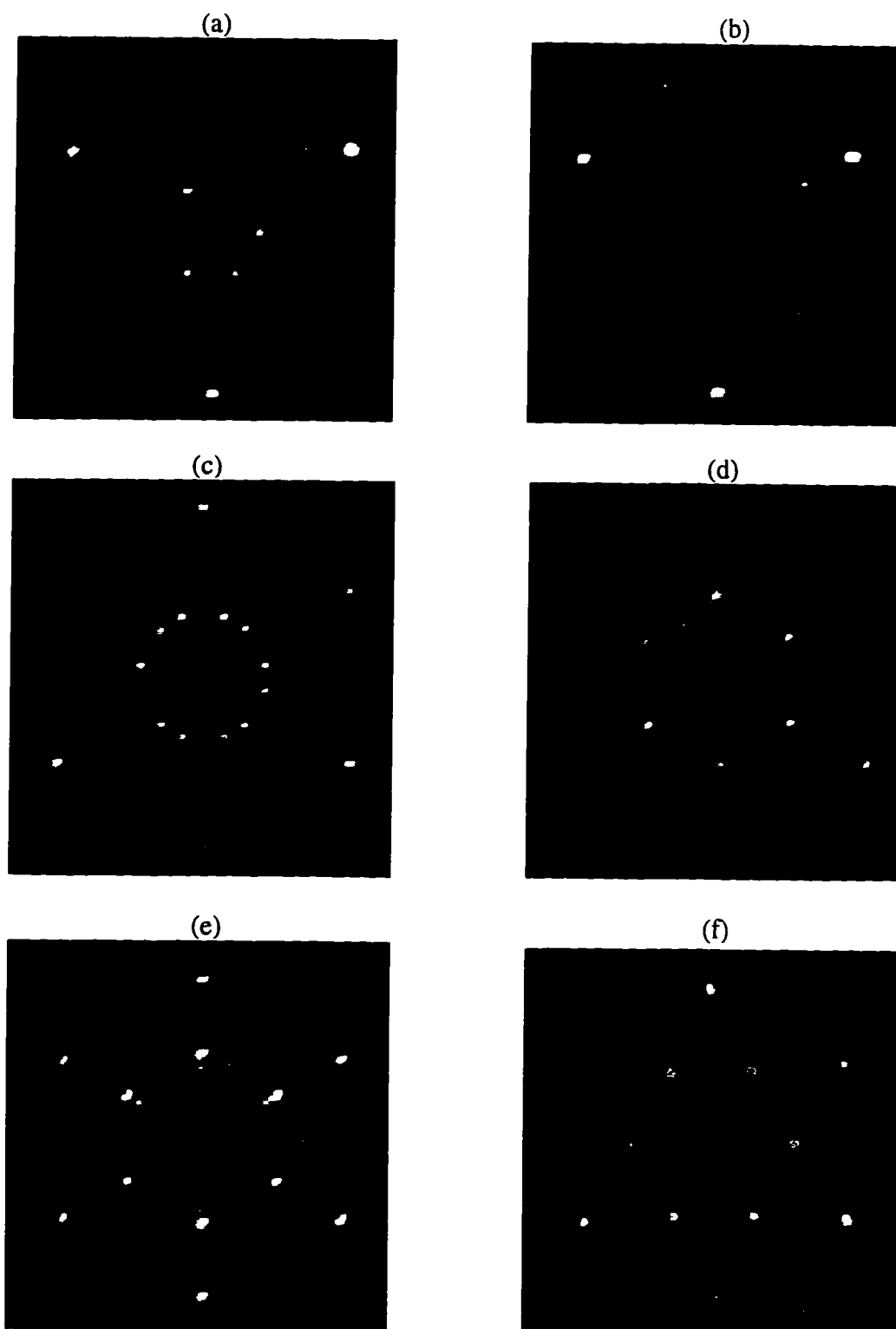


Figure 5.6. LEED patterns for Cs/Ag(111). (a) Commensurate $(2\sqrt{3} \times 2\sqrt{3})R30^\circ$ phase at $\Theta=1/12$, energy=125 eV. (b) Commensurate $p(3 \times 3)$ phase at $\Theta=1/9$, energy=125 eV. (c) Commensurate $(\sqrt{7} \times \sqrt{7})R19.1^\circ$ at $\Theta=1/7$, energy=145 eV (two equivalent domains are present.) (d) Commensurate $p(2 \times 2)$ at $\Theta=1/4$, energy=115 eV. (e) Aligned incommensurate phase at $\Theta=0.29$, energy=188 eV. (f)

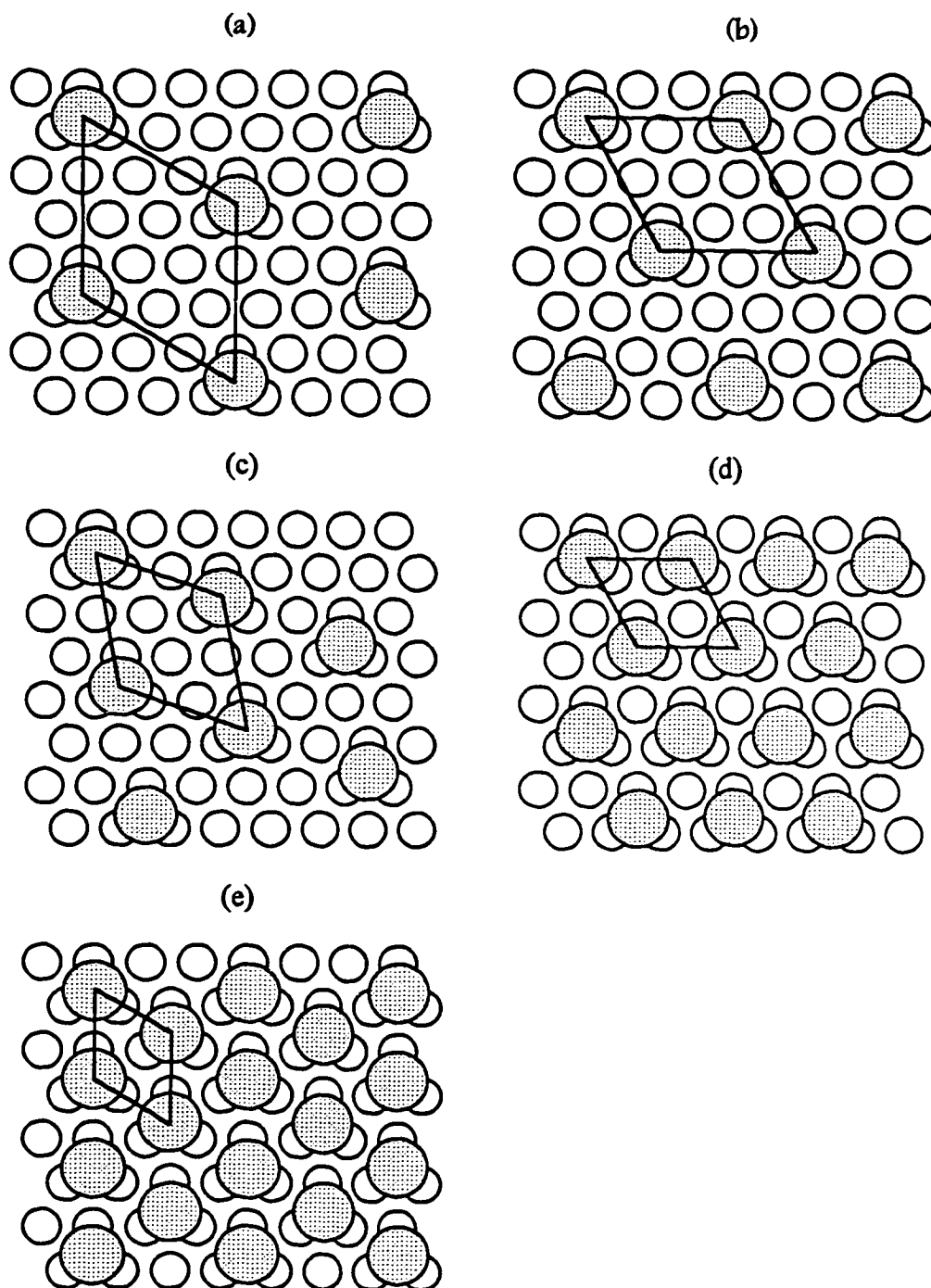


Figure 5.7. Real space structures for commensurate phases: (a) $(2\sqrt{3} \times 2\sqrt{3})R30^\circ$, (b) $p(3 \times 3)$, (c) $(\sqrt{7} \times \sqrt{7})R19.1^\circ$, (d) $p(2 \times 2)$, (e) $(\sqrt{3} \times \sqrt{3})R30^\circ$.

The saturation coverages of the three alkalis are shown in Table 5.2. In each case the radius of the alkali atom is compressed a few percent with respect to its metallic radius. Because of the lower mobility of the adatoms at high coverages, the saturation densities could only be achieved by annealing the sample. Also, for Cs and Rb annealing was necessary to form the commensurate $(\sqrt{3}\times\sqrt{3})R30^\circ$. For Rb a density of 0.33 could be attained by dosing at low temperature, but the overlayer remained incommensurate and aligned with the substrate until it was annealed to at least 250 K. Cs would only form the $(\sqrt{3}\times\sqrt{3})R30^\circ$ phase by populating the second layer significantly and then annealing for a few minutes to a temperature higher than about 270 K but lower than about 290 K, where it begins to desorb.

Because of the lower mobility of the adatoms at low temperatures, overlayers dosed to high coverages at low temperature usually contained a significant amount of frozen-in disorder. When the surface was warmed, the fractional order spots became sharper while the lattice parameter typically decreased slightly as the disorder was annealed out. This can be seen for the case of Rb at a coverage of 0.33 in Figure 5.8. The change is irreversible; upon cooling the spots are sharp and the lattice parameter remains constant. It is likely that the decrease in lattice parameter is caused by demotion of alkali atoms in the second layer, rather than by a condensation transition. A condensation transition would likely be sharper and the final value of the lattice parameter would be independent of coverage, which it is not.

Table 5.2. Saturation coverage for alkalis, compared with the ionic and covalent alkali radii.²³

Alkali	Ionic Diameter	Metallic Diameter	Ag(111) Saturation Coverage	NN Distance at Saturation
Li	1.36	3.12	0.63*	3.64*
Na	1.94	3.82	0.58*	3.79*
K	2.66	4.76	0.41	4.54
Rb	2.96	5.10	0.36	4.76
Cs	3.34	5.46	0.33	5.01

*these results represent only an lower (upper) bound on the saturation coverage (NN distance)

5.3.2. Disordering Transitions

With increasing temperature, the alkali overlayers pass through what appears to be a melting transition. For the commensurate phases, the transition takes the form of an abrupt change from sharp diffraction spots to a fluid phase where only uniform rings can be seen in the diffraction pattern, as seen in Figure 5.9. Figure 5.10 shows the behavior of the intensities and widths of Lorentzian peaks fitted to radial profiles through the fractional order spots in the K p(2x2) commensurate phase. The spot intensities decrease exponentially due to the Debye-Waller factor until the critical temperature is reached, at which point there is a sudden decrease in the diffracted intensity. At the same time the spot width begins to increase.

For one of the commensurate phase melting experiments, the overlayer appeared to become incommensurate shortly before it melted. Figure 5.11 shows the results of fitted profiles through the fractional spots of the K ($\sqrt{7} \times \sqrt{7}$)R19.1° phase. Just before the melting occurs, the lattice parameter increases slightly from the 7.65 Å of the commensurate phase. At the same time the radial spot width (but not the azimuthal width, interestingly) increases slightly. This behavior probably indicates a rounding of the commensurate phase regions of the phase diagram, as shown in Figure 5.12. It is likely that the coverage in this particular experiment was not exactly that of the commensurate phase, but is off by a small amount, so that the overlayer had to go through the incommensurate region shown in the figure. Unfortunately since the coverage range over which the commensurate phases are observed (at low temperature) is so narrow, it would be difficult to map out the exact form of Figure 5.12.

The data shown in Figure 5.10 were analyzed to obtain critical exponents for the melting transition. These exponents are shown in Table 5.3, along with the predictions for the four-state Potts

Table 5.3. Critical exponents for disordering of the K p(2x2) phase on Ag(111), compared to lattice-gas model predictions.

	α	β	γ	ν
K p(2x2) / Ag(111)	0.87 ± 0.01	0.075 ± 0.01	0.43 ± 0.06	0.31 ± 0.09
Ising Model	0	0.125 (1/8)	1.75 (7/4)	1.0
Four-State Potts Model	0.667 (2/3)	0.0833 (1/12)	1.166 (7/6)	0.667 (2/3)

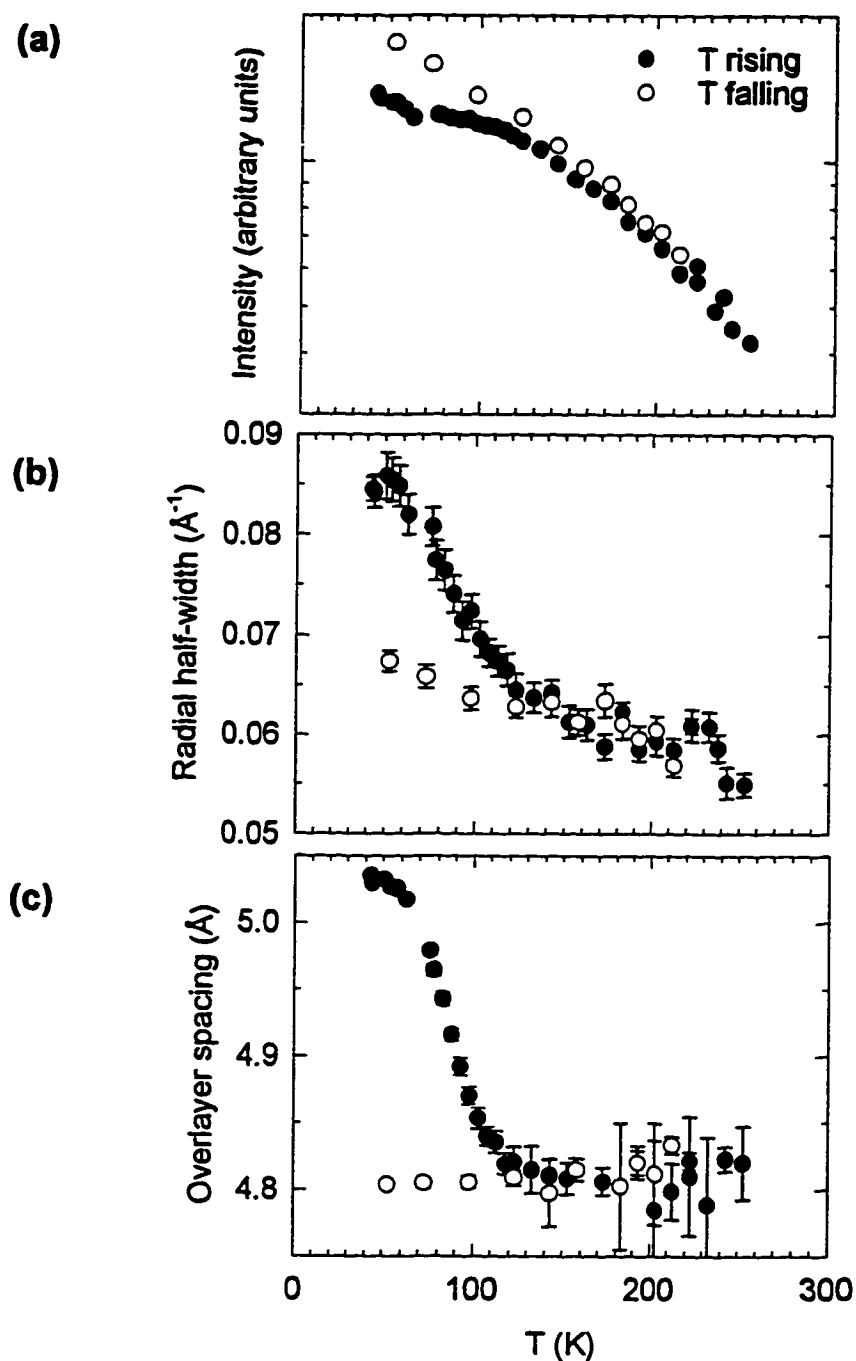


Figure 5.8. Annealing out of frozen-in disorder in Rb/Ag(111) overlayer at a coverage of 0.30. Rb was dosed with the sample at 50 K. The filled circles in each graph show the behavior of the overlayer as the temperature is increased, and the empty circles as it is decreased. (a) Diffraction spot intensity, (b) diffraction spot half-width measured by fitting a Lorentzian to a radial profile through the spot, and (c) overlayer spacing, determined from diffraction spot position.

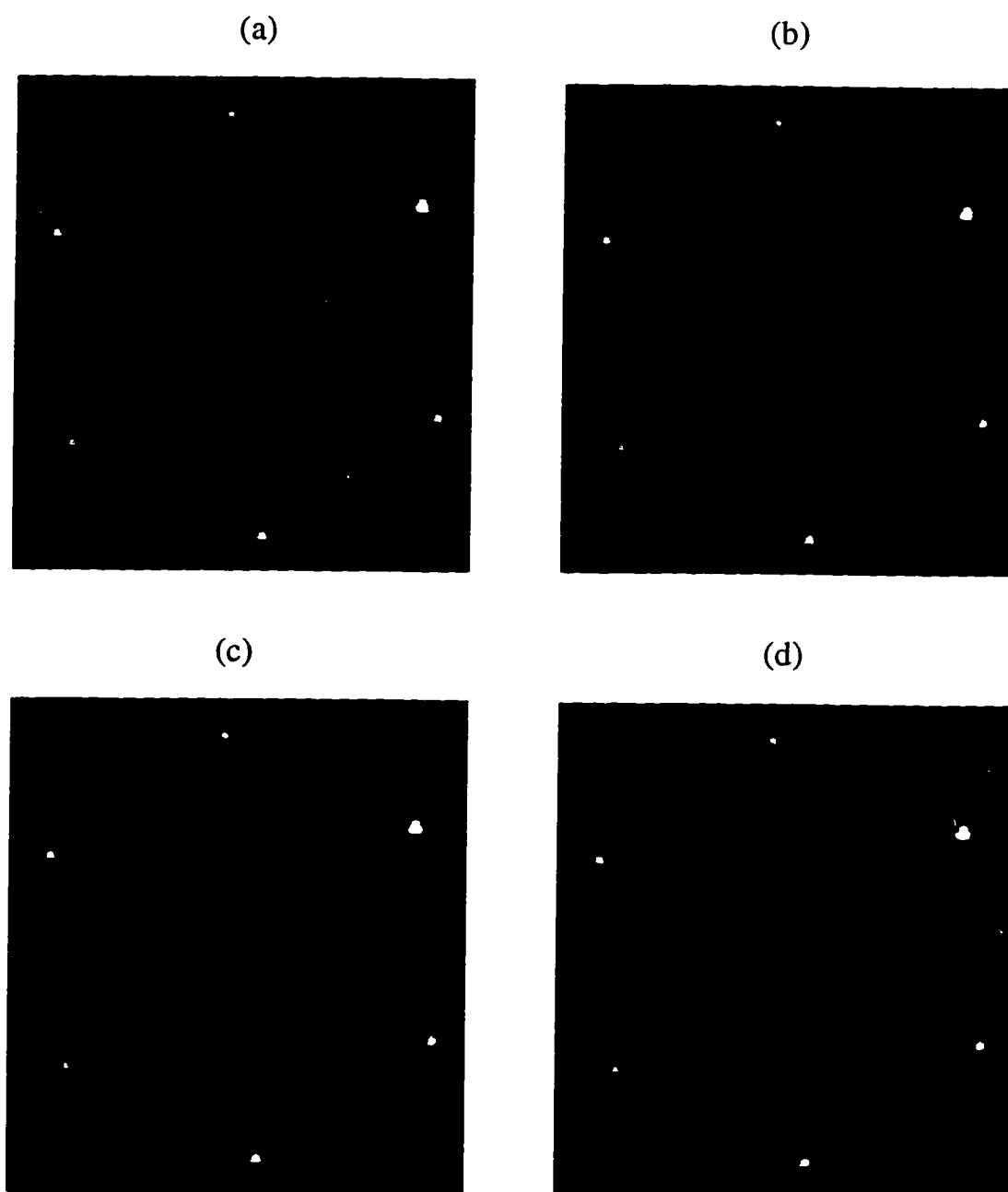


Figure 5.9. LEED patterns showing melting of the $(\sqrt{7} \times \sqrt{7})R19.1^\circ$ commensurate phase. (a) 63 K, (b) 65.5 K, (c) 67 K and (d) 69 K.

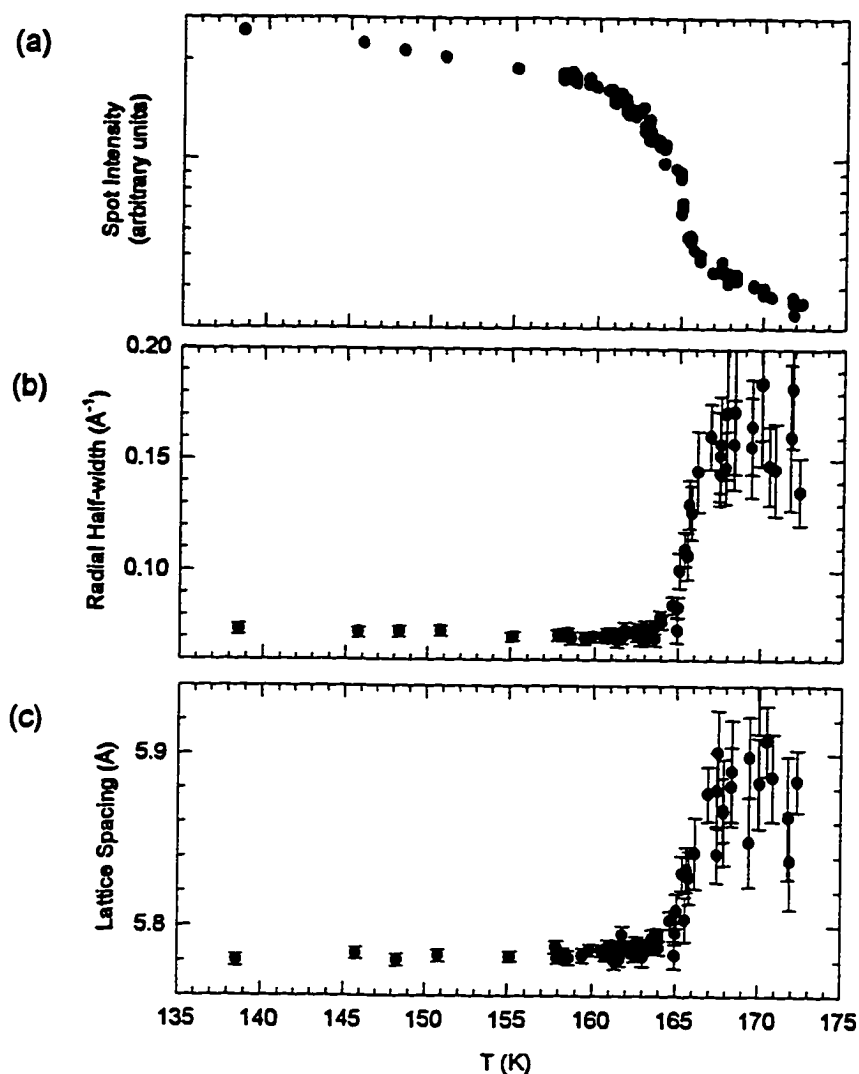


Figure 5.10. Melting of the K $p(2 \times 2)$ phase. (a) Spot intensity, (b) spot half width (obtained by fitting a Lorentzian to a profile), and (c) nearest-neighbor spacing, as a function of temperature. The data is taken with increasing T , and is from several different temperature sweeps.

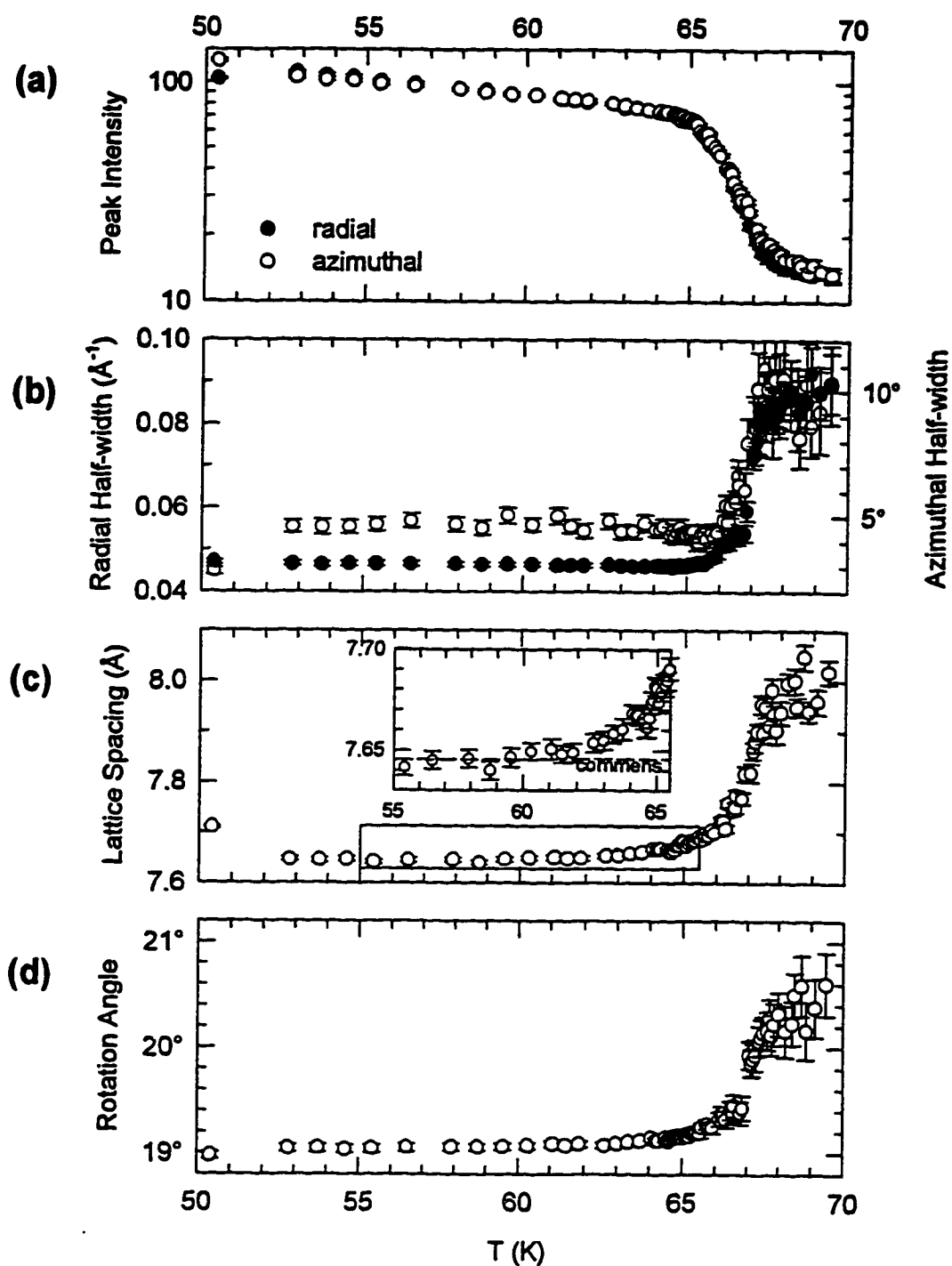


Figure 5.11. Melting of the K ($\sqrt{7} \times \sqrt{7}$)R19.1° phase. (a) Peak intensity and (b) half-width of fitted Lorentzian, (c) lattice parameter, and (d) rotation angle as a function of T .

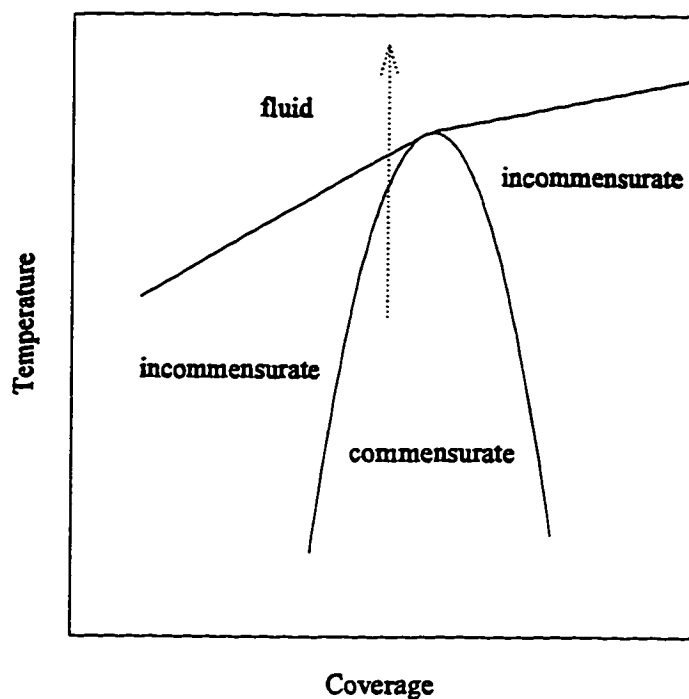


Figure 5.12. Diagram showing the possible fine detail of a phase diagram in the vicinity of a commensurate phase. The dotted line represents a possible temperature path taken in an experiment. If the experiment is not done at precisely the commensurate coverage, a commensurate-incommensurate transition may be seen before the melting occurs.

model, which models the overlayer as a lattice gas with four degrees of freedom.²⁴ (Four degrees of freedom are present because there are four possible ways to construct a $p(2 \times 2)$ lattice using the FCC sites on an FCC (111) surface).²⁵ Also shown are the predictions for the Ising model. The value of T_C , taken as the inflection point of the intensity decrease, was determined to be 164.2 K. While measured value of the exponent β agrees with the theory fairly well with the four-state Potts prediction and α is at least reasonably close, the other exponents do not agree with either the Potts or Ising prediction. The behavior of the lattice parameter of the overlayer, shown in Figure 5.10, may provide an explanation for this discrepancy. Above T_C , the lattice parameter (now actually an average spacing between atoms in the fluid phase) increases slightly from the 5.78 Å value of the commensurate phase. This indicates that the layer is becoming incommensurate, i.e. that overlayer atoms occupy positions other than the FCC sites of the commensurate phase, and that the system can no longer be accurately described using a lattice-gas model. The increase in lattice parameter could easily be accommodated by promoting 0.01 ML of the overlayer into the second layer. Since the α and β exponents are obtained from data below the critical temperature, their values agree reasonably well with the lattice-gas prediction. The γ and ν exponents are calculated from data above the critical temperature, where the system is no longer behaving as a lattice gas.

The melting behavior of the incommensurate phases is different from that of the commensurate ones. Instead of a very sharp transition, the change is more gradual, occurring over a much larger coverage range. Instead of the spots changing suddenly into a uniform ring, they gradually decrease in intensity and increase in width, eventually changing into a modulated ring structure. As the temperature increases further the modulations in the ring decrease until it becomes azimuthally uniform. This is shown for K in Figure 5.13. Figure 5.14 shows the fitted intensities for a range of coverages. It can be seen that while the transition is very sharp for the commensurate phases, it is blurred almost to the point of nonexistence for some of the incommensurate coverages. Similar behavior has been seen for alkalis on tungsten, molybdenum, and nickel.^{26,27,28} This has been attributed to a qualitative difference in the vibrational spectra between commensurate and incommensurate layers.^{29,30} In a commensurate phase, since the adatoms (being in equivalent sites) are all at the center of an equivalent potential well, the lowest energy vibrational mode does not go to zero as the wave vector goes to zero. For incommensurate phases where each atom is in a different site, there are acoustic-like modes which approach zero energy at zero wave vector. Interestingly, the contrast between the behavior of the commensurate phases to the incommensurate phases was not as great for Cs as it was for K. This is probably because Cs, being larger, feels a smaller substrate corrugation than K.

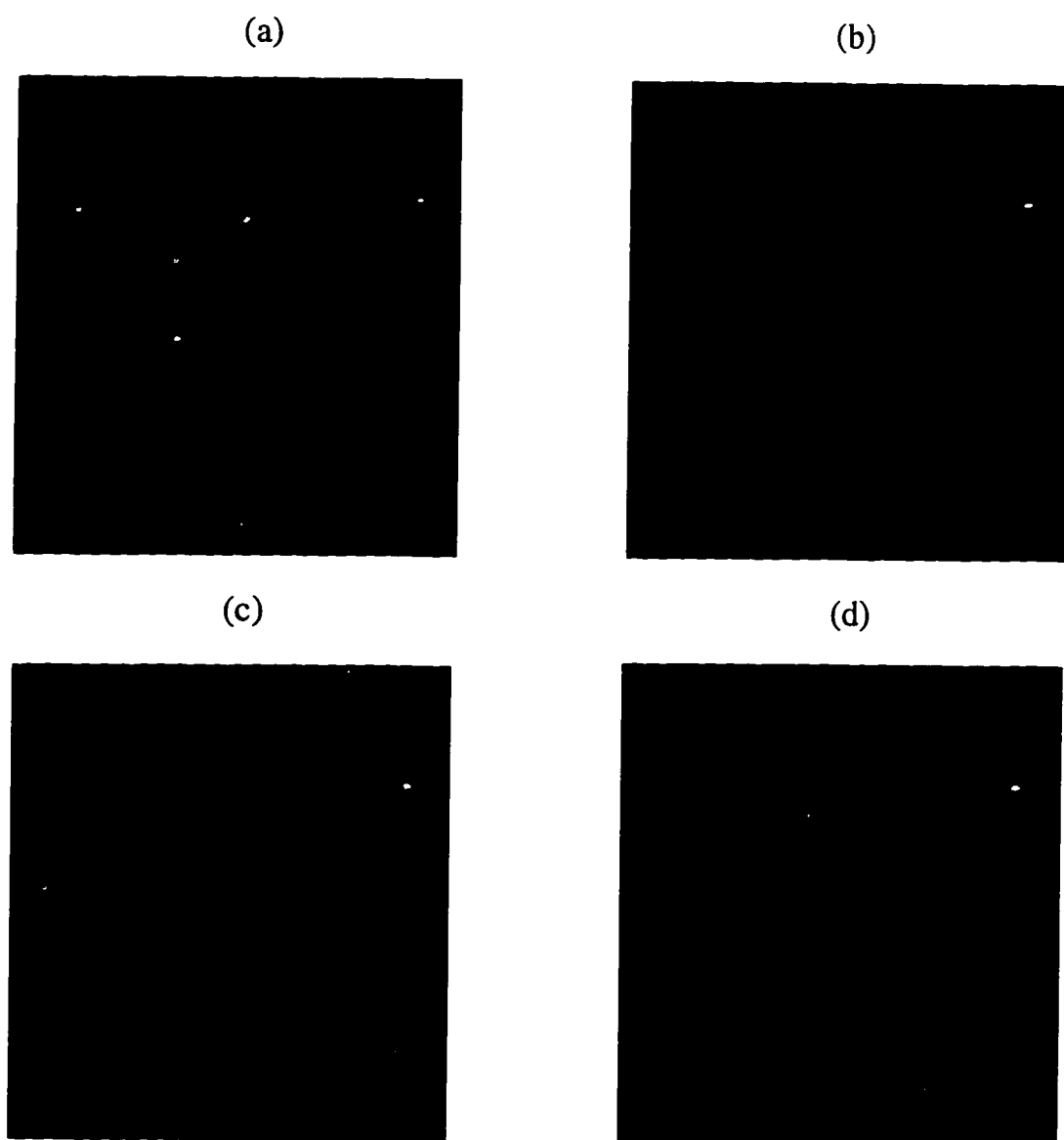


Figure 5.13. LEED patterns showing the melting of the K/Ag(111) incommensurate phase at a coverage of 0.201. (a) 44 K, (b) 56 K, (c) 86 K, (d) 108 K. Incident beam energy is 125 eV for all.

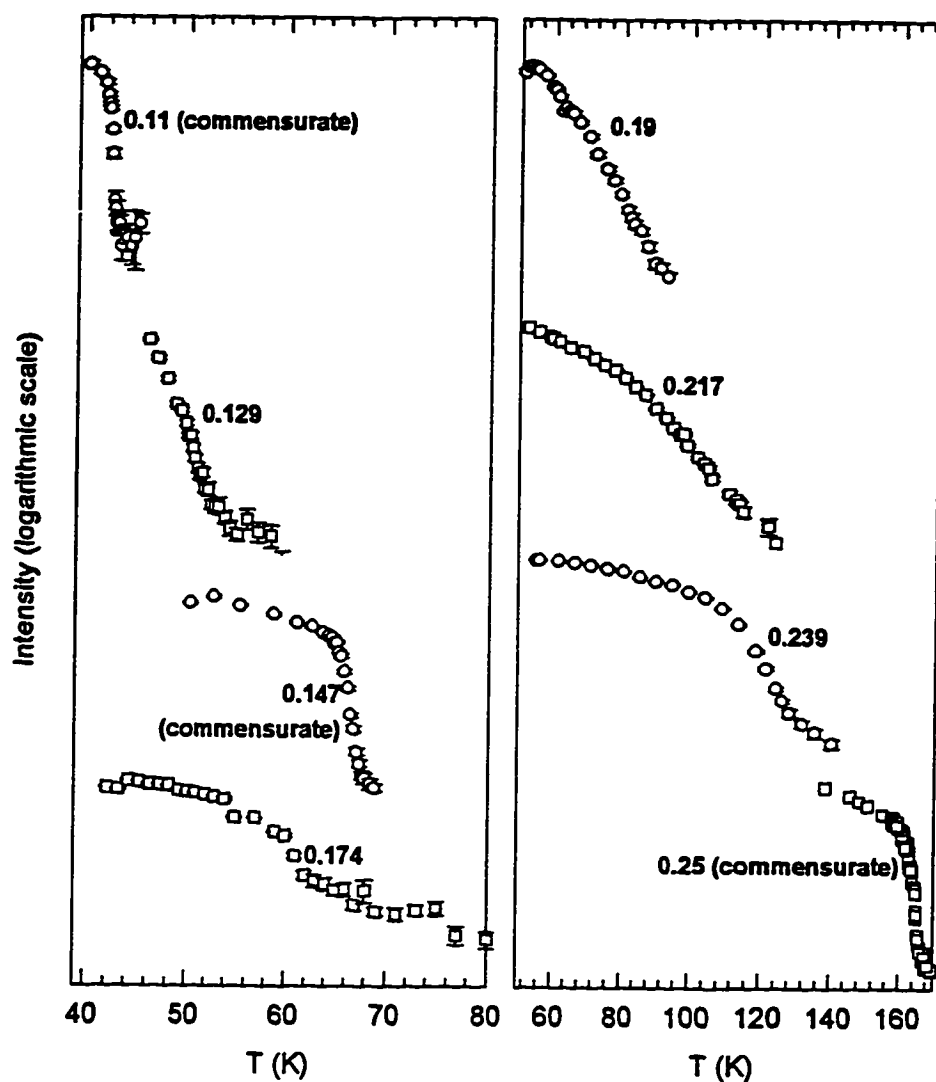


Figure 5.14. Various melting curves for K/Ag(111), as a function of coverage. Intensity values were obtained by fitting a Lorentzian to a radial profile through the diffraction spot. The transition is considerably sharper for the commensurate coverages: 0.11, 0.147, and 0.25. Curves are offset for clarity.

The melting behavior of the incommensurate phase is very similar to with that seen for K on Ni(111).^{31,32} The diffraction pattern of the intermediate phases suggests a fluid which still retains some bond-orientational order. In the case of K/Ni(111), it was suggested that this was the hexatic fluid phase expected for two-dimensional melting transitions.³³ However, this phase was not observed in the melting of the incommensurate phase of K on Ni(100),²⁷ and so it was concluded that the bond-orientational order existed because of the hexagonal symmetry of the substrate, and not as an intrinsic property of the overlayer itself.

The main exceptions to the melting behavior described in this section occur for very high and very low coverages. At low coverages (below about 0.6 for Cs and about 0.8 for K) only rings can be seen in the diffraction pattern down to 30 K, lowest temperature experimentally available. These rings increase in radius with increasing coverage, consistent with the behavior of a compressible fluid. It is probable that for these coverages the overlayer is already above the melting transition temperature, and if lower temperatures were available solid phases would be observed.

The other exception to the melting behavior occurs for Cs at saturation, the commensurate $(\sqrt{3}\times\sqrt{3})R30^\circ$ phase. As the temperature is increased, the overlayer does not melt but begins to desorb at about 290 K. The change can be seen in the LEED pattern as a sudden disappearing of the $(\sqrt{3}\times\sqrt{3})R30^\circ$ spots concurrent with the appearance of new spots from an incommensurate phase.

5.3.3. Higher Order Commensurate Phases

In addition to these commensurate phases, Rb and K form two higher order commensurate (HOC) phases. Their LEED patterns are shown in Figure 5.15. The first, a $(\sqrt{21}\times\sqrt{21})R10.8^\circ$ phase, exists inside the coverage range of the rotation mentioned in the previously. The phase was recognized due to the rotational behavior of the overlayer. As the coverage approaches 0.19, the rotation angle approaches 10.8° . As the coverage increases past 0.19 however, an additional set of rotated spots form at a rotation angle a few degrees lower than the original spots. As the coverage increases further these spots grow brighter and their rotation angle changes (consistent with the behavior of an incommensurate overlayer), while the other spots (identified as the HOC phase) remain stationary but grow dimmer, until they cannot be seen at all at coverages greater than about 0.205.

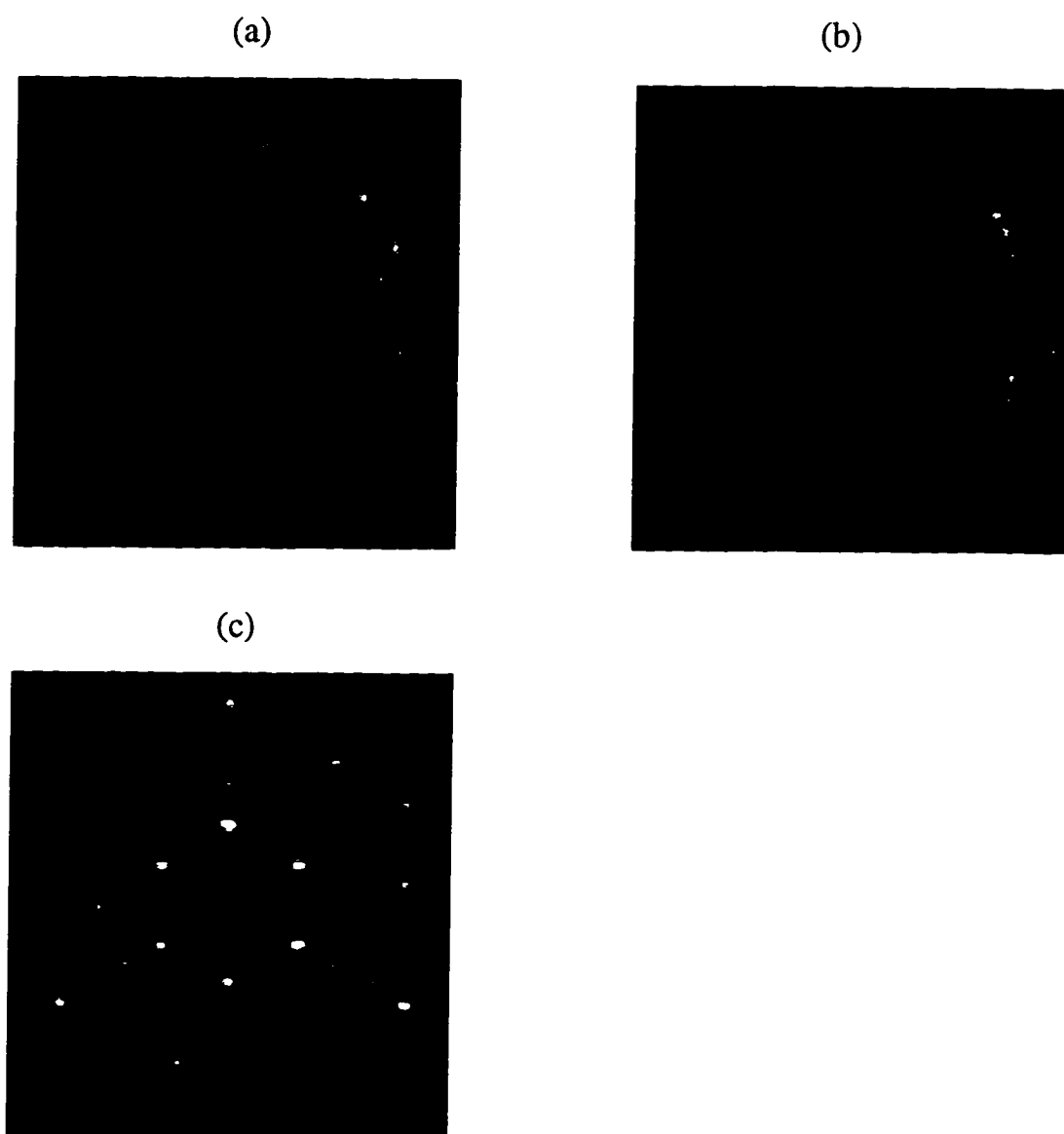


Figure 5.15. LEED patterns of higher-order commensurate phases. (a) $K (\sqrt{21} \times \sqrt{21})R10.8^\circ$ phase (brighter spots) coexisting with rotated incommensurate. Coverage is 0.195. (b) Same as (a), but at a coverage of 0.202. (a) and (b) were taken at an incident beam energy of 58 eV, and show only overlayer beams. (c) Rb (5x5) phase, at a coverage of 0.36. Incident beam energy 145 eV.

Additional evidence that these spots constitute a commensurate phase is shown in Figure 5.16. In panel (b) the lattice parameter of both of the coexisting phases is shown as the temperature is increased. One phase expands with increasing temperature, while the other remains essentially constant in density. This is the only case observed for alkalis on Ag(111) where two different phases of different densities coexist. The behavior is consistent with a locking in of the higher order commensurate phase while the coexisting incommensurate phase is free to expand thermally. Similar behavior was seen for higher order commensurate phases of Kr and Ar on Pt(111).^{34,35}

With increasing temperature the $\sqrt{21}$ phase does not undergo a disordering transition as the other commensurate phases do. Instead there is a first order transition to the incommensurate rotated phase, mentioned in the previous paragraph. With increasing temperature the HOC diffraction spots become dimmer and are eventually replaced by the incommensurate spots. The relative intensities of the two phases as a function of temperature is shown in Figure 5.16a.

Two proposed structures for the $\sqrt{21}$ phase is shown in Figure 5.17, panels (a) and (b). Based on the coverage, there must be four atoms per unit cell. Panel (a) shows a proposed structure formed by placing the atoms at the corners of the $\sqrt{21}$ cell in hollow sites (the preferred site for the commensurate phases) and the other three atoms at the midpoint of lines adjoining the atoms at the corners. This would give the overlayer, considered alone, a periodicity of $\sqrt{21}/2$ (rather than $\sqrt{21}$). This would in fact agree with the observation that in the LEED pattern the diffraction spots attributed to the HOC phase are actually second-order $\sqrt{21}$ spots, with first-order spots not being observed. It is evident however from the figure that all of the atoms could reside in hollow sites if the three atoms not in hollow sites were allowed to move a small distance. The distance necessary to translate these atoms to the hollow sites is 0.84 Å. In this configuration, shown in panel (b) of Figure 5.17, half of the overlayer atoms would reside in FCC hollows and the other half in HCP. It would normally be assumed however that an overlayer in this configuration would produce first order $\sqrt{21}$ diffraction spots, which were not seen in the LEED pattern. To test this, structure factors were calculated for atomic configurations in which these three atoms were shifted a small distance in the direction of the hollow sites. Figure 5.18 shows the calculated structure factor (which includes only overlayer atoms) for two cases: (a) the atoms have not been translated at all, and only second-order spots are visible, and (b) the atoms have been translated 0.36 Å, i.e. they all reside in hollow sites. The structure factors were calculated from a circular patch of 900 atoms, which would correspond to a patch diameter of about 90 Å. Panel (c) shows the relative intensity of the first-order to second-order spots, as a function of the distance that the atoms are translated toward the hollow sites.

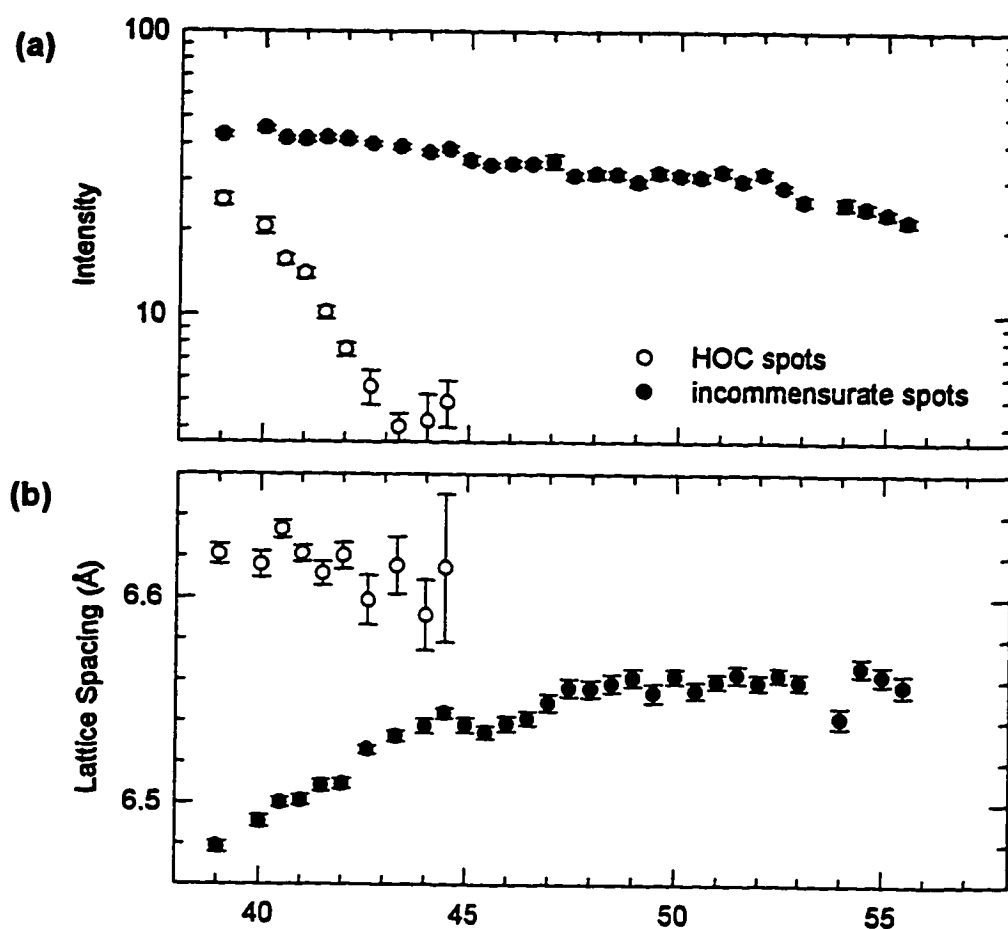


Figure 5.16. K/Ag(111), two coexisting phases at a coverage of 0.19: HOC (higher order commensurate) and incommensurate. (a) Fitted intensity and (b) measured lattice parameter. Solid circles are from the incommensurate phase and empty circles are from the HOC phase.

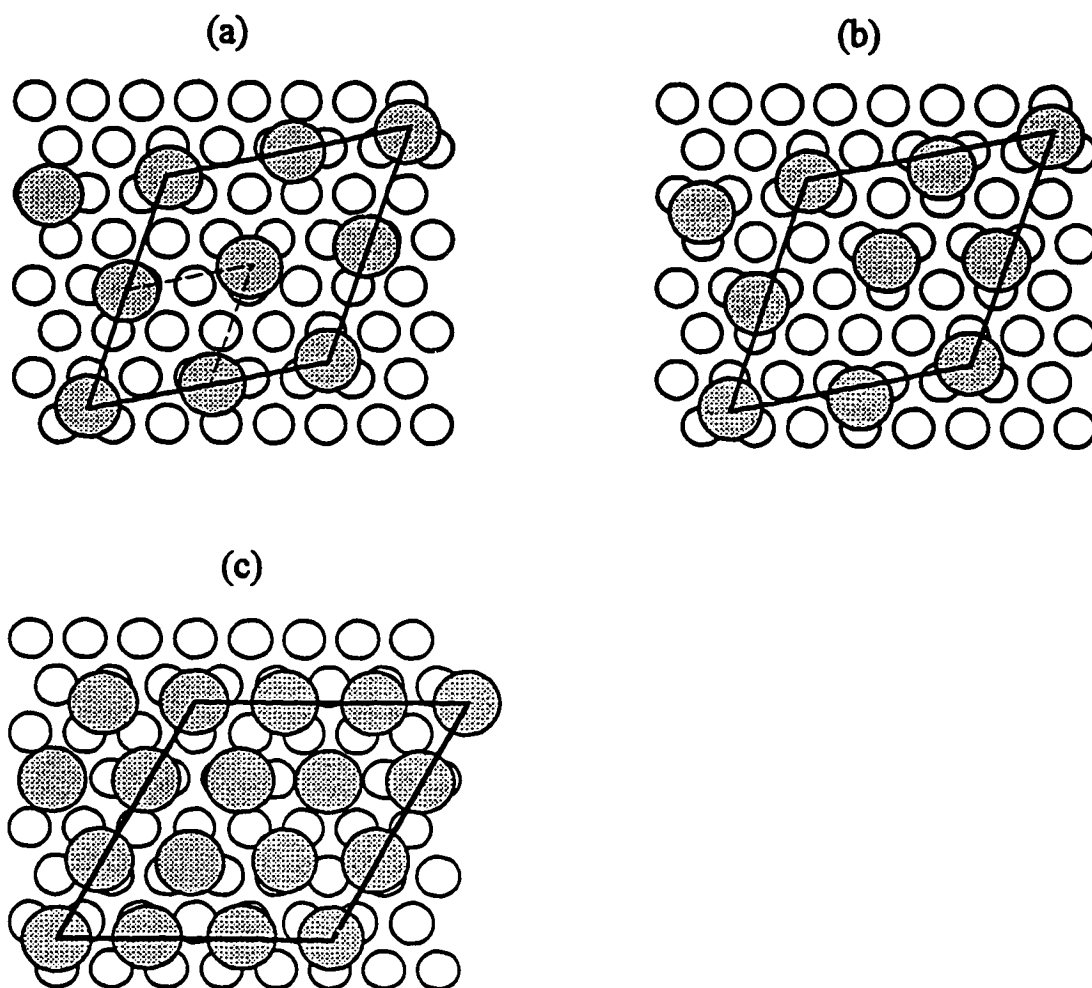


Figure 5.17. Proposed structures for higher-order-commensurate phases: (a) and (b) $(\sqrt{21} \times \sqrt{21})R10.8^\circ$. In (a) the atoms inside the unit cell are positioned at the half-way positions, making the overlayer considered alone have half the periodicity of the HOC structure, shown by the dotted line. In (b) $3/4$ of the atoms are translated 0.84 \AA , so that they all reside in hollow sites. (c) $(5/3 \times 5/3)$ phase. $2/9$ of the atoms reside in hollows, $1/9$ in top sites, and $2/3$ in pseudo-bridge sites.

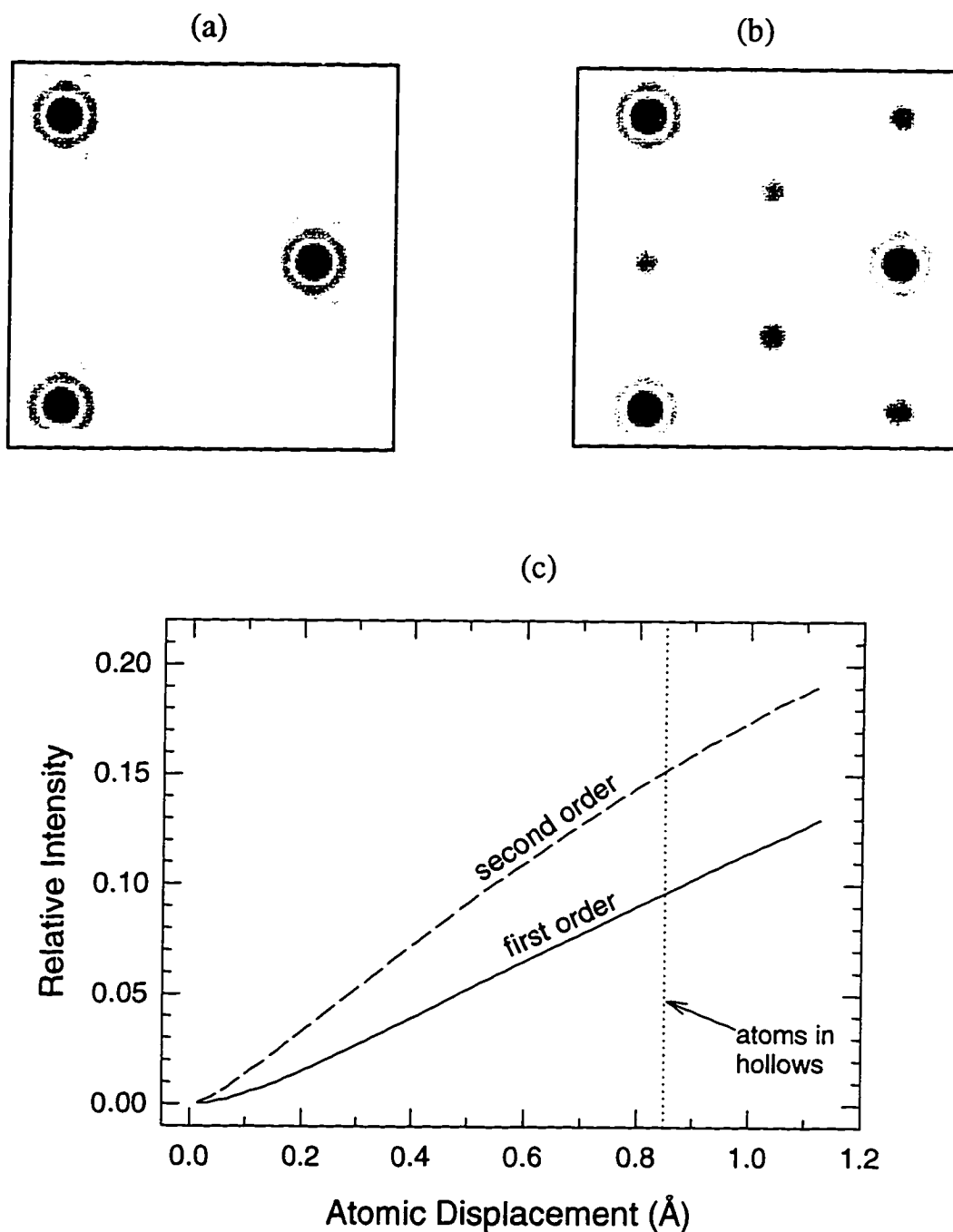


Figure 5.18. Results of a structure factor calculation on the $(\sqrt{21} \times \sqrt{21}) R10.8^\circ$ HOC phase. (a-b) Calculated structure factors for the two structures in Figures 5.19a and 5.19b. The structure factors include only overlayer atoms, not substrate. The dark spot in the upper left corner is the (0,0) spot and the other two dark spots are second-order corresponding to the overlayer $(\sqrt{21} \times \sqrt{21})$ periodicity, and the light spots in (b) are first-order spots. (c) Shows the ratio of the first-order to second-order intensity, as a function of atom displacement toward the hollow sites.

Moving the atoms all the way to the hollow site position results in (1,0) overlayer spots which are only a tenth as intense as the second order spots. Nevertheless, at this intensity the first order spots should have been easily noticeable. It is estimated that under standard experimental conditions diffraction spots would become observable at an intensity of about 0.04 of the intensity of the second-order HOC spots. This puts an upper limit of about 0.25 Å on the movement of the atoms toward the hollow sites. This result reinforces the notion that the alkali atoms see a very weakly corrugated surface potential, compared with the magnitude of the dipole-dipole repulsion between the adatoms.

Another higher order commensurate phase was observed for Rb only: a (5x5) phase with 9 atoms per unit cell at a coverage of 0.36. This phase does not coexist with an incommensurate one, and was identified due to the sharpness and enhanced brightness of the fractional order spots. The (5x5) LEED pattern is shown in Figure 5.15c and a proposed structure in Figure 5.16c. In this structure, 2/9 of the atoms reside in hollows, 1/9 in top sites, and 2/3 in pseudo-bridge sites. First order (5x5) spots were seen for this structure, indicating that the periodicity is truly (5x5). Moreover, the possibility of atoms inside the unit cell relaxing toward favored position seems unlikely.

5.3.4. Alkali Bilayers

For Cs, Rb or K, an ordered alkali second layer can be formed on top of the saturated monolayer by dosing a multilayer amount onto the surface and then annealing. The second layer could be distinguished from the first because it produced diffraction spots at a slightly different position from the first and with a different $I(E)$ signature. In each case the second layer was incommensurate and rotated with respect to the first.

Table 5.3 shows the second layer rotation angles measured with respect to the first layer and densities. The second layer lateral spacing was within 4% of the metallic alkali spacing in each case, and the rotation angle within a few degrees of the Novaco-McTague prediction, which is also shown in Table 5.4. These Novaco-McTague angles were calculated for a dipole potential, based on the misfit between the first and second layers. For Cs (and possibly the others as well) the second layer spacing could be changed somewhat by annealing to different temperatures.

Table 5.4. Spacing and Rotation Angles for Second Layer Alkalis on Ag(111).

Alkali	2 nd Layer Nearest-Neighbor Distance (Å)	Metallic Nearest-Neighbor Distance (Å)	2 nd Layer Rotation Angle	Novaco-McTague Rotation Angle
Cs	5.66	5.46	$9.6 \pm 0.1^\circ$	7.36°
	5.48		$7.5 \pm 0.1^\circ$	4.86°
Rb	5.17	5.10	$5.1 \pm 0.1^\circ$	5.56°
K	4.88	4.76	$3.8 \pm 0.1^\circ$	5.44°

The fact that the second layer spacings are close to the alkali metallic radii indicate that the second layer is not affected strongly by the substrate. This is not surprising, since at saturation the first layer is believed to be in a metallic state very similar to that of the bulk alkali. It is also interesting to note that the second layer does not exist as a dilute phase which compresses with coverage as the first layer does. This is an indication that the dipole potential is probably not the correct one to use for the Novaco-McTague calculation, possibly explaining the small discrepancy between the measured rotation angles and the Novaco-McTague prediction.

5.3.5. Sodium or Lithium on Ag(111)

Experiments were also performed on the Na/Ag(111) and Li/Ag(111) systems. The Li experiments, which were done first chronologically, caused the quality of the Ag(111) surface to degrade considerably over the course of the experiments. This was probably due to diffusion of Li into the surface region, as reported in reference 20. Because of this the Li experiments were terminated early and the Na experiments, for which diffusion into the bulk has also been reported,¹⁹ were of very limited extent. The results of these experiments will therefore be presented qualitatively without detailed phase diagrams.

When Na is dosed onto the Ag(111) surface at about 35 K, uniform rings around the substrate diffraction spots are seen. As with the larger alkalis, the radii of these rings grow with the square root of the dosing time, indicating an overlayer that compresses uniformly with coverage. As with the larger alkalis the exact coverage was taken as the density calculated from the ring radius. The fact that rings

rather than sharp spots are seen most likely indicates that the temperature is above the disordering transition and the layer is in a fluid phase. At a coverage of about 0.2 the rings give way to diffraction spots which indicate an incommensurate overlayer aligned with the substrate.

Because of the limited extent of the Na/Ag(111) experiment, the coverage range immediately above 0.2 ML was not investigated. However, because of the similarity of Na at low coverages to the larger alkalis and the similarity of the larger alkalis to each other, it is probable that the Na overlayer passes through commensurate $p(2 \times 2)$ and $(\sqrt{3} \times \sqrt{3})R30^\circ$ phases at coverages of 0.25 and 0.33. It was found experimentally that at even higher coverages the overlayer exists in a rotated incommensurate phase, similar to that seen for K. The first-layer saturation coverage (obtained by assuming the brightest rotated spots were first order from a primitive triangular lattice) is at least 0.58. This is equivalent to a nearest-neighbor spacing of 3.79 Å, which is nearly identical to the metallic spacing for Na (shown in Table 5.1.)

Li adsorption on Ag(111) is dramatically different from the larger alkalis. With initial dosing at 35 K the only change in the diffraction pattern is an increase in the diffuse intensity. At some point faint but very sharp diffraction spots begin to be visible. This diffraction pattern is shown in Figure 5.19a and corresponds to a $(\sqrt{13} \times \sqrt{13})R13.9^\circ$ periodicity, which is shown schematically in Figure 5.19b. This phase disorders reversibly at a temperature of about 55 K into a phase where no ordered diffraction pattern (including rings) is visible. With further dosing of Li the $\sqrt{13}$ diffraction spots increase in intensity without changing in sharpness or position. At a certain coverage they reach a maximum intensity and then begin to fade. With further dosing, broad rotated incommensurate spots appear which move and rotate with increasing coverage. If these spots are interpreted as first order from a primitive triangular lattice, a saturation coverage of at least 0.63, corresponding to a spacing of 3.64 Å, is obtained. Unlike the other alkalis, this corresponds to a radius which is substantially higher than the metallic Li spacing of 3.12 Å. However, due to the limited extent of the experiments, this should only be taken as a lower limit of the saturation coverage.

Figure 5.20 shows a schematic phase diagram for Li/Ag(111). The coverage scale was determined by assuming that the rotated spots represent a primitive lattice, as described above. The fact that the $\sqrt{13}$ spots are sharp when they first appear may be indicative of a condensation transition at a coverage of about 0.3. Similar behavior was seen for the condensation transition of K on Al(111)³⁶ and Li on Be(0001).³⁷ Since the commensurate $\sqrt{13}$ phase occurs over such a wide coverage range and its diffraction spots grow more intense with dosing, it is probably a phase which exists as islands which grow with increasing coverage. The transition to incommensurate rotated probably occurs after the entire surface becomes

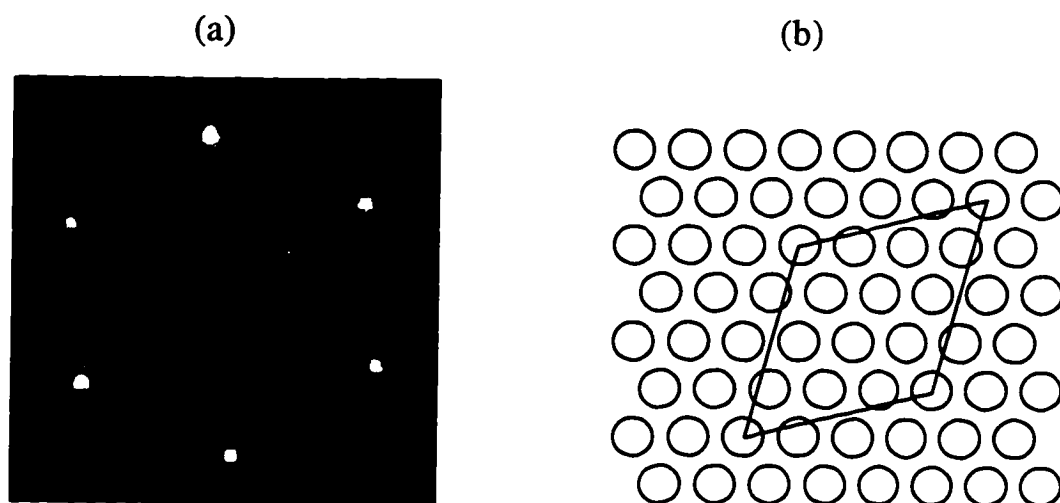


Figure 5.19. $(\sqrt{13} \times \sqrt{13})R13.9^\circ$ diffraction pattern from Li/Ag(111). The diffraction pattern (a) contains spots from two domains rotated plus and minus 13.9° . (b) A real-space schematic of the $(\sqrt{13} \times \sqrt{13})R13.9^\circ$ unit cell.

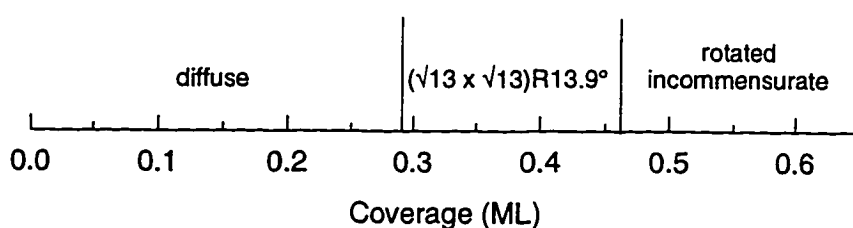


Figure 5.20. Schematic phase diagram for Li/Ag(111). The coverage scale was calculated by assuming that the rotated spots in the highest-coverage phase are from a primitive triangular lattice.

covered with the $\sqrt{13}$ phase. If this is the case and the coverage scale shown in Figure 5.20 is accurate, then the $\sqrt{13}$ phase should contain six atoms per unit cell.

Based on the unusual periodicity of the $\sqrt{13}$ phase and on the tendency of Li to diffuse into the bulk or form surface alloys, it is possible that some substrate reconstruction occurs in the $\sqrt{13}$ phase. However if this were the case it might be expected that the fractional order spots would be more intense. In fact they do not get brighter than about an order of magnitude less than the intensity of the substrate beams. This would argue for the view that the $\sqrt{13}$ periodicity is entirely or nearly entirely caused by an overlayer formation. In addition, a substrate reconstruction would probably cause the relative intensities of the integer order beams to change as well. Although full $I(E)$ curves were not taken for any beams, diffraction patterns from the $\sqrt{13}$ phase were acquired for six different energies and the relative intensities between substrate beams was compared to those for the clean surface. In each case, the ratios were approximately the same, indicating that there is probably no major substrate reconstruction. It is probable that the entering of Li into the bulk (which would imply a surface reconstruction) only occurs temperatures significantly higher than the 35 K at which this experiment was done.

5.4. Site Determinations

5.4.1. Procedure

For the low-order commensurate phases, LEED $I(E)$ data was collected in order to determine the adsorption geometries. Dynamical LEED calculations, described in Chapter Two, were performed for the $p(3 \times 3)$, $p(2 \times 2)$, and $(\sqrt{3} \times \sqrt{3})R30^\circ$ phases. These calculations were done by collaborators P. Kaukasoina and M. Lindroos of the Tampere University of Technology, Tampere, Finland.

The Van Hove and Tong package was used for the calculations.³⁸ The imaginary part of the inner potential was proportional to the cube root of the electron energy, being -3.8 eV at an electron energy of 90 eV. The real part of the inner potential was varied for each system to find the optimum value. A Debye temperature of 170 K was used for the substrate layers, and for the first layer the vibrational amplitudes were enhanced by a factor of $\sqrt{2}$. The alkali adatoms were allowed to have anisotropic vibration amplitudes, as described in Chapter Two. For each of the structures the first two or three substrate layers were allowed to rumple in the periodicity of the adsorbate phase, if it was allowed by symmetry.

The calculated and measured $I(E)$ spectra were compared using the Pendry R factor (also described in Chapter Two). Prior to R factor analysis both sets of curves were convolved with a Lorentzian of width 2 eV in order to reduce noise. After the minimum R factor was found, the response of the R factor to variations in each parameter was measured near the minimum in order to provide information about the uncertainty in the parameter. The same coordinate system as that defined in Chapter Two for the clean Ag(111) surface was used to label the beams.

In order to find the optimum structure, top site and HCP as well as FCC hollow site adsorption were tested. In each case there was a clear preference for one site.

5.4.2. Results

For all the structures, it was determined that the adatom resides in a three-fold hollow. However, for the $(\sqrt{3}\times\sqrt{3})R30^\circ$ phases it is the HCP hollow, while for the $p(2\times 2)$ phases it is the FCC hollow. The difference between these two sites is shown in Figure 5.21. In the HCP hollow, there is a substrate atom in the second layer directly beneath the adsorbate, while for the FCC hollow there is not. The adsorption geometries are shown in Figures 5.22, 5.23 and 5.24, and are qualitatively identical for the same phase from one species to the next. The values corresponding to the parameters in these figures are shown in Table 5.5. No significant lateral movements of the substrate atoms was found for any of the structures. The best fit LEED spectra are shown in appendix C. The chemisorption bond lengths, shown Figure 5.25a, are about half-way between the metallic and ionic radii of the alkali in each case.

Significant vertical rumpling was measured in the first two substrate layers for the $p(3\times 3)$ and $p(2\times 2)$ structures. The rumpling was such that the top layer substrate atoms which are coordinated to the alkali adatom are displaced downward into the surface. In the second layer, atoms highly coordinated with downward displaced atoms in the first layer are also displaced downward. For the $p(3\times 3)$ phases, rumpling was also measured in the third substrate layer.

For the hollow site adsorption in the $(\sqrt{3}\times\sqrt{3})R30^\circ$ geometry, rumpling in the first substrate layer is not allowed by symmetry because all substrate atoms are in equivalent sites with respect to the overlayer. However rumpling is allowed in the second layer. It was found that by introducing a rumpling of the second layer the R factor was improved by about 0.02, a relatively large amount. The rumpling in the second layer is such that the atom directly beneath the adatom is pulled up slightly.

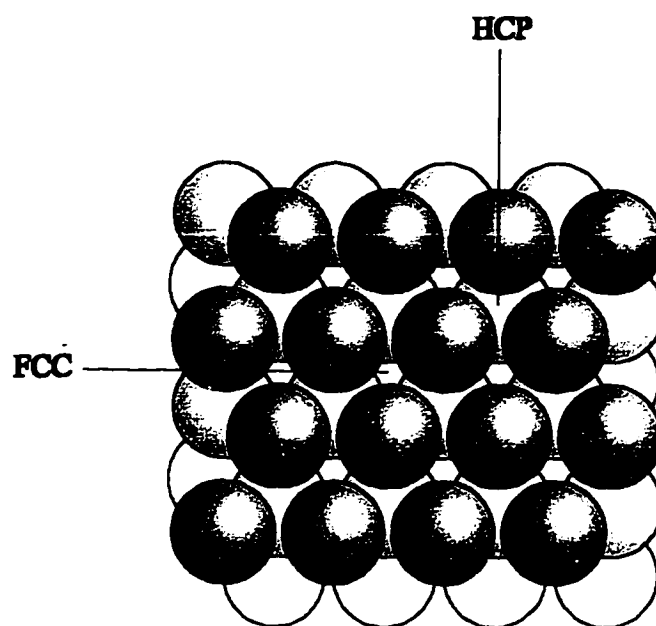


Figure 5.21. Diagram of an FCC(111) surface, showing the difference between HCP and FCC hollow sites. An adatom adsorbed in an HCP site has an atom directly beneath it in the second layer, while an adatom in the FCC site does not.

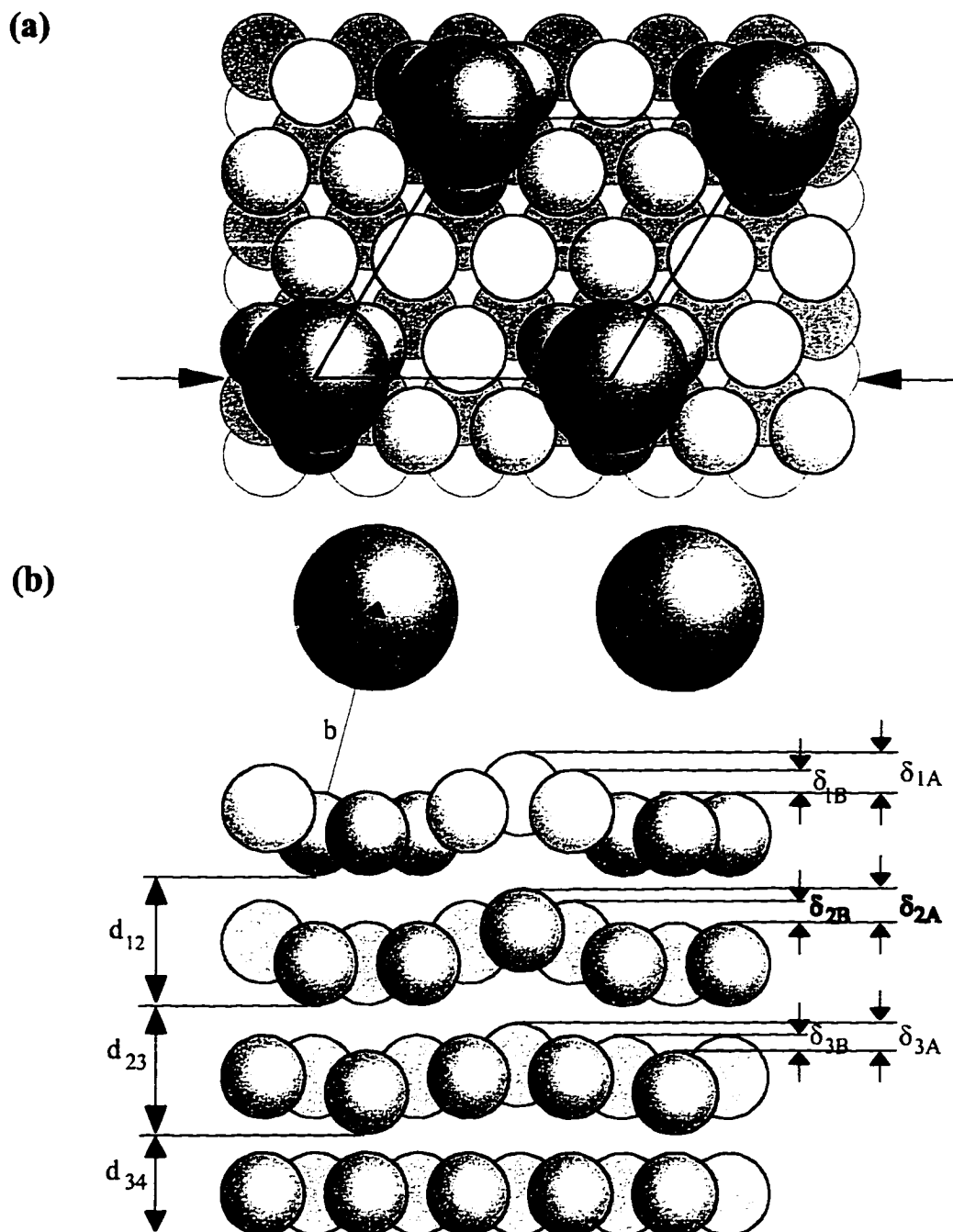


Figure 5.22. Structure of the alkali $p(3 \times 3)$ phase on $\text{Ag}(111)$, with adsorption in the FCC hollow site. Diagram is not to scale. (b) is a vertical slice through the arrows in (a). The values of the quantities shown are listed in Table 5.5. The atoms in the top substrate layer are darkness-coordinated with the atoms in (a). b denotes the chemisorption bondlength.

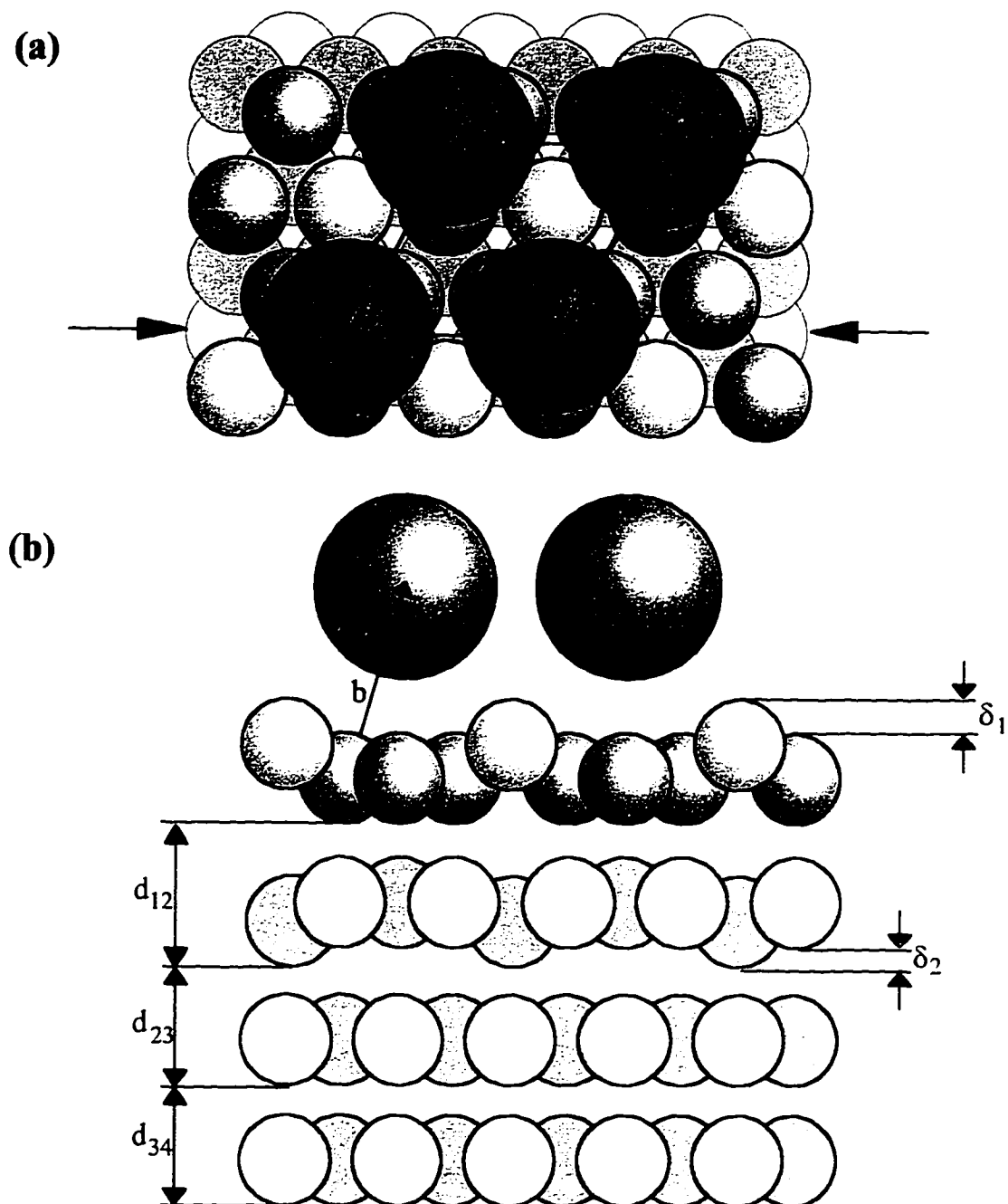


Figure 5.23. Structure of the alkali $p(2 \times 2)$ phase on $\text{Ag}(111)$, with adsorption in the FCC hollow site. Diagram is not to scale. (b) is a vertical slice through the arrows in (a). The values of the quantities shown are listed in Table 5.5. The atoms in the top substrate layer are color-coordinated with the atoms in (a). In the first substrate layer, three of the four atoms per unit cell are displaced downward by δ_1 . In the second substrate layer, the adatom which is coordinated with the three downward-displaced atoms in the first layer is displaced downward by δ_2 . b denotes the chemisorption bondlength.

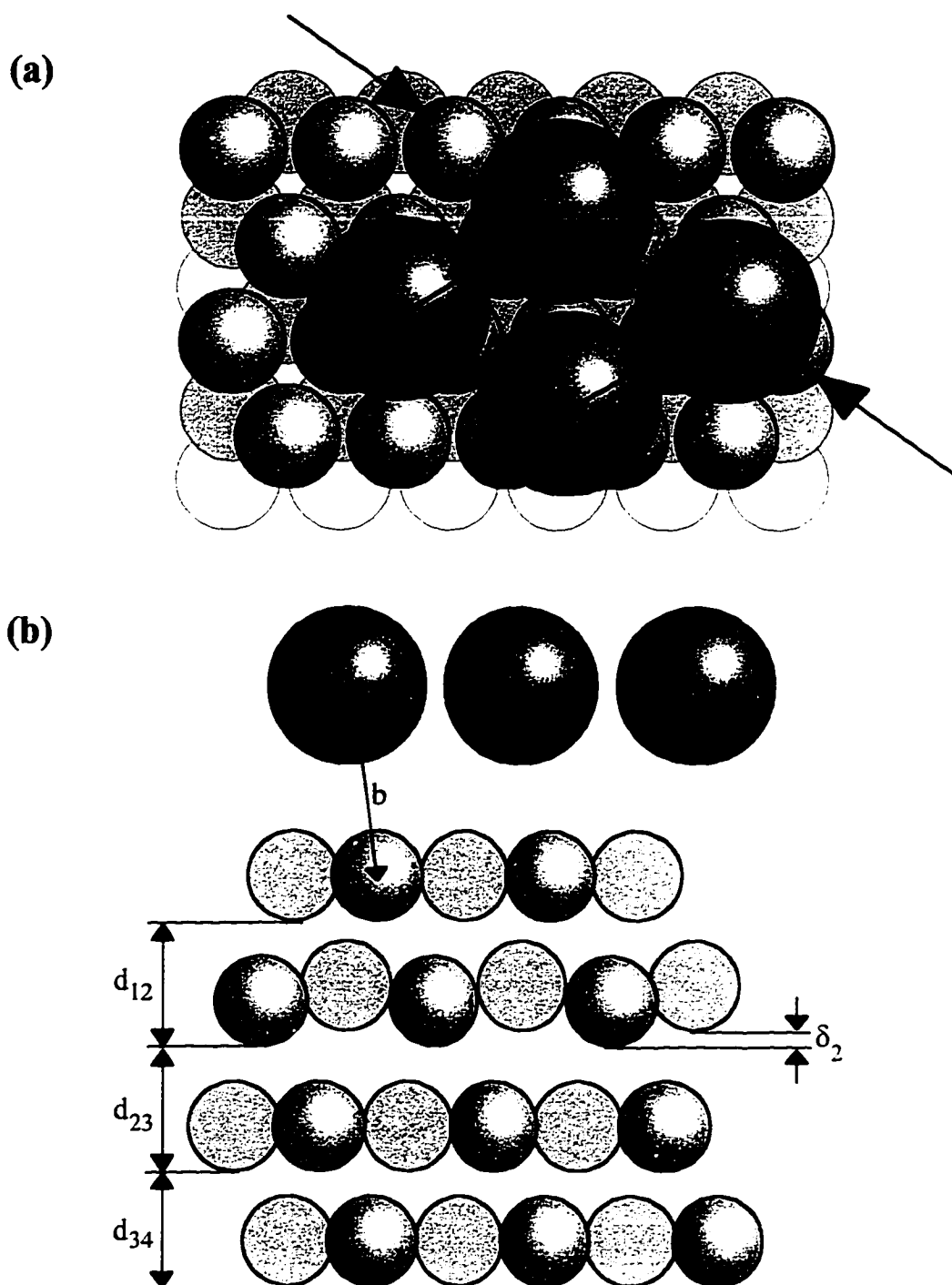


Figure 5.24. Structure of the $(\sqrt{3}\times\sqrt{3})R30^\circ$ phase, with adsorption in the HCP hollow site. Diagram is not to scale. (b) is a vertical slice through the arrows in (a). The values of the quantities shown are listed in Table 5.5. Rumpling in the top substrate layer is not allowed by symmetry for HCP hollow adsorption. In the second layer, the atom directly beneath the adsorbate is displaced upward by δ_2 . b denotes the chemisorption bondlength.

Table 5.5 Structural parameters of alkali phases on Ag(111), determined by LEED I(E) analysis. The parameters are defined in the diagrams in Figures 5.23, 5.24, and 5.25.

System	Site	b	d ₁₂	d ₂₃	d ₃₄	δ_1	δ_2	δ_3	R _F
K p(3x3)	FCC	3.27 ± 0.03	2.34 ± 0.03	2.34 ± 0.05	2.31 ± 0.09	A: 0.09 ± 0.03	A: 0.06 ± 0.03	A: 0.03 ± 0.04	0.176
						B: 0.08 ± 0.03	B: 0.04 ± 0.03	B: 0.04 ± 0.06	
Rb p(3x3)	FCC	3.42 ± 0.03	2.34 ± 0.02	2.33 ± 0.03	2.33 ± 0.04	A: 0.10 ± 0.02	A: 0.06 ± 0.02	A: 0.04 ± 0.03	0.261
						B: 0.09 ± 0.03	B: 0.04 ± 0.02	B: 0.02 ± 0.03	
Cs p(3x3)	FCC	3.55 ± 0.03	2.32 ± 0.02	2.34 ± 0.03	2.32 ± 0.04	A: 0.11 ± 0.03	A: 0.06 ± 0.03	A: 0.04 ± 0.03	0.270
						B: 0.10 ± 0.03	B: 0.04 ± 0.03	B: 0.03 ± 0.02	
K p(2x2)	FCC	3.27 ± 0.03	2.37 ± 0.02	2.33 ± 0.02	2.35 ± 0.03	0.10 ± 0.03	0.03 ± 0.02	-----	0.179
Rb p(2x2)	FCC	3.38 ± 0.03	2.37 ± 0.02	2.32 ± 0.02	2.35 ± 0.04	0.10 ± 0.03	0.03 ± 0.02	-----	0.217
Cs p(2x2)	FCC	3.52 ± 0.04	2.37 ± 0.02	2.32 ± 0.02	2.36 ± 0.03	0.09 ± 0.03	0.03 ± 0.02	-----	0.240
K p($\sqrt{3} \times \sqrt{3}$)R30°	HCP	3.29 ± 0.03	2.38 ± 0.02	2.34 ± 0.03	2.35 ± 0.03	-----	0.02 ± 0.02	-----	0.244
Rb ($\sqrt{3} \times \sqrt{3}$)R30°	HCP	3.40 ± 0.03	2.38 ± 0.03	2.34 ± 0.03	2.35 ± 0.03	-----	0.02 ± 0.02	-----	0.227
Cs ($\sqrt{3} \times \sqrt{3}$)R30°	HCP	3.52 ± 0.03	2.37 ± 0.03	2.34 ± 0.03	2.35 ± 0.03	-----	0.01 ± 0.03	-----	0.238

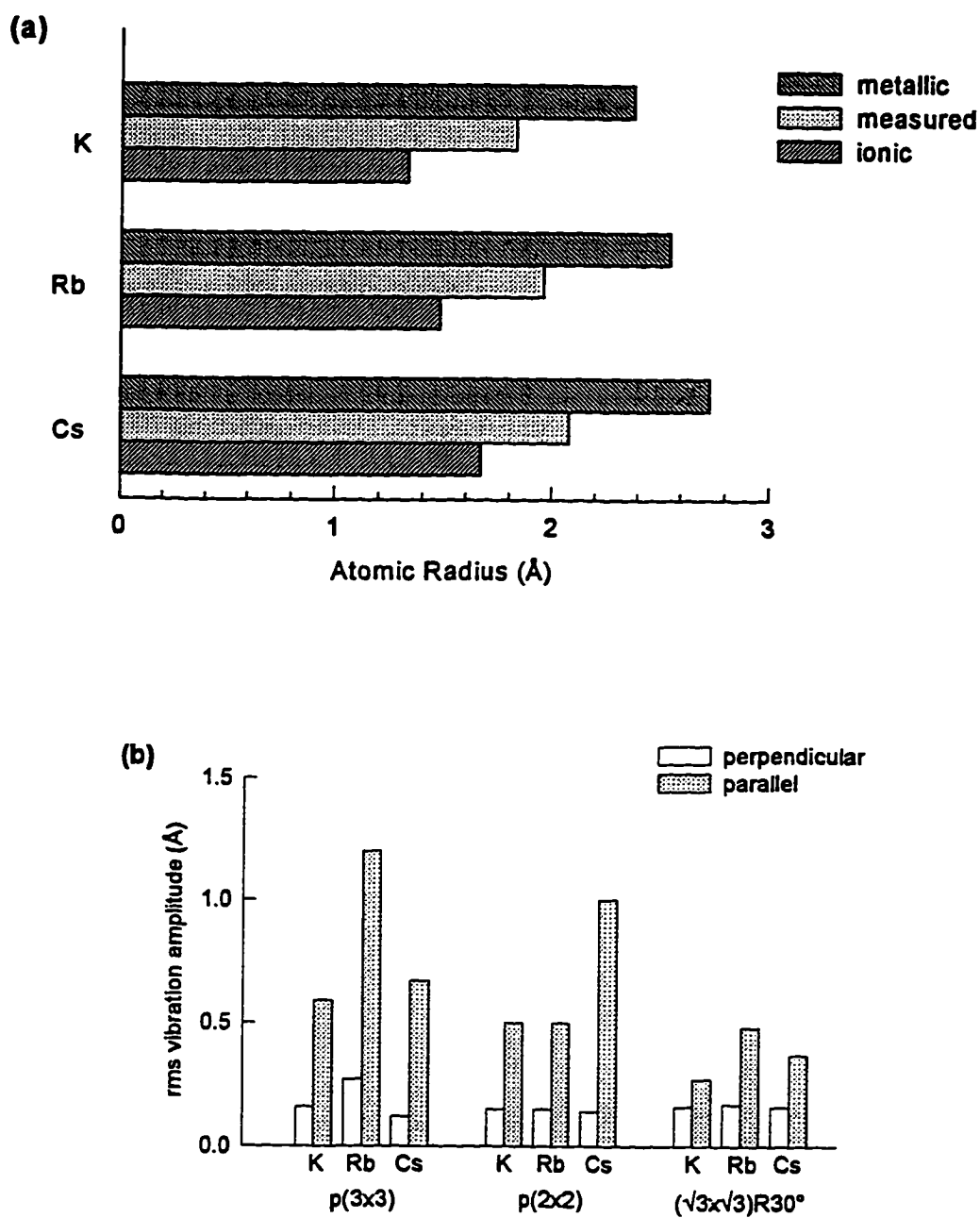


Figure 5.25. Chemisorption bondlength and anisotropic vibrational amplitudes for alkalis on Ag(111). (a) Measured chemisorption bondlength for each alkali, compared to its ionic and covalent radius. (b) Vibration amplitudes for alkali adsorbates.

The alkali vibrational amplitudes are shown in Figure 5.25b. In each case they were found to be highly anisotropic, being as much as several times larger in the surface plane than perpendicular to it. This is consistent with the behavior of other alkali metal adsorption systems, where anomalously large in-plane vibrations were found.⁴

To determine the uncertainty in each of the determined parameters, the curvature of the R factor was evaluated in the vicinity of the minimum. The uncertainties were then calculated as described in reference 39, and these uncertainties are shown as \pm values in Table 5.5. The value of the R factor close to the minimum for the structural parameters of the K $p(3 \times 3)$ phase is shown in Figure 5.26.

For the phases which could be formed without annealing, the experiment was done using an annealed and an unannealed overlayer to check for temperature-activated phases. For the annealed overlayer, the alkali was deposited at low temperature, then annealed to a temperature which resulted in the desorption of some alkali leaving an overlayer of the desired coverage, and then cooled again for data collection. In each case no significant change was found in the $I(E)$ curves after annealing the surface. Figure 5.27 shows a subset of the $I(E)$ data for the K $p(2 \times 2)$ phase, using two different methods of overlayer preparation: (a) overlayer deposited at 40 K, (b) overlayer deposited at 40 K and annealed to room temperature. As can be seen, there is no significant difference between the curves from these differently-prepared samples.

For the lower-coverage commensurate phases (the $(\sqrt{7} \times \sqrt{7})R19.1^\circ$ and $(2\sqrt{3} \times 2\sqrt{3})R30^\circ$), LEED $I(E)$ data were taken but the full analysis was not completed. However, some information can still be obtained from the spectra. The $I(E)$ intensities of fractional-order LEED spectra are mostly sensitive to the local environment of the adatom. Because of this, equivalent beams or averaged beams from equivalent reciprocal space positions, taken from different phases but with an adatom of the same species, will be similar if the local environment of the adatom is similar between the two phases, i.e. if the adatom is in the same adsorption site. Figure 5.28 panels (a), (b) and (c) show a subset of the spectra from the K, Rb and Cs $p(2 \times 2)$ phases, compared with spectra obtained by averaging beams around the equivalent positions in reciprocal space from the $(\sqrt{7} \times \sqrt{7})R19.1^\circ$ phase of the same alkali. The $(1/2 \ 0)$ beam is compared to an average of the $(2/7 \ 1/7)$ and $(4/7 \ 1/7)$ beams, $(0 \ 1/2)$ is compared to an average of $(1/7 \ 2/7)$ and $(1/7 \ 4/7)$, and the $(1/2 \ 1/2)$ is compared to an average of the $(2/7 \ 4/7)$, $(4/7 \ 2/7)$, $(3/7 \ 5/7)$, and $(5/7 \ 3/7)$ beams. In each case the spectra show many similarities between the $p(2 \times 2)$ and $(\sqrt{7} \times \sqrt{7})R19.1^\circ$ phases, indicating that the adatom is probably adsorbed in the FCC site in the lower coverage phase as well. Panel (d) of Figure 5.28 shows beams of the Cs $(2\sqrt{3} \times 2\sqrt{3})R30^\circ$ phase compared to beams of the $p(3 \times 3)$ and $(\sqrt{3} \times \sqrt{3})R30^\circ$ phases. The first curve compares the first order beams of the two lower coverage phases: the $(1/6 \ 1/6)$ for the $(2\sqrt{3} \times 2\sqrt{3})R30^\circ$ phase and an average of the $(1/3 \ 0)$ and $(0 \ 1/3)$ for the $p(3 \times 3)$. (These are not compared to spectra from the $(\sqrt{3} \times \sqrt{3})R30^\circ$ phase, since there are no beams

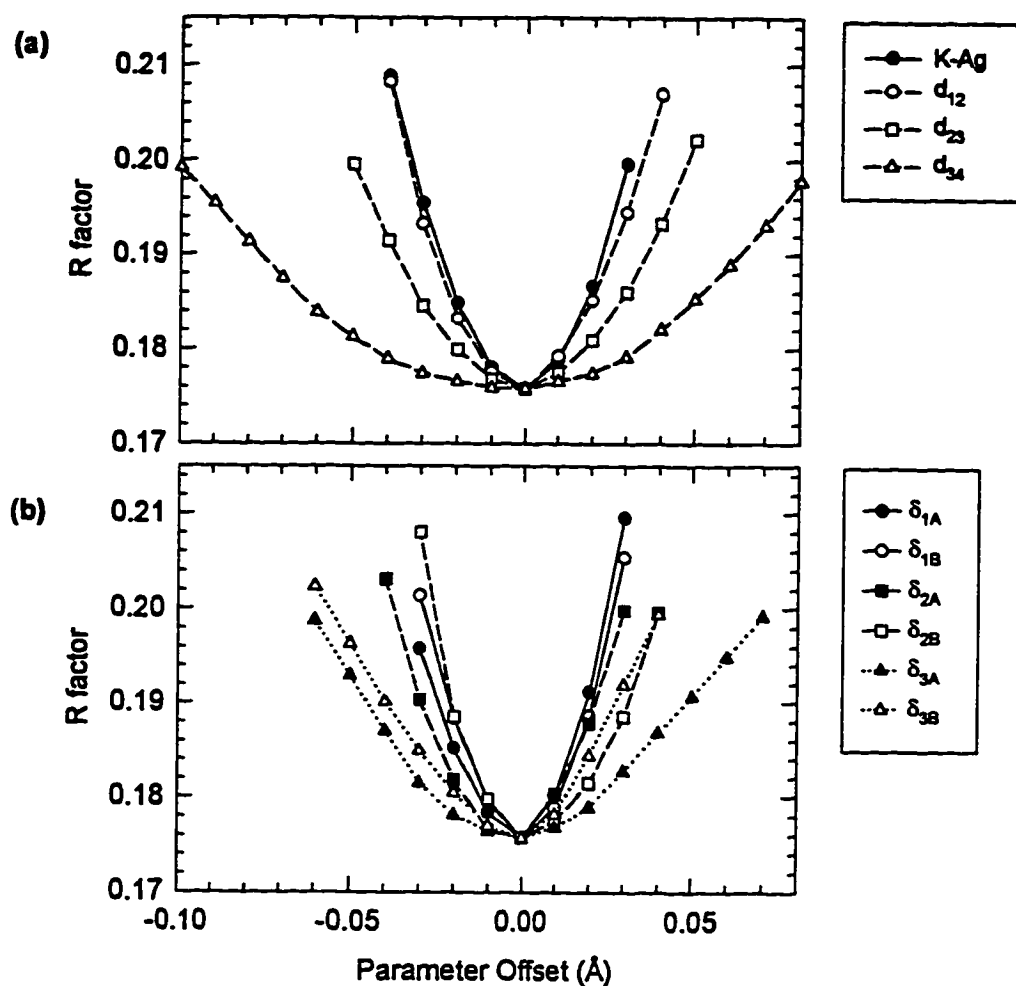


Figure 5.26. Variation of the Pendry R factor near the minimum with the structural parameters, for the K p(3x3) / Ag(111) phase. While varying each parameter, the other parameters are held constant at the minimum. (a) Shows the interlayer spacings and (b) shows the rumpling amplitudes. The quantity K-Ag is the perpendicular spacing between the overlayer and the uppermost atom in the top substrate layer. The other quantities are defined in Figure 5.23.

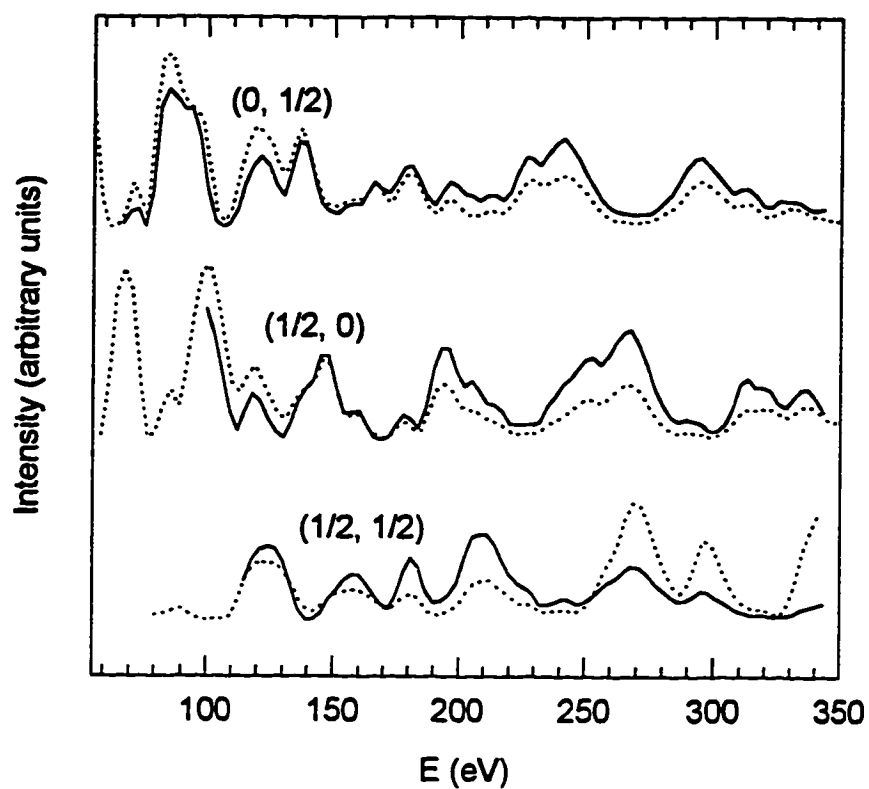


Figure 5.27. (a) Comparison of K p(2x2)/Ag(111) for an overlayer deposited at 35 K and not annealed to an overlayer deposited at 35 K, annealed to room temperature, and then cooled again for data collection. Solid lines represent the data from the annealed overlayer and dotted lines represent the data from the unannealed overlayer.

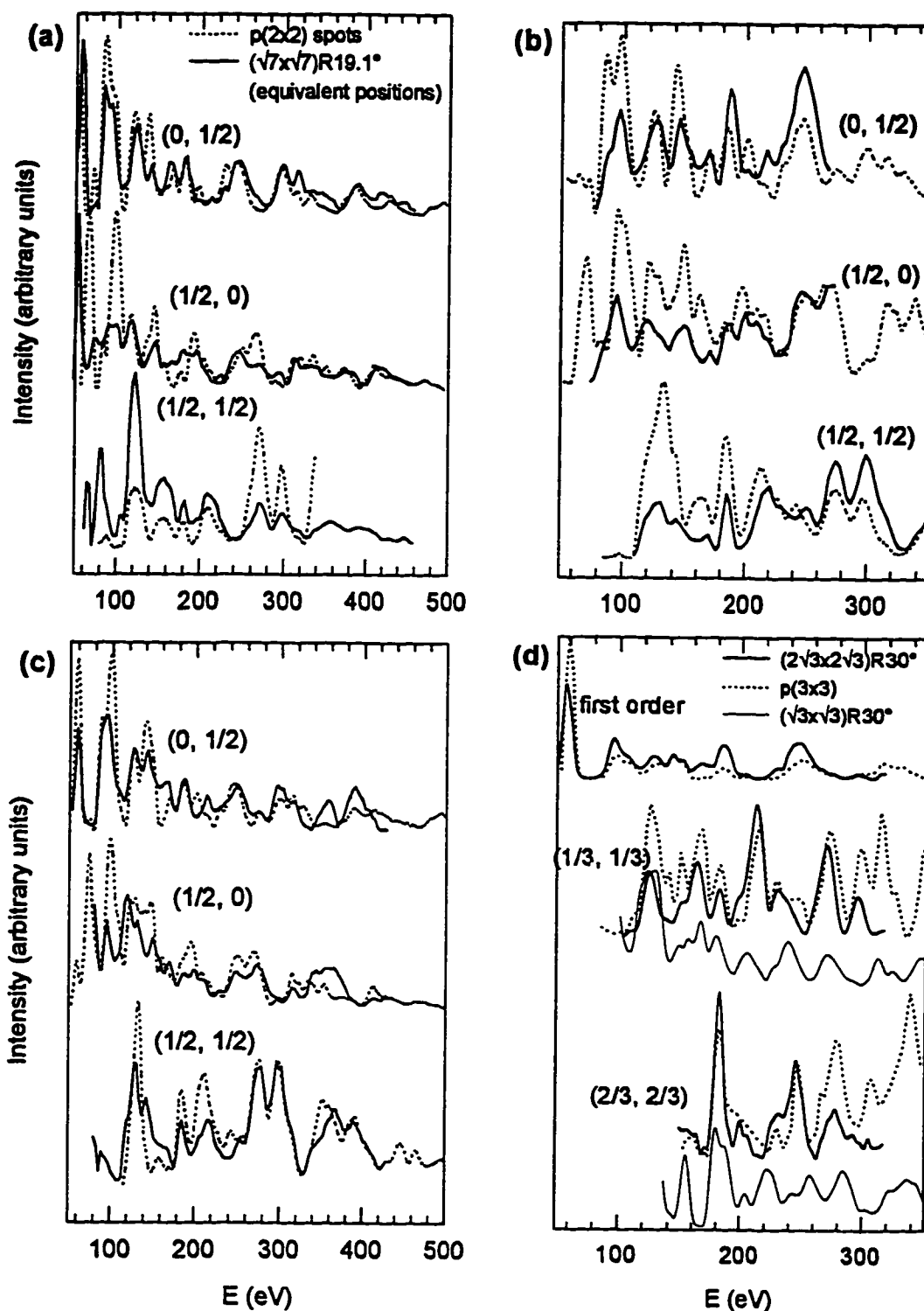


Figure 5.28. Comparison of equivalent LEED beams of solved structures to low-coverage unsolved structures. (a-c) Comparison of beams from the $p(2 \times 2)$ structure (FCC site) to equivalent averaged beams from the $(\sqrt{7} \times \sqrt{7})R19.1^\circ$ structure for K, Rb, and Cs respectively. (d) Comparison of equivalent beams for Cs $(2\sqrt{3} \times 2\sqrt{3})R30^\circ$ (unsolved) to Cs $p(3 \times 3)$ (FCC site) and Cs $(\sqrt{3} \times \sqrt{3})R30^\circ$ (HCP site). $\sqrt{3} \times \sqrt{3} R30^\circ$ beams in each set are offset slightly for clarity.

reasonably close in reciprocal space.) Below, the $(1/3\ 1/3)$ and $(2/3\ 2/3)$ beams, which are common to all three structures, are compared. It is evident that the similarities between the $(2\sqrt{3}\times 2\sqrt{3})R30^\circ$ phase and the $p(3\times 3)$ phase are much greater than between the $(2\sqrt{3}\times 2\sqrt{3})R30^\circ$ and $(\sqrt{3}\times\sqrt{3})R30^\circ$ phases. Thus it is probable that in the Cs $(2\sqrt{3}\times 2\sqrt{3})R30^\circ$ phase the adatom is in the FCC site also.

5.4.3. Discussion

Many of the experimental results presented here are consistent with previous experiments, while some are not. The LEED patterns recorded for Cs are consistent with those reported in reference 12. The rings reported at lower coverages (interpreted as a rotationally disordered solid) are consistent with the fluid phase we measure. Also the spot splitting described at other coverages can be explained as the incommensurate phases between a coverage of 0.18 and 0.30, where the spots due to multiple diffraction through an overlayer and substrate vector produce the appearance of split spots. The fact that the experiments reported in references 10 and 11 did not report any LEED patterns can be explained by the fact that the experiments were done at room temperature. Except for the extreme end of the monolayer coverage range, the Cs monolayer is disordered at room temperature. The existence of a monolayer above a coverage of 0.30, and especially the $(\sqrt{3}\times\sqrt{3})R30^\circ$, would be easily missed since the overlayer must be either dosed or annealed for several minutes inside of a critical temperature range which is only 20-30 K wide. Temperatures too low do not give the overlayer enough mobility to change its orientation from the 0° of the phase below to the 30° of the commensurate $(\sqrt{3}\times\sqrt{3})R30^\circ$, and temperatures too high will desorb some of the layer.

The change in chemisorption bondlength reported for Cs/Ag(111) in reference 14 is not in agreement with our results. Figure 5.29 shows our chemisorption bondlength as a function of coverage for the three alkalis, compared with the previous results. It is clear that the increase in bondlength with coverage is not reproduced in these experiments. It is possible that the discrepancy is the result of the experiments being done at different temperatures; the LEED experiment was done at about 35 K while the SEXAFS study was done at 120 K, a temperature where the monolayer in the low coverage experiment would have been in a fluid phase. However, it is unlikely that this could account for such a large change. It is more likely that in the low-coverage SEXAFS experiment a larger number of impurities were present on the surface. It has been shown for Cs/Ru(0001) that the presence of oxygen coadsorbed with an alkali metal can cause a decrease in the chemisorption bondlength.⁴⁰

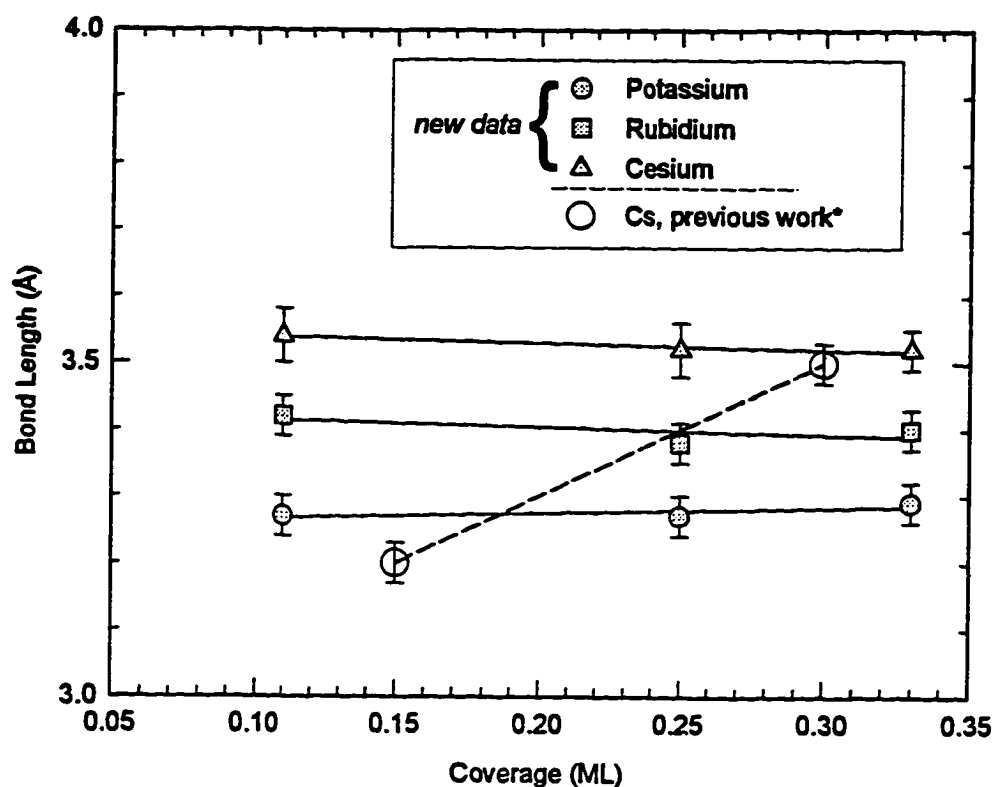


Figure 5.29. Alkali chemisorption bondlength as a function of coverage, for K, Rb, and Cs on Ag(111). No significant change in bondlength is measured. The data are compared to a previous SEXAFS result which found a change in bondlength with respect to coverage.

*Source: reference 14.

At first reading the Rb study¹⁶ appears to be completely at odds with the results presented here. However, upon closer inspection some of the results may be consistent if it is assumed that the surfaces reported as multilayer were actually in the monolayer regime. The (9x9) pattern measured may have actually been the aligned incommensurate phase at a coverage greater than 0.25 and less than 0.33. Again, multiple diffraction spots may give the appearance of a two spots close together which could have been interpreted as high order fractional spots. Annealing to 450 K, by which a ring pattern was produced, would have desorbed part of the monolayer leaving a coverage at which the room-temperature monolayer was disordered, producing rings in the diffraction pattern. Further dosing would have reproduced the (9x9) pattern as reported. It is likely that the (3x3) phase produced by annealing to higher temperatures was the result of impurities, as conjectured in the paper.

The previous results for K are also largely consistent with the present results. It is likely that the two lattice orientations reported in reference 17 were 30° and 0°, and that the coverage was slightly higher than the 0.33 reported. The other results reported for K (references 17 and 18) are not directly verifiable by these LEED experiments, but they are consistent with the general picture obtained for K/Ag(111). These experiments found electronic changes in the monolayer between a coverage of 0.25 and monolayer saturation, attributed to metallization of the overlayer. Interestingly, this is the coverage range over which we measure a change in adsorption site from FCC to HCP hollow. It is possible that the change in site is somehow connected with overlayer metallization. Other possible reasons for the change will be discussed below.

The conclusion in reference 19 that the first layer of Na on Ag(111) grows in registry with the substrate is obviously at odds with the present results. However this conclusion was based solely on the absence of a LEED pattern during the growth of a Na monolayer at room temperature. Based on the fact that only rings were seen in the Na diffraction pattern for coverages less than 0.2 ML, it seems that the Na monolayer disorders at significantly lower temperatures than the other alkalis. Because of this higher thermal mobility it is likely that the rings would be very difficult to see at room temperature.

The Li results¹⁷ are quite consistent with our results. Again, this experiment was done at room temperature and so no ordered diffraction patterns would have been seen. The uptake of Li into the bulk is consistent with our observation of a degraded surface region.

Unfortunately, the work function results reported in the literature cannot be verified by the experiments reported here. The reason for this is that the Kelvin Probe was only acquired after most of the experiments were completed, and so systematic studies of the work function behavior of these systems were not done. This is unfortunate, since the previous results are not all in agreement with each other.

For the three larger alkali metals, at monolayer saturation coverage the nearest-neighbor bondlength is compressed several percent from that of the bulk metallic phase. This is a general

phenomenon and has been seen for nearly all alkali adsorbate systems investigated in recent years.⁴ This has been shown in a calculation to be the result of the two-dimensional nature of the adsorbate layer.⁴¹ Because of the reduced coordination number of the atoms in the overlayer (compared to the same atoms in the bulk) more charge is concentrated in the metallic bonds between the atoms. This screens the ion cores more effectively from each other, making the lattice able to compress to a smaller spacing.

The R factors obtained in the LEED structural determination are quite good compared to most other alkali overlayer phases which have been solved until now. It is not uncommon for these phases to yield R factors larger than 0.3 for the best fit structure. A possible reason for the poor agreement between experiment and theory is a large amount of in-plane dynamic disorder in the overlayer which has been demonstrated to be present in these systems.⁴ The anomalously large parallel vibrational amplitudes measured in the experiments reported here support the view that the alkali adatoms have a lot of freedom to move about in the plane, even at low temperatures. The reason for the significantly better agreement between theory and experiment shown in this study is probably the low temperature at which the experiments were performed, which would have the effect of limiting the in-plane disorder somewhat. Very few of the structural determinations up until now have been done at less than 100 K.

The adsorption sites measured (hollow sites in all cases) are surprising for a number of reasons. First of all, it was expected that top site adsorption would be found for at least some of the phases. As detailed in section 5.1 above, top site adsorption has been found to be quite common for the large alkalis on close-packed metal surfaces. In all of the cases where top site adsorption was observed a significant substrate rumpling was also observed. For one particular system it has actually been shown theoretically that this rumpling is a necessary component of top site adsorption.⁹ Therefore it has been suggested that substrates which are able to deform more easily to accommodate this rumpling will be more likely to exhibit top site adsorption. It might then be expected that a low substrate bulk modulus would be a good indication that top site adsorption will occur. Figure 5.30 shows various substrates on which adsorbed alkali phases have been measured, plotted as a function their bulk modulus. With the exception of Ag(111), top site adsorption seems to be much more common on the substrates with low bulk modulus, while hollow site adsorption seems to be more prevalent for high bulk modulus substrates. Ag however has a low bulk modulus, yet it exhibits only hollow site adsorption. Moreover, we find that the Ag(111) surface rumples significantly under hollow site adsorption, so the inability to rumple is not the cause of hollow site adsorption in this case. Unfortunately the reason for hollow site rather than top site adsorption is not apparent in this case, and total energy calculations will probably be needed to understand the behavior.

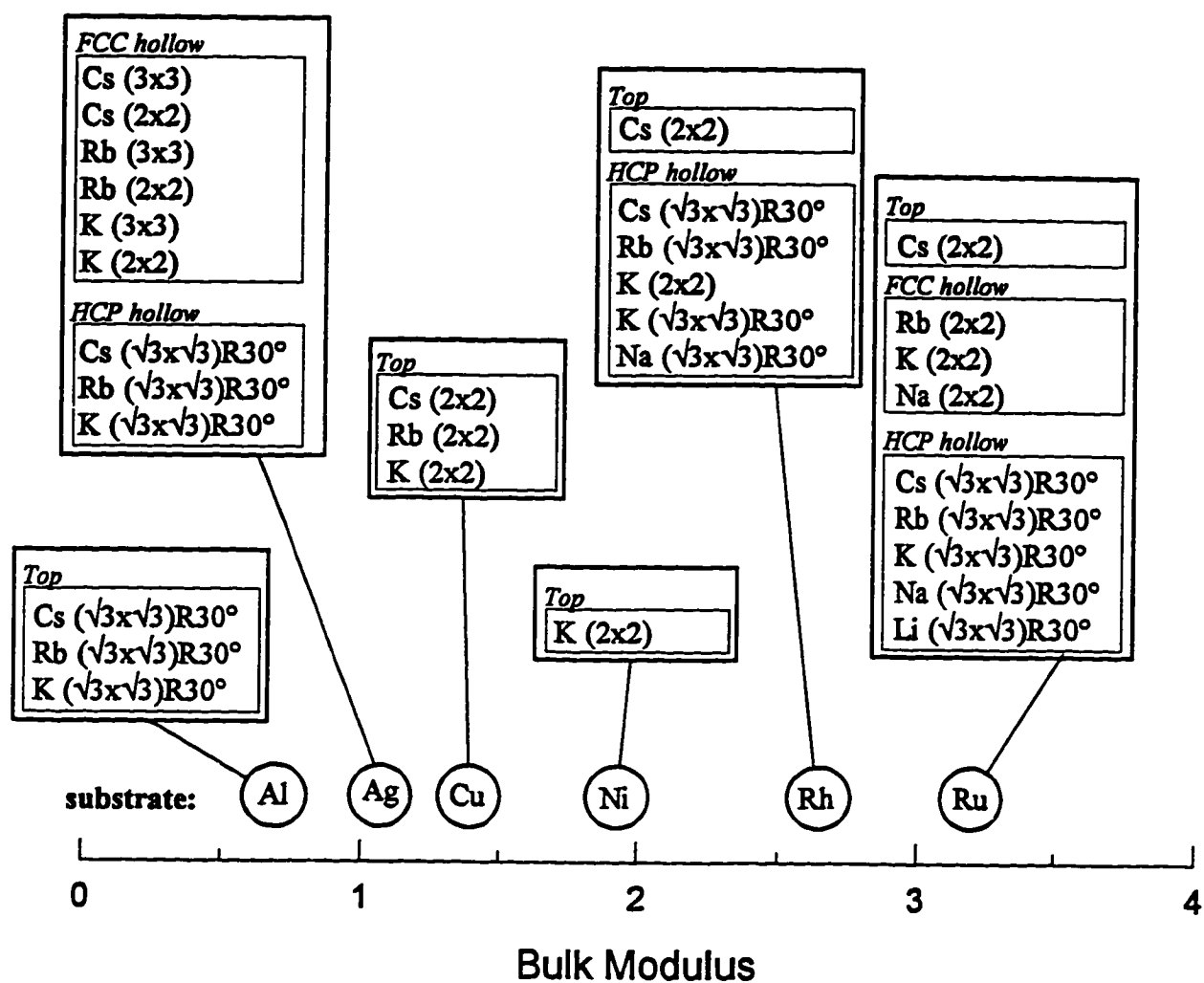


Figure 5.30. Bulk moduli of various substrates, shown together with alkali phase which form on them.⁴

Another possibility which was considered quite likely was substitutional adsorption.

Substitutional adsorption had been observed for all of the alkali metals on Al(111), and is possible because it is relatively easy for the Al(111) surface to form the vacancy structure in the $(\sqrt{3}\times\sqrt{3})R30^\circ$ geometry necessary for the substitutional phase. Density theory calculations had predicted that other metal surfaces with a low energy of vacancy formation include Ag(111) and Cu(111).⁴² Thus it was expected that by annealing the overlayer it might be possible to produce one of these temperature-activated substitutional structures. However none was found. Thus it appears that while the energy of vacancy formation may be low for Ag(111), either it is not low enough to make a substitutional structure advantageous or else the layer desorbs at a temperature lower than that necessary to activate the phase.

Still another feature which was suspected but not found was metallic condensation at a critical coverage. Again, this feature is found on Al(111)⁵ and a number of other systems including possibly Ag(100).⁴³ In fact no condensation was found, and the adatom interactions appeared to be repulsive over the entire submonolayer range.

In conclusion, alkali metals on Ag(111) seem to conform in most ways with the older ideal picture of alkali metal adsorption, with the exception of Li. The adatoms occupy high-coordination hollow sites without inducing any novel reconstructions of the substrate. The adatoms experience a repulsive interaction over the entire monolayer range, and they feel a small enough lateral potential corrugation that they form incommensurate phases over most of the monolayer coverage range. Unlike the classical picture however the chemisorption bondlength is not strongly dependent on coverage, remaining essentially constant from less than a third to a full saturated monolayer.

An important point illustrated by these results is that even after years of fairly concentrated effort, alkali metal adsorption is still not understood well enough to predict adsorption sites based on qualitative physical properties of the adsorption system. Perhaps the largest triumph so far has been the ability (in at least the case of one substrate, Al(111)) to predict the top and substitutional sites, based on intensive density functional theory calculations.⁴² It may be that, due to the delicate balance of energy responsible for these varied behaviors, reliable prediction of adsorption sites will never be possible except by such energy calculations.

5.5. Rotational Epitaxy

5.1.1. Results

Between a coverage of about 0.13 and 0.25, the Cs, Rb, or K overlayer on Ag(111) is rotated at a non-symmetry angle with respect to the substrate. This angle changes continuously (with the exception of the $(\sqrt{21} \times \sqrt{21})R10.8^\circ$ higher order commensurate phase) as the lattice parameter changes. The rotational behavior at about 30 K, the lowest experimentally available temperature, is shown in Figure 5.31, along with the predictions of various models. These models were introduced in Chapter Two.

Although the experimental data do not agree exactly with any of the experimental models, several trends can be observed. The curves for all three alkalis follow trajectories which move at least quasi-continuously from the aligned direction of the $p(2 \times 2)$ phase to the 19.1° of the $(\sqrt{7} \times \sqrt{7})R19.1^\circ$ phase, consistent with the trajectory selected according to the Novaco-McTague theory. However, there is a strong tendency of the overlayers to rotate toward alignment with nearby commensurate structures, as predicted by the Shiba theory. For instance, the K and Rb overlayers align with the 0° direction well before reaching the $p(2 \times 2)$ density while the Cs aligns with the 0° direction at a much smaller misfit. The fact that Cs aligns at a smaller misfit is consistent with the general predictions of the Shiba theory, since the smaller adatoms will probably experience a greater substrate corrugation due to their size. Therefore stronger domain walls (which are the cause of the deviation from Novaco-McTague to Shiba-like behavior) would be expected in the K or Rb overlayers than for Cs at the same density. The same tendency to align with the commensurate phase is also evident near the $(\sqrt{7} \times \sqrt{7})R19.1^\circ$ phase, although the difference between the alkalis is less.

There could

Figures 5.32 shows the temperature dependence of the rotation angle for Rb/Ag(111). At most coverages in this range, increasing the temperature causes the overlayer rotation angle to decrease toward 0° . In all the coverages investigated however the rotation angle never makes it to 0° before the overlayer melts. In fact the overlayer (which retains some orientational order after melting) is still rotated in the fluid phase. In Figure 5.32, the melting temperature for each scan is marked with a dotted vertical line. Figure 5.33 shows the temperature dependence of the rotation angle for K and Cs. These changes in rotation angle are fully reversible if the temperature is changed slowly enough to keep the overlayer in equilibrium. For Rb and K the behavior was always fully reversible at the time-scales of a normal experiment (i.e. cooling the sample at least 1 K/s after a temperature scan), while for Cs the sample had to be cooled significantly slower to observe reversibility in the rotation angles. This is consistent with the larger size of the Cs atom which makes the overlayer more crowded, limiting the mobility of the adatoms.

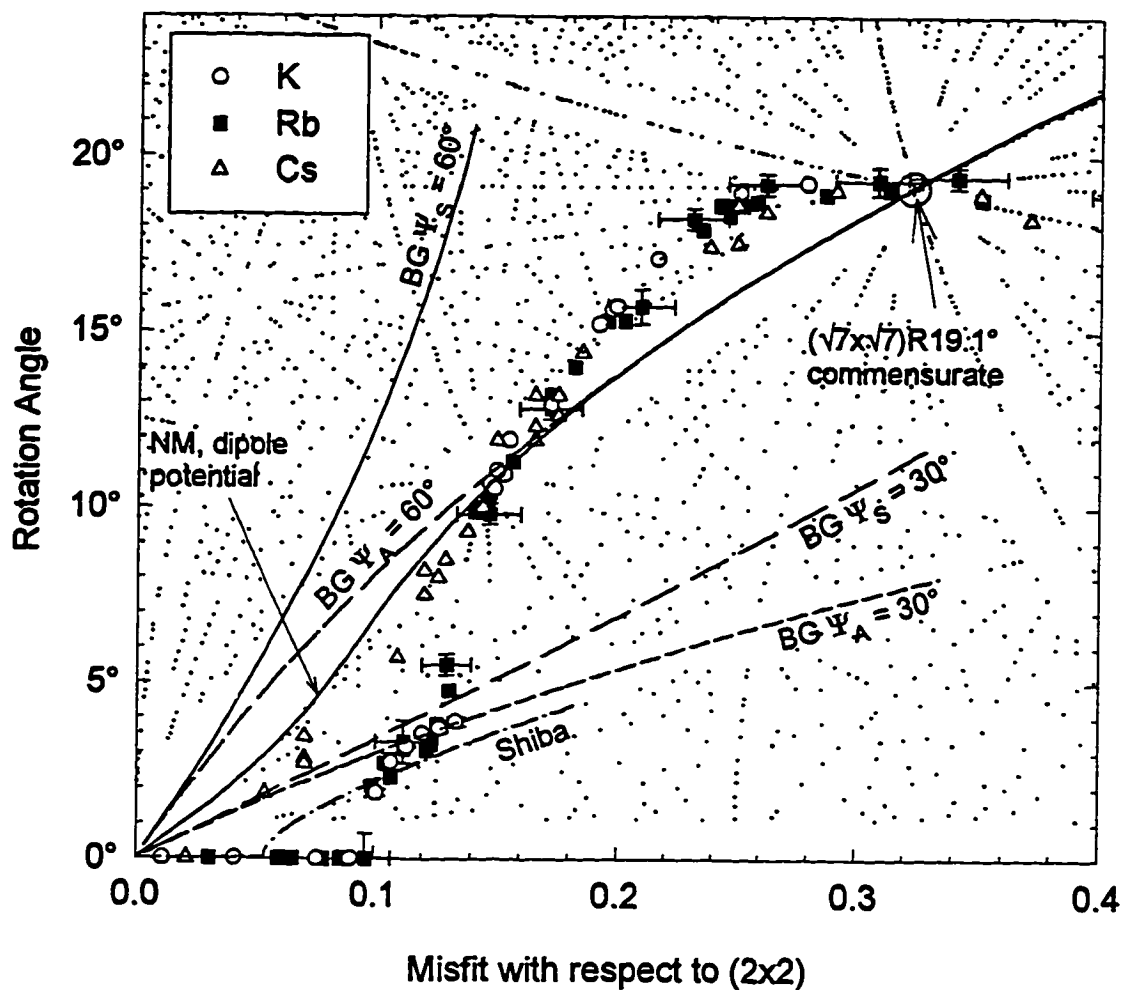


Figure 5.31. Rotational behavior of Cs, Rb, or K on Ag(111), compared with various theoretical models. The data points represent data taken at 35 K. The “BG”, “NM”, and “Shiba” lines represent predictions of the Bohr-Grey, Novaco-McTague, and Shiba theories, respectively. These are discussed in Chapter Two. The fine dots represent higher-order commensurate positions, also discussed in Chapter Two.

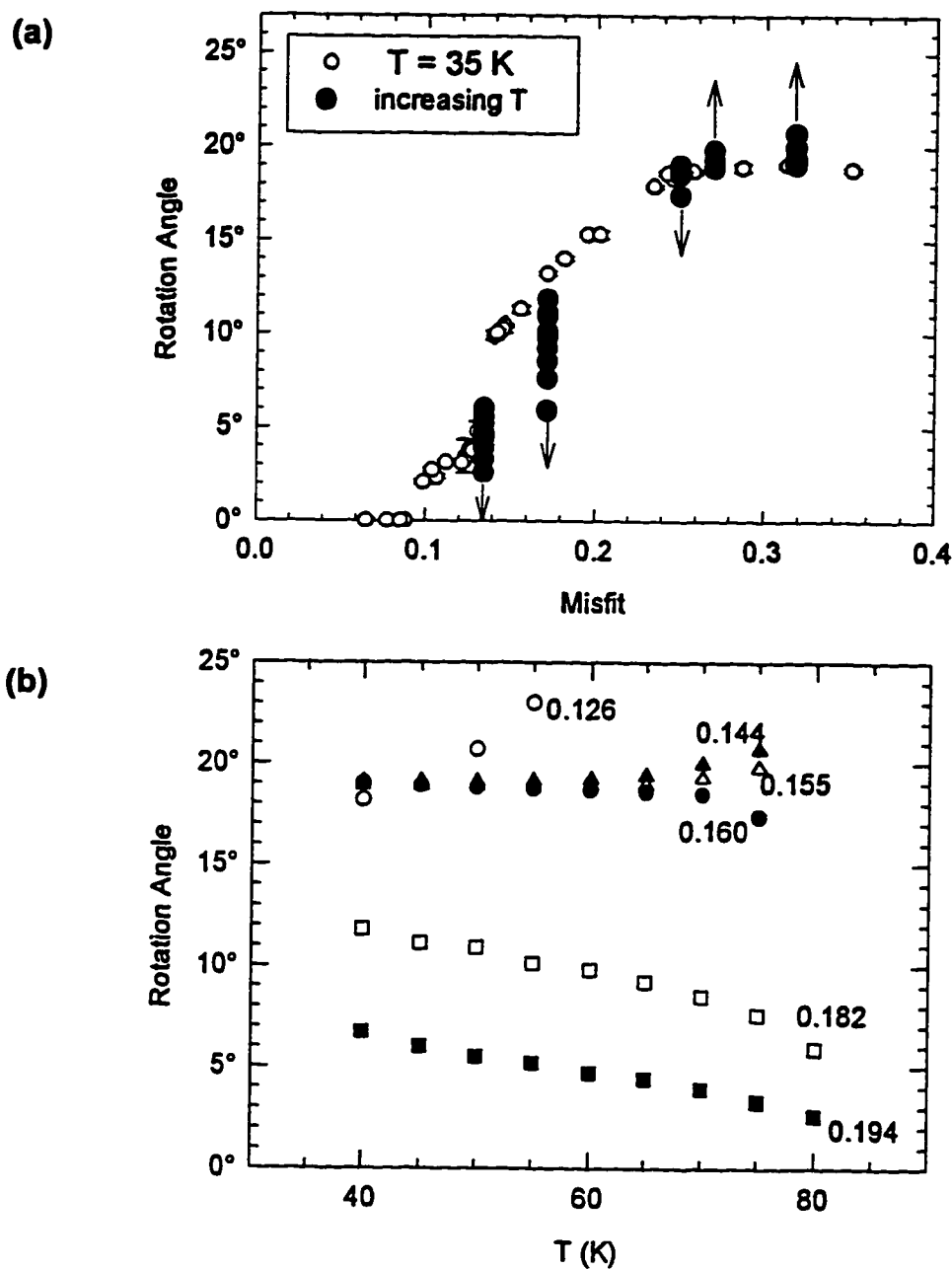


Figure 5.32. Rotational behavior of Rb/Ag(111) as a function of temperature. (a) Temperature dependence shown on an angle vs. misfit graph. The filled circles represent the behavior of the overlayer as a function of increasing temperature. Misfit is defined as $(d-2d_0)/2d_0$, i.e. misfit with respect to the $p(2 \times 2)$. (b) Rotation angle as a function of temperature for several coverages.

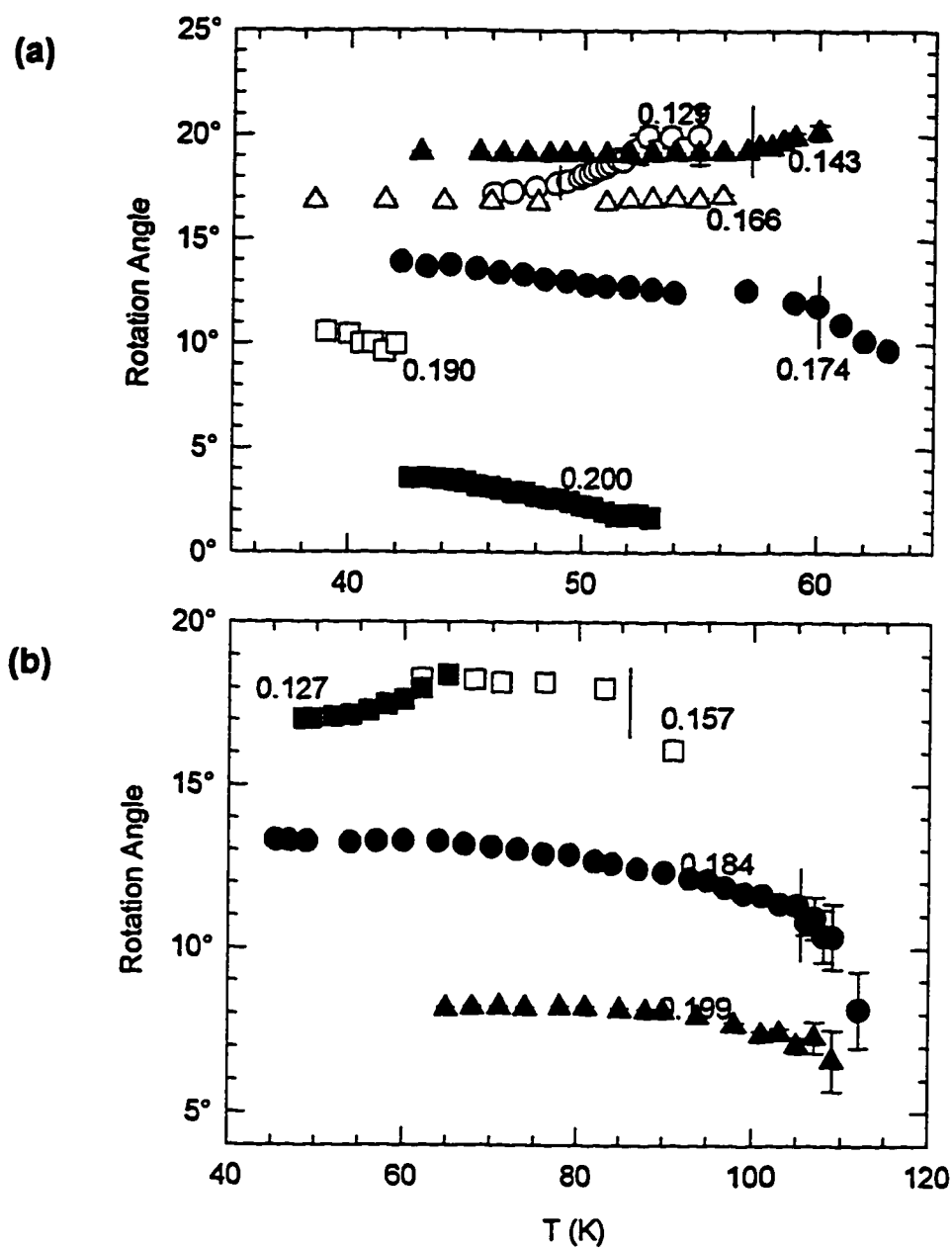


Figure 5.33. Rotation angle as a function of temperature for K or Cs on Ag(111). (a) K data, (b) Cs data. The numbers represent the alkali coverage in ML. The vertical lines show the temperature at which the disordering transition occurs.

5.5.2. Discussion

While the low-temperature data follow the general trend of the Novaco-McTague prediction, there is significant departure at most misfits. Near the commensurate positions, the departure is well explained, at least qualitatively, by the Shiba theory. The reason for the lack of agreement at other misfit however is not completely apparent. The fact that the interatomic potential is not well approximated by the dipole interaction could explain some of the discrepancy. The work function curves shown in Figure 5.1 indicate that significant depolarization begins at approximately 0.1 ML (evidenced by the non-linearity of the curve). As the coverage increases the inter-adsorbate bond will begin to take on some metallic character. Another reason for the failure of the Novaco-McTague theory may be relaxation of the substrate atom positions. The substrate atoms were observed to relax significantly in the commensurate phases. One could easily envision a lateral mass-density wave in the top substrate layer, similar to that which occurs in the overlayer, which could affect the rotational behavior. To date there are no theories of epitaxial rotation which address this possibility.

While rotational epitaxy has been observed for many diverse systems, temperature dependence of the rotation angle has rarely been measured. One exception is for Ar, Kr, or Xe on graphite.^{47,44} All three were observed to change their rotation angle as a function of temperature, although the changes could be explained by the changing overlayer density with temperature. On clean Pt(100) and Au(100) surfaces, the top layer reconstructs into a hexagonal lattice and is rotated with respect to the substrate. The rotation angle in this case changes about 1° over a 250 K temperature range, going from rotated to aligned; in this case the change in lattice constant is not sufficient to explain the change in rotation angle.⁴⁵ The only other case where a temperature dependent rotation angle not driven by changing density was observed is for Cs-intercalated graphite.⁴⁶ For this system the rotation angle went from about 15° to 0° over a range of 100 K. This is the only study that has shown a rotation angle change with a magnitude comparable to what has been reported here.

Another interesting feature of the data is that the rotation angle of the orientationally-ordered fluid continues to change after the melting transition. In most cases where this occurs however, there is also a change in the slope of the rotation angle change with temperature. This is not surprising, since the type and extent of order in an overlayer plays an important part in epitaxial rotation. Epitaxial rotation of a liquid phase has also been seen for Ar/graphite.⁴⁷ In that case, the changing rotation angle was driven by a density which changed with temperature and so the rotation angle was plotted as a function of misfit. However, a change in slope of the rotation angle was seen at the melting transition for that system.

One way to explain the tendency of the overlayer to align with increasing temperature is in terms of the decrease in the overlayer's shear modulus as it is heated toward its melting point. The loss in the

overlayer rigidity makes it less able to sustain a macroscopic rotation. Eventually, if the overlayer ever got to the point where all correlation between adatoms is lost, the lowest energy situation would be that where each adatom is closest to a potential minimum, i.e. the overlayer is aligned with the substrate.

Another way to understand the behavior, suggested by D'Amico et al,⁴⁷ is in terms of fluctuations of the domain sizes. At $T=0$ the system will be perfectly ordered and all domains will be the same size. With increasing temperature, there will be increasing fluctuations in the domain sizes because of entropy. Because of the distribution of domain sizes, the majority of atoms will be in domains larger than the mean domain size. Since larger domains correspond to a lower rotation angle (as seen in the Moiré pattern in Figure 2.10), the mean rotation angle averaged over the lattice will decrease with increasing T .

A mean-field theory was developed for the rotational behavior observed on the reconstructed metal surfaces.⁴⁵ This theory predicts an exponent of $1/2$ associated with the temperature dependence of the rotation angle. This prediction agrees reasonably well with the experimental results obtained for both the reconstructed metals and for alkali-intercalated graphite. Figure 5.34 shows data for K/Ag(111) with the straight lines representing the $1/2$ power law. It can readily be seen that these data are consistent with the mean-field result. However, the fit is sensitive to the value used for T_c and reasonable fits can also be found for exponents which are at least 20% different from the mean-field result.

The temperature dependence of these overlayers at lower densities is not as easy to explain, however. At low densities, the rotation angle increases with increasing temperature. This might be explained again as the overlayer being more strongly influenced by the substrate periodicity as the dynamic disorder increases, heading toward the 19.1° value of the nearby commensurate $(\sqrt{7}\times\sqrt{7})R19.1^\circ$ phase. However, as temperature is increased, the equilibrium rotation angle continues to increase beyond this value, as shown in Figures 5.32 and 5.33, and it is not clear from these data where it might be headed. One possibility is the 30° angle of the $(\sqrt{3}\times\sqrt{3})R30^\circ$ phase, but there is no obvious reason why this angle should be preferred at these densities. It is interesting to note that the overlayer melts at, or in some cases before the rotation angle reaches the 19.1° , and that the rotation to greater angles is a rotation of bond-orientational order in the fluid. It may be that the overlayer is only affected by the $(\sqrt{7}\times\sqrt{7})$ periodicity of the substrate if there is sufficient translational order in the overlayer, and that because of the reduced translational order after melting the overlayer is pulled toward 30° , a high symmetry direction of the substrate, rather than the 19.1° of the commensurate overlayer phase.

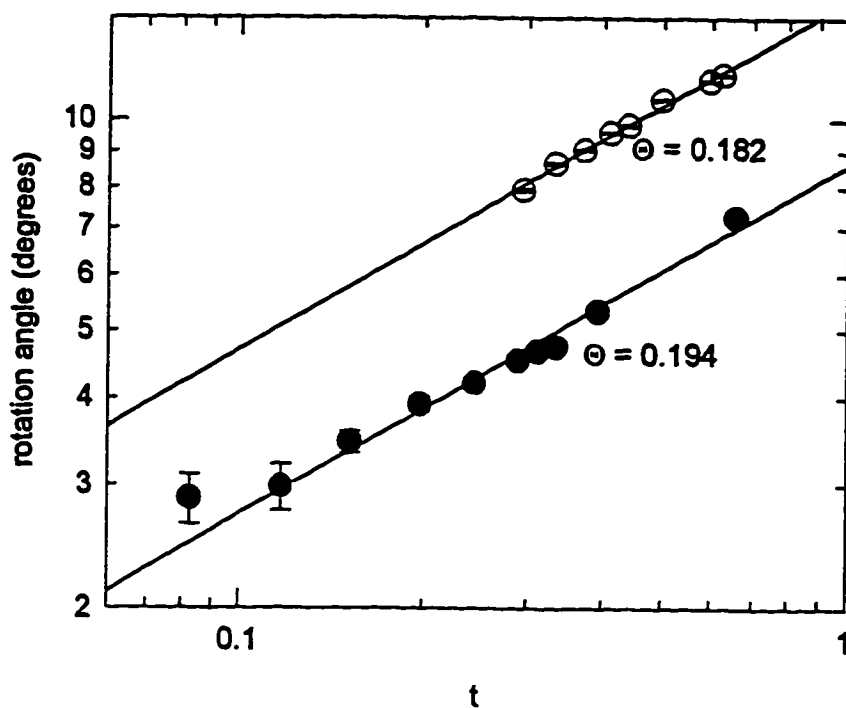


Figure 5.34. Comparison of the temperature dependent Rb/Ag(111) data at two coverages to a power law having the exponent 0.5. t is the reduced temperature $(T_c - T)/T_c$, where T_c is the (extrapolated) temperature at which the angle becomes 0° .

5.6. References

- ¹ S. Å. Lindgren, L. Walldén, J. Rundgren, P. Westrin and J. Neve, *Phys. Rev. B* **28**, 6707 (1983).
- ² D. Fisher, S. Chandavarkar, I. R. Collins, R. D. Diehl, P. Kankasoia and M. Lindroos, *Phys. Rev. Lett.* **68**, 3204 (1992).
- ³ D. L. Adler, I. R. Collins, X. Liang, S. J. Murray, G. S. Leatherman, K. -D. Tsui, E. E. Chaban, S. Chandavarkar, R. McGrath, R. D. Diehl and P. H. Citrin, *Phys. Rev. B* **48**, 17445 (1993).
- ⁴ R. D. Diehl, R. McGrath, *Surface Science Reports* **23**, 43 (1996).
- ⁵ M. Nielsen, J. Burchhardt, D. L. Adams, E. Lundgren and J. N. Andersen, *Phys. Rev. Lett.* **72**, 3370 (1994).
- ⁶ J. N. Andersen, M. Qvarford, R. Nyholm, J. F. van Acker and E. Lundgren, *Phys. Rev. Lett.* **68**, 94 (1992).
- ⁷ C. Stampfl, M. Scheffler, H. Over, J. Burchhardt, M. M. Nielsen, D. L. Adams and W. Moritz, *Phys. Rev. Lett.* **69**, 1532 (1992).
- ⁸ D. L. Adams, *Appl. Phys. A* **62**, 123 (1996).
- ⁹ C. Stampfl and M. Scheffler, *Surf. Rev. Lett.* **2**, 317 (1995).
- ¹⁰ R. B. Grant and R. M. Lambert, *Langmuir* **1**, 29 (1985).
- ¹¹ R. B. Grant and R. M. Lambert, *J. Catal.* **93**, 92 (1985).
- ¹² C. T. Campbell, *J. Phys. Chem* **89**, 5789 (1985).
- ¹³ C. Argile and G. E. Rhead, *Surface Science* **203**, 175 (1988).
- ¹⁴ G. M. Lamble, R. S. Brooks, D. A. King, *Phys. Rev. Lett.* **61**, 1112 (1985).
- ¹⁵ *Physics and Chemistry of Alkali Metal Adsorption*, eds. H. P. Bonzel, A. M. Bradshaw and G. Ertl, Elsevier, Amsterdam (1989).
- ¹⁶ P. J. Goddard and R. M. Lambert, *Surface Science* **79**, 93 (1979).
- ¹⁷ Å. Fäldt, *Surface Science* **114**, 311 (1982).
- ¹⁸ P. M. Blass, X. -L. Zhou and J. M. White, *Surface Science* **215**, 74 (1989).
- ¹⁹ P. J. Goddard, J. West and R. M. Lambert, *Surface Science* **71**, 447 (1978).
- ²⁰ S. D. Parker, *Surface Science* **157**, 261 (1985).

- ²¹ H. Over, H. Bludau, M. Skottke-Klein, G. Ertl, W. Moritz and C. T. Campbell, *Phys. Rev. B* **45**, 8638 (1992).
- ²² S. Schwegmann and H. Over, *Surface Science*, submitted.
- ²³ C. Kittel, *Introduction to Solid State Physics*, New York: Wiley (1986).
- ²⁴ E. Domany, M. Schick, J. Walker and R. Griffiths, *Phys. Rev. B* **18**, 2209 (1978).
- ²⁵ Z. Li, X. Liang, M. L. Stutzman, J. A. Spiznigo, S. Chandavarkar and R. D. Diehl, *Surface Science* **327**, 121 (1995).
- ²⁶ A. G. Naumovets, *Sov. Sci. Rev. A Phys.*, **5**, 445 (1984).
- ²⁷ D. Fisher, PhD. Thesis (1990).
- ²⁸ D. Fisher and R. D. Diehl, *Phys. Rev. B* **46**, 2512 (1992).
- ²⁹ S. C. Ying, *Phys. Rev. B* **3**, 4160 (1971).
- ³⁰ V. L. Pokrovsky and G. V. Ulmin, *J. Phys. C* **11**, 3535 (1978).
- ³¹ S. Chandavarkar, PhD Thesis (1989).
- ³² S. Chandavarkar and R. D. Diehl, *Phys. Rev. B* **40**, 4651 (1989).
- ³³ K. J. Strandburg, *Rev. Mod. Phys.* **60**, 161 (1988).
- ³⁴ K. Kern, P. Zeppenfeld, R. David and G. Comsa, *Phys. Rev. Lett.* **59**, 79 (1978)
- ³⁵ K. Kern and G. Comsa in *Phase Transitions in Surface Films 2*, eds. H. Taub, G. Torzo, H. J. Lauter and S. C. Fain, New York, Plenum Press (1990).
- ³⁶ J. N. Andersen, E. Lundgren, R. Nyholm and M. Qvarford, *Surface Science* **289**, 307 (1993).
- ³⁷ T. Aruga and Y. Murata, *Prog. Surf. Sci.* **31**, 61 (1989).
- ³⁸ M. A. Van Hove and S. Y. Tong, private communication.
- ³⁹ J. B. Pendry, *J. Phys. C: Solid St. Phys.* **13**, 937 (1980).
- ⁴⁰ H. Over, H. Bludau, M. Skottke-Klein, W. Moritz and G. Ertl, *Phys. Rev. B* **46**, 4360 (1992).
- ⁴¹ E. Wimmer, *Surface Science* **134**, L487 (1983).
- ⁴² H. M. Polatoglou, M. Methfessel and M. Scheffler, *Phys. Rev. B* **48**, 1877 (1993).
- ⁴³ S. Modesti, C. T. Chen, Y. Ma, G. Meigs, P. Rudolf and F. Sette, *Phys. Rev. B* **42**, 5381 (1990).

⁴⁴ K. L. D'Amico, D. E. Moncton, E. D. Specht, R. J. Birgeneau, S. E. Nagler and P. M. Horn, *Phys. Rev. Lett.* **53**, 2250 (1984).

⁴⁵ D. L. Abernathy, S. G. J. Mochrie, D. M. Zehner, G. Grüber and D. Gibbs, *Phys. Rev. B* **45**, 9272 (1992).

⁴⁶ R. Clarke, N. Caswell, S. A. Solin and P. M. Horn, *Phys. Rev. Lett.* **43**, 2018 (1979).

⁴⁷ K. L. D'Amico, J. Bohr, D. E. Moncton and D. Gibbs, *Phys. Rev. B* **41**, 4368 (1990).

Chapter Six

Rare Gas Coadsorption with Alkali Metals or CO on Ag(111)

6.1. Introduction and Historical Summary

This chapter will report on experiments which investigated the nature of the interaction between adsorbed rare gases and alkali metals, mostly when they coexist in the same layer together. The experiments are more exploratory in nature than those reported in the previous chapter, and therefore the results will be more tentative, in some cases creating more questions than they answer. However some conclusions will be drawn.

Rare gases and alkali metals differ only in that the alkali metal has one additional valence electron. This minor difference however makes a great difference in the chemical behavior of the two. While alkali metals are among the most reactive elements, rare gases are chemically inert, having only closed electron shells. This striking difference makes it interesting to look at the interactions of the two species on a surface.

While alkali metal atoms bond chemically to the surface, rare gas atoms interact only weakly via Van-der Waals forces and physisorb to the surface. Rare gases typically grow in a layer-by-layer mode on metal surfaces, completing each layer before beginning the next. However recent studies have shown that this is not the case for some rare gases on alkali surfaces.^{1,2} In light of this unexpected behavior, it is important to understand the interactions between adsorbed rare gases and alkali metal atoms at the beginning stages of film growth – in the monolayer regime.

Rare gas atoms adsorbed on a metal surface typically polarize toward the substrate, creating a dipole in the same direction as adsorbed alkali metals only much weaker. One might therefore expect a repulsion between the two. However, if the rare gas is very polarizable, its proximity to the strong dipole of the alkali may cause it to polarize in the opposite direction resulting in a net attractive interaction. Since the larger alkalis polarize more strongly and the larger rare gases are more easily polarizable, one might expect an attraction for large atoms such as Cs and Xe and a repulsion for the smaller ones such as K and Ar.

Another way of understanding the polarization is the “optical switch” model of Flynn and Chen³. An adsorbed rare gas atom may have charge transferred either from the atom to the substrate or vice-versa. For example consider Xe, which has a $5p^6$ filled shell ground state. The orbitals of an adsorbed Xe atom may hybridize with the surface states of the substrate, and the ground state may take on some character of the first excited Xe state, $5p^5 6s$. If charge transfer occurs from the Xe to the substrate, it must

occur out of this $5p^56s$ excited state. If the $6s$ level of this state is above the Fermi level of the substrate, charge transfer or polarization will occur from the Xe atom to the substrate. If however conditions at the surface (for example the field resulting from an decreased work function) cause the Xe binding energies to shift down with respect to the substrate Fermi level, transfer of charge may occur from the substrate to the Xe $6s$ state, resulting in an adsorbate polarized away from the surface.

It has become an accepted premise that the electron binding energy of rare gas atoms on metal surfaces align to a certain level with respect to the vacuum level, regardless of the environment of the rare gas atom. This statement is supported by measurements of rare gas binding energy on a variety of clean metal surfaces, as well as surfaces with different work functions.^{4,5,6} Thus the local work function (or electrostatic potential) of the surface, which sets the Fermi level with respect to the vacuum level, will set the Xe energy levels with respect to the Fermi level as shown in Figure 6.1, determining the degree and sign of charge polarization of the Xe atom.

On a surface with strongly polarized adsorbates such as alkali metals the work function will vary with position, being lower close to the alkali atoms. Thus the substrate Fermi level seen by an adsorbed rare gas atom will vary depending on the rare gas atom's proximity to an alkali atom, as shown in Figure 6.2. A rare gas atom far from an alkali will be polarized as on the bare substrate (in the same direction as the alkali) leading to a long range dipole repulsion between the two. On the other hand a rare gas atom close to the alkali will see a much lower work function, causing it to polarize in the opposite direction and be attracted to the alkali. It may be expected that a rare gas atom in such a position would be bound more tightly to the surface than one on the bare substrate. Whether the rare gas can get close enough to the alkali to enter the attractive region may depend on the sizes of the rare gas and alkali atoms as well as the degree of polarization of the alkali atoms. If for some reason the attractive region is not accessible to the rare gas atoms, adsorbed rare gas will prefer to segregate into islands, due to their attractive interactions. If the alkali - rare gas attractive region is accessible and the attraction between the alkali and rare gas is stronger than the rare gas - rare gas interaction, the rare gas atoms will mix with the alkali lattice, perhaps forming a new ordered phase. The polarized rare gas atoms will also contribute to the average work function of the surface, so in the absence of other effects work function measurements may yield some information as to which mode is preferred.

To date, only a few studies have been done on rare gas / alkali metal coadsorption. Most of these have used a technique called PAX (Photoemission of Adsorbed Xenon) which uses Xe (or other rare gas atoms) as a probe to measure the local electronic environment where the rare gas is adsorbed. Since electron binding energies are usually measured with respect to the Fermi level, the measured binding energies will vary depending on the work function. Since photoelectron emission is sensitive to the local environment of the emitting atom, it can be used to probe the local work function (i.e., electrostatic

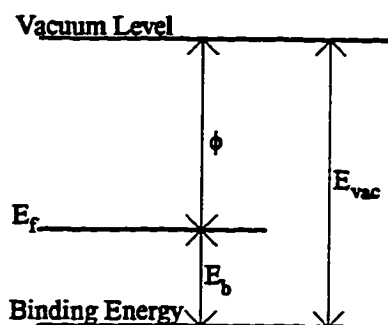


Figure 6.1. Energy level diagram showing the electron binding energy of an adsorbed rare gas atom. E_f is the substrate Fermi energy and ϕ is the work function of the surface. For physisorbed rare gases, the value of E_{vac} is an inherent property of the rare gas and is not dependent on the substrate. Thus since it is usually the quantity E_b which is measured experimentally, the binding energy will appear to change in response to changes in the work function.

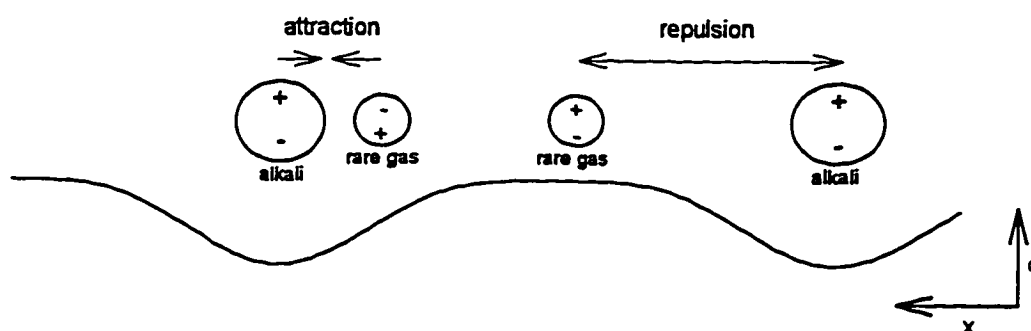


Figure 6.2. Diagram showing the expected work function variation across a surface when alkali atoms are adsorbed. A rare gas adsorbate normally forms a dipole in the same direction as the alkali and thus would experience a repulsion. If the rare gas comes close enough to the alkali however it may flip its polarization and experience an attraction.

potential) around the adsorbed rare gas atom. In the case of a rare gas atom adsorbed next to an alkali metal atom this technique can potentially measure the local work function close to the alkali, while conventional work function techniques such as Kelvin Probe measurements record an average value. This is of course dependent on the assumption that the rare gas will adsorb in the vicinity of the alkali. A repulsion between the two species may prevent this.

The systems which have been studied in this way are Ar or Xe + K / Ni(100),^{7,8} Xe + K / Ni(111),⁹ Xe + K / Ru(0001),¹⁰ and Xe + Cs / Ni(110).¹¹ In each case at least two distinct rare gas adsorption sites in the monolayer were measured, one unperturbed and the other with shifted energy levels due to the proximity of an alkali atom. In every case except on Ni(110), the rare gas dosed onto the surface adsorbed preferentially at the perturbed sites, next to the alkali adatoms.

The study on Ni(110) observed the opposite behavior, but this study was done before it was realized that the Ni(110) surface undergoes a significant reconstruction upon alkali adsorption,¹² which was not considered in the interpretation of the photoemission data. A large substrate reconstruction such as the alkali-induced missing-row structure found for Ni(110) will radically alter the lateral interadsorbate interactions, and therefore a reanalysis of these results is necessary before conclusions can be drawn from this system.

The alkali - rare gas coadsorption issue is also complicated by the presence of surface steps, as is inevitable in any experiment. The first rare gases or alkali metals to adsorb onto a clean substrate are assumed to preferentially bind to defect sites such as steps. Being more strongly bound, these atoms will probably be more strongly polarized, although the direction of polarization for an adsorbed atom at a step site may not be the same as that for an atom on a terrace. It is known that Xe atoms adsorbed on Pt(111) adsorb preferentially at the top step edge and are repelled at the bottom step edge.^{13,14} For alkali metal adsorption it is not known which step edge is preferred. Studying the behavior of small amounts of one species coadsorbed with the other, i.e. just enough to cover the step sites, may provide some valuable information about the nature of bonding at step sites.

Such an experiment has been done using CO and rare gases on Pt(111).^{15,16} Ar on clean Pt(111) forms an incommensurate lattice aligned with the substrate lattice. Normally one would expect that an incommensurate overlayer would be rotated at some preferred angle, so it was assumed that the Ar layer was aligned because it nucleates at the step edges, which on a flat surface are usually aligned in a high symmetry direction of the substrate. When the surface was precovered by a very small amount of CO however, the lattice rare gas lattice was rotated at 30° with respect to the substrate. It was concluded that the predosed CO blocks the step sites and causes the rare gas islands to nucleate on the terraces. However it was not understood why the rare gas overlayer aligned at 30° rather than at the predicted Novaco-

McTague angle. A similar behavior was seen for Kr, except that it was rotated at 30° on the clean surface but aligned with CO.

It is known that rare gases on the Ag(111) surface also align with the substrate,¹⁷ presumably because of alignment with the step edges. CO is known to physisorb on clean Ag surfaces,¹⁸ although in cases where there is a high defect density chemisorbed CO is also seen.¹⁹ Thus it seems likely that CO may chemisorb to defect sites such as steps or vacancies. Alkali atoms are also expected to bind strongly to step sites, so either CO or alkalis on Ag may provide a way to force the rare gas lattice to nucleate on the terraces.

6.2. Procedure

LEED studies were done of the coadsorption of three rare gases (Ar, Kr, and Xe) with K, Kr coadsorption with Cs, and Ar, Kr and Xe coadsorption with CO. By measuring the substrate, overlayer, and diffusely scattered beam intensities as a function of temperature, various quantities could be measured. Total overlayer coverage was measured by the decrease in the substrate beam intensity. In cases where more than one type of ordered overlayer were present, the changes in the amount of each type could be measured independently by monitoring the beam intensities of the different diffraction spots. In cases where the overlayer was disordered, amounts of disordered overlayer were obtained by measuring the diffusely scattered electron intensity. These quantities were measured for a surface on which some species had been deposited, while slowly increasing the temperature. In this way the rare gas desorption temperature was measured for different alkali or CO coverages at zero rare gas pressure. Since this is a non-equilibrium experiment, it is difficult to extract quantitative information about the system from the results. However, care was taken to always use approximately the same rate of temperature increase for each experiment (about 2 K / minute), so that results can be compared and some information obtained.

A smaller number of equilibrium experiments were done to supplement the non-equilibrium experiments. In these experiments a constant flux of rare gas atoms was provided by back-filling the UHV chamber with rare gas and monitoring the LEED pattern as a function of sample temperature. In this way rare gas adsorption isobars were measured for the clean surface and the surface precovered with various amounts of alkali. These experiments were more difficult to do because of the high rare gas pressures (10^{-7} to 10^{-3} mbar) required for equilibrium in a reasonable amount of time. With such high pressure being used in the chamber, contaminants were inevitably introduced which greatly shortened the time available for completing an experiment. Even though the sample was held at an elevated temperature to study the adsorption of a single monolayer, the cold finger remained at a low temperature

causing bulk rare gas to grow on the cold surfaces. The slow sublimation of this solid rare gas then prevented the chamber from being quickly pumped down to a pressure lower than approximately 10^{-7} mbar after introducing rare gas at a pressure higher than that. For these reasons the equilibrium experiments had to be done more quickly and fewer data points could be taken per experiment than with the non-equilibrium experiments.

In addition to amounts of overlayer, overlayer lattice parameters for ordered phases were measured from the LEED pattern and thermal expansion coefficients were calculated. Expansion coefficients measured at zero pressure correspond to the unconstrained case discussed in Webb^{20,21}, while measurements with a finite pressure of rare gas represents the case of a constrained monolayer.

6.3. Rare Gases on Clean Ag(111)

Most of the results for rare gases adsorbed on clean Ag(111) are consistent with previous works.^{20,21} Xe, Kr, and Ar form incommensurate triangular lattices aligned in the substrate (10) direction. The lattice parameter in each case is slightly higher than that of the bulk rare gas. The lattice parameters and thermal expansion coefficients were found to agree with the previous work on this system. Heats of adsorption were also measured by doing isobar experiments to measure (P,T) points for monolayer and second-layer condensation and plotting them on a $\log P$ vs. $1/T$ graph, as shown in Figure 6.3. The heat of adsorption for a layer is then given by the slope of the line:²¹

$$q = - \frac{\partial(\ln P)}{\partial\left(\frac{1}{T}\right)} \quad (6.1)$$

The heats of adsorption for the first and second layers are shown in Table 6.1, compared with the results from references 20 and 21. The results show a discrepancy of 6 - 15% between the previous results cited and the results presented here. The reason for this discrepancy may lie in the temperature calibration. An error in T of δT will result in an error δq of

$$\frac{\delta q}{q} = - \frac{2\delta T}{T} \quad (6.2)$$

An error of three degrees at the Ar condensation temperature would thus result in a 15% error in q .

It is not well understood why the rare gas lattice on the clean surface is aligned with the substrate rather than rotated. According to the Novaco-McTague prediction, Ar, Kr, or Xe should be rotated by approximately 18° , 22° , and 25° respectively. It has been suggested, in light of experiments on Pt(111) mentioned above,^{15,16} that rare gases on Ag(111) nucleate at step edges causing the lattice to be aligned rather than rotated. The diffraction spots for rare gases on Ag(111) are much broader azimuthally than

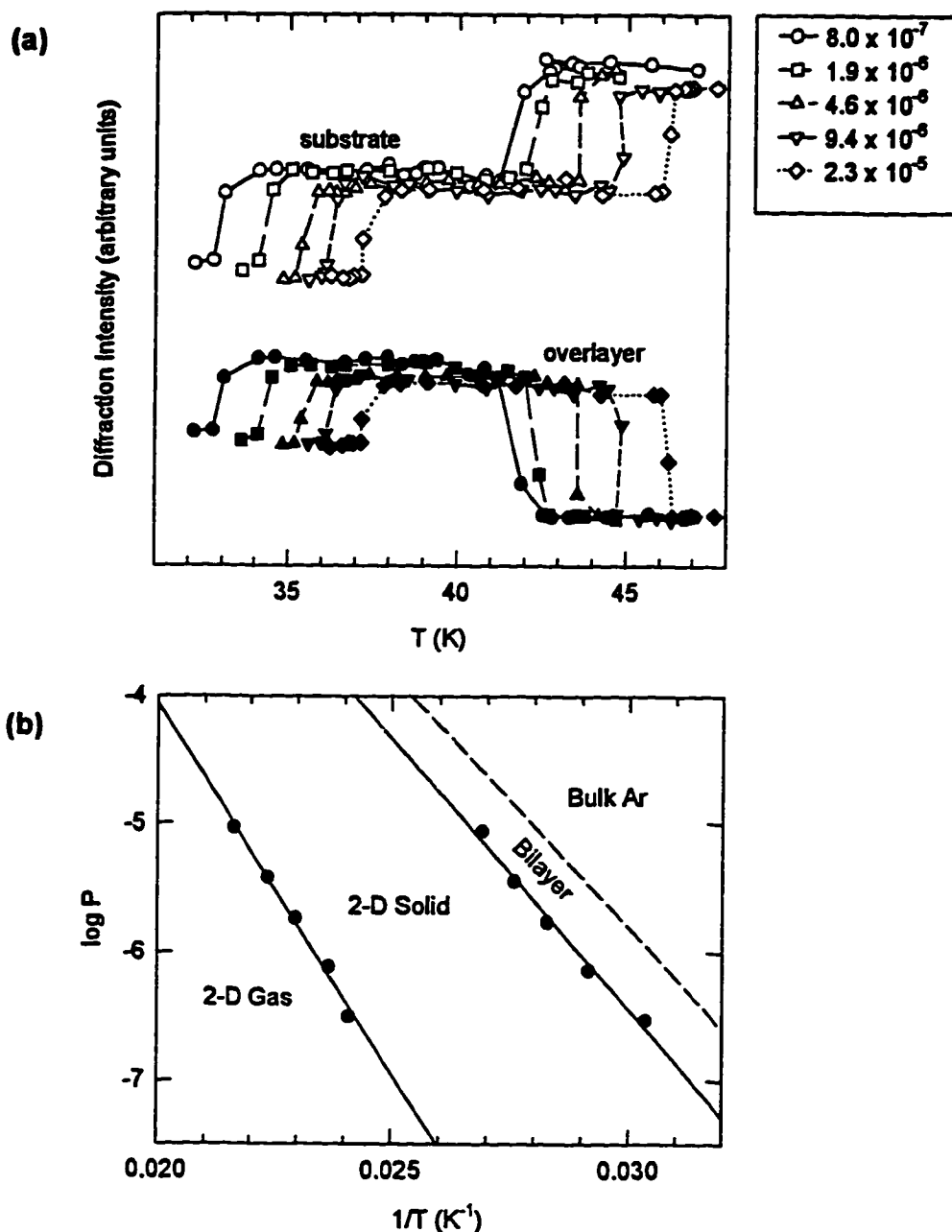


Figure 6.3. Isobars and phase diagrams for Ar / Ag(111). The isobars (a) are taken by monitoring the diffraction pattern while lowering the sample temperature with a fixed flux of gas incident on the sample. On the isobar graph empty data points represent the substrate spot intensity and filled points represent the Ar overlayer intensity. The points in the phase diagram (b) were obtained from the positions of the steps seen in the isobar curves. The slopes of the lines in the phase diagram are equal to the negative of the latent heat of adsorption. Similar data was taken for Kr and Xe, and the values of the heats of adsorption are shown in Table 6.1.

Table 6.1. Heats of adsorption for rare gases on Ag(111), measured using LEED isobar experiments. The numbers in parentheses are the results from references 20 and 21.

Gas	Monolayer (meV)	Bilayer (meV)
Ar	115 ± 7 (99 ± 7)	84 ± 5 (89 ± 4)
Kr	160 ± 3 (151 ± 5)	97 ± 6 (118 ± 4)
Xe	240 ± 5 (225 ± 5)	

radially, suggesting that the lattice is not strongly locked in at the 0° alignment. If the step-site nucleation picture is correct, then a likely explanation for this is the meandering of steps. While step edges are more likely to run in substrate high-symmetry directions, there will be some step edges which deviate.

6.4. Rare Gases Coadsorbed with Potassium on Ag(111)

6.4.1. Rare Gas Rotation Angle

When rare gases are adsorbed on a surface precovered by a small amount of K (0.02 ML), the rare gas lattice consists of two phases coexisting: a rotated and an aligned phase. For slightly higher precoverage of K the diffraction spots from the rotated phase are stronger and those from the aligned phase are weaker, with the rare gas lattice becoming completely rotated for K precoverages higher than 0.04 ML. LEED patterns for Xe on the clean surface and the K precovered surface are shown in Figure 6.4. The rare gas rotation angles are shown in Figure 6.5 as a function of rare gas misfit, along with Novaco-McTague and Bohr-Grey predictions. For each rare gas a range of rotation angles can be obtained by varying the temperature (which changes the misfit via thermal expansion), and in some cases by varying the alkali metal coverage. The data for lower alkali pre-coverages (<0.14 ML) are represented by the shaded data points and higher coverages (Kr only) by empty points.

It is not certain why the rare gas lattice becomes rotated rather than aligned with the substrate when some alkali is present. One possibility is that the K atoms which go down first occupy all the step sites and block the rare gas islands from nucleating there. This would be consistent with the repulsive interaction between K and rare gas atoms, which will be presented in the next section. In that case the

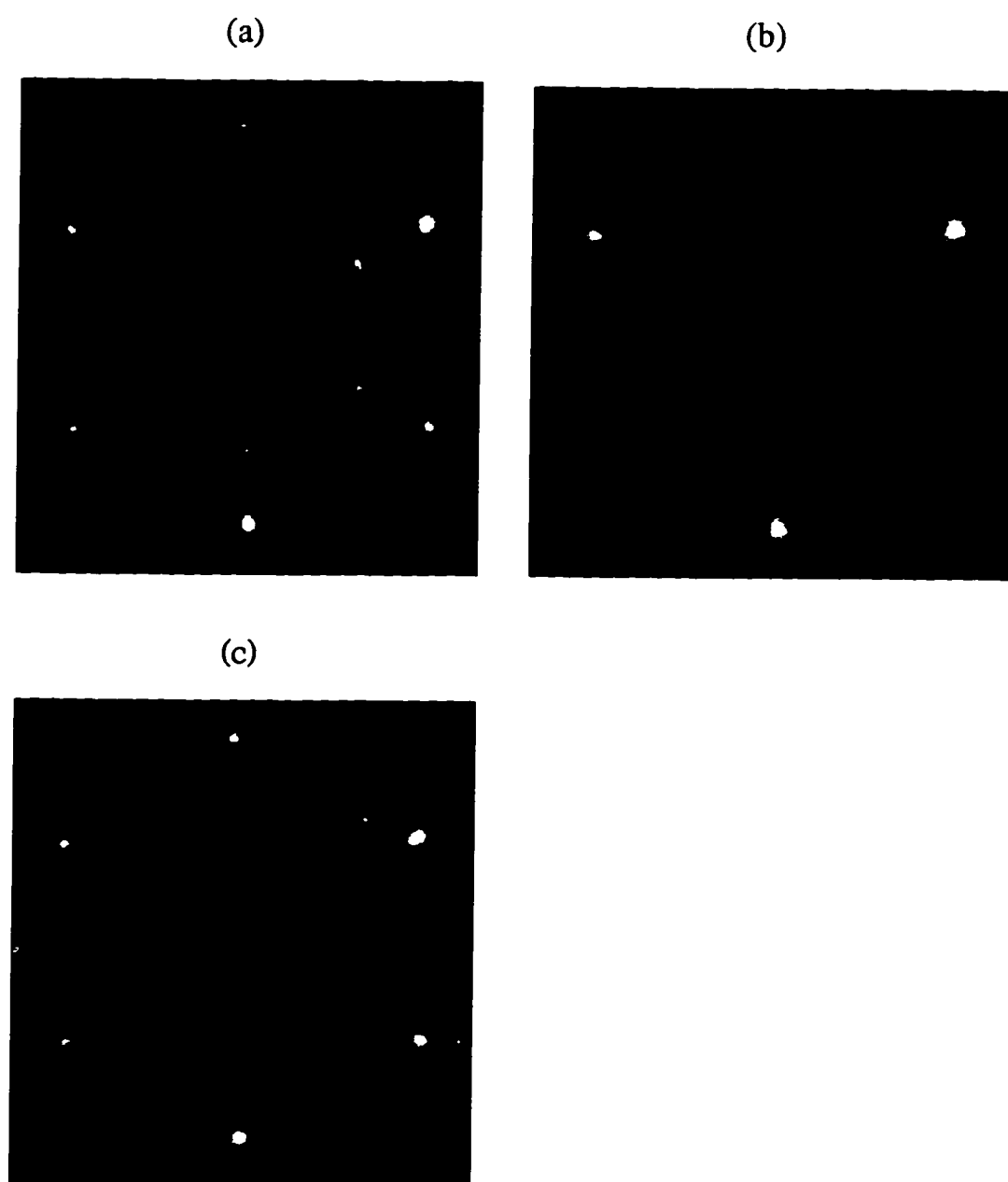


Figure 6.4. LEED patterns for Xe on Ag(111), precovered with a small amount of K. (a) No K present, (b) 0.02 ML of K, and (c) 0.04 ML of K.

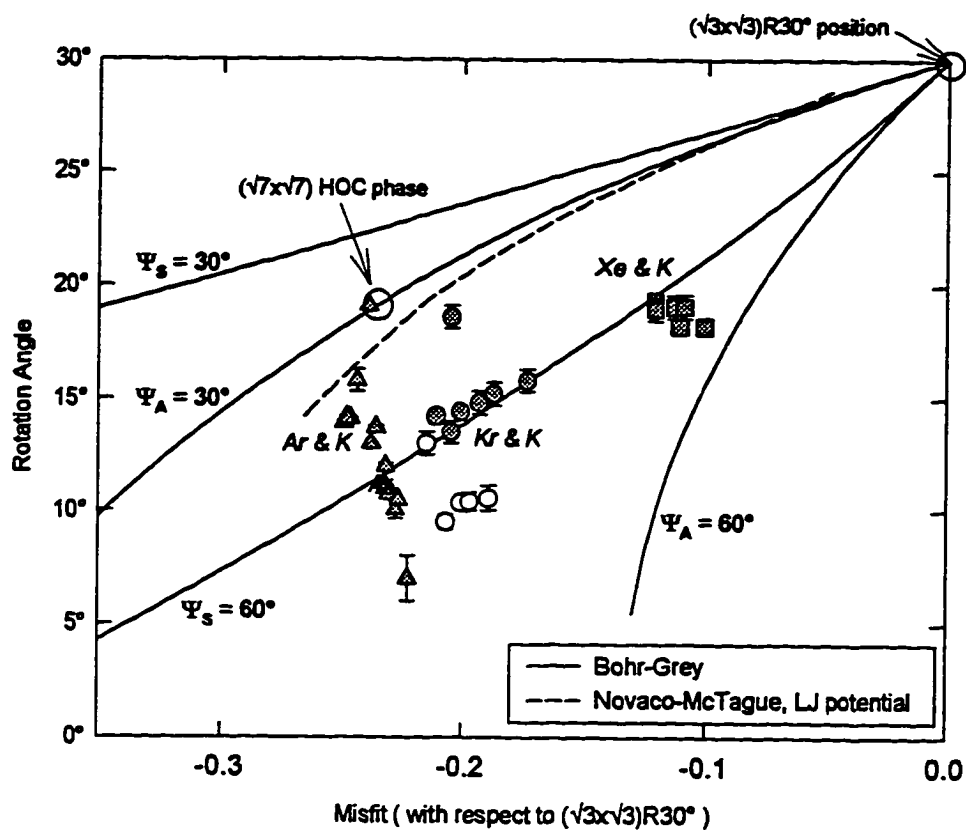


Figure 6.5. Rare gas rotation angle as a function of misfit with respect to the $(\sqrt{3} \times \sqrt{3})R30^\circ$ phase, for a rare gas monolayer on potassium-precovered Ag(111). Rotation angle is with respect to the substrate primary symmetry direction, not the 30° of the $\sqrt{3}$ phase. Data are compared to Bohr-Grey and Novaco McTague prediction using a Lennard-Jones potential. The Ar data are denoted by triangles, Kr by circles, and Xe by squares. Shaded points represent data taken at K precoverages below 0.14 ML, and empty points (Kr only) above 0.14.

rare gas islands would be forced to nucleate on the terraces where one would expect them to be rotated at a non-symmetry angle with respect to the substrate. However, the amount of K which is needed to completely change the alignment is significantly greater than the amount that should be needed to block the steps. Since the average terrace width of the sample has been determined to be at least 150 Å, and assuming that one row of K atoms adsorbed at every other Ag atom along a step are needed to block it, the coverage needed should be less than 0.01 ML. Thus it would be necessary to assume either that more than one row of alkali atoms were needed to block a step, or that only a fraction of the first alkali atoms to adsorb actually go to step sites.

Another possibility which could explain the rotational behavior is the magnitude of the Ag(111) surface corrugation potential. The presence of a finite rotation angle is dependent on having a non-zero corrugation amplitude. In the absence of a significant corrugation, the overlayer may be more likely to align with the step edges. It is known that rare gases on Ag(111) experience very little if any lateral potential corrugation.²² Using He scattering, it has been shown that the surface potential (as experienced by a He atom) of Al(111) becomes much more corrugated when a small amount of alkali is added.²³ This may also be the case for Ag(111), and could explain the change from non-rotated to rotated when a small amount of K is added.

It is evident that the data do not follow the Novaco-McTague prediction, but in general are closer to the Bohr-Grey $\Psi_s = 60^\circ$ trajectory. One branch of the Kr data in particular follow that trajectory rather closely. The fact that the data do not follow the Novaco-McTague prediction may be an indication that finite size effects are important, or that substrate effects are important. It has been shown that in either of these cases where the long-range elastic distortions of the overlayer play a smaller role, the behavior is expected to follow one of the substrate-alignment Bohr-Grey lines.²⁴ Finite size restrictions may be caused either by the locking of the rare gas lattice at the orientation angle at which it nucleated by lack of thermal mobility, or it may be constrained or fragmented into small islands by the presence of the widely-spaced potassium atoms.

For Ar, the rare gas in which the most deviation from either the Bohr-Grey or Novaco-McTague predictions is seen, the behavior may be influenced by the $(\sqrt{7} \times \sqrt{7})R19.1^\circ$ higher-order-commensurate phase having four atoms per unit cell. The position of this phase is labeled in Figure 6.4. For certain alkali pre-coverages this higher order commensurate phase was actually seen. This HOC structure was also seen for Ar coadsorption with CO, and will be discussed later in this chapter.

6.4.1. Segregation of Rare Gas and Potassium

When rare gas is dosed on a surface with a higher K precoverage, rare gas goes into the layer, compressing the K lattice. If the K precoverage is in the range of the epitaxial rotation described in Chapter Five, the diffraction spots due to the K overlayer move continuously in the same manner they would if the K overlayer density was increased – the rotation angle changes while the lattice parameter decreases. This behavior is shown in Figures 6.6 and 6.7. Figure 6.6 shows diffraction patterns obtained as a function of Kr dosage for a K precoverage of 0.13, which is slightly less dense than the commensurate $(\sqrt{7}\times\sqrt{7})R19.1^\circ$. Panel (a) shows the LEED pattern for the incommensurate overlayer with no Kr present. Panel (b) shows the LEED pattern after a small amount of adsorbed Kr has compressed the overlayer into the commensurate $(\sqrt{7}\times\sqrt{7})R19.1^\circ$ structure. The increased sharpness of the alkali spots at this coverage is due to the overlayer being commensurate. In panel (d), the spots due to the alkali again indicate an incommensurate overlayer, which is now denser than the $(\sqrt{7}\times\sqrt{7})R19.1^\circ$ phase. Panel (e) shows the LEED pattern after the K has been compressed into the commensurate $p(2\times 2)$ structure. The intensities of these $p(2\times 2)$ spots as a function of incident energy are shown in Figure 6.8, compared with spectra taken from the K $p(2\times 2)$ phase reported in Chapter Five. Figure 6.7 shows the measured rotation angle of the lattice as a function of misfit as the lattice is compressed by rare gas (filled circles), compared with the behavior seen for K alone on Ag(111) (solid line). The density of the overlayer represented by the alkali spots saturates at a coverage of 0.25 to 0.28, significantly lower than the saturation coverage of 0.40 for a pure K layer on Ag(111).

In addition to the compression and rotation of the alkali spots shown in Figure 6.6, weak additional spots appear due to a rotated overlayer of smaller lattice parameter than the K lattice. These spots can be seen in panels (d) and (e) of Figure 6.6. The spacing of these spots indicates a lattice parameter very similar to that observed for Kr on the clean Ag(111) surface (approximately 4.05 Å), and so these spots will be called “rare gas spots” from here on.

With additional dosing of Kr, the Kr spots decrease in intensity while the alkali spots remain constant, indicating that a second layer of Kr forms on the first layer of Kr but not on the alkali layer. In experiments where the K precoverage was higher, diffraction spots due to rare gas were not observed initially, but the diffusely scattered intensity increased. If the layer was then annealed, in many cases the rare gas spots appeared or increased in intensity, suggesting that the higher coverage of alkali reduces the mobility of the rare gas on the surface. Some additional experiments were carried out using Xe or Ar in place of Kr, with similar results. From here on, the results reported for Kr also apply to Xe or Ar coadsorption cases unless otherwise noted.

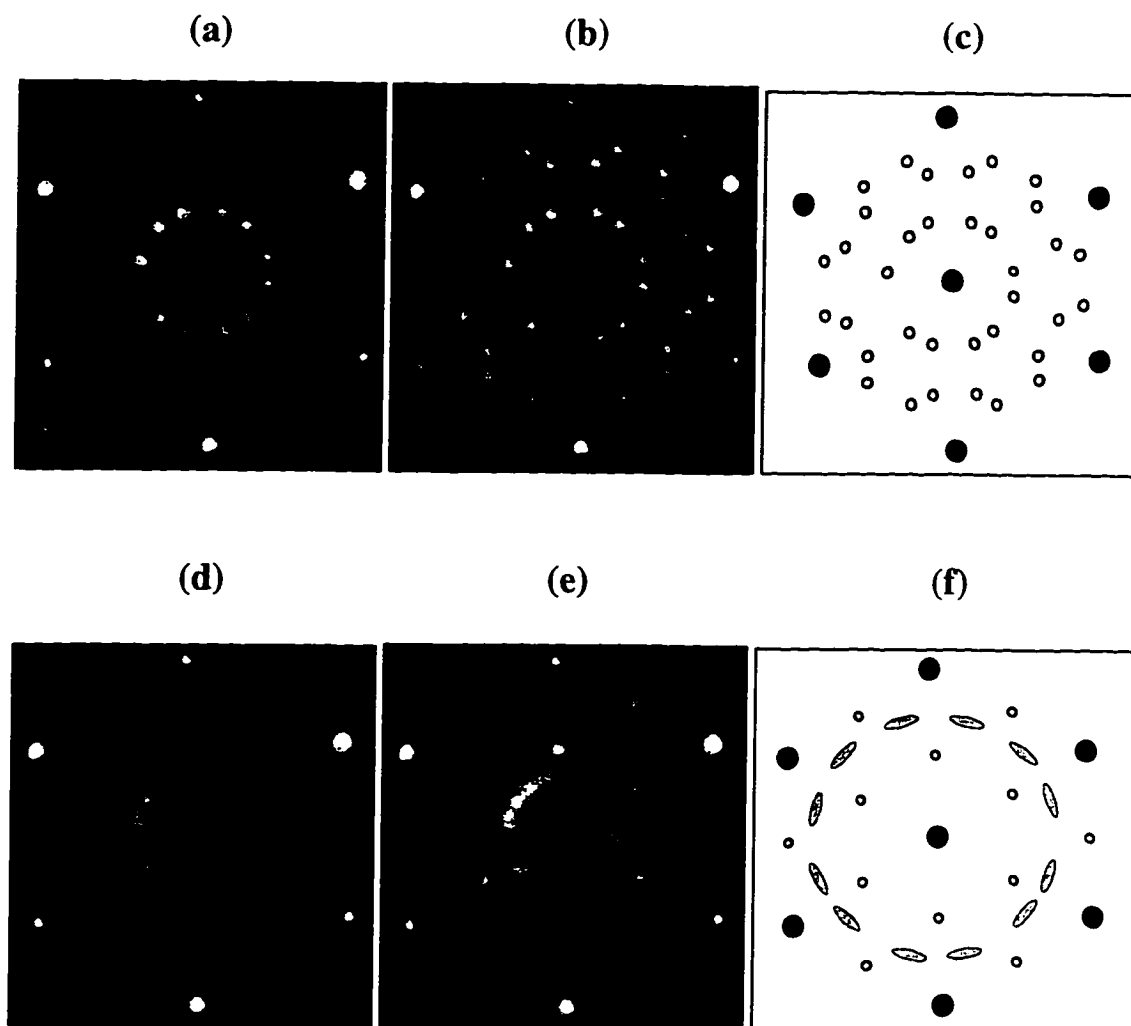


Figure 6.6. LEED patterns for Kr adsorption on Ag(111) predosed with 0.13 ML potassium. (a) Incommensurate K/Ag(111) phase. (b) Diffraction pattern after dosing 2.0 L of Kr. The spots are sharper because the alkali metal is in a commensurate $(\sqrt{7} \times \sqrt{7})R19.1^\circ$ phase. (c) Schematic of the diffraction pattern shown in (b). (d) Diffraction pattern after dosing 4.0 L of Kr, and (e) after dosing 5.2 L Kr. Commensurate $p(2 \times 2)$ alkali spots coexist with a ring of spots which correspond to an expected Kr-Kr spacing. (f) Schematic of the diffraction pattern shown in (e). Small shaded circles represent the commensurate $p(2 \times 2)$ spots, and shaded ellipses represent the new Kr-Kr diffraction spots. All LEED patterns were taken using an incident beam energy of 125 eV.

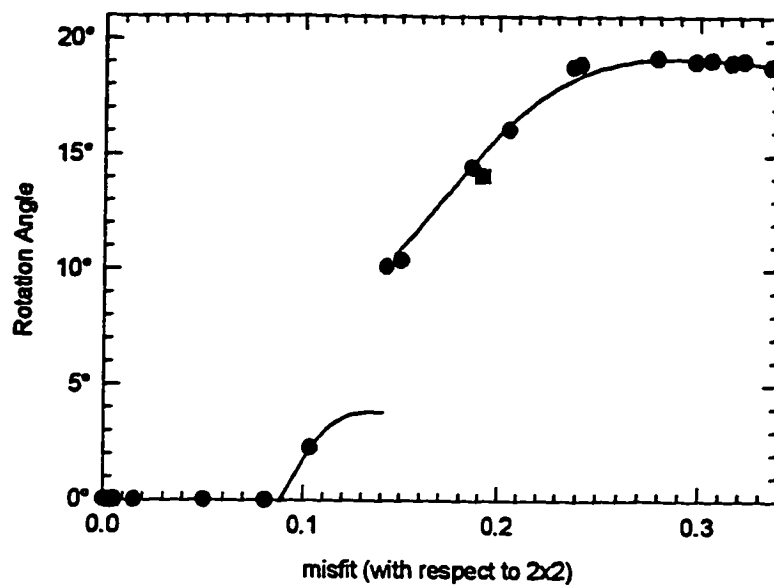


Figure 6.7. Rotation angle of a potassium lattice coadsorbed with Kr, compared with the behavior of the rotated K / Ag(111) phase. The coadsorbed phase is represented by the data points, and the K / Ag(111) phase is represented by the curve. Misfit is defined as $(d-2d_s)/2d_s$, where d is the overlayer spacing and d_s is the substrate spacing. The discontinuity at a misfit of 0.15 is caused by a K higher order commensurate structure discussed in Chapter Five.

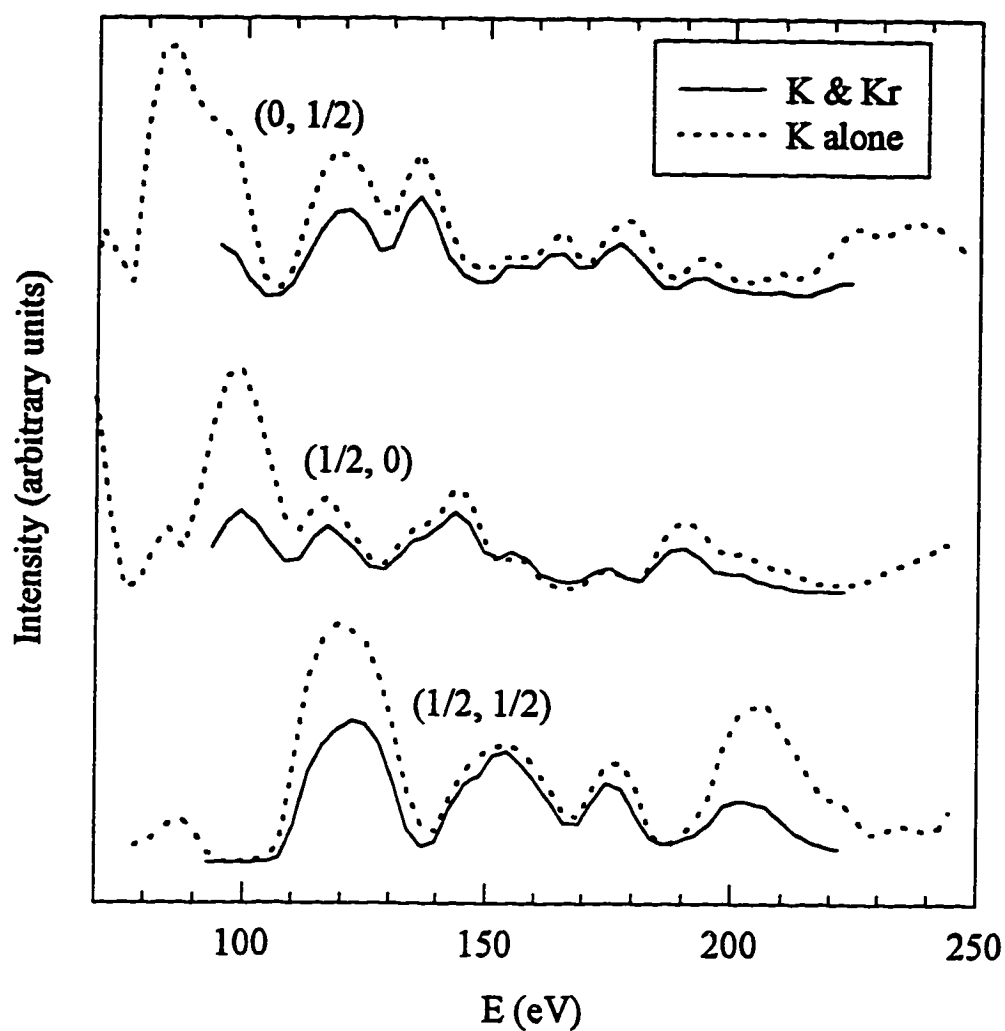


Figure 6.8. LEED intensities for the $p(2 \times 2)$ phase of K coadsorbed with Kr, compared with the $p(2 \times 2)$ phase of K alone on Ag(111). The Pendry R factor between the two sets of data is 0.09. The similarity between the two spectra indicate that the local environment of the K atom is the probably the same for the two phases.

The data described above suggests phase segregation of the potassium and rare gas on the surface. The fact that the rotation angle of the alkali lattice when compressed by Kr agrees well with the rotation angle of K alone indicates that these diffraction spots come from regions of fairly pure K concentration. The LEED I(E) spectra from the $p(2 \times 2)$ phase coexisting with rare gas are essentially identical to those of the pure K $p(2 \times 2)$ phase, indicating that the local environment of the K adatom is the same in both cases. Furthermore, since K has a much larger radius than Kr, the fact that the additional spots are consistent with a Kr-Kr spacing indicates that they are probably due to regions of pure or nearly-pure Kr.

The notion of phase segregation, which probably implies a repulsive interaction between the alkali and rare gas atoms, is further supported by rare gas desorption experiments. Figures 6.9 and 6.10 shows desorption curves for Kr or Xe coadsorbed with various amounts of K. These data are obtained by measuring the intensity of a substrate diffraction spot while slowly increasing the temperature at zero rare gas pressure after dosing more than a monolayer of rare gas. The data show two steps: the first caused by desorption of the rare gas from the second layer and the second by monolayer desorption. Desorption of first layer rare gas from the clean surface occurs abruptly over a range of about two K. When the Xe is coadsorbed with potassium however the first layer desorption occurs over a slightly larger temperature range. In addition, the first-layer desorption temperature is depressed by up to 10 K for Kr and 20 K for Xe.

A few equilibrium adsorption isobars, done by monitoring the LEED pattern while slowly decreasing the temperature at a finite rare gas pressure, were also performed. A similar depression of the rare gas adsorption temperature was measured this way. As with the zero-pressure non-equilibrium experiments, two steps corresponding to second and first layer rare gas are observed. This is shown in Figure 6.11 for Kr coadsorption with K at coverages of 0.14 and 0.19.

6.4.2. Alkali Spreading Pressure Determination

The results reported in the previous section can be used to measure the spreading pressure of the alkali layer, a quantity which is difficult to measure using other means. This can in fact be done in two independent ways, one using the results of the non-equilibrium desorption experiments and the other using the equilibrium desorption isobars. These spreading pressure results will then be integrated to obtain the free energy of the lattice, and this value compared with the dipole energy obtained from work function experiments.

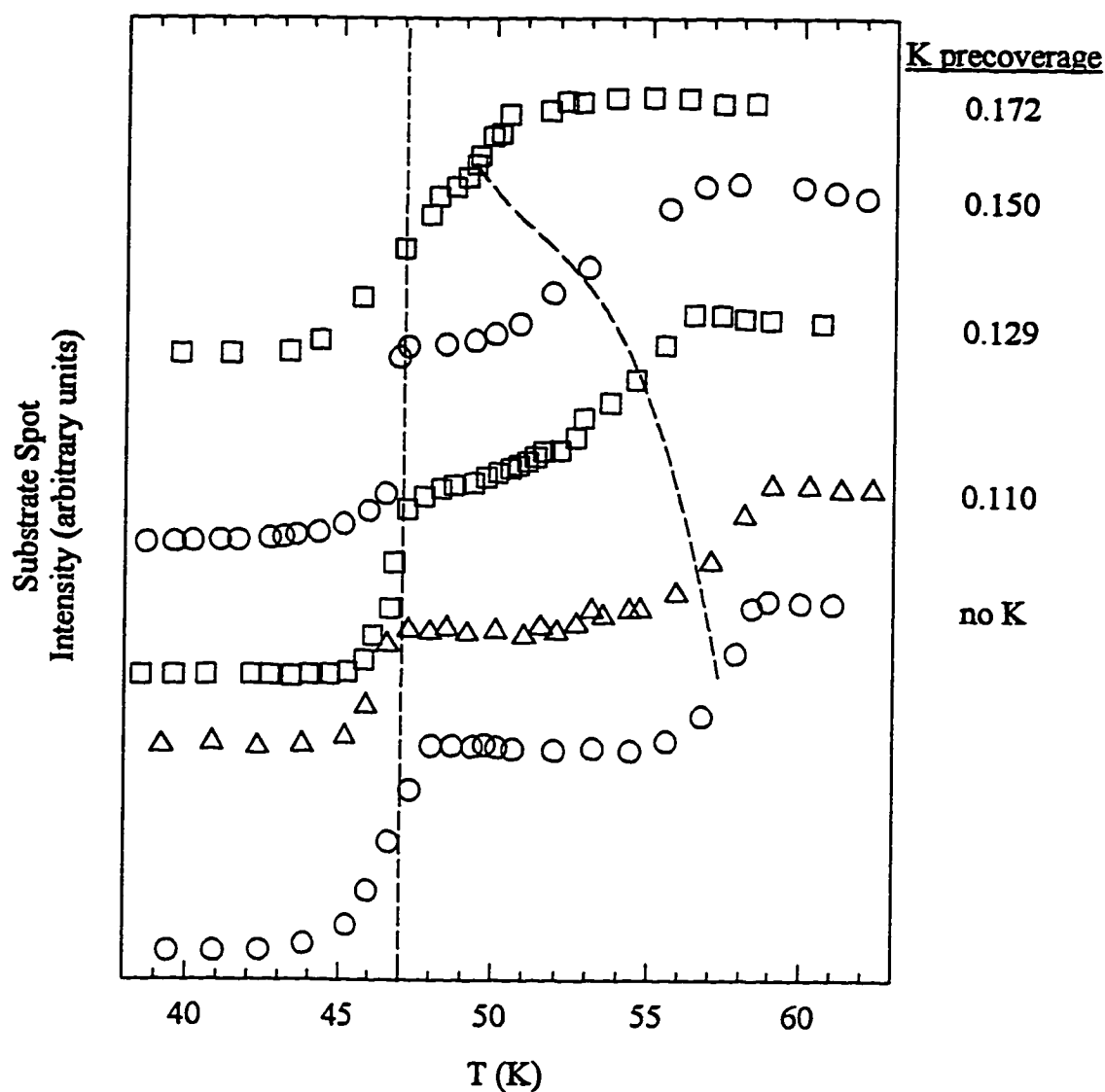


Figure 6.9. Zero-pressure desorption curves for Kr coadsorption with various precoverages of K on Ag(111). The data are taken by measuring the intensity of a substrate diffraction spot while increasing the sample temperature at zero Kr pressure. The vertical dashed line indicates second layer desorption of Kr. The curve is a guide to the eye indicating first-layer Kr desorption. The desorption curves are offset for clarity.

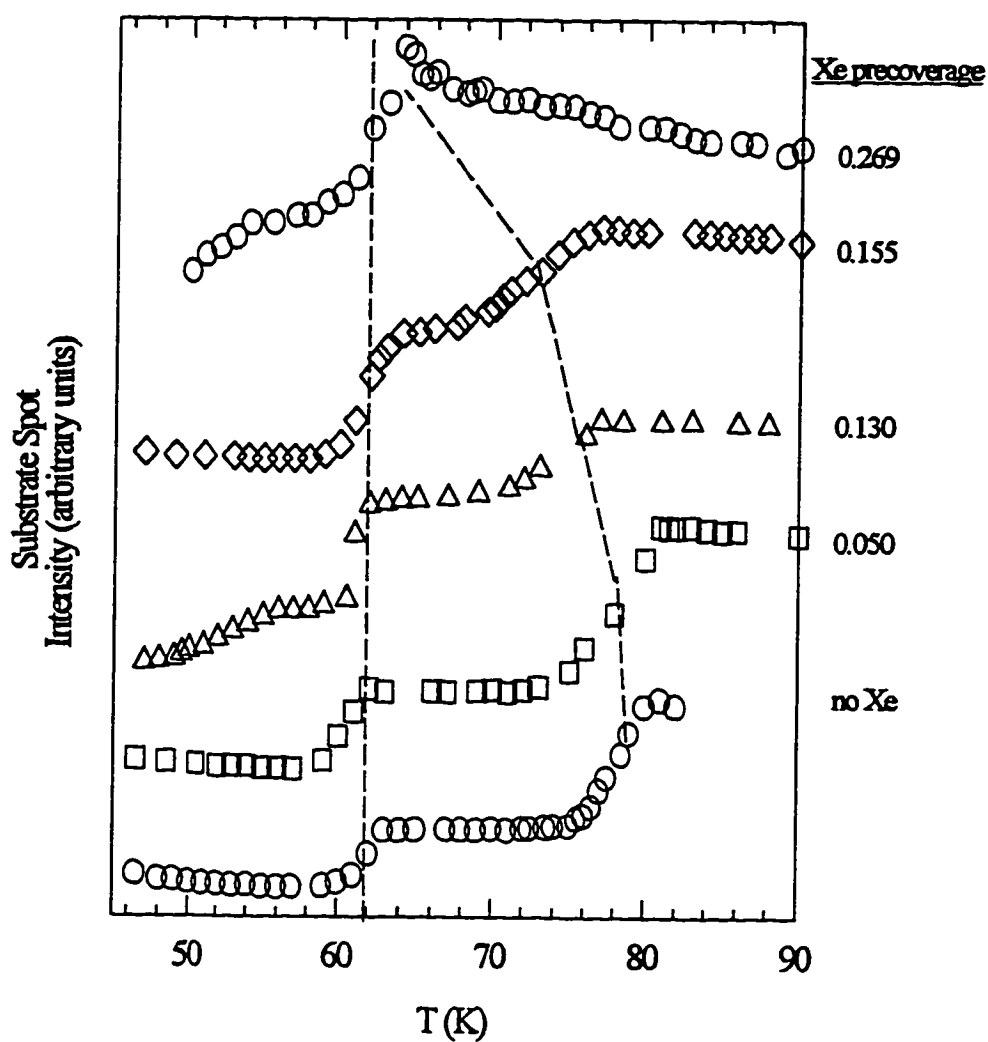


Figure 6.10. Zero-pressure desorption curves for Xe coadsorption with various precoverages of K on Ag(111). The data are taken by measuring the intensity of a substrate diffraction spot while increasing the sample temperature at zero Xe pressure. The vertical dashed line indicates second layer desorption of Xe. The curve is a guide to the eye indicating first-layer Xe desorption. The desorption curves are offset for clarity.

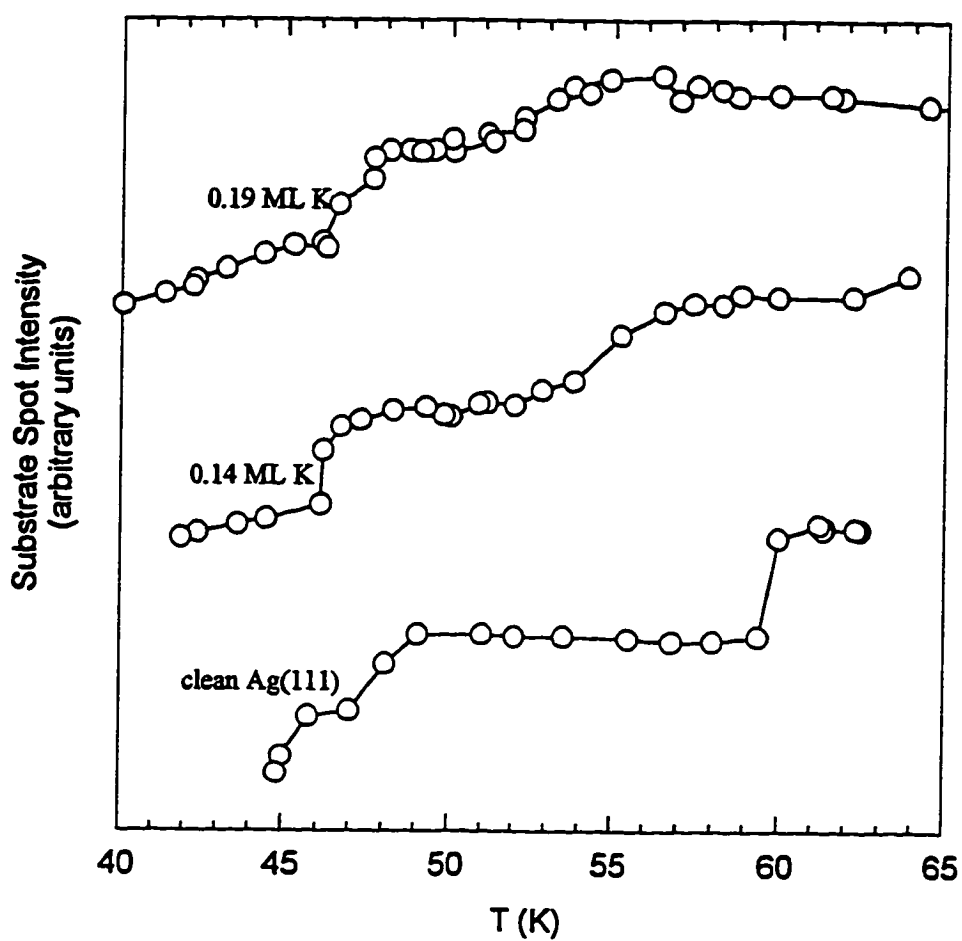


Figure 6.11. Isobars at 1.9×10^{-6} mbar for Kr coadsorption with K on Ag(111). The data are taken by monitoring the diffraction intensity while slowly lowering the temperature.

6.4.2.1. Non-equilibrium Method

The desorption rate of a non-interacting species from a homogenous surface is equal to²⁵

$$\frac{dN}{dt} = CNe^{-E_d/kT} \quad (6.3)$$

where C is a constant and E_d is the desorption energy, the energy cost associated with moving an adsorbate from the surface to a point infinitely far from the surface. For the non-homogenous case of patches of K coexisting with patches rare gas, E_d should be replaced by the enthalpy of adsorption, which is the total work necessary to move a rare gas atom away from the surface. We assume a repulsive interaction and segregation of the alkali and rare gas atoms on the surface. For the coadsorption case some additional energy is gained as the alkali lattice expands to fill the vacancy. The amount of this energy gain will be ϕa , where ϕ is the two-dimensional spreading pressure of the alkali lattice and a is the area per adatom for the rare gas lattice. In addition, if the desorbing rare gas atom is close to the edge of a patch of rare gas atoms, there will be a term V , the interaction energy with the alkali adatoms. We make the approximation that V will only be significant for rare gas atoms at the perimeter of the patch. For a repulsive interaction, desorbing rare gas atoms will always come from the edges of the rare gas patches, and the alkali lattice will expand causing new rare gas atoms to come into proximity with the alkalis. Thus the change in energy from the term V will be proportional to the change in the perimeter of the rare gas island as rare gas atoms desorb. Assuming circular islands, this quantity is

$$\left(\frac{\pi a}{n}\right)^{\frac{1}{2}} V \quad (6.4)$$

where n is the number of atoms in the patch. (V will of course change slightly as the patch becomes very small and a rare gas atom on the edge is exposed to more alkali atoms. V may also change with alkali coverage as the strength of the alkali dipole changes.) The change in energy due to the desorption of a rare gas atom (i.e. the quantity with which to replace E_d in Equation 6.3) is therefore

$$E_d - \phi a - \left(\frac{\pi a}{n}\right)^{\frac{1}{2}} V \quad (6.5)$$

This will have the effect of depressing the temperature at which the desorption rate becomes significant, causing the rare gas to desorb at a lower temperature. Since most of the desorption occurs when the patches are large, the last term will not be important. Let T be the temperature at which the rare gas desorbs off the clean surface, i.e. the temperature at which the desorption rate becomes significant with respect to the time scale of the experiment. If T' is the temperature where desorption of rare gas coadsorbed with alkali metal begins (defined as the temperature at which desorption occurs at the same rate as it occurs for temperature T on the clean surface), then the alkali spreading pressure is given by

$$\phi = \frac{E_d}{a} \left(1 - \frac{T^*}{T} \right) \quad (6.6)$$

As the patches of rare gas desorb and the coexisting alkali metal lattice expands, the spreading pressure will decrease due to the larger spacing between the alkali dipoles. This will have the effect of increasing the desorption temperature of the remaining rare gas, so that the desorption will occur over a wider temperature range than for the clean surface. There will also be a competing effect as the island size gets smaller, causing the alkali-rare gas interaction term in Equation 6.5 to get larger. This would work in the opposite direction as the decreasing spreading pressure, causing a narrowing of the width over which desorption occurs. A broadening of the temperature range over which desorption occurs is however measured (shown in Figures 6.9 and 6.10), indicating that the effect of the interaction term is smaller than the effect of the changing alkali pressure as the layer expands.

Using Equation 6.6, the spreading pressure as a function of alkali coverage is calculated from the desorption temperature data and is shown as circles in Figure 6.12b. (The triangles represent spreading pressure measurements using equilibrium experiments, which will be discussed in the next section.) The desorption temperatures used here are those at which all of the rare gas has desorbed from the surface for a particular alkali coverage. At any particular temperature the spreading pressure of the K overlayer should of course not depend on which gas is coadsorbed with it. However the spreading pressure should increase with temperature, so the different temperatures used in the desorption experiments are probably the cause of the different spreading pressures measured with Kr or with Xe coadsorption.

It would be useful to be able to compare the alkali spreading pressures determined above with those measured by some other method. From the work function change due to the alkali on the clean Ag(111) surface, the dipole per alkali adatom may be calculated using Equation 2.13. The internal energy of a lattice of dipoles, at $T = 0$, may be approximated by summing the pair potentials between the dipoles:

$$E = \frac{1}{2} \sum_{i \neq j}^N \frac{p^2}{|r_j - r_i|^3}$$

$$\frac{E}{N} = \frac{p^2}{s^3} \beta \quad \text{where } \beta = 5.513 \text{ (for a hexagonal lattice)} \quad (6.7)$$

where p is the dipole moment per alkali adatom and s is the spacing of the alkali lattice. Using Equations 2.13 and 6.7 with the work function for K on Ag(111) shown in Figure 5.1, the internal energy of the alkali lattice as a function of density at $T = 0$ is calculated and shown in Figure 6.12d. Since for most of these experiments the temperature is low compared to the melting temperature of the alkali lattice, this should provide a good approximation to the total internal energy for the alkali lattice in this experiment.

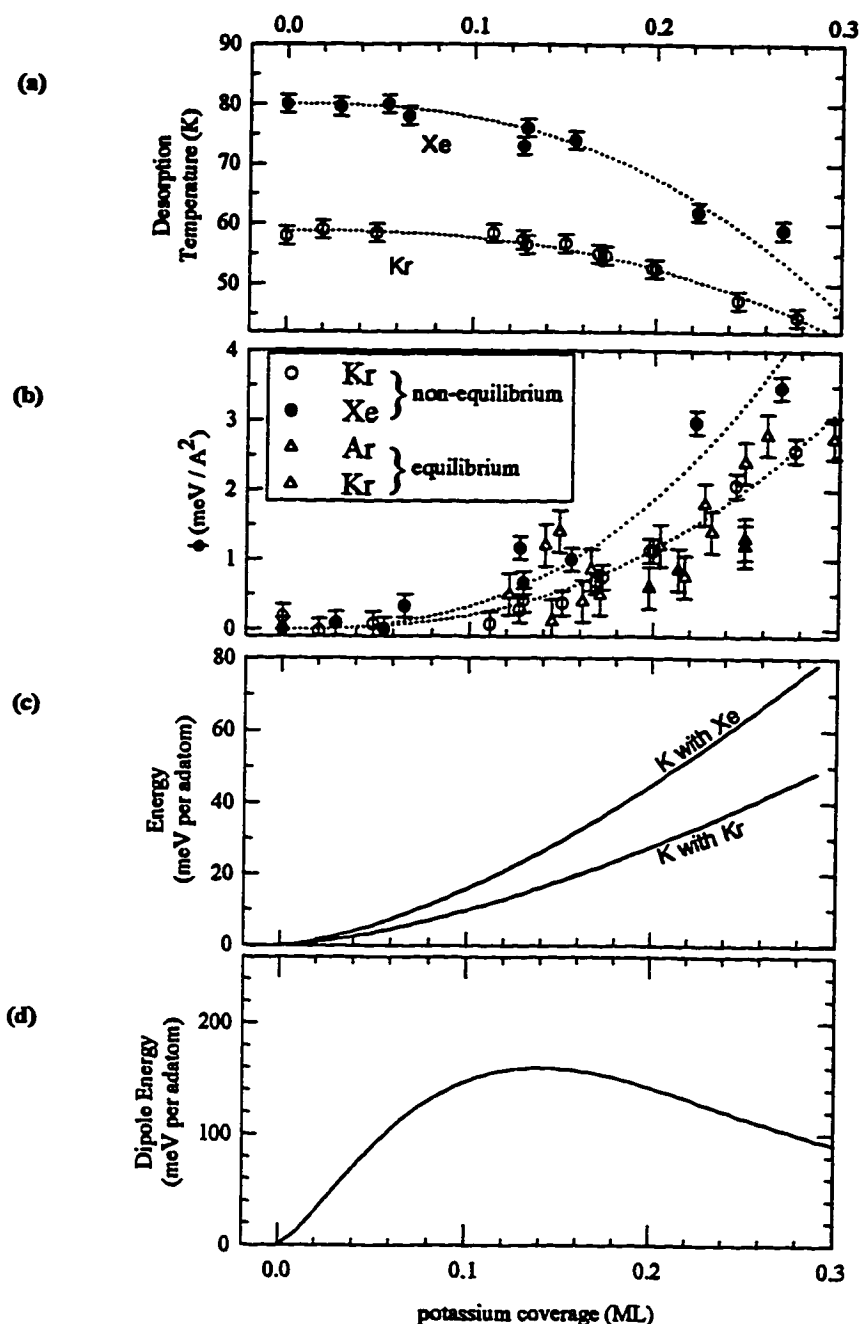


Figure 6.12. Potassium spreading pressure determination using coadsorbed rare gas. (a) Rare gas desorption temperature as a function of potassium precoverage. The data points represent the temperature at which all rare gas has desorbed from the surface and the curves are a guide to the eye. (b) The spreading pressure of the potassium lattice calculated from the data points in (a) using Equation 6.3. Points denoted by triangles were obtained from Ar and Kr equilibrium experiments described in the text.

The free energy of the alkali lattice may be calculated from the spreading pressure shown in Figure 6.12b by integrating the spreading pressure over coverage using the relation

$$\phi = - \left. \frac{\partial F}{\partial A} \right|_{T \text{ const.}} \quad (6.8)$$

where F is the Helmholtz free energy of the alkali lattice and A is the area per adatom for the alkali lattice. Integrating this equation over coverage to obtain F yields

$$F = A_s \int_0^\theta \phi \frac{d\theta}{\theta^2} \quad (6.9)$$

Figure 6.12c shows the value of F , calculated by analytically integrating a fit to the spreading pressure data for the experiment with Xe (upper curve) and with Kr (lower curve). Again, the fact that the F is higher for coadsorption with Xe can be explained by the higher temperatures used in the Xe experiment. G is related to the internal energy of the alkali lattice using

$$F = E - TS \quad (6.10)$$

Unfortunately there is not direct way of determining the entropy of the lattice, S . At low alkali coverages where the dipole energy is expected to be the main contribution, the difference between the dipole energy (shown in Figure 6.12d) and the energy shown in 6.12c is equal to the TS term in Equation 6.10. At alkali coverages higher than about 0.1 there will be additional energy terms which will contribute to the difference: a depolarization energy of the alkali dipoles and an energy having to do with the metallic bonding between alkali atoms which develops at high coverages.

It should be emphasized that form of the curve shown in Figure 6.12 panel (c), which was calculated by integrating a fit to the data in panel (b), is quite sensitive to the form of the equation used to fit the spreading pressure panel (b). The fits used for the spreading pressure data are shown as dotted lines in panel (b), and they are based on a constant times the alkali coverage to the 5/2 power. This is the coverage dependence which would be expected from a lattice of unpolarizable dipoles at zero temperature, and after integrating yields a coverage dependence of the energy shown in panel (c) to the 3/2 power. A satisfactory fit to the data in panel (b) can also be found for other forms of the coverage dependence, leading to a drastically different result for the energy integral. For example, a coverage dependence to the 3/2 yields an energy to the 1/2 power. This yields free energies at the lower end of the coverage range which are many times the values shown in panel (c), and are in fact on the same order of magnitude as the dipole energy shown in panel (d). The difficulty lies in the fact that the values obtained by integrating Equation 6.9 to obtain the free energy are strongly weighted by the spreading pressures used at the low end of the coverage range, because of the θ^{-2} factor in the integrand. This low end of the coverage range are just where the spreading pressure is most difficult to measure based on the desorption temperature,

because the desorption temperature change is small for low coverages. Thus it is questionable whether it is worthwhile to compare the energies shown in Figure 6.12 panels (c) and (d).

6.4.2.2. Equilibrium Method

Another method of using the rare gas as a probe to measure the spreading pressure of the alkali metal monolayer is possible using the equilibrium isobar experiments. If the rare gas is truly phase separated on the surface, then the spreading pressure inside the rare gas islands should be the same as that for a rare gas monolayer at the same temperature and 3-D rare gas pressure. Since rare gas monolayers on clean Ag(111) have already been extensively characterized,^{20,21} this information is available. If the system is in thermal equilibrium, the spreading pressure of the rare gas must equal the spreading pressure in the alkali metal patches. Thus it is possible to obtain the alkali spreading pressure as a function of alkali lattice parameter by equating it to the “known” rare gas spreading pressure for a particular temperature and 3-D rare gas pressure.

The rare gas spreading pressure is extracted from the data in references 20 and 21 in the following way: thermodynamically the spreading pressure is given by

$$\phi = kT \int_0^P \frac{dP}{a(P, T)P} \quad (6.11)$$

where $a(P, T)$ is the area per adatom as a function of P and T .²⁶ In references 20 and 21 the P - T phase diagram for Xe, Kr or Ar on Ag(111) was determined as well as the monolayer lattice spacing at monolayer condensation as well as at second-layer condensation. For a given T we obtain the lattice spacing as a function of P by extrapolating between these two values and assuming that the lattice parameter decreases linearly in $\log P$ between monolayer and bilayer condensation. Figure 6.13 shows the derived rare gas spreading pressures as a function of T , for a number of different values of P . The spreading pressure for K at any equilibrium (P, T) point can thus be obtained by looking up the rare gas spreading pressure. Spreading pressures determined in this way for various equilibrium points for Kr and Ar coadsorption are shown in Figure 6.12b, along with the spreading pressures determined using the non-equilibrium experiments.

Although there is a lot of scatter in the spreading pressure points, they are in general agreement with the spreading pressures determined in the non-equilibrium experiments. This reinforces the notion that the assumptions made in the derivation are in fact valid, particularly that the alkali-rare gas interaction energy term is not significant. The pressures measured for coadsorption with Xe are the

highest, as they should be, because the Xe experiment was done at the highest temperature: between 60 and 80 K.

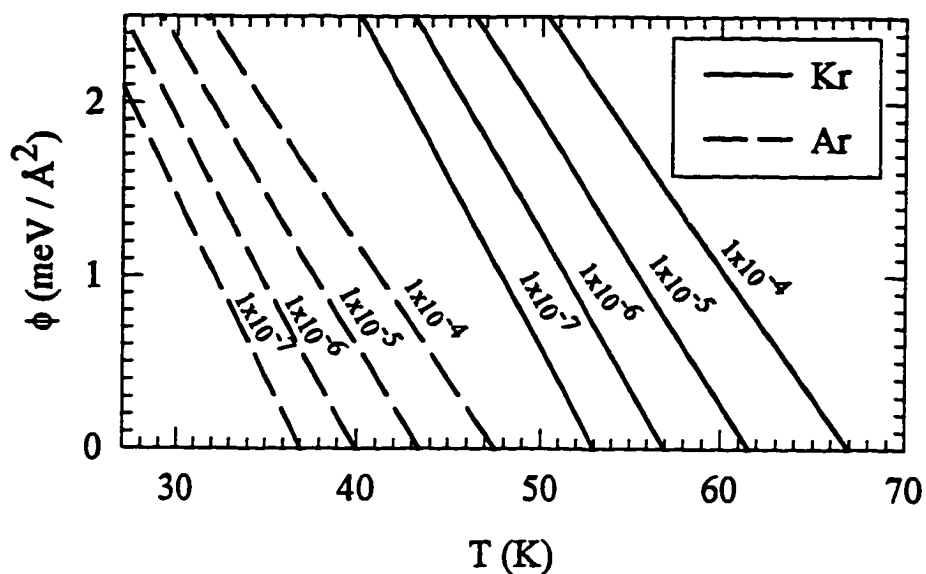


Figure 6.13. Rare gas spreading pressure as a function of three-dimensional pressure and temperature, obtained from equilibrium experiments reported in references 20 and 21. The labels on the curves represent the 3-D pressure in torr.

However, the equilibrium experiment spreading pressure values using Ar (done at temperature of 35 to 40 K) are not lower than those for Kr (done at 60 to 70 K), as would be expected based on the temperatures that the two experiments were done. However, one would expect that spreading pressure difference between the alkali layer at the temperatures of the Ar and Kr experiment would be much smaller than that for the difference between the Kr and Xe experiment, since for most of the Xe experiments the K overlayer is much closer to its melting temperature.

6.4.3. Energy of Alkali Commensurate Phases

When rare gas is dosed onto a partial K monolayer causing it to compress, the K lattice constant generally changes continuously without any jumps or kinks. The exception to this behavior is when the overlayer passes through a commensurate phase. Figure 6.14 shows the behavior of the lattice parameter as it passes through the commensurate $(\sqrt{7} \times \sqrt{7})R19.1^\circ$ and through the commensurate $p(2 \times 2)$ during rare gas isobar experiments. The lattice parameter sticks at the commensurate $(\sqrt{7} \times \sqrt{7})R19.1^\circ$ spacing for a little while, and then continues to compress. It again sticks at the $p(2 \times 2)$, but never compresses further.

If the experiment is done in the equilibrium mode described in the previous section, then the energy of commensurability, i.e. the energy that the overlayer gains by becoming commensurate, can be determined. The rare gas applies a force to the K lattice, which can be thought of as a compressing piston. When the K lattice is far from any commensurate phases, the pressure of the rare gas pushing on the K lattice equals exactly the internal pressure in the K lattice. However, when the K lattice nears a commensurate phase an additional force or pressure will be exerted to push the K lattice toward the commensurate phase. The magnitude of this "commensurate pressure" will be equal to the difference between the rare gas and alkali pressures. This force will cause the K lattice to slip into the commensurate phase earlier than it would otherwise and to stick there, causing a flat region in the lattice parameter seen in the graphs in Figure 6.14 for coadsorption with Ar and Kr. At the midpoint of the flat region, the "commensurate pressure" will be zero. Thus by taking the difference between the rare gas pressure at the middle and the edge of the flat region, the maximum "commensurate pressure" can be determined. This pressure difference can be converted into the free energy per K adatom associated with the commensurateness of the phase by multiplying it by the area per adatom. Following this procedure and using Ar for the coadsorbate, this free energy was found to be 5 meV for the K $(\sqrt{7} \times \sqrt{7})R19.1^\circ$ phase. The free energy of commensurateness for the K $p(2 \times 2)$ phase was also measured in this way, except that Kr adsorption was used, and a value of 11.5 meV was obtained.

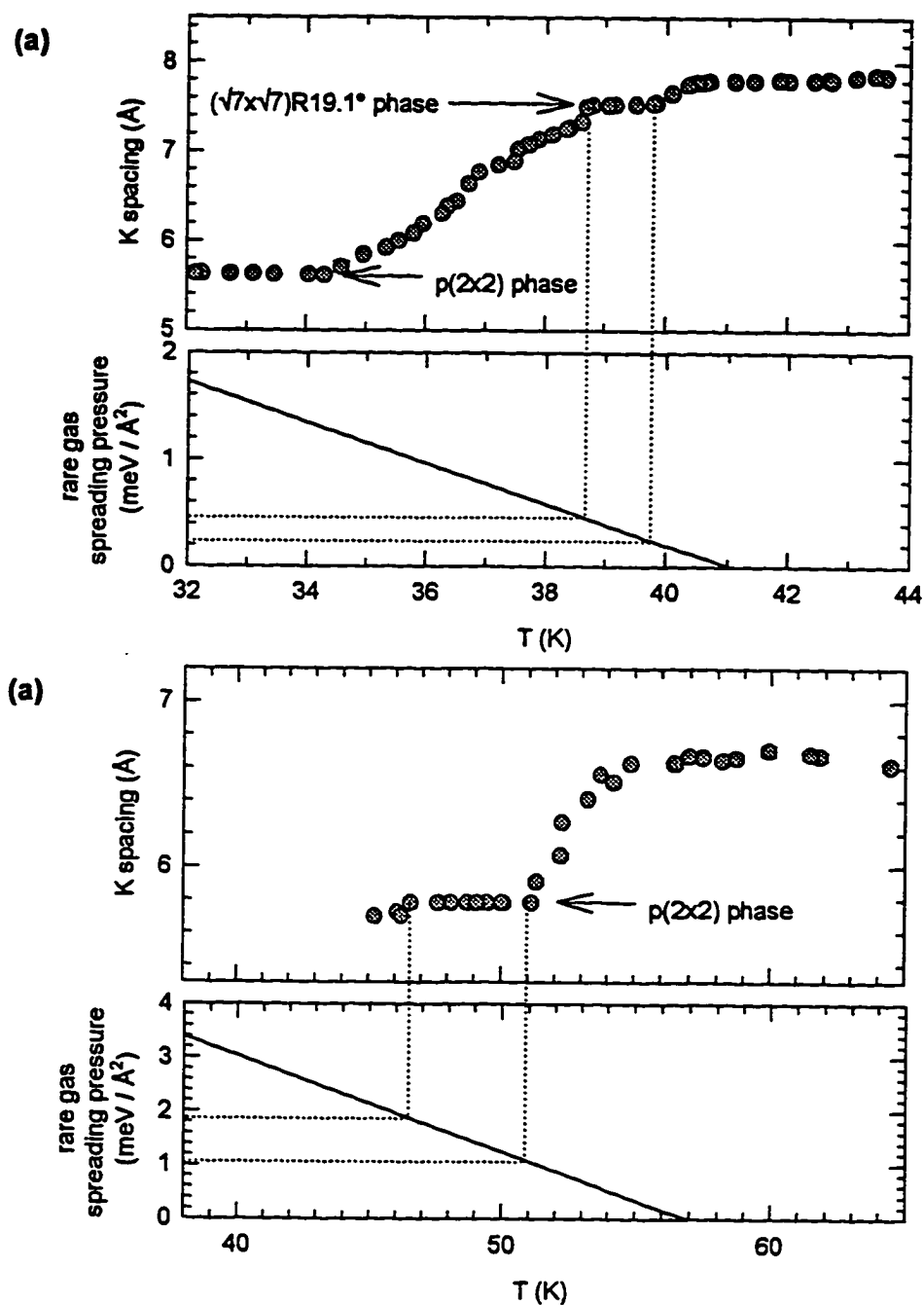


Figure 6.14. Commensurate sticking behavior of a K monolayer being compressed by rare gas. (a) Lattice parameter of a K monolayer which is being compressed by Ar during an isobar experiment at a pressure of 1×10^{-6} torr. The initial coverage of the K is 0.13 ML. The spacing "sticks" at the 7.65 Å of the commensurate $(\sqrt{7} \times \sqrt{7})R19.1^\circ$ phase, and again at the p(2x2) phase. The Ar is not able to compress the K past the p(2x2) phase, and a second layer of Ar begins to grow around 32 K. (b) Results of a similar experiment done using a Kr isobar at 1×10^{-6} torr and an initial coverage of 0.19 ML. In this case, after "sticking" in the p(2x2) phase over a temperature range of about 4.5 K, the lattice becomes incommensurate.

In practice the internal energy is a more useful quantity than the free energy. The internal energy will contain the additional positive term $S \Delta T$, where ΔT is the temperature range over which the “sticking” shown in Figure 6.14 occurs, and S is the entropy of the commensurate phase. However since ΔT is quite small, being 4.5 and 1.1 K for the $p(2 \times 2)$ and $(\sqrt{7} \times \sqrt{7})R19.1^\circ$ phases respectively, this term will probably not be significant.

6.5. Rare Gases Coadsorbed with Cs on Ag(111)

Kr adsorption with Cs is qualitatively different from coadsorption with K, at least for Cs precoverages up to about 0.19. For Cs precoverages up to about 0.06 the coadsorbed Kr lattice is aligned with the substrate, rather than becoming completely rotated by 0.04 as seen for K coadsorption. For coverages above 0.06, additional rotated spots form upon Kr adsorption. These spots can be seen in the LEED patterns shown in Figure 6.15. Unlike the case with K coadsorption, these new rotated spots are quite intense and do not improve significantly upon annealing. Figure 6.16a shows the rotation angles of these spots as a function of Cs precoverage. A number of different rotation angles are seen at different Cs precoverages, and for some Cs precoverages two or three rotated phases coexist. As with K coadsorption, these new spots initially correspond to a lattice spacing in the range for normal Kr adsorption on the clean Ag(111) surface: approximately 4.05 \AA . However, for the larger Cs precoverages when the sample is warmed this lattice spacing expands reversibly to a value as large as 4.40 \AA and exhibits a much larger coefficient of thermal expansion than for Kr on the clean surface. Figure 6.16b shows the maximum spacing as well as the coefficient of thermal expansion (taken at zero pressure) obtained for the new diffraction spots, as a function of Cs precoverage.

When Kr is dosed onto the Cs precovered surface, instead of remaining intense and changing position significantly, the alkali spots fade out quickly and only change position slightly. LEED patterns for Kr adsorption at two Cs precoverages are shown in Figures 6.15 and 6.17. In Figure 6.17, the initial Cs overlayer is in the $(\sqrt{7} \times \sqrt{7})R19.1^\circ$ structure and here an interesting observation is made. When Kr is dosed onto this surface, the intensities of inequivalent $(\sqrt{7} \times \sqrt{7})$ diffraction spots change with respect to each other. This indicates a change in the atomic positions and / or number of atoms inside the $(\sqrt{7} \times \sqrt{7})R19.1^\circ$ unit cell. Upon further dosing, the $(\sqrt{7} \times \sqrt{7})$ spots fade out completely and are replaced by new diffraction spots.

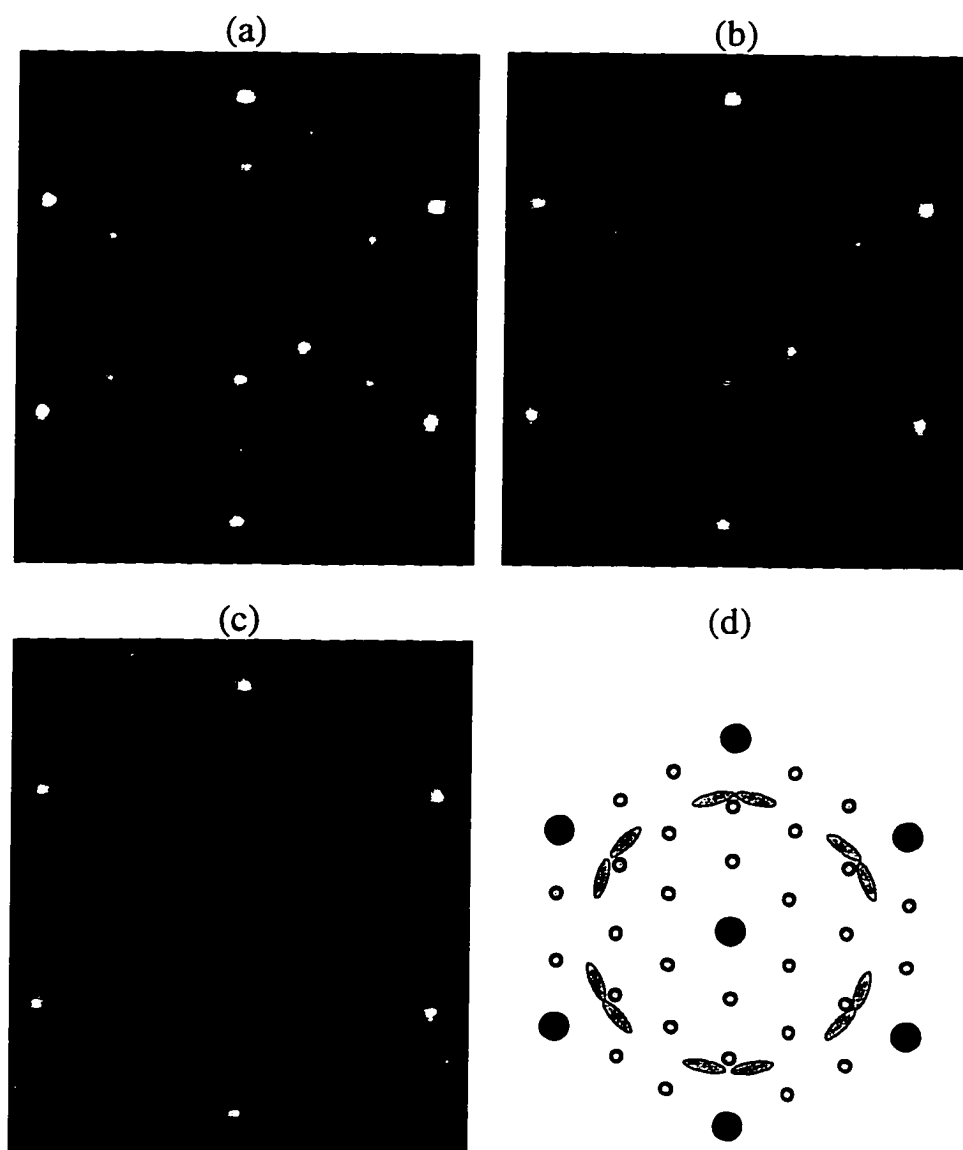


Figure 6.15. LEED patterns for Kr / Ag(111) precovered with 0.11 ML Cs. (a) No Kr adsorbed. Cs is in the commensurate $p(3 \times 3)$ phase. (b) After deposition of 2.3 L Kr, and (c) after deposition of 4.4 L Kr. (d) Schematic drawing of the diffraction pattern in (b). The large black circles represent substrate spots, small shaded circles represent $p(3 \times 3)$ spots, and the shaded ellipses represent additional spots which form upon adsorption of Kr. The incident electron beam energy is 250 eV.

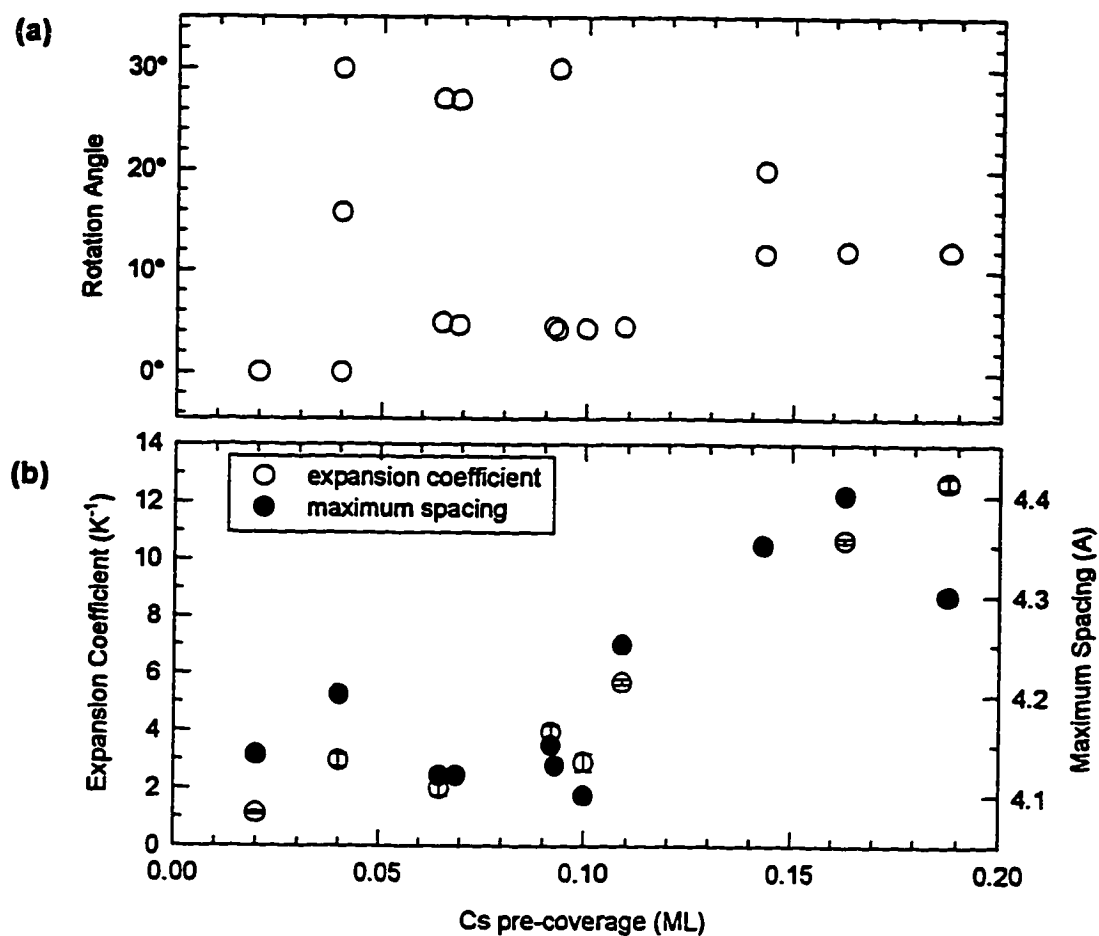


Figure 6.16. Data for the new phase which appears upon adsorption of Kr onto a Cs precovered Ag(111) surface. (a) Lattice rotation angles, and (b) maximum unit cell spacing (empty circles) and coefficient of thermal expansion (filled circles). Expansion coefficients were measured at zero Kr pressure.

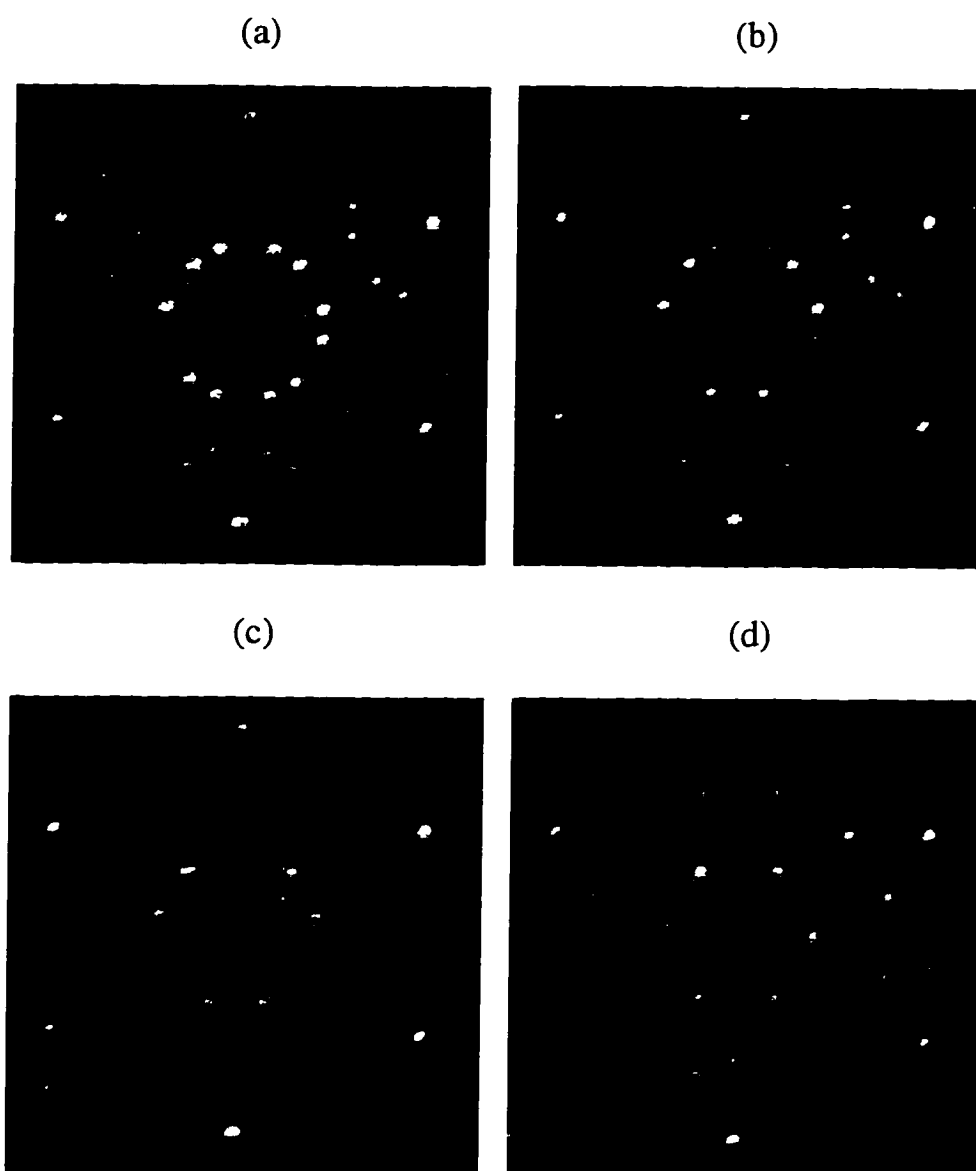


Figure 6.17. LEED patterns for Kr adsorption on Ag(111), precovered with 0.14 ML Cs. LEED patterns were taken at a constant flux of 1.5×10^{-6} mbar of Kr while decreasing the sample temperature. (a) $T = 68.9$ K. No Kr is yet adsorbed and the Cs is in a commensurate $(\sqrt{7} \times \sqrt{7})R19.1^\circ$ phase. (b) $T = 57.4$ K. The $(\sqrt{7} \times \sqrt{7})R19.1^\circ$ diffraction spots have changed their relative intensities, indicating a change in the positions and/or number of atoms in the unit cell. (c) $T = 56.5$ K. Additional spots have begun to form. (d) The $(\sqrt{7} \times \sqrt{7})R19.1^\circ$ spots have faded completely and only spots from the new phase remain. The incident beam energy is 150 eV.

For Cs precoverages higher than 0.19, the behavior changes again and is similar to that which is observed with K preadsorption: the additional spots do not appear and the alkali lattice compresses as it did for K. As with K preadsorption, the saturation value of the alkali compression is much lower than that for alkali on the clean surface: 0.25 compared to 0.33 alkali atoms per substrate atom.

Non-equilibrium desorption experiments were also done for Kr coadsorption with Cs. The desorption temperature for Kr coadsorbed with Cs is shown in Figure 6.18 as a function of Cs coverage. For Cs coverage up to about 0.14, the Kr desorption temperature is greater than that for the clean surface, indicating that the Kr is more tightly bound to the surface in the presence of Cs. At coverages greater than 0.14 of Cs however the Kr desorption temperature decreases, ending up for high Cs precoverages at a temperature 10 K below the desorption of Kr from the clean surface.

Based on the evidence presented it seems possible that the Kr coadsorbed with Cs adsorbs in a different mode for high Cs precoverage than it does for low Cs precoverage. All of the observations for Cs precoverages below 0.19 are consistent with the mixing of Kr and Cs on the surface. The disappearance of the Cs diffraction spots suggests a disordering of the Cs lattice which is probably caused by the mixing of the much smaller Kr atoms into the lattice. The raising of the desorption temperature is consistent with a Kr atom more strongly bound to the surface, which implies an attractive interaction and would result in mixing. There is no evidence for a pure phase of Cs, and the new phase which appears has characteristics which, while not well understood, are clearly not those of pure Kr. Thus, the interaction of Kr and Cs at low coverages appears to be attractive rather than repulsive.

For coverages higher than about 0.15, the behavior appears to change to a repulsive interaction. This is supported by the depression of the Kr desorption temperature and the compression of the alkali lattice when Kr is dosed. An alternate interpretation of this data is possible however. The apparent change from an attractive to a repulsive interaction may simply be the result of the competing second and third terms in Equation 6.5. For an attractive interaction V would be negative, and so the rare gas atoms would prefer to adsorb in patches of $n=1$, i.e. they would mix with the Cs lattice. At low coverages the spreading pressure term would be small, so the third term would dominate, resulting in an increased desorption temperature. At higher coverages the alkali spreading pressure is greater, causing the second term to be larger and the desorption temperature to be depressed. It is also likely that V will change with Cs coverage as the Cs atoms become depolarized. If V remains negative however, the rare gas should still mix with the Cs lattice. Since the Cs density is so high, the amount of rare gas which can fit into the lattice is not large, and so patches of Cs large enough to produce ordered diffraction patterns may still be seen. The intensity of the Cs diffraction spots should however decrease as a small amount Kr is adsorbed and mixes into the lattice. This is in fact observed; as the Cs lattice compresses the diffraction spots decrease in intensity by as much as a factor of three. Thus it is likely that the decrease in rare gas

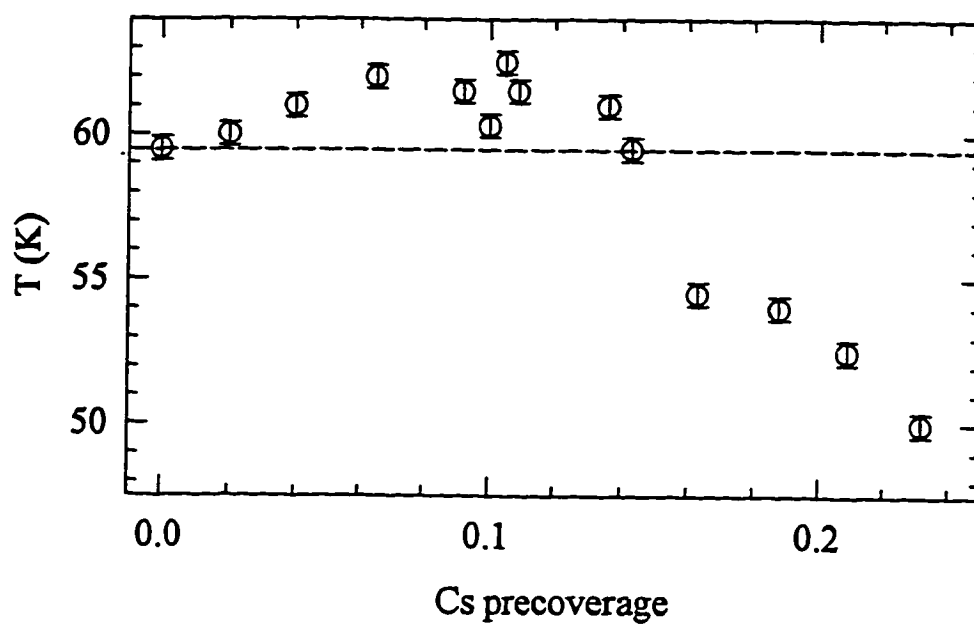


Figure 6.18. Temperature at which all Kr coadsorbed with Cs on Ag(111) has desorbed, as a function of Cs precoverage. Data were taken at zero Kr pressure. The horizontal line denotes the desorption temperature of Kr from the clean surface.

adsorption temperature at higher Cs coverages is caused by the alkali spreading pressure and possibly also a decrease in the magnitude of V as the alkalis depolarize; however there is no convincing evidence for a change in the sign of V .

The change from a repulsive to an attractive interaction from Cs to K is consistent with what might be expected based on the strength of the alkali dipole. Cs, being more electropositive, forms a stronger dipole when it adsorbs, and thus would be more likely to cause the rare gas polarization to change. A size effect, which is often the factor which determines the miscibility of two species, appears not to play a deciding role here. The metallic radius of K differs from the radius of the Xe atom by only about 5%, yet these results indicate that K and Xe are much less likely to mix than Cs and Kr, which have a much larger size difference.

The new phase formed upon adsorption of Kr for low coverages of Cs is not understood. The behavior of this phase shown in Figure 6.16b is clearly not that of a Kr monolayer. It is probably a mixed phase; however the details of its structure are beyond the scope of this experiment. The rotation angles, shown in panel (a), seem to change discontinuously with Cs coverage, perhaps suggesting stepwise changes in the stoichiometry of a mixed phase. In any case, additional studies using other probes will probably be necessary to obtain this information.

6.6 Work Function Results for Rare Gases Coadsorbed with K or Cs on Ag(111)

The behavior of the work function of a surface when a species is adsorbed provides information about the electrical polarization of that species perpendicular to the surface, as discussed in Chapter Two. With alkali metal adsorption the electrons polarize strongly toward the substrate, causing a large initial decrease in the work function. Rare gas atoms adsorbed on clean metal surfaces polarize in the same direction as the alkali metal atoms, causing a similar but much smaller decrease in the work function.

The change in the work function when a rare gas is adsorbed onto a partial monolayer of alkali metal should give us information about the effect of the alkali metal on the coadsorbed rare gas. In principle, the direction of the work function change should indicate the type of interaction between the alkali metal and rare gas atoms. An increase in the work function would indicate a polarization of the rare gas away from the substrate, suggesting an attractive alkali-rare gas interaction, whereas a decrease in the work function would indicate a polarization of the rare gas toward the substrate, suggesting a repulsive alkali-rare gas interaction. However, if the adsorption of the rare gas is accompanied by a compression of the alkali lattice, as for coadsorption of rare gas with potassium and the coadsorption of Cs at higher coverages, there will be an additional increase in the work function due to the depolarization of

the alkalis caused by their increased density. (This depolarization was also discussed in Chapter Two.) Therefore in the case of a repulsive interaction it may be difficult to draw conclusions based on the sign of the work function change.

This is demonstrated in Figure 6.19, which shows the measured work function changes upon coadsorption of Kr, as a function of Cs or K coverage. The behavior is similar to that observed for Xe and K on Ni(100).⁷ The dark curves show the behavior of the work function due to the alkali alone, and the light curves show the additional change due to the adsorption of a monolayer of Kr. Qualitatively the behaviors of Cs and K are similar: a precoverage of alkali causes the work function to increase when Kr is adsorbed, rather than to decrease as on the clean surface. Since it has been demonstrated that the Cs-Kr interaction is attractive while the K-Kr interaction is repulsive, the work function measurements cannot be interpreted simply as described above.

For Kr and Cs coadsorption at low Cs coverage, the increase in work function is probably caused by the reversal of the polarization of the Kr atoms caused by their interaction with the Cs dipoles. However, for Cs coverages higher than 0.19 where compression rather than disordering of the alkali lattice is seen, the increase in work function is much smaller or nonexistent. This is consistent with the largely-depolarized Cs atoms now having a much smaller effect on the K atoms. The work function increase for Kr and K coadsorption, on the other hand, must be caused by the depolarization of the K atoms due to the compression of the lattice. The increase is not as large as the largest increase observed for Cs. Also the amount appears to increase with the curvature of the K work function curve, as it would if the work function increase were caused by K depolarization.

6.7 Xe Adsorbed on an Alkali Monolayer

In addition to the coadsorption of rare gas with a partial monolayer of alkali metal, some experiments were done in which Xe was grown on top of a full monolayer of either K or Rb. In such an experiment, several modes of growth are possible. First of all, the rare gas overlayer might grow in a layer-by-layer mode as on the clean Ag(111) surface. A second possibility is the Stranski-Krastanov growth mode in which one or more monolayers grow in a layer-by-layer fashion, followed by a transition to the growth of three dimensional clusters of Xe. Thirdly, it may be that growth will start immediately by the formation of three dimensional clusters, without the formation of a monolayer.

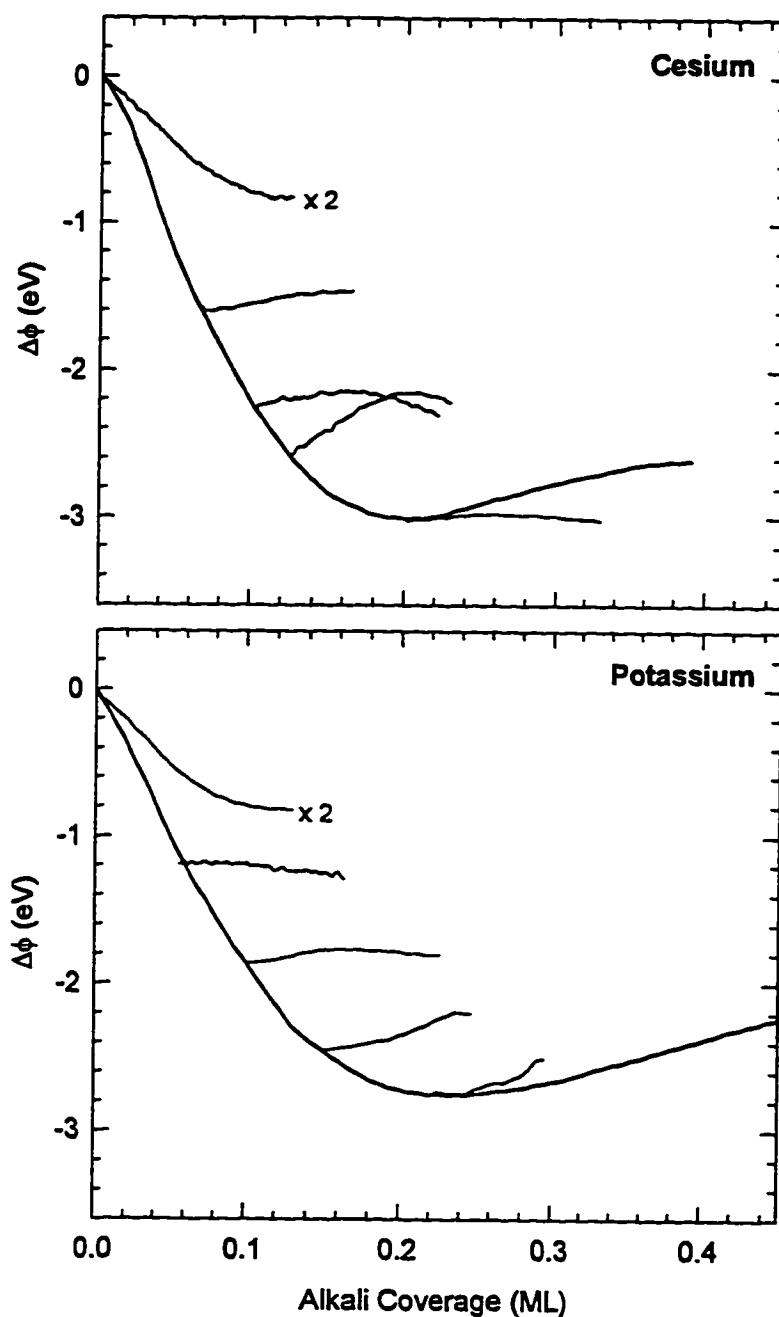


Figure 6.19. Work function change due to the adsorption of Kr on Ag(111), precovered with Cs or K. The dark curves indicate the dependence of the work function during alkali adsorption on the clean metal surface.²⁷ The light curves indicate the change in the work function during Kr adsorption, starting from various alkali precoverages. The magnitude of the changes due to Kr adsorption are magnified by a factor of two.

Using LEED, the first two modes may or may not be distinguishable, depending on the number of layers at which the transition to 3-D clusters occurs. The instrument used in these experiments is not able to distinguish the difference after second-layer growth. The third mode however should be clearly distinguishable by a sudden dimming or disappearance of the substrate and overlayer beams at the bulk rare gas sublimation temperature and the lack of a monolayer adsorption step in the beam intensities.

In the experiment, alkali metal was first dosed to a coverage sufficiently high that Xe adsorption would not result in any Xe entering the alkali layer (i.e. above 0.28 ML). Next Xe was dosed while monitoring the LEED pattern. For Xe on K, no Xe could be grown at all using non-equilibrium dosing (i.e. low sample temperature and Xe pressure at about 1×10^{-8} mbar.) By dosing at equilibrium (slowly lowering the sample temperature at a Xe pressure $> 5 \times 10^{-7}$) bulk Xe clusters could be grown. This was evidenced by the sudden disappearance of all diffraction beams, without the prior condensation of a monolayer. Thus it appears that Xe grows in the third mode on a monolayer of K.

In contrast to K, Xe on Rb could be grown using non-equilibrium dosing. However the LEED pattern did not show sharp diffraction spots due to the Xe, as observed for Xe on clean Ag(111). The first Xe to go down had the effect of decreasing the intensity of the Rb and Ag diffraction beams and increasing the diffusely scattered intensity. If this surface was annealed to about 50 K, a modulated ring appeared which corresponded to an expected Xe-Xe spacing. Heating the layer further resulted in an increase in the intensities of all beams accompanied by a decrease in background intensity at about 55 K, the desorption temperature of bulk Xe. At about 62 K the Xe ring suddenly disappeared and the Rb spots became brighter. With further increases in temperature the LEED pattern did not change significantly. This behavior suggests that a monolayer of Xe was able to grow on the Rb layer. The desorption temperature of this monolayer, about 62 K, is much lower than the desorption temperature for monolayer Xe on clean Ag(111), which is about 78 K, indicating that the Xe layer on Rb is bound significantly weaker than Xe on Ag. In fact this desorption temperature is approximately the same as that seen for the desorption of the second layer of Xe from clean Ag(111). Bilayer Xe condensation was not observed. Thus it appears that Xe on a monolayer of Rb grows in the Stranski-Krastanov mode.

In the case where a dim modulated ring appeared upon Xe adsorption, the experiment was done on several differently prepared Rb monolayers. A Rb monolayer of density 0.3 may be either incommensurate and aligned with the substrate, commensurate with the substrate in a $(\sqrt{3} \times \sqrt{3})R30^\circ$ phase, or a coexistence of these two phases, depending on dosing conditions and annealing temperature. To test whether the Xe monolayer was actually adsorbed on top of the Rb layer (rather than on bare spots of the substrate), the Xe adsorption experiment was done on a Rb monolayer which was almost completely in the 0° aligned incommensurate phase, and on one in which 30° aligned Rb coexisted with 0° aligned. Figure 6.20 shows schematics of these diffraction patterns. (The actual diffraction patterns are not shown

because the diffraction spots are dim and it is difficult to see the diffraction spots on a printed reproduction.) For the 0° aligned Rb monolayer, the Xe ring is modulated in the 0° direction, while for the other Rb monolayer phase it is modulated in both the 0° and the 30° direction. This indicates that the Xe layer is forming on top of the Rb.

These results are consistent with a number of previous studies which have shown non-wetting of rare gases on alkali-dosed surfaces. These experiments were done by comparing the adsorption of a rare gas on a clean metal surface to its adsorption on alkali mono- or multilayers adsorbed on the same substrate. These studies include Xe + Na / Ni(111),²⁸ Xe + K / Ag(110),^{29,30} Ar, Kr, or Xe + K / Ru(0001),³¹ and Ar + K or Cs / Ru(0001).³² In each of these cases the rare gas could be grown in a layer-by-layer or wetting mode on the clean metal surface, but the introduction of one or more monolayers of alkali caused it to grow in a non-wetting mode. This is consistent the results presented here for Xe on both Rb and K. In each case it is clear that the Xe does not grow in a layer-by-layer mode, but condenses suddenly into the bulk phase. The difference between K and Rb is hard to understand however. The non-wetting of rare gases on an alkali monolayer has been attributed to the reduced work function of the surface. Rb however should cause a larger work function change and thus it should be less likely for Xe to be grown on it.

6.8 Rare Gases Coadsorbed with Carbon Monoxide on Ag(111)

CO coadsorption with rare gases was investigated because it was hoped that the results might yield some insight into the rotational behavior of the rare gas coadsorbed with alkali. In particular, if the rotation of the rare gas coadsorbed with alkali is caused by step site blocking by alkali atoms, it was assumed that the same behavior might be seen using CO. It was uncertain however whether an attraction or repulsion should be expected between the two species.

As a precursor to the coadsorption experiments, CO alone on Ag(111) was investigated. When CO is dosed onto the clean Ag(111) surface, at first no change is seen in the LEED pattern. After a dose of about 0.3 L, sharp LEED spots form and grow brighter as more CO is dosed, indicating that the CO grows as islands. This LEED pattern is shown in Figure 6.21a. The CO lattice is incommensurate hexagonal having a spacing of 4.15 ± 0.02 Å for the unconstrained monolayer, and compresses to 3.89 ± 0.02 Å when monolayer saturation is reached at a dose of about 1.8 L. The rotation angle varies from $8.8^\circ \pm 0.1^\circ$ to $8.4^\circ \pm 0.1^\circ$ as the layer compresses. At zero pressure the CO monolayer desorbs (as measured by the disappearance of the ordered LEED pattern) at 45 K, and further heating does not result in any further change of the LEED pattern. If the sample is annealed only to just above the disappearance of the LEED

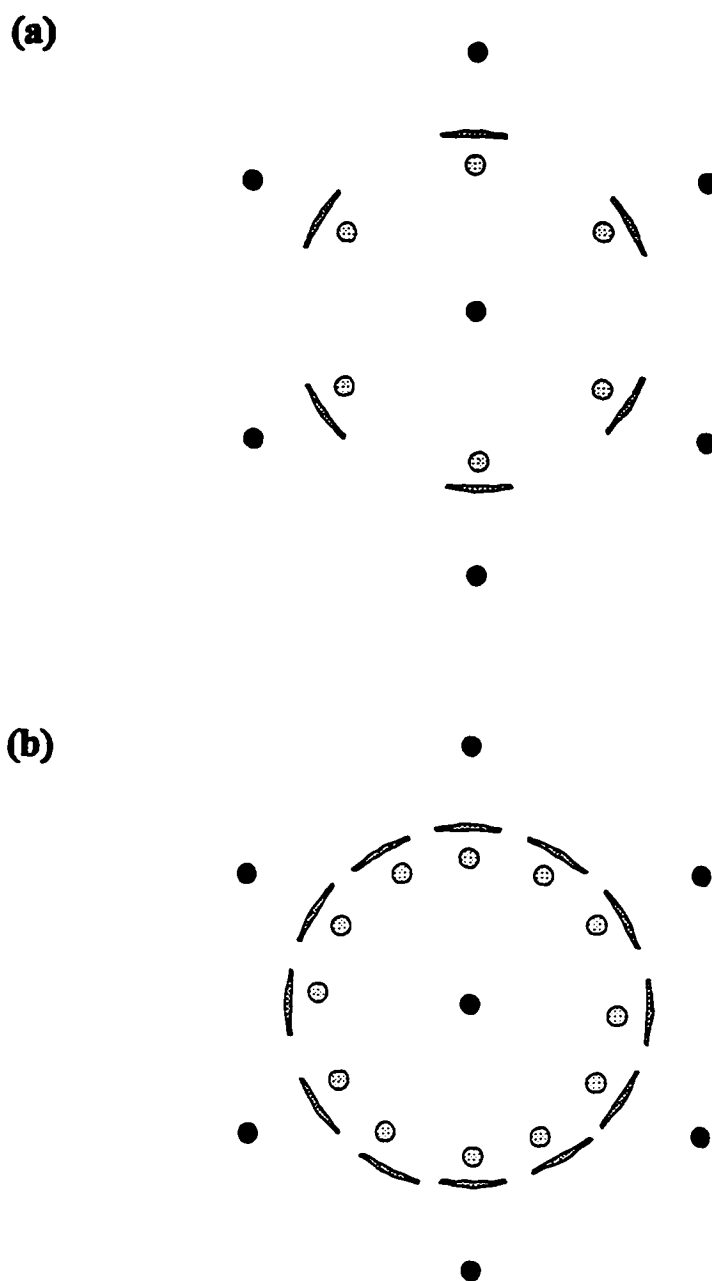


Figure 6.20. Schematics of the LEED patterns seen for Xe adsorbed on a monolayer of Rb on Ag(111). Filled circles represent substrate spots, shaded circles represent Rb overlayer spots, and dark shaded crescents represent the modulated Xe ring. The Rb coverage is 0.30, a coverage at which the layer is incommensurate and may be aligned at either 0° or 30° with respect to the substrate, depending on dosing conditions and annealing temperature. (a) Rb monolayer is completely aligned with the substrate, causing the Xe layer also to be aligned. (b) The Rb monolayer consists of two coexisting phases, aligned at 0° and at 30° . The Xe layer in this case is also aligned both at 0° and at 30° . This behavior reinforces the view that the Xe is growing on top of the Rb layer.

pattern (about 46 K) and then cooled again, no CO can be measured using Auger. From this it appears that only one species of CO adsorbs on the Ag(111) surface, or that the quantities of other species are too small to measure. This is consistent with the previous result^{18,19} which showed only physisorption of CO on Ag surfaces with low defect densities.

If Ar is dosed on a surface which has been pre-dosed with 0.2 L of CO, the Ar goes down rotated at 19.1° rather than aligned as on the bare surface, and the Ar diffraction spots are very sharp, also unlike Ar on the bare surface in which the spots are azimuthally broader. For a CO precoverage of 0.1 L however, the Ar is rotated at two angles: 19.1° and 12°, with the 12° spots being azimuthally broad. For a CO precoverage of 0.05 L or smaller, Ar aligned with the substrate can also be seen. LEED patterns are shown in Figure 6.21 panels (b) through (d). The spacing corresponding to the positions of these diffraction spots is within the range of the expected Ar-Ar spacing. This range does not overlap with the CO-CO spacing measured for CO on clean Ag(111).

For the case where all three Ar phases coexist, if the sample is heated (not high enough to desorb the CO) the aligned and 12° lattices undergo thermal expansion from about 3.78 to 3.95 Å – essentially identical to that of Ar on the clean surface – while the 19.1° spots first expand a very small amount and then remain at a constant lattice parameter of 3.82 Å. This is shown in Figure 6.22. The 19.1° phase is therefore recognized as a higher order commensurate phase, a $(\sqrt{7}\times\sqrt{7})R19.1^\circ$ with four atoms per unit cell. (This HOC phase was also seen with Ar coadsorbed with K).

In order to more carefully investigate the transition from one kind of Ar adsorption to another, an experiment was done where 0.3 L of CO was deposited and then sequentially annealed to higher temperatures and cooled, each time depositing Ar on the surface and observing the LEED pattern, until the CO was completely desorbed. Ar has a normal desorption temperature lower than that of CO, and was completely desorbed between each cycle. Figure 6.23 shows the relative amounts of each kind of Ar as a function of annealing temperature. For annealing temperatures higher than 43 K, the amount of 19° rotated Ar decreases sharply, while the 12° Ar grows in. The amount of 12° Ar remains essentially constant 43.5 to 45.2 K, while the amount of aligned Ar increases and 19° Ar decreases. Finally by about 47 K, the Ar overlayer is completely aligned. Notice that while the 19° Ar begins to decrease at the temperature where an ordered CO monolayer is desorbed, the Ar is affected by CO above this temperature.

When Kr or Xe are adsorbed with CO, the rare gas also goes down rotated: Kr at about 5.0° and Xe at about 6.5°. These rotation angles are shown in Figure 6.24 (filled data points) along with the data which has already been presented for potassium coadsorption with rare gases (empty points). For Xe and Kr, unlike Ar, only one rare gas rotation angle is seen and the spacing of the rare gas is similar to that of the rare gas on the clean surface. For Kr (Xe was not investigated in as much detail) the rotation angle of

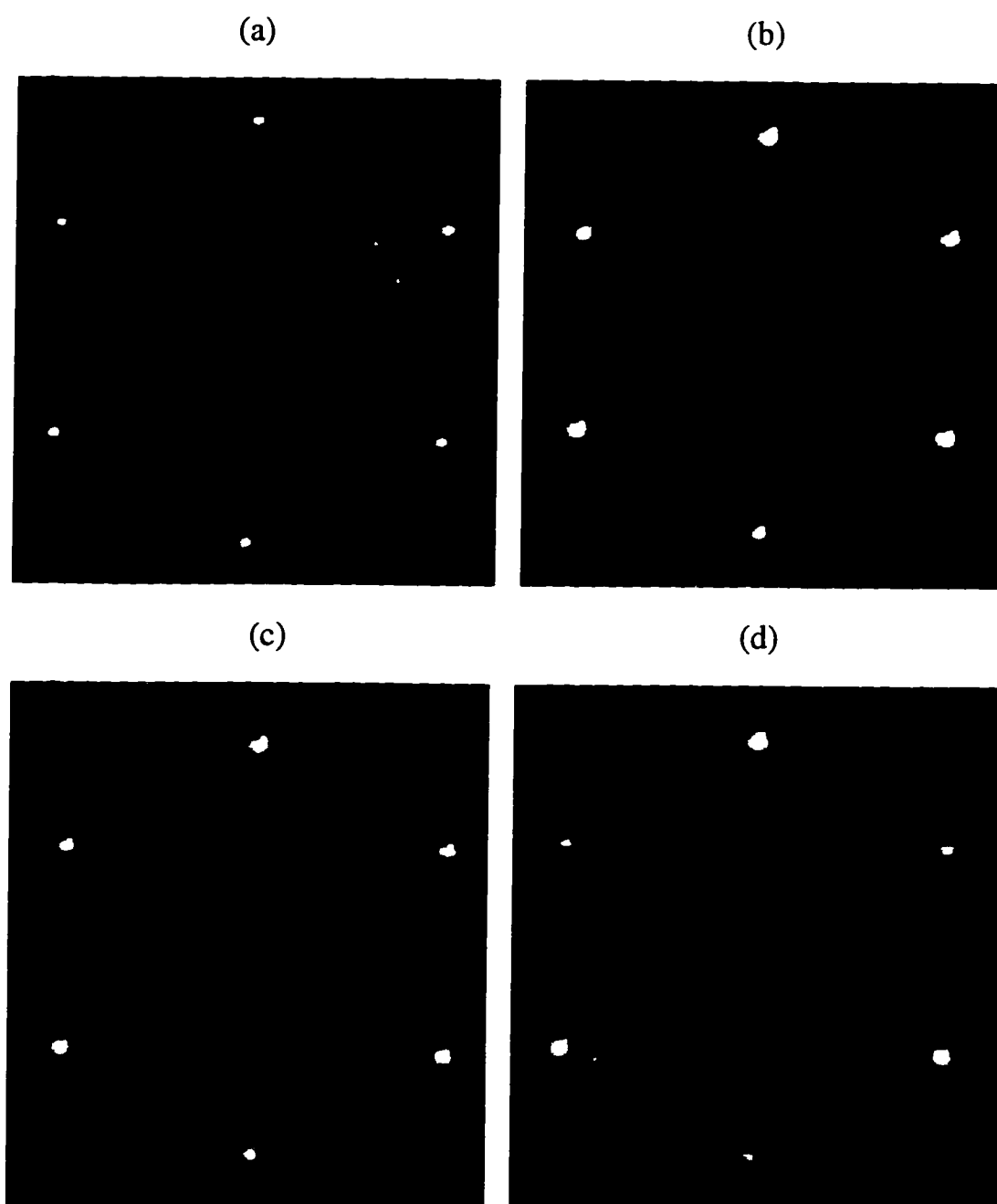


Figure 6.21. LEED patterns showing CO coadsorption with Ar on Ag(111). (a) Diffraction pattern of about 1.5 L of CO on Ag(111). The diffraction pattern indicates an incommensurate lattice with a spacing of 3.99 Å and a rotation angle of 8.6°. (b) - (d) LEED patterns for Ar coadsorption with CO on Ag(111). (a) no CO is present, (b) predosed with 0.07 L of CO, and (c) predosed with about 0.25 L of CO. In (c) the diffraction spots are from a commensurate ($\sqrt{7} \times \sqrt{7}$)R19.1° phase.

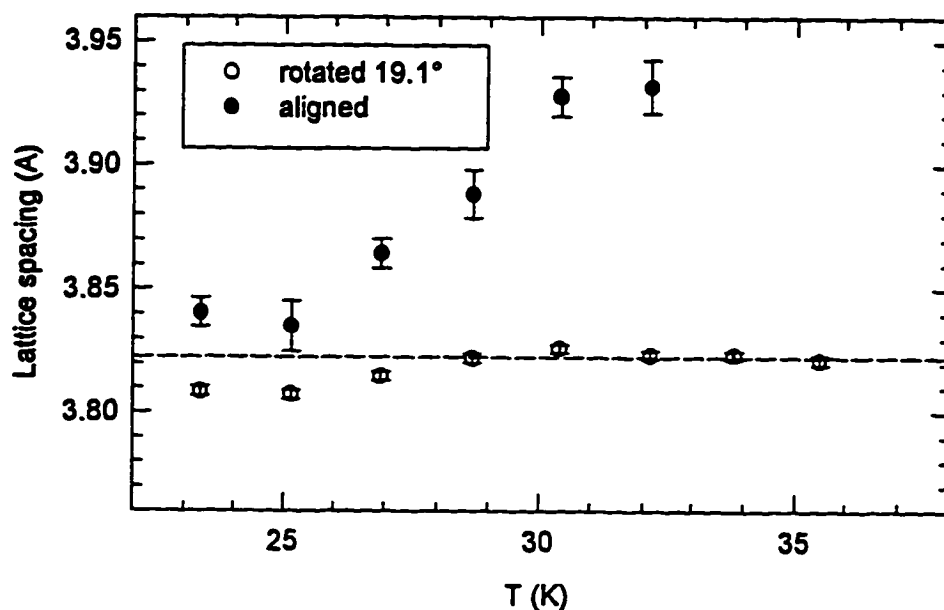


Figure 6.22. Lattice parameter of the $(\sqrt{7}\times\sqrt{7})R19.1^\circ$ Ar + CO / Ag(111) phase as a function of temperature. Two phases coexist: one rotated and one aligned. The filled circles represent the spacing calculated from the positions of the aligned spots, and the empty circles from the rotated spots. The lack of expansion of the rotated phase with temperature indicates that the phase is commensurate. The horizontal dashed line indicates the Ar atomic spacing in the $(\sqrt{7}\times\sqrt{7})R19.1^\circ$ phase, assuming four equally-spaced atoms per unit cell.

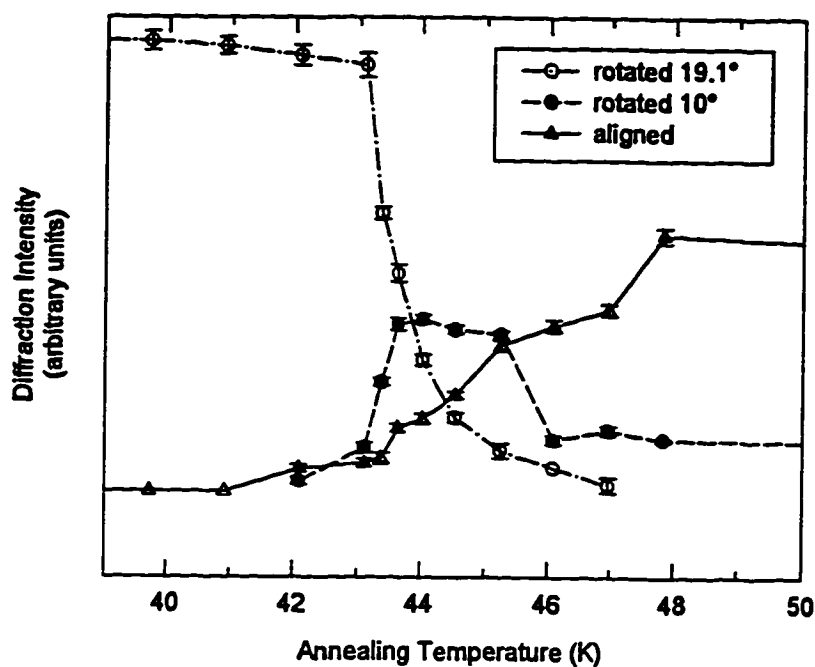


Figure 6.23. Behavior of the Ar overlayer adsorbed on Ag(111) pretreated with CO, as a function of annealing temperature. The graph shows the intensities of the three overlayer diffraction spots from the LEED pattern shown in Figure 6.21c. The surface was prepared by first dosing 0.24 L of CO, and then repetitively dosing Ar, recording the LEED pattern, and annealing to a higher temperature. Ar was fully desorbed and redeposited during each anneal cycle.

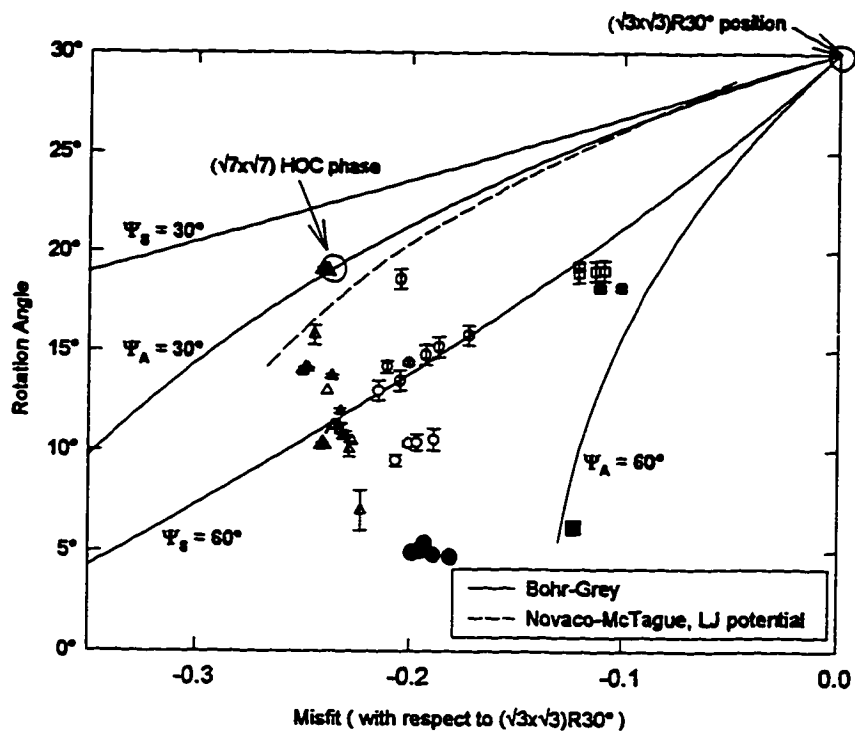


Figure 6.24. Overlayer rotation angle for rare gases coadsorbed with CO on Ag(111). Rare gas + CO data are represented by filled points. Also shown for comparison are the results for rare gases coadsorbed with potassium on Ag(111) (empty points). Xe is denoted by squares, Kr by circles, and Ar by triangles.

the rare gas does not depend on the amount of CO predosed, at least down to 0.05 L of CO. Also unlike Ar, Kr and Xe both desorb at higher temperatures than CO, so the behavior of the Kr monolayer can be observed while the CO is desorbed. As the sample is heated, the Kr layer undergoes thermal expansion identical to that of Kr on the clean surface, and the rotation angle decreases continuously from 5° to about 4.5° . No discontinuous changes in the spacing or angle (or discernible changes in the LEED pattern) are observed at the temperature of normal CO desorption, 43 - 46 K. The diffraction spots remain rotated until the Kr desorbs, although the rotation angle does decrease by a degree or so. If the Kr is deposited first and CO is dosed onto the Kr-covered surface, the rotation angle of the Kr lattice spontaneously and continuously changes from zero the 5° value at the onset of CO adsorption.

There are several questions that arise here. The first is why does the CO cause the rare gas lattice to rotate? Since the rotation angle is different from that seen with alkali metal, it seems likely that a different mechanism is responsible for the rotation here. The CO, a physisorbed species, should not have the effect on the surface of increasing the substrate corrugation, as we attribute to the alkalis. A possible explanation is step-site blocking, to which was attributed the behavior for CO and rare gases adsorbed on Pt(111).^{15,16} Assuming a terrace width of 150 Å and a constant sticking coefficient for the CO, a dose of about 0.012 L of CO should be sufficient to line the steps with a single row of CO. As with the potassium coadsorption, this is significantly less than the amount which is actually needed to change the rare gas orientation angle. Yet another possibility is that the lattice rotation is caused by a mixed phase of Kr and CO, which are nearly the same size. However it is puzzling that such a small amount of CO (only 0.03 of a saturated monolayer) should have such a large effect, and that the rotation angle should not depend strongly on the amount of CO present.

Another puzzling observation is that the Kr remains rotated even after the CO should have desorbed. If the sample is heated just high enough to desorb this rotated Kr, and then Kr is deposited again immediately, it goes down aligned. This seems to indicate that the Kr lattice simply does not have sufficient mobility to change its orientation angle. This however seems unlikely, since the rotation angle changes spontaneously upon CO adsorption. Another possibility is that the Kr equilibrium angle on the clean Ag(111) surface is actually non-zero, and the CO somehow unpins the Kr lattice from alignment with the steps, and that it remains unpinned after desorption of the CO. This would imply that the step pinning can only occur during nucleation of the rare gas.

These unresolved questions elude easy answers. It seems likely that the interaction between the CO and rare gas is complicated, involving possibly step-site blocking plus some additional interaction. A more detailed study, probably utilizing some complementary probes, is needed to understand this behavior.

6.9 References

- ¹ E. Cheng, M. W. Cole, J. Dupont-Roc, W. F. Saam and J. Treiner, *Rev. Mod. Phys.* **65**, 557 (1993).
- ² M. Onellion and J. L. Erskine, *Surface Science* **177**, L983 (1986).
- ³ C. P. Flynn and Y. C. Chen, *Phys. Rev. Letters* **46**, 447 (1981).
- ⁴ J. Küppers, K. Wandelt and G. Ertl, *Phys. Rev. Lett.* **43**, 928 (1979).
- ⁵ K. Jacobi and H. H. Rotermund, *Surface Science* **116**, 435 (1982).
- ⁶ K. Wandelt and B. Gumhalter, *Surface Science* **140**, 355 (1984).
- ⁷ D. R. Mullins, J. M. White and H. S. Luftman, *Surface Science* **160**, 70 (1985).
- ⁸ D. R. Mullins, J. M. White and H. S. Luftman, *Surface Science* **167**, 39 (1986).
- ⁹ J. Lee, C. P. Hanrahan, Jose Arias, R. M. Martin, and H. Metiu, *Surface Science* **161**, L543 (1985).
- ¹⁰ K. Markert and K. Wandelt, *Surface Science* **159**, 24 (1985).
- ¹¹ H. H. Rotermund and K. Jacobi, *Surface Science* **126**, 32 (1983).
- ¹² P. Statiris, P. Häberle and T. Gustafsson, *Phys. Rev. B* **47**, 16513 (1993).
- ¹³ S. Horch, P. Zeppenfeld and G. Comsa, *Appl. Phys. A* **60**, 147 (1995).
- ¹⁴ P. Zeppenfeld, S. Horch and G. Comsa, *Phys. Rev. Lett.* **73**, 1259 (1994).
- ¹⁵ K. Kern, P. Zeppenfeld, R. David, R. L. Palmer and G. Comsa, *Phys. Rev. Lett.* **57**, 3187 (1986).
- ¹⁶ K. Kern, P. Zeppenfeld, R. David, R. L. Palmer and G. Comsa, *J. Vac. Sci. Tech. A* **6**, 639 (1988).
- ¹⁷ R. H. Roberts, J. Pritchard, *Surface Science* **54**, 687 (1976).
- ¹⁸ S. Krause, C. Mariani, K. C. Prince and K. Horn, *Surface Science* **138**, 305 (1984).
- ¹⁹ P. Dumas, R. G. Tobin and P. L. Richards, *Surface Science* **171**, 555 (1986).
- ²⁰ J. Unguris, L. W. Bruch, E. R. Moog and M. B. Webb, *Surface Science* **109**, 522 (1981).
- ²¹ J. Unguris, L. W. Bruch, E. R. Moog and M. B. Webb, *Surface Science* **87**, 415 (1979).
- ²² L. W. Bruch and J. M. Phillips, *Surface Science* **91**, 1 (1980).
- ²³ J. Lakin, S. Finberg and R. D. Diehl, unpublished.
- ²⁴ E. Vives and P. A. Lindgård, *Phys. Rev. B* **47**, 7431 (1993).

- ²⁵ A. Zangwill, *Physics at Surfaces*, Cambridge University Press (1988).
- ²⁶ W. A. Steele, *The Interaction of Gases with Solid Surfaces*, New York, Pergamon Press (1974).
- ²⁷ C. Argile and G. E. Rhead, *Surface Science* **203**, 175 (1988).
- ²⁸ W. Weiss and E. Umbach, *Surface Science* **249**, L333 (1991).
- ²⁹ E. Bertel, W. Jacob and V. Dose, *Phys. Rev. B* **36**, 2421 (1987).
- ³⁰ E. Bertel, W. Jacob and V. Dose, *Appl. Phys. A* **44**, 93 (1987).
- ³¹ W. Friess, E. Steinacker, T. Brunner and D. Menzel, *Surface Science* **298**, L173 (1993).
- ³² W. Friess, T. Brunner and D. Menzel, *Surface Science* **307**, 182 (1994).

Chapter Seven

Summary and Conclusion

The results presented in this thesis fall into three categories: first a brief characterization of the clean Ag(111) surface, secondly a systematic description of the structural behavior of alkali metal mono- and bilayers on Ag(111), and thirdly a more exploratory study of the interactions of alkali adsorbates with physisorbed atoms or molecules. The work has utilized a variety of techniques. Low-energy electron diffraction has been used in a number of capacities, including surface morphology characterization, measurements of overlayer periodicities and lattice parameters, quantitative structural determination, and temperature dependent measurements of adsorption/desorption phenomena. Auger Electron Spectroscopy and Kelvin Probe measurements have been used to measure the surface composition and work function, respectively.

This chapter will summarize the results which have been presented and make some comments about their significance.

7.1. The Ag(111) Surface

The results presented for clean Ag(111) provide two important pieces of information, as a precursor to the adsorbate studies. The LEED structural determination determined that at 120 K the Ag(111) surface exhibits a perfect or nearly perfect bulk termination. The relaxation of the top layer was found to be 0.00 ± 0.01 Å. This result is in agreement with expectations for a noble metal such as silver, and in agreement with two older structural determinations. However it is not in agreement with a more recent MEIS (Medium Energy Ion Scattering) experiment on Ag(111) which showed at 0.06 Å contraction of the first layer.

7.2 Alkali Adsorption on Ag(111)

Detailed systematic studies were performed for Cs, Rb, or K adsorption on Ag(111). The monolayer phase diagrams were mapped out as a function of coverage and temperature. Qualitatively these phase diagrams are very similar, with the main differences being attributable to the size of the alkali. The adsorbates are mutually repulsive at all submonolayer coverages, confirming a classical picture of dipole-dipole repulsion between adsorbed alkali atoms. At most coverages the overlayer forms

an incommensurate solid on the surface, and compresses monotonically with increasing coverage. The overlayer densities saturate at 0.33, 0.36, and 0.41 ML for Cs, Rb, and K, respectively. The in-plane lattice spacing at these densities is slightly compressed by a few percent compared to that expected for a metallic alkali bond.

The effect of the substrate corrugation potential is small but significant. Even at low temperatures the alkali atoms are not strongly bound to specific sites, but have a large amount of mobility in the surface plane. However the substrate effect is large enough to cause the alkali lattice to form commensurate phases at densities where the overlayer and substrate lattice parameters coincide in a superlattice periodicity. These commensurate phases are primitive triangular, and include a $(2\sqrt{3} \times 2\sqrt{3})R30^\circ$ at a coverage of $1/12$, a $p(3 \times 3)$ at $1/9$, a $(\sqrt{7} \times \sqrt{7})R19.1^\circ$ at $1/7$, a $p(2 \times 2)$ at $1/4$, and a $(\sqrt{3} \times \sqrt{3})R30^\circ$ at $1/3$. The coverage range over which each phase exists is only a few hundredths of a monolayer or less, indicating again that the effect of the substrate is not large. Besides these commensurate phases of primitive unit cell, two higher-order commensurate phases were observed. These include a $(\sqrt{21} \times \sqrt{21})R10.8^\circ$ with four atoms per unit cell at a coverage of $4/21$ for K and Rb, and a (5×5) with nine atoms per unit cell at a coverage of $9/25$ for Rb. Due to the absence of first order diffraction spots in the K $(\sqrt{21} \times \sqrt{21})R10.8^\circ$ phase, it appears that the overlayer considered alone actually has $\sqrt{21}/2$ periodicity, indicating that the substrate corrugation is not strong enough to cause an overlayer atom to be significantly displaced from its position in the minimum of the potential due to the neighboring adsorbate atoms.

Another effect of the substrate corrugation is to cause the overlayer lattice to align at a particular angle, rather than exist in patches of all orientation angles. Over much of the coverage range the incommensurate lattice is aligned either in a high symmetry direction of the substrate, either 0° or 30° . However between coverages of about 0.13 and 0.20 and for coverages higher than 0.33 for K, the overlayer exhibits epitaxial rotation. This effect, which is due to a competition between the substrate corrugation and the elastic forces in the overlayer, causes the lattice to align at a non-symmetry orientation angle with respect to the substrate. Over the lower coverage range the behavior of this phase was compared to several theoretical predictions, including the coincidence lattice model, the Bohr-Grey symmetry principle, and the Novaco-McTague and Shiba theories. While the behavior does not follow any model exactly, it followed the general prediction of the Novaco-McTague theory. The main deviation from Novaco-McTague behavior is an alignment of the overlayer at the angle of nearby commensurate structures, a feature due to domain-wall formation predicted by the Shiba theory.

As already mentioned, at low temperatures the overlayer exists as an incommensurate or commensurate solid. When the temperature is increased a melting transition is seen. Above the melting

transition rings around the substrate beams are observed in the diffraction pattern, indicating a fluid with a well-defined nearest-neighbor distance. At some coverages, particularly for the incommensurate phase, the fluid is also rotationally ordered. At very low coverages (less than about 0.06 ML) only this fluid phase is seen, and it is assumed that the temperatures necessary to form the solid are below the experimentally accessible limit of about 25 K.

A second layer of alkali metal could be grown on the alkali monolayer, and it was found to be incommensurate with an in-plane lattice parameter slightly expanded with respect to the first layer. In all three cases the second layer spacing was close the bulk spacing expected for the alkali. The second layer was rotated with respect to the first, and the angle of rotation was found to be within a few degrees of the Novaco-McTague prediction.

Complete LEED structural determinations were done for three of the five commensurate phases: the $(\sqrt{3}\times\sqrt{3})R30^\circ$, the $p(2\times 2)$, and the $p(3\times 3)$. The alkali adatoms reside in three-fold hollow sites for all of the phases, confirming early notions of alkali adsorption but going against more recent results which have shown that alkalis on close-packed metal substrate more often reside in the top sites. Along with the hollow determination, a rumpling of up to 0.11 Å was observed in the top two or three substrate layers for the two lower coverage phases. The effect of the rumpling is to push the adsorbate atoms slightly into the surface, so an advantage is gained because the coordination of adsorbate-to-substrate atoms increases slightly. This type of rumpling is a feature which has always been observed to accompany top-site adsorption, and in fact top site adsorption itself has been attributed to the ability of the substrate to undergo this rumpling. Thus it is rather puzzling that alkalis on Ag(111) do not adsorb in the top site. This result illustrates the fact that alkali metal adsorption is still not understood well enough to accurately predict adsorption sites without performing detailed energy calculations.

In addition, the results show that there is a change from the FCC hollow site for the $p(3\times 3)$ and $p(2\times 2)$ phases to the HCP hollow site for the $(\sqrt{3}\times\sqrt{3})R30^\circ$ phases. This was seen for all three alkali metals. It was attributed to the energy difference afforded by the slightly higher adsorbate-to-substrate coordination possible in the HCP site, in view of the fact that the top layer of a close-packed surface cannot rumple in the $(\sqrt{3}\times\sqrt{3})R30^\circ$ phase by symmetry. Moreover, in this phase the second layer rumples by a small amount, again in such a way as to increase the adsorbate coordination to substrate atoms.

The structural results show that there is no appreciable change in chemisorption bondlength for a particular alkali as a function of coverage. This result is in contradiction with a previous SEXAFS (Surface Extended X-ray Adsorption Fine Structure) result, which found a fairly dramatic increase in chemisorption bondlength with coverage. This previous result was taken as evidence for a transition from an ionically bound adsorbate to a covalently bound one, predicted in the classical picture of alkali adsorption. Moreover, the result has remained one of the only results which support the idea of a change

in bondlength, and as such has been cited often. Thus the result presented here casts a strong doubt on this particular aspect of the classical picture of alkali adsorption.

The behavior of Li and Na on Ag(111) was also investigated to a limited extent. The behavior of Na is similar to the larger alkalis, in that it forms an incommensurate phase which compresses with coverage. The differences between Na and the other alkalis are expected based on its smaller size: it disorders at much lower temperatures and the monolayer saturates at a higher coverage of at least 0.58 ML. Li however exhibits completely different behavior. At low coverages it is disordered on the surface, but no well-defined nearest-neighbor spacing is observed as with the larger alkalis. At a critical coverage it apparently condenses into an ordered island phase having $(\sqrt{13} \times \sqrt{13})R13.9^\circ$ periodicity. At higher coverages it becomes incommensurate with the substrate and compresses, as the other alkalis do, saturated at a coverage of at least 0.63 ML.

7.3. Rare Gases Coadsorbed with Alkali Metals or CO on Ag(111)

The careful characterization of the alkali metals on Ag(111) enabled some interesting results to be obtained for physisorbed rare gases which coexist with these alkali phases. When rare gases are coadsorbed with a submonolayer amount of either K or Cs, some rare gas is able to adsorb in the first layer together with the alkali. However, there is a marked difference in the behavior of the system depending on whether K or Cs is used.

Rare gases coadsorbed with K appear to prefer to segregate from the K lattice. This is supported by a number of observations. The adsorbing rare gas causes the K lattice to compress, and as it does so it exhibits behavior which is practically identical to that seen for increasing K coverage without the rare gas. This behavior includes the incommensurate phases, the details of the epitaxial rotation, and the commensurate phases seen over which the density change occurs. Simultaneously, diffraction spots appear from a new phase which has a lattice spacing equal to that of the rare gas on the clean Ag(111) surface. When the rare gas is desorbed by increasing the temperature, it desorbs at a temperature lower than it does from the clean surface. These results indicate a repulsive interaction between the rare gas and the potassium. This goes against nearly all of the few previous experimental results for coadsorption of alkalis and rare gases on other substrates, and previous notions which held that the decreased work function in the vicinity of the alkali metal atom should cause rare gas atoms to polarize in the opposite direction from the alkali, causing an attraction between the two.

Using the change in desorption or adsorption temperature of the rare gas in the presence of potassium, it is possible to calculate the two-dimensional spreading pressure of the potassium lattice. This

assumes that the rare gas and the K on the surface are truly phase segregated. In this way the spreading pressure of the alkali lattice was measured as function of alkali coverage. The result is a spreading pressure which increases monotonically with K coverage from zero to about $0.003 \text{ eV}\cdot\text{\AA}^{-2}$.

Rare gases coadsorbed with Cs exhibit a completely different behavior from that observed with K, for coverage below 0.14. The rare gas appears to mix with the Cs lattice, disordering it. A new phase appears, as with K coadsorption, but its properties differ from those of the rare gas on the clean surface. The rare gas then desorbs at a higher temperature than the temperature at which it desorbs from the clean surface. These observations indicate an attractive interaction between the alkali and rare gas. At higher Cs precoverages the behavior changes and becomes similar to that seen for coadsorption with K: the Cs lattice compresses and the desorption temperature is depressed. This is probably happens because the Cs spreading pressure becomes large enough overcome the effect of the attractive interaction between the Cs and rare gas, as well as a probable decrease in the magnitude of the attractive interaction due to the Cs having a smaller dipole at higher coverages.

Work function experiments were also performed for the coadsorption of rare gases with K or Cs. The same qualitative behavior is seen for both: when some alkali is present the work function increases or remains constant upon the adsorption of rare gas, rather than decreasing as it does for rare gas adsorption on the clean surface. Based on this result and the fact that it is impossible to separate the effect of the work function change due to compression of the alkali from that caused by the adsorption of the rare gas, it is argued that work function results from these systems are not easily interpreted.

The rare gas lattice coexisting with K, while it is similar spacing to a rare gas lattice on the clean surface, is rotated with respect to the substrate rather than aligned as on the clean surface. As little as 0.04 ML of K is required to cause the rare gas lattice to be rotated. This effect is probably due to an increased substrate corrugation potential felt by the rare gas when there is a small amount of alkali metal on the surface. The rotation angle however does not follow the Novaco-McTague prediction, but is closer in general to one of the Bohr-Grey symmetry lines. This is probably due to the presence of finite-size effects or surface defects. The new phase which appears when rare gas is adsorbed with Kr is also rotated with respect to the substrate, but the rotation angle is completely different for that seen for coadsorption with K and it changes dramatically depending on the Cs precoverage, consistent with the conclusion that these diffraction spots are due to a complicated phase involving both Cs and rare gas.

Rare gases were also coadsorbed with small amounts of CO. As with alkalis, very small amounts of CO caused the rare gas lattice to rotate rather than align with the substrate. With CO, as little as 0.03 ML was required to cause rotation of the rare gas. Again however, the rotation angles were different from that observed with K coadsorption. Coadsorption with a CO precoverage of 0.06 ML or greater caused Ar to go into a rotated higher order commensurate phase: a $(\sqrt{7}\times\sqrt{7})R19.1^\circ$ with four atoms per unit cell.

The cause of the changes in the rotation angle with CO adsorption are not understood, and may involve step-site blocking and/or a complicated interaction between the two species.

As a prerequisite to the CO and rare gas coadsorption experiments, the behavior of CO alone on Ag(111) was investigated. The results showed that CO forms an incommensurate lattice of spacing 3.89 to 4.14 Å which is rotated at an angle of about 8.8° with respect to the substrate. The CO completely desorbs from the surface at about 48 K, indicating that it is weakly physisorbed on the surface. These results are consistent with previous studies, which showed that CO physisorbs on Ag(111) and does not chemisorb on silver, as it does on many other metals, unless there is a large defect density. No previous structural studies had been done on the system however.

This thesis has presented results which characterize and attempt to draw some conclusions from the adsorption of alkali metals on Ag(111) and their coadsorption with rare gases. Some of the experiments have repeated in more detail work which had already been done, in order to test the validity of previously drawn conclusions. In some cases previous results have been corroborated, and in other cases they have been challenged. Much of the work presented in this thesis has reported in detail on experimental ground that was previously unexplored or not mapped in great detail. These experiments were designed to test certain assumptions which have been made about the nature of alkali metal adsorption and interaction of alkali and physisorbed species. Again, the results have in some cases strengthened previous assumptions and in some cases have challenged them. Hopefully these results will enable other researchers to gain some insights into these systems.

Appendix A

LEED I(E) Spectra for Commensurate Phases

This appendix contains the experimental and best-fit calculated LEED I(E) spectra for the $p(3 \times 3)$, $p(2 \times 2)$, and $(\sqrt{3} \times \sqrt{3})R30^\circ$ phases of Cs, Rb, and K on Ag(111). The experiment is described in Chapter Five, and the structures are shown in Figures 5.22, 5.23, and 5.24. The structural parameters and Pendry R factors are shown in Table 5.5. The calculations were performed by collaborators P. Kaukasoina and M. Lindroos of the Tampere University of Technology, Tampere, Finland.

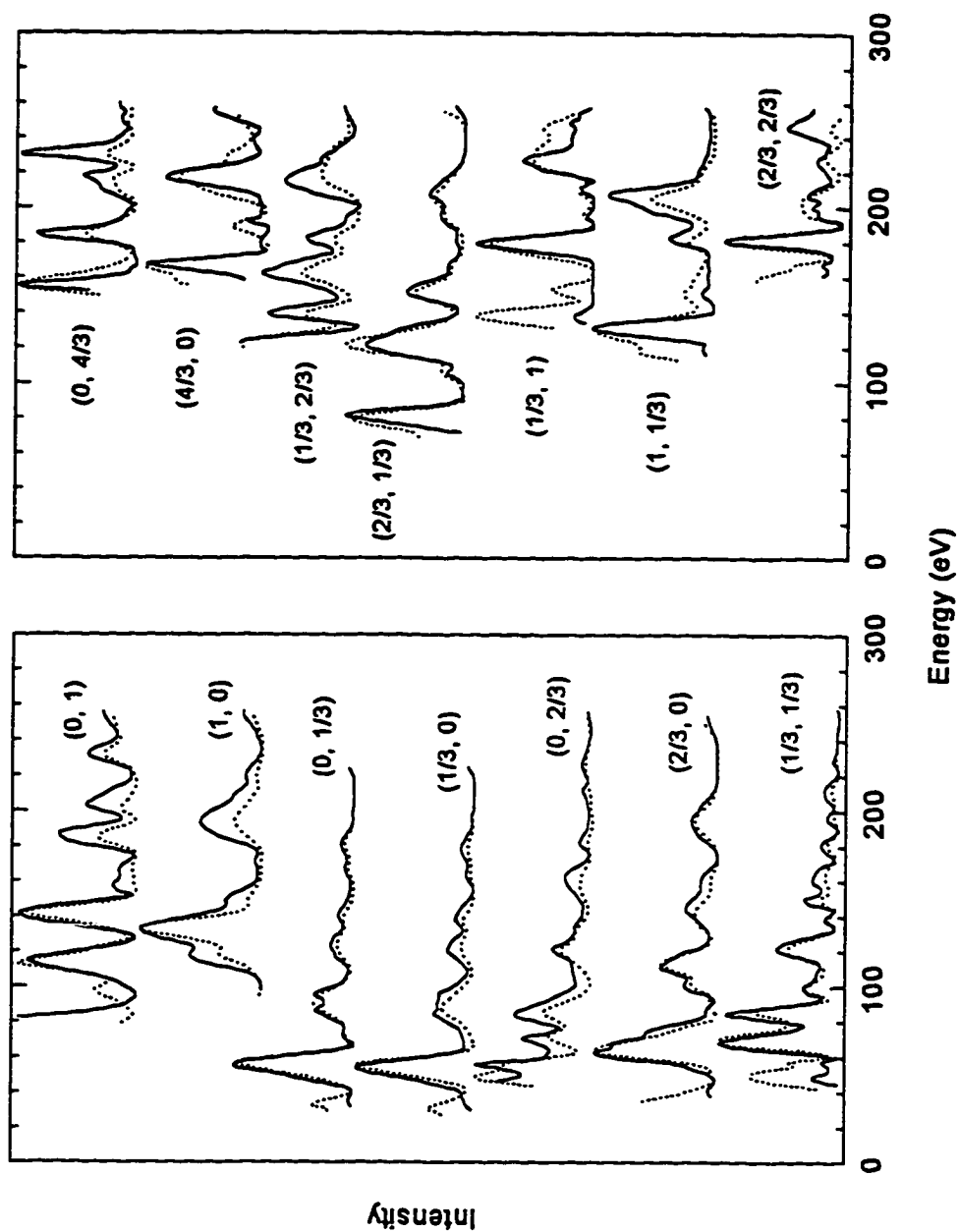


Figure A1. LEED $I(E)$ spectra for the $K p(3 \times 3)$ phase on $Ag(111)$. Solid lines indicate experiment and dotted lines indicate the best-fit calculation. Data taken at 35 K.

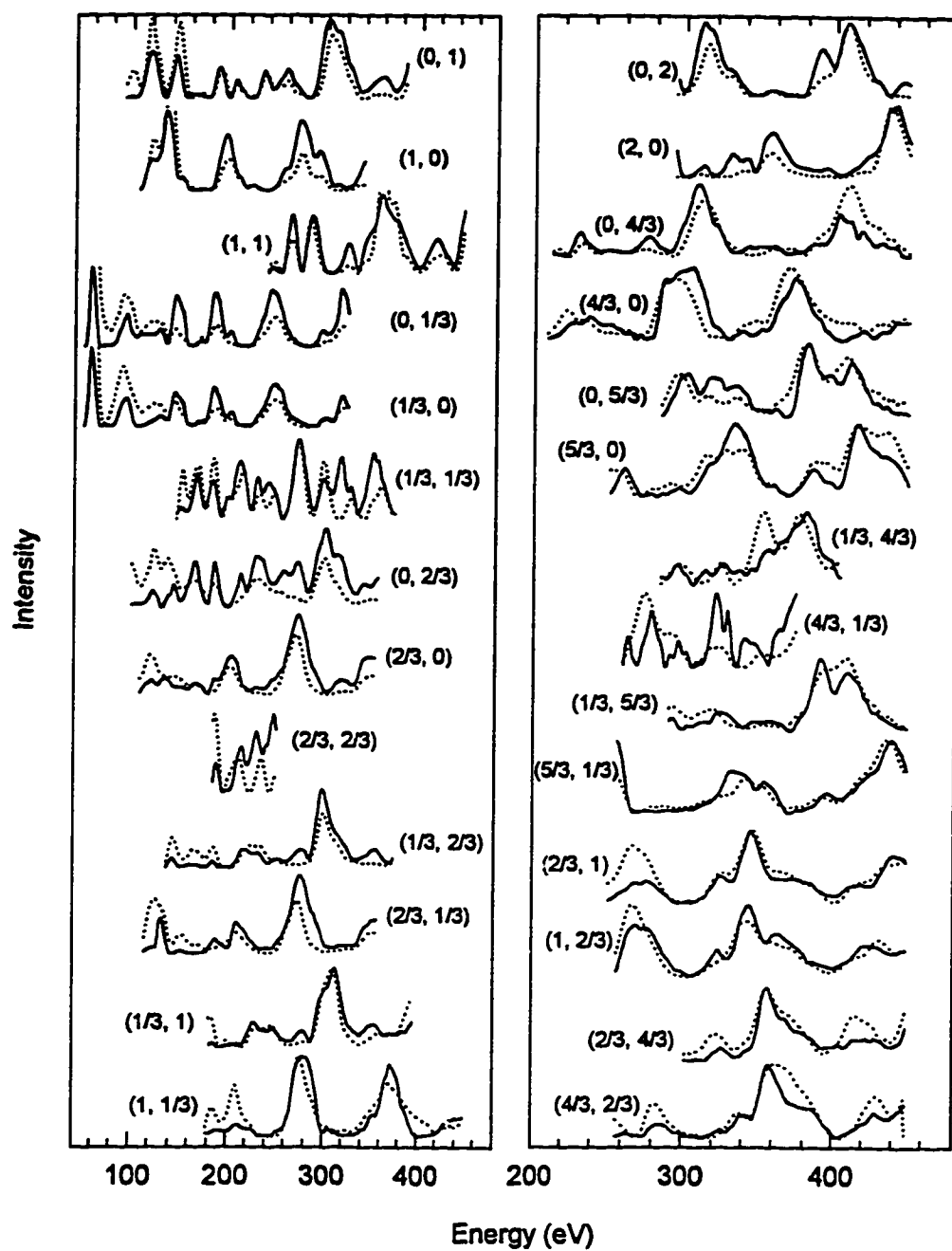


Figure A.2. LEED $I(E)$ spectra for the Rb $p(3 \times 3)$ phase on Ag(111). Solid lines indicate experiment and dotted lines indicate the best-fit calculation. Data taken at 35 K.

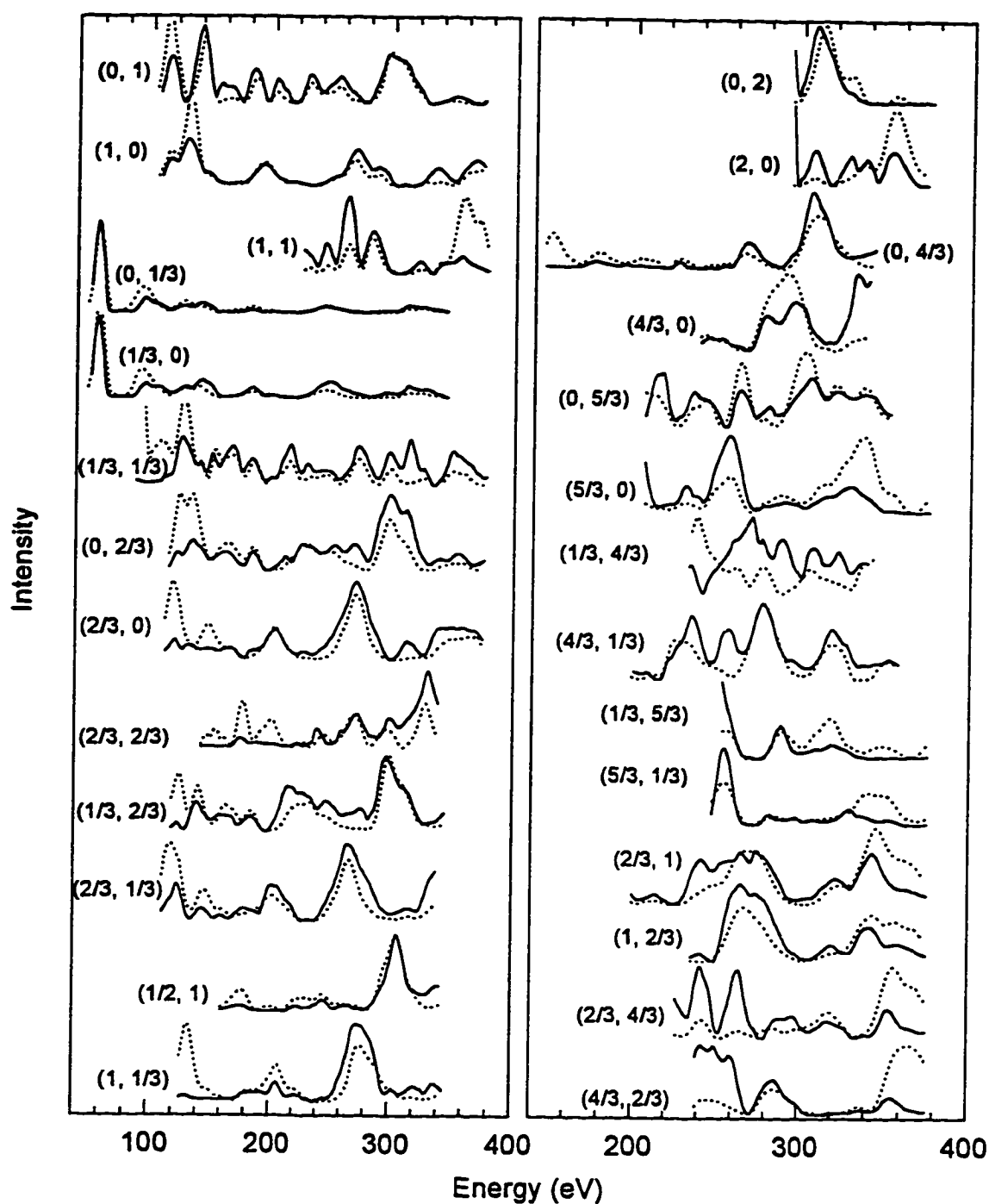


Figure A.3. LEED I(E) spectra for the Cs p(3x3) phase on Ag(111). Solid lines represent data and dotted lines represent the best-fit calculation. Data taken at 35 K.

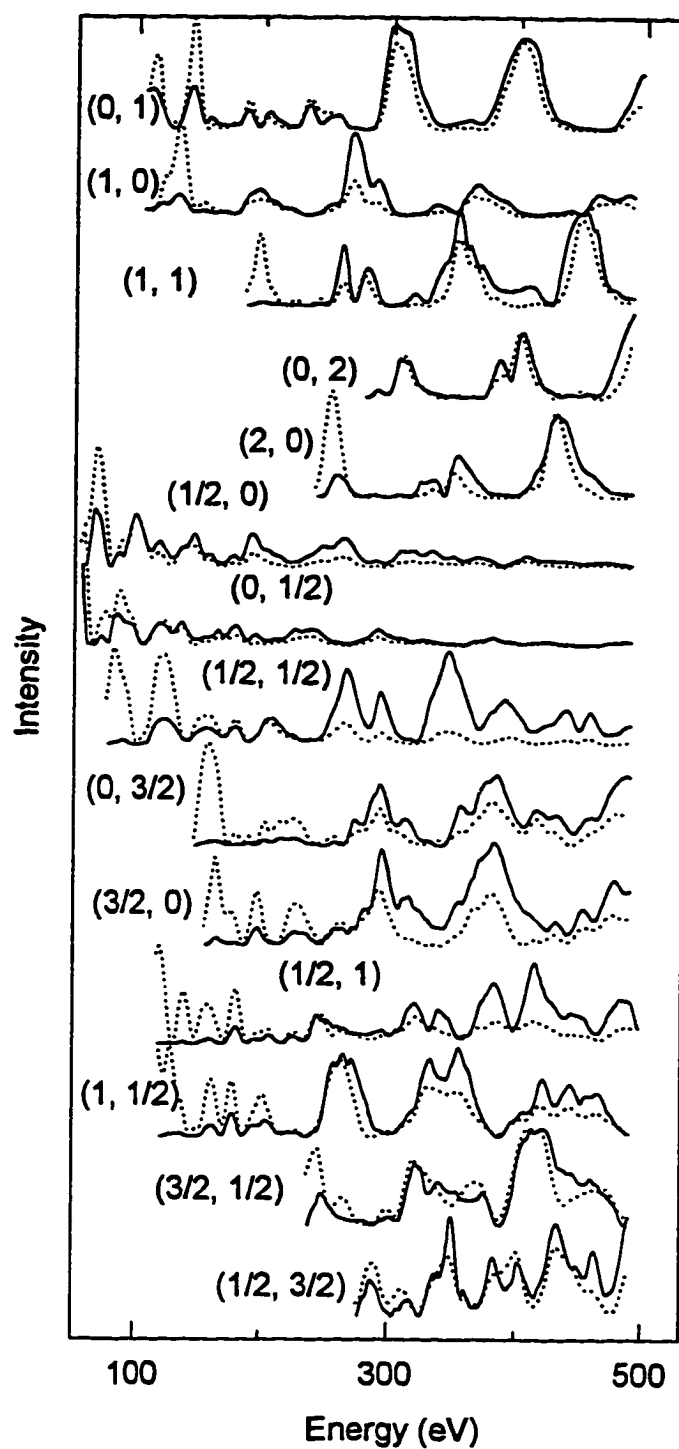


Figure A.4. LEED $I(E)$ data for the K $p(2 \times 2)$ phase on $Ag(111)$. Solid lines represent experiment and dotted lines represent the best-fit calculation. Data taken at 40 K.

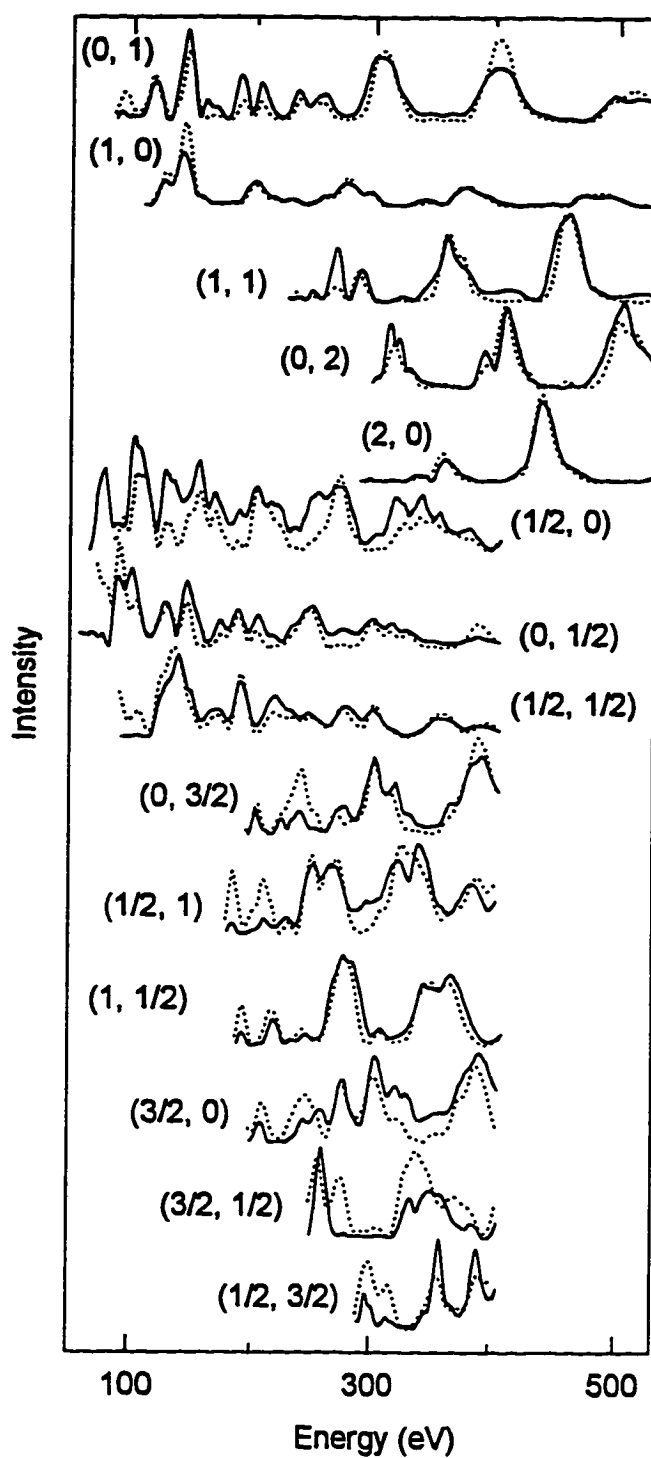


Figure A.5. LEED I(E) spectra for the Rb p(2x2) phase on Ag(111). Solid lines represent the data and dotted lines represent the best fit calculation. Data taken at 40 K.

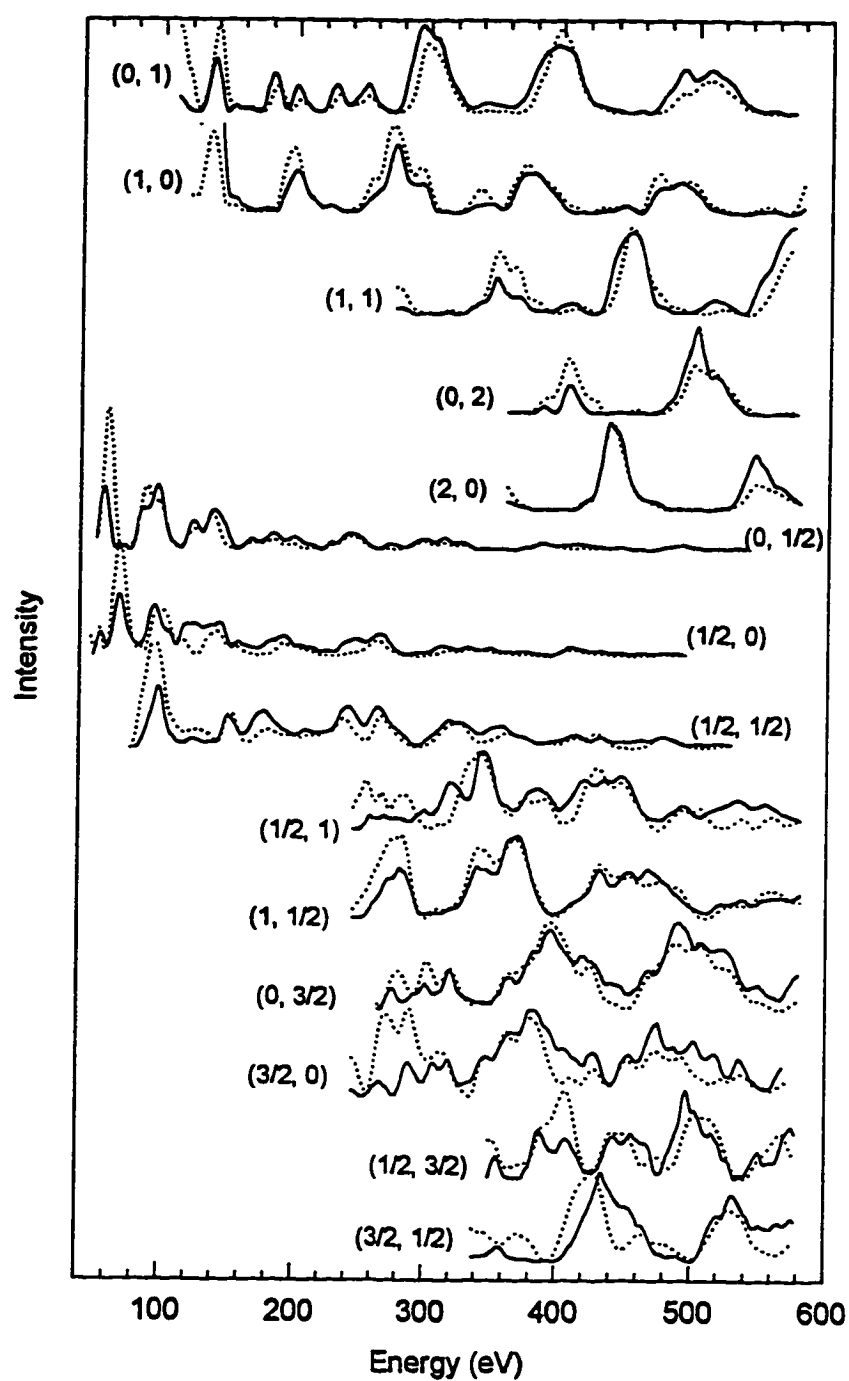


Figure A.6. LEED $I(E)$ spectra for the Cs $p(2 \times 2)$ phase on Ag(111). Solid lines indicate experiment and dotted lines indicate the best-fit calculation. Data taken at 40 K.

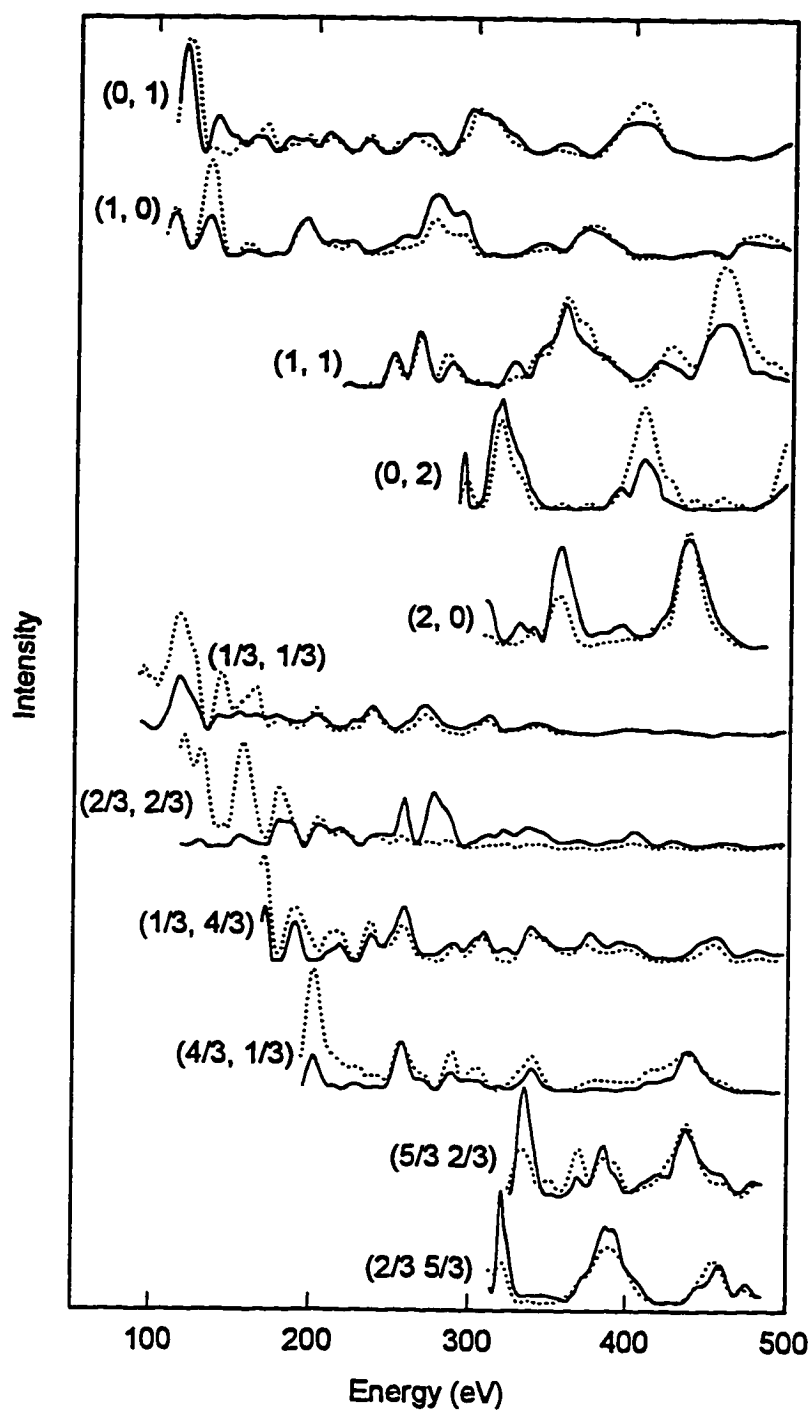


Figure A.7. LEED $I(E)$ spectra for the $K (\sqrt{3} \times \sqrt{3})R30^\circ$ phase on $\text{Ag}(111)$. Solid lines represent data and dotted line represent the best-fit calculation. Data taken at 35 K.

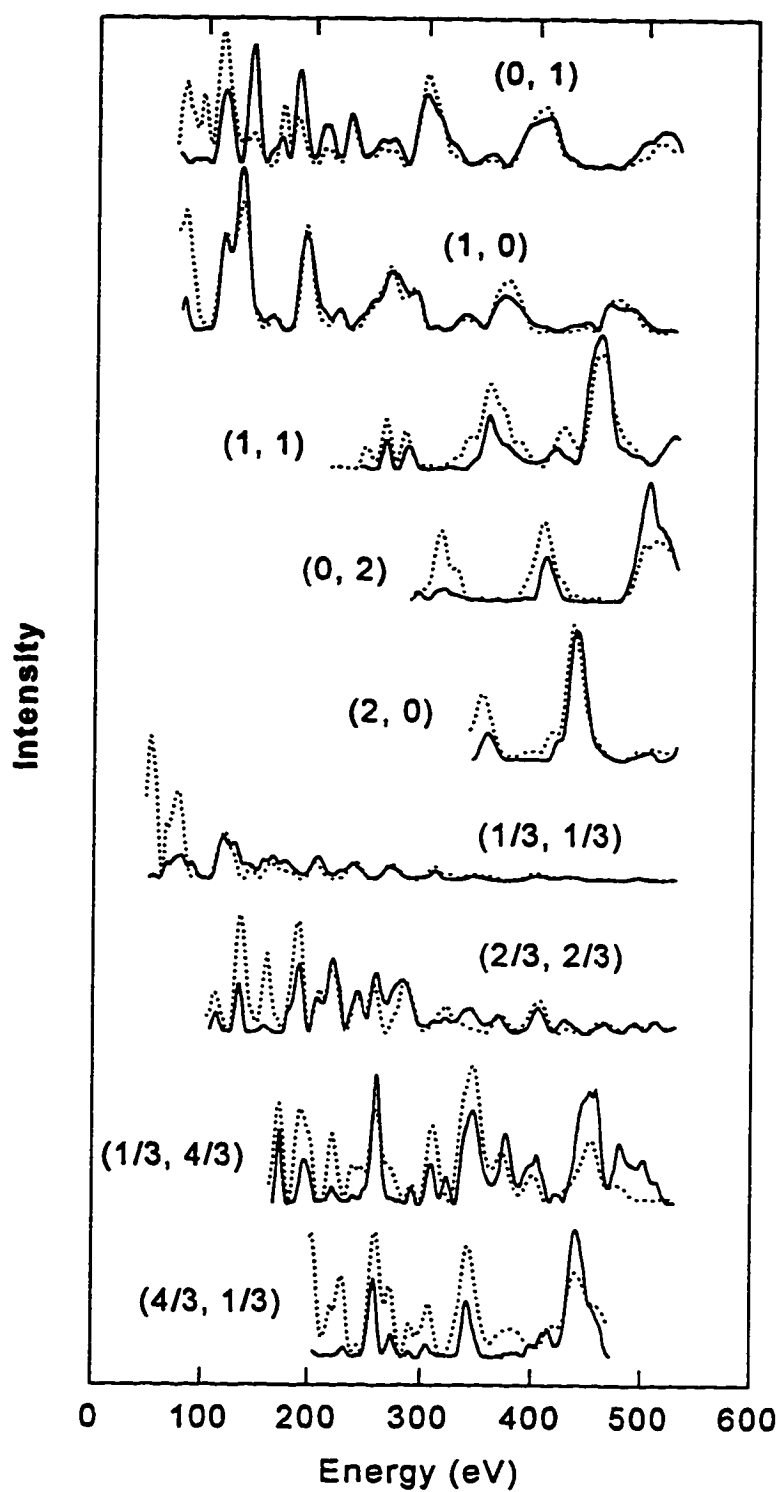


Figure A.8. LEED $I(E)$ spectra for the Rb $(\sqrt{3} \times \sqrt{3})R30^\circ$ phase on Ag(111). Solid lines represent the data and dotted lines represent the best-fit calculation. Data taken at 35 K.

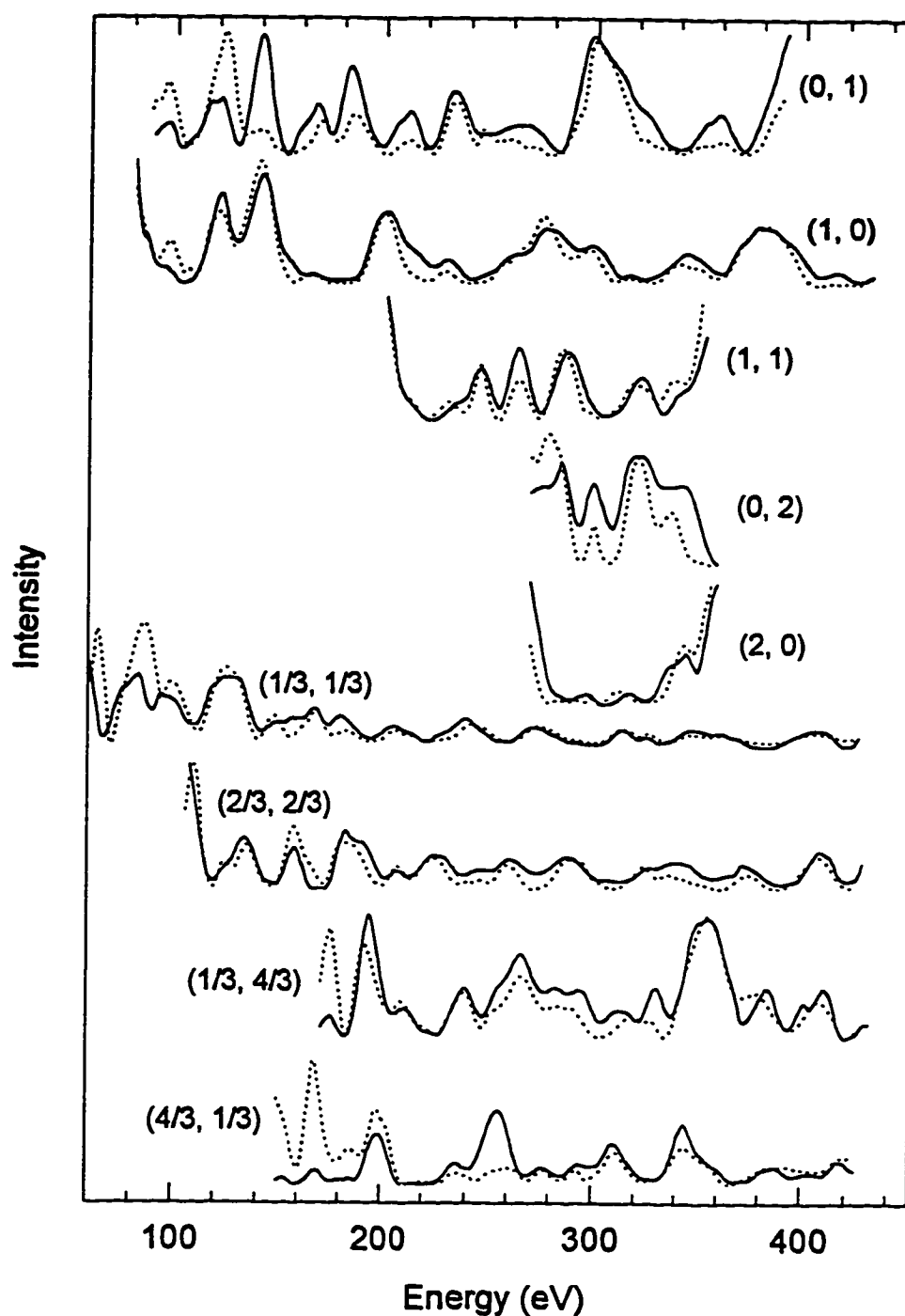


Figure A.9. LEED $I(E)$ spectra for the $\text{Cs } (\sqrt{3} \times \sqrt{3})\text{R}30^\circ$ phase on $\text{Ag}(111)$. The solid lines indicate experiment, and the dotted lines indicate the best fit calculation. Data taken at about 35 K.

Appendix B

Documentation of Video-LEED Data acquisition Program

B.1. Introduction

LEED data acquisition is achieved using Data Translation DT2851 and DT2858 video frame grabber and processor cards, which reside in a PC-compatible desktop computer. At the time of this writing, no commercial software existed for acquiring LEED data from these cards and processing such data. A few general-purpose video acquisition and analysis packages were available, but they were not well suited to the requirements of LEED data acquisition. For this reason software has been written by the author for these purposes. Although writing such software was a major time-consuming endeavor, the advantage of having acquisition and analysis software tailored to the specific needs of LEED has proved worthwhile in the long run.

The software which has been written can be divided into two groups: (1) software for acquiring and viewing or interactively analyzing data, and (2) software designed for the automated analysis of LEED data. Software in the second category will be documented in Appendix B. Programs in both categories use the same set of files (units, in Pascal terminology) which serve as libraries of procedures. The programs have been written in object-oriented Borland Pascal 7.0, and should be easily recompilable. The requirements to run the program include several megabytes of RAM and a video card and monitor capable of displaying 800 x 600 resolution in 256 colors. The video frame grabber and processor cards are not necessary, although if they are not present the LEED acquisition and some video analysis functions will not be available.

The first category mentioned above consists essentially of the Lvideo program (previously Video, Video2, or Newvid.) This is a large application which is used for data acquisition and for interactively viewing and processing data. Since it was written before multitasking operating systems had come in common use on PCs, it has the capability of running not only the video-LEED instrument, but the other instruments as well (Auger, Kelvin Probe, and sample temperature measurement and control.) It also has the capability of performing various operations on one-dimensional (curve) data, which may be needed when analyzing or viewing line profiles or I(E) curves. Most of these 1-D curve functions are of course available through a large variety of commercial programs; providing capability to perform them inside the Lvideo program however eliminates the need to switch applications often when interactively studying or analyzing LEED data, making it possible to perform these tasks more efficiently. This appendix will only document the LEED acquisition and analysis features of the program.

B.2. Lvideo Program Description

Lvideo performs the following functions:

1. Video-LEED data acquisition.
 - a) Frame acquisition.
 - b) I(E) data acquisition.
 - c) Window intensity integration as a function of time.
2. Video frame analysis.
 - a) Linear or arc profile extractions.
 - b) Frame addition, subtraction, scaling, and averaging.
 - c) Flat screen correction.
 - d) Histograms of gray-scale levels.
 - e) Frame integration or convolution with a kernel matrix.
 - f) Fitting of two-dimensional functions (lorentzians and gaussians with polynomial background).
3. AES data acquisition.
4. Kelvin Probe data acquisition.
5. Linear curve analysis.
 - a) Curve-constant arithmetic (addition, subtraction, multiplication, division).
 - b) Curve-curve arithmetic (addition, subtraction, multiplication, division).
 - c) Non-linear fitting of spectral functions (lorentzian and gaussian with polynomial background).
 - d) Various additional operations including smoothing, splines, FFTs, linear regressions, histograms, integrals and derivatives, and calculation of Pendry R factors
6. Monitoring and regulating of chamber conditions.
 - a) Sample temperature control and monitoring.
 - b) Chamber pressure monitoring.

The program is invoked by typing "Lvideo" at the command prompt. When running the program on a computer which does not have a frame grabber present, it should be run with the -n switch (type "Lvideo -n" at the command prompt.) When the program terminates, it saves a number of current parameters in a file called config.dt. Occasionally this file becomes corrupted because of bugs in the program, and this may result in the program not being able to run correctly. This can be fixed by simply deleting this file, which will be created again automatically by Lvideo the next time it is executed.

Lvideo was originally intended to be a menu-driven program. However, as time went on and a plethora of new functions and capabilities were added, it has changed into being more of a keystroke-driven program. The result is that many of the basic operations are available as menu items, there are many other operations which can only be accessed through keystrokes. The menu is shown along the bottom of the screen as a list of sometimes cryptic abbreviations, and can be access in two ways: by clicking with the left mouse button in the appropriate area or by hitting the function key corresponding to that menu item. Each menu consists of ten items, which correspond to function keys F1 through F10, from left to right. The menus are organized in a two-level hierarchical arrangement. The first level

contains menu entries which take you to different submenus. When you move from a menu to a submenu, the entire menu bar is replaced by a new bar containing a different set of items. For most submenus the last menu item is labeled "main menu" and will return the main menu. Many of the submenus contain more than ten items (the number which will fit on the bar at the bottom of the screen.) These additional commands may be accessed by hitting the enter key, which has the effect of cycling the menu bar display through sets of commands of a particular submenu. Keystroke commands are accessed simply by striking the key (or key combination) corresponding to that command. Keystroke commands do differentiate between upper and lower case. Exit the program by striking the escape key, and then answering "y" when you are asked if you wish to quit. If the program is in the middle of performing some operation however, it may be necessary to strike the escape key more than once in order to first abort the current operation.

Two types of data are displayed by the program: 2-D (image) and 1-D (curve). Curve data is displayed on the computer screen inside of a rectangular area, which can display up to twelve curves at a time. At any time one of the curves is the "active curve", on which any operations selected will be performed. A message in the lower right corner of the screen tells which is the active curve, and the active curve may be switched by striking the space bar. Image data is displayed on the video monitor which is plugged directly into the frame grabber card. This monitor displays the contents of one of the two video frame buffers on board the frame grabber card. These buffers are numbered 0 and 1, and the display may be switched from one to the other at any time through the "switch buffer" menu item in the "frame anal" submenu. When a video frame is save, additional information about the acquisition parameters of the LEED experiment is also saved. This information for the frame in the active buffer can be viewed by hitting the "?" key. The program may also run in a mode where the current image buffer is displayed on the computer screen. This mode may be entered or left at any time by striking the "v" key. This mode is useful for using the program on a computer where a video frame grabber is not present, or for zooming in on a particular region of the current video frame.

B.2.1. File Formats

One-dimensional data (curves) are saved in text files. The format consists of two columns of numbers, separated by a space. Each column is 23 spaces wide, and the numbers are written in scientific notation. In some cases various additional information containing experimental parameters, etc., is stored with the data in the form of a text header. In this case the header is separated from the rest of the file by a line which consists of the word "DATA". The data may be saved using a filename with any extension.

The Lvideo program will read as a valid curve file any file which contains two or more columns of numbers. The width of each column is not important; it is only important that the columns be separated by a comma, a tab character, or one or more spaces. If more than two columns are present, only the first two columns are read.

Two-dimensional data (images) are each saved as a set of two files. The first file uses an extension of ".imp", and is a text file which contains various information necessary to load the image, as well as various parameters from the LEED experiment. This information includes the height, width, and granularity of the image, the time and date the image was acquired, the electron beam energy, sample temperature (thermocouple reading in millivolts), chamber pressure (read as an analog output of the ion gauge controller), and maximum intensity video frame illumination. The other file is a binary file which contains uncompressed, raw image data. It uses the same filename which was used for the .imp file, except that an extension of ".img" is used. Each byte represents a pixel, starting with the upper left hand corner and moving to the right. The last pixel on the first line is followed by the first pixel on the second line. The Lvideo program will read an 8-bit raw image file even if there is no accompanying .imp file, provided that the user supplies the image width in pixels.

B.2.2. Specific Video Frame Acquisition and Analysis Functions

Saving and Loading Video Frames

Save Frame

command: menu LEED / SAVE FRAME *or*
menu FRAME ANAL / SAVE FRAME *or*
keystroke S

description: Saves the video frame in the active frame buffer to a file. Default extension is .img. Only the portion of the screen defined by the active window will be saved. Two files are written: one with the extension given (or the default .img extension) and the other with an .imp extension. The .img file is a binary raw bitmap file with one byte per pixel, and the .imp is a text file which contains various LEED experimental parameters about the video frame. The frame can be saved with granularity 1, 2, or 4, meaning that every first,

second, or fourth pixel is saved. The granularity is set when defining the active window.

Load Frame

command: menu LEED / LOAD FRAME *or*
menu FRAME ANAL / LOAD FRAME *or*
keystroke L

description: Loads a video frame into the active frame buffer. Default extension is .img. Typing a filename with a wildcard will cause the computer to retrieve a list of files from the current directory.

Define Active Window

command: keystroke V

description: Defines a rectangular patch (or list of rectangular patches) to be saved. When a video frame is saved, only the image inside this region will be saved.

Increment (decrement) Frame

command: keystroke i (I)

description: This causes the computer to load up the next (or previous) video frame in a sequence of video frames, such an I(E) sequence or a temperature scan sequence. A sequence is defined as a set of video frames which have a base string in common, with an integer appended to the string to generate the file name. For this to work correctly, the last character in the string (before the integer) must be a non-numeric character.

Change Current Directory

command: keystroke p

description: Sets the current directory for all file operations. The program will save and load all files from this directory, unless a different directory path is supplied with the filename.

Save ASCII Data

command keystroke | (pipe character)

description: Saves a portion of the active frame as ASCII data. The file contains three columns: two for (x, y) pixel coordinates and one for the intensity value.

Acquiring Video Frames

Acquire Frame

command: menu LEED / ACQUIRE

description: Acquires either a single frame, or multiple frames which are then averaged into a single frame, to the active frame buffer. See 'Set Parms' for further information. After being acquired, a frame is not automatically saved, but must be saved manually using the *Save Frame* command. The entire video frame is acquired; not just the active window.

Passthrough

command: menu LEED / PASSTHRU

description: Switches the current frame buffer into passthrough mode. In this mode the live video image from the camera is displayed.

Set Acquisition Parameters

command: menu LEED / SET PARMS

description: Sets the parameters for acquiring video frames. The computer will display a screen of the following fields with their current values. To change a field strike the key shown in the column on the left, then type in the new value of the field. To exit and return to the main program, hit escape. The parameters set here are used for all subsequent frame acquisitions using the *Acquire Frame* function. The parameters are as follows:

Comment: An 80-character comment to be saved with the video frame.

Number of frames: The number of video frames to be averaged. May be 1 - 255.

Camera F-stop: Video camera aperture setting. This field is only provided for record-keeping -- changing it does not alter the way the video frame is acquired.

Normalization mode: This is an integer between 0 and 4:

0: When multiple frames are acquired, they are simply added together, instead of being averaged. As each frame is acquired it is added to the 16-bit-per-pixel buffer on the DT-2858. This frame data is then transferred back to the active buffer on the DT-2851. Since this is only an 8-bit buffer, rather than 16 bit, the high byte is lost.

1: When multiple frames are acquired, they are added together and then divided by 256 time the number of frames acquired.

2: Frames are added together (in the 16-bit buffer) and then normalized so that the maximum intensity pixel in the frame corresponds to a level of 255. Thus the entire range of sensitivity of the 8-bit buffer is used. When you specify this option the computer will take approximately 0.5 seconds longer to perform the acquisition.

3: Similar to 1, except that intensity values are mapped into a log scale.

4: Similar to 2, except that intensity values are mapped into a log scale.

Beam voltage: This is the LEED beam voltage which is used when frames are acquired. The computer sets the beam voltage automatically just before acquiring frames. Note: make sure the LEED beam voltage control (on the LEED control box) is set to computer control, rather than manual.

Subtr. background: If this is specified, each time after the computer acquires a frame it will automatically the beam voltage to zero, take another frame, and the subtract this frame from the previously acquired frame.

Convert f-stop: If this is specified, the computer will automatically use the appropriate f-stop conversion table (these are stored as 'f-stop.***' files, where *** are the three digits of the f-stop --e.g. 340 for .340, 085 for .085) as the input LUT when it acquires frames. This compensates for non-linear response in the camera.

Window acquire: If this is specified, the video frame will only be acquire to the active window defined using *Define Active Window*. This will be faster if only a small section of the screen is to be acquire, but slower if a large portion of it is to be acquired.

Load parameter set: Loads all of the above parameters from a file.

Save parameter set: Saves all of the above parameters to a file.

Video Acquire Session

command keystroke alt-v

description: Starts a video frame acquisition session. This simply puts the computer in a mode where it will acquire a frame whenever F1 is hit, will automatically generate a filename by adding an incremented integer to a base string obtained from the previous frame. This filename is suggested and the frame is saved if you hit enter, or you can specify a different filename by typing it in. For the first file saved you have to supply the entire filename. The purpose of this is to speed the process of repetitively acquiring and saving video frames. To exit the session, hit escape.

IV Acquire

command: menu LEED / IV ACQUIRE

description: Performs a LEED I(E) scan or a time scan of an integrated window intensity. The parameters set using *IV Parameters* determine what kind of scan is performed. Several types of scans are possible: (a) A scan over incident beam energy, where the entire active window of each video frame is saved, (b) a scan over incident beam energy, where the intensities of a set of previously defined beams are measured by integrating the intensities inside a window, and plotted as curves on the computer screen, (c) a scan over time, where

the intensities in a set of predefined windows are integrated and plotted. See the section under *IV parameters* for more information. The procedure can be interrupted by hitting either escape or enter during the acquisition. Escape causes data acquired up until that time to be lost (unless entire video frames are being saved, in which case each frame is saved immediately after it is acquired), while enter causes the already-acquired curve data to remain on the screen after the procedure is aborted. In the interest of speed, integrated intensity curves acquired with this procedure are integrated from square windows rather than round ones, as is done when extracting intensity curves from previously acquired video frames.

IV Parameters

command: menu LEED / IV PARMS

description: Sets the parameters used in the *IV acquire* operation. These parameters can be set to perform a number of different operations in different ways, as mentioned under *IV acquire*. Many parameters only have an effect if certain other parameters are set to certain values, and certain combinations of parameters are incompatible with each other and may give an error message or even result in a runtime error. Therefore it is recommended to save sets of parameters for performing particular tasks.

Background Subtraction: (applies only when intensity curves are to be calculated)
Subtracts a planar background obtained from the pixels at the perimeter of each window.

Starting energy: Starting electron beam energy. If the intensity from fixed windows is to be measured, this and eV Range should be set to the same value.

eV Range: Beam voltage range for the scan.

No. of steps: Number of voltage steps used in the scan. If the voltage is not changing, this specifies the number of steps, or points in the intensity curves.

Frames to avg: (applies only when entire video frames are to be saved.) The number of frames which are averaged for each eV point.

Camera F-stop: Video camera aperture setting. As with single frame acquisition, this need be entered only for record keeping purposes.

Norm. mode: (applies only when entire video frames are to be saved.) An integer code which specifies how the video frame normalization is done. See *Set Acquisition Parameters* for a description of each mode.

File base: (used only when entire video frames are to be saved.) A character string which is used to construct the filename for each video frame. The filename is constructed by appending an integer to the end of this string. The first frame to be save will be filebase1.img, the second filebase2.img, etc. Be aware that since DOS filenames may not exceed eight characters, the number of characters in filebase must be less than eight minus the maximum number of digits in the total number of steps in the scan. For example, if 150 steps are to be scanned, filebase must be five characters or less.

Save raw vid. data: Specifies whether to save the actual each video frame.

Calculate Iv Curve: Specifies whether to produce the integrated intensity curve as the scan is being done. (The alternative is to save the raw video data and then do the analysis later.) If this is set to true, then the leaves the curves on the computer screen when it is finished, and they must be manually saved. Also if this is true, the computer automatically calculates Pendry R factors (without smoothing of course) between successive beams and shows the result on the screen after completing the scan. If this field is set to true, the "initial spot pos" and "final spot pos" fields must be set as well.

Window size: This specifies the size (in pixels) of the window the computer uses for spot integration or for saving the spot images.

Manual Verify: (applies only if the curves are being calculated) If this is true, the computer waits for the user to verify and possible modify the position of the each integration window for each step. The computer will draw a rectangle on the screen representing the window (the rectangle is not drawn if "Manual Verify" is not selected.) To accept the position, hit return; to change it, hit any other key and then click on the new position where the center of the window should be.

Sat. Compensation: (applies only if the curves are being calculated). If you select this option, the computer will compensate for video camera saturation when it computes the IV curve. It does this by fitting a line profile in the x direction through the maximum to a lorentzian + a linear offset. In the fitting, however, any intensity values of 255 are ignored, so that the fit is not influenced by these points. Then the fitted amplitude is used together with the number of saturated pixels (intensity 255) to compute the missing volume of the peak--the volume which extends above 255. This number is added to the integrated intensity. This may take up to a second longer per spot per energy. (However it is only done if the camera is saturated at some point inside the window.) Note: this option is not usually used; saturation compensation is usually only done when extracting curves from previously saved video frames. Since this feature has not been used often in the Lvideo program, it may contain a significant number of bugs.

Number of Sweeps: (applies only if the curves are being calculated). Specifies how many times the computer will sweep through the specified energy range. The data on each sweep are simply added to those obtained in the last sweep, and the final curve contains the sum of all the sweeps.

Save only windows: (applies only if entire video frames are being saved.) Causes the computer to save only a rectangular window around each spot. If this is set, the spot positions below must also be set, and the window positions are determined from those numbers.

Number of spots: (applies only if the curves are being calculated, or windows are being saved.) In the first case this specifies the number of spots which are to be measured. In the second case it specifies the number of window regions which are to be saved.

Initial spot pos: (applies only if the curves are being calculated, or windows are being saved.) This parameter consists of n pairs of points, which represent the (x,y) pixel coordinates of the positions of the integration windows for the first step. These numbers cannot be typed in, but must be entered by clicking on the appropriate position using the mouse. The computer will automatically set the beam energy to the starting energy while you do this. See the explanation under "final spot pos" below for an explanation of how these positions are used.

Final spot pos: (applies only if the curves are being calculated, or windows are being saved.) The user changes these coordinates in the same way as the "initial spot pos" coordinates are changed, with the exception that the computer will first ask whether you want to use the same coordinates for the final positions as for the initial, in which case you don't have to supply the coordinates. The coordinate positions in the "final spot pos." field determine the positions for the final step. For each step, new positions are calculated by moving the point in a straight line between the initial and final points in step sizes proportional $1/\sqrt{E}$ where E is the beam energy, a dependence which is correct for normal incidence and a flat screen. If you do not want the window to move, set the final spot positions equal to the initial positions. If you are not scanning energy (i.e. if the final energy is the same as the initial) then the initial positions will be used for all of the steps.

Memory Acquire: This is an experimental option which has not been used widely yet. If this option is set, the computer will acquire a window in the video frame to a memory buffer repetitively, and then save all of the video frames in one large file. These "movie" frames also have .img extensions and can be loaded the same way a normal frame is loaded. The frame shown can then be decremented or incremented using alt-i or alt-o. The advantage of acquiring frames this way is that the entire image can be acquired very quickly, possibly several frames per second, particularly if the window is not large and the granularity is 2 or 4. The window size and granularity used are those defined under *define active window*. The disadvantage is that a lot of memory is needed to acquire a significant number of frames.

Temp Monitor: If this is set, the computer measures the sample temperature at each step and puts it into a curve. The curve is not saved automatically, but is left on the screen and may be saved manually.

Press Monitor: Similar to "temp monitor" except that the pressure in the chamber is recorded. These two options are usually not used when LEED I(E) data is being recorded, and are more useful for isobar or isotherm measurements.

Time Step: The computer delays this long, in milliseconds, between each step.

Load Parameter Set: Loads a set of parameters from a file.

Save Parameter Set: Saves a set of parameters from a file.

Video Frame Operations

Frame Copy

command menu FRAME ANAL / FRAME COPY

description: Copies a video frame from the active 8-bit buffer to another 8-bit buffer, mapping the intensity values through one of the input DT2851 frame grabber lookup tables. Specify lookup table 0 for a straight copy. The source and destination buffers may be the same buffer, resulting in a feedback operation.

Add Buffers

command menu FRAME ANAL / ADD BUFFRS

description: Adds the contents of the other frame buffer to the current frame buffer. Intensities above 255 are mapped to 255.

Subtract Buffers

command menu FRAME ANAL / SUBTR. BUFFRS

description: Subtracts the contents of the other frame buffer from the current buffer. Intensities below zero are mapped to zero.

Scale Buffer

command menu FRAME ANAL / SCALE BUFFER

description: Multiplies the intensities of the current frame buffer by a constant. Values which go above 255 are mapped to 255.

Zoom Window

command: menu FRAME ANAL / SCREEN PLOT

description: This allows you to zoom in on a region of the active video frame. This is done by first letting you select a region by clicking and dragging the mouse, and then the program switches to the screen-display mode and shows the zoomed section of the image on the computer screen. The actual data in the buffer remains the same when this operation is performed; only the display is changed.

Integrate Frame

command: menu FRAME ANAL / INTEG FRAME

description: Replaces each pixel in the current frame by the average of the pixel values contained within a rectangle around it.

Flat-plate Correction

command: menu FRAME ANAL / SPHER CORR

description: Performs flat-plate correction on the image in the active buffer. The user is asked to supply the screen center, a y-micrometer distance (which is translated into a screen-to-sample distance) and whether or not to use bipixel interpolation. By simply hitting return when asked for the screen center, you use the previously defined screen center. If you specify a screen center, it replaces the previously defined one for subsequent operations. Bipixel interpolation refers to the interpolation of the intensity value of a point between four pixels, rather than simply using the intensity of the nearest pixel. While this takes significantly longer, it results in an image of much better quality. The flat-plate correction is a correction which always makes the image smaller physically than it was to start with. In order to minimize the loss of spatial resolution, the entire image is enlarged by a factor concurrently with the flat-plate correction, so that the final image is about the same size as the original one.

Offset / Zoom Buffer

command: menu FRAME ANAL / OFFSET BUFFER

description: Uses a function built into the frame grabber to performs an offset and zoom operation to the data in the active buffer. Possible zoom factors are 1, 2, 4, and 8. When this operation is performed, the image in the buffer is actually replaced by the zoomed image, which now contains redundant pixels if the zoom factor is other than one. This results in the loss of part of the image.

Convolve Frame

command: menu FRAME ANAL / CONVOLUTION

description: Convolves the current frame using a kernel which can be loaded from a file. Convolution files have the extension .cnv and are text files. The format will become obvious upon inspection of one.

Edit Lookup Table

command: menu FRAME ANAL / EDIT LUT

description: Allows the user to edit one of the input or output lookup tables (LUTs). (See the Data Translation documentation for a description of the LUTs). First you are asked whether the table should be an input or output LUT and which of the input or output LUTs should operate on, then you may edit the table by clicking and dragging the mouse. When you are finished hit enter; to cancel the modifications hit escape.

Related items:

Menu item **FRAME ANAL / SELECT LUT** allows you to change the currently selected input or output LUT (acquired frames pass through the selected input LUT, and the video monitor displays frames through the selected output LUT.)

Menu items **FRAME ANAL / SAVE LUT** and **LOAD LUT** allow you to save or load LUTs from files.

Filter Pixel Value

command: **keystroke F**

description: Allows you to map all pixels with a particular intensity in the active frame to another intensity.

Filter Pixel Range

command: **keystroke R**

description: Allows you to map a range of pixel intensities in the active buffer to another range, or to a single value. You specify a beginning and ending range and an output value, and whether to map the output to that single value or to add that intensity value to all pixels in the input range. You also have the option of setting all pixels outside of the range to zero intensity.

ALU Operation

command **keystroke o**

description: Performs an operation between two video frames using the arithmetic-logic unit on the DT2858 frame processor. The user is asked to select an input buffer 1, input buffer 2, output buffer, LUT 1, LUT 2, and integer values for the logic, carry, and operation no. registers of the ALU. (See the Data Translation documentation for a description of these registers. LUT 1 and LUT 2 are indices to 16-bit input LUTs on the frame processor board. The computer then sends the data in buffer 1 to the 16-bit buffer on the frame processor board via LUT1, sets the registers on the ALU to the values specified, then sends the data in buffer 2 to the processor where it operates on the data from buffer 1, and the result is sent back to the 8-bit output buffer.

Convert Aspect Ratio From Square

command **keystroke 3**

variations: *Convert to square:* **keystroke 4**

description: Alters an image which was generated with square pixels so that it appears with the right aspect ratio in on the video monitor. This is done by elongating the image by a ratio of

5/4. The elongation is done simply by repeating a video line twice at every fourth line.

Convert to square: Performs the inverse of the above operation. In this case every fifth video line is removed from the image.

Normalize Frame

command **keystroke N**

description: Re-normalizes a video frame which was acquired and normalized to utilize the entire 0 - 255 intensity range. This is possible since the maximum intensity value from the pre-normalized frame is saved with the frame.

Map Pixel Range

command **keystroke t**

description: Linearly maps a range of pixel intensities in the active frame to another range. You supply the endpoints of each range.

Clear Active Buffer

command **keystroke W**

description: Sets all pixels intensities in the active buffer to zero.

Set Display Aspect Ratio

command **keystroke T**

description: Only used when the program is running in screen display mode. (That is, the current video buffer is being displayed on the computer screen.) Sets the aspect ratio for the display. This does not effect the data in the frame buffer; it only changes how it is displayed. Should be 0.8 for video frames, and 1.0 for other (square-pixel) images.

Crop Frame

command **keystroke [**

description: Crops an image outside of a certain window, which you define. Alternatively all pixels inside of the window may be set to zero, depending on whether you set windowcopy or windowblank when the program asks for a choice between the two.

2-D Fit

command **keystroke }**

description: Fits 2-D image data to a function (lorentzian or gaussian). The program will ask you to select, with the mouse, pixels to be included in the fit. Then the fitting is done, and the fitted function may optionally be generated in the other frame buffer. This function is useful for background subtractions.

Generate Frame Function

command **keystroke 9**

description: Generates pixel intensities in a lorentzian or gaussian peak in the current frame buffer.

Frame-Frame Multiply

command **keystroke 8**

description: Multiplies each pixel in a frame with the corresponding pixel in another frame. Division may also be performed.

Pixel-smoothing Session

command **keystroke alt-s**

description: This allows you to interactively alter the image by clicking on pixels to change their intensity values. The new intensity value of a pixel is obtained by averaging the intensities of pixels on the four sides of it, a certain number of pixels away. You set this distance. This is best done when a frame is in zoomed screen-display mode. It is usefull for getting rid of a few noisy pixels somewhere, or even removing a diffraction spot if you feel you must do that.

Video Frame Measurement Functions

Frame Cursor

command menu FRAME ANAL / FRAME CURSOR *or*
 keystroke #

description: Toggles on or off a crosshair cursor on the current video frame buffer. A line at the top of the computer screen shows the pixel position, polar position, and pixel intensity.

Channel Plate Correction

command keystroke “

description: This toggles on or off the correction of pixel intensities for variations in channel plate gain due to angle of incidence. It also allows you to tell the computer what the value of the electron suppresser is. This should be given as a fraction of the beam voltage, i.e. a number less than one. This correction is used in the extraction of line profiles.

Extract Linear Profile

command: menu FRAME ANAL / XTRACT LINEAR *or*
 keystroke X

variations: *Using previous slope:* keystroke x
 Radial Profile: keystroke C
 Azimuthal Integration: keystroke Z

description: Extracts a linear intensity profile. First the computer will ask you to specify the path of the profile using the mouse by clicking and dragging. The computer will then plot the line on the video monitor and give you the opportunity to move it or rotate it in a pixel-by-pixel manner using the arrow keys (for translating it) or pageup, pagedown, insert, or delete to rotate it. Hit enter when the line is in the desired position. The computer will then ask if you wish to confirm the endpoints. If you answer yes the computer will show you the pixel coordinates of the endpoints and let you modify them. Finally, you will be asked to supply the width, in pixels, of the profile. The computer then calculates the profile in the manner described in Chapter Three.

Using previous slope: this will allow you to extract a line profile having the same slope as the previous line profile extracted. In this case you select only the midpoint of the line, by clicking on a point. In this case you will not have the opportunity to confirm the endpoints.

Radial profile: Extracts a linear profile which, if extended, would go through the screen center. The screen center is stored (x,y) coordinate which can be specified by the user. (See *Specify Screen Center*). In this case the user selects one point and provides a relative length and path width for the profile. The line is constructed so that it goes through the point selected and its length is determined by the relative length entered, and is calculated as a fraction of the radius at the point selected.

Azimuthal integration: Obtains an azimuthal integration of a region by extracting multiple line profiles rotated at different angles, but with the same length and a common midpoint. These curves are then averaged to obtain the azimuthal integration. The user is asked for the center point, the diameter in screen inches, the number of angles increments at which to extract profiles, and the pixel width to use for each profile.

Comment: whenever a profile is extracted (with the exception of an *azimuthal integration*), the trace of the profile is shown on the video monitor. The trace remains there indefinitely until it is removed using either menu item FRAME ANAL / REMOVE TRACE or FRAME ANAL / REMOVE CV&TRC, which also removes the active curve.

Select Screen Center

command: keystroke q

variations: *Average screen center:* keystroke Q

description: Allows the user to define the screen center, using the mouse. This screen center is used in various operations, including flat-plate correction and extracting radial profiles.

Average screen center: allows you to select the screen center by asking you to click on several points, and then averaging their positions.

Measure Distance

command keystroke m

description: Measures the distance, in screen inches, between two points on the screen. You select the points by clicking the mouse.

Integrate Box

command keystroke B

description: Integrates the pixel intensities inside a box defined by the user, and generates various statistics.

Histogram

command: menu FRAME ANAL / HISTOGRAM

description: Performs an intensity histogram on the current frame buffer. The result is left on the screen as a curve which may be saved.

Frame Display Functions

Set Display Aspect Ratio

command **keystroke T**

description: Only used when the program is running in screen display mode. (That is, the current video buffer is being displayed on the computer screen.) Sets the aspect ratio for the display. This does not effect the data in the frame buffer; it only changes how it is displayed. Should be 0.8 for video frames, and 1.0 for other (square-pixel) images.

Scale Display

command **keystroke **

description: Only to be used when in screen display mode, displaying a zoomed image. This scales the values of a lookup table which is used to display zoomed images. This does not change the data -- only the way it is displayed.

Un-zoom Frame

command **keystroke _**

description: Only to be used when in screen display mode, displaying a zoomed image. Unzooms a zoomed frame buffer.

Set Display Palette

command **keystroke {**

description: Only used when in screen display mode. This selects a different palette for the display of images on the computer screen. Number two is a gray-scale palette. Since 16 of the 256 colors are set aside for displaying other things on the screen, it also asks you for a code with which to generate the 16-color palette.

Appendix C

Documentation of Video-LEED Data Analysis Programs

C.1. LEED I(E) Analysis

General Description

The purpose of the LEED I(E) analysis program is to take a series of video frames and extract I(E) curves for various diffraction spots. A description of various issues involved in this process is given in Chapter Three. This section will present a detailed description and operating instructions for the LEED I(E) program, Iveral.

The input to the program consists of a text file which contains parameters for the I(E) extraction, a second file which contains pixel coordinates of a subset of the diffraction spots at two energies, and a set of video frames. The parameter file contains a list of reciprocal-space coordinates for the diffraction spots to be extracted. The subset of spots mentioned above are called the tracking spots. Since the program is given the positions of these spots at two different beam energies and their coordinates in reciprocal-space, it is able to calculate the pixel position of any other position in reciprocal-space. In doing so it is assumed that (a) the diffraction patterns were taken at normal incidence, and (b) that the tracking spots have been symmetrically chosen around the center of the screen. By this it is meant that the average position of the reciprocal-space tracking spot coordinates must be (0, 0). Using this method the computer places an integration window the position of each diffraction spot and integrates the intensity. It then moves on to the next frame, calculates the new position based on the beam energy, and integrates the windows again, and repeats this until all video frames have been processed. For reasons that will become obvious later, it is strongly recommended that the tracking spots chosen all be the same distance from the center of the screen, i. e. be a set of equivalent diffraction spots. Positions are calculated assuming a flat-screen geometry. Currently the program does not have the capability to operate on data taken using a hemispherical screen. The I(E) curves are then saved as 1-D curve data. These filenames may be constructed in a number of ways (specified in the parameter file).

As was alluded to earlier, the diffraction spots specified in the parameter file are divided into two groups: tracking spots and data spots. Usually the tracking spots are used only for tracking, and the data is saved only from the data spots. However, the program has the capability to also extract data (with identical procedures and enhancements) from the tracking spot positions. All of this information, including what information to save, is supplied by the parameter file. The coordinates supplied in the

parameter file for the reciprocal-space positions may be in any units (i.e. \AA^{-1} , or they may be miller indices of spots), and a hexagonal or square coordinate system may be used. The units used are not important to the operation of the program: the units are “defined” by the reciprocal-space coordinates given for the tracking spots.

Each video frame to be processed is loaded into a buffer of the DT2851 frame grabber. (The program should be capable of running on a computer without the frame grabber using the `-nfg` switch; however this has not been tested.) As a frame is being processed, each integration window in turn is shown on the screen. Thus it is possible to tell as the program is running whether the coordinates have been set correctly, by whether each window is properly centered around its diffraction spot. For efficiency, the windows are shown as rectangular boxes; however the actual integration is done in a round window with diameter equal to the side of the box.

Alternative methods of spot tracking (rather than supplying coordinates for the tracking spots at two energies) were supported in previous versions of Ivalan. These included tracking by point of maximum intensity, and combinations of maximum-intensity tracking and movement of the spot position an amount based on previous moves. However, none of these methods gave satisfactory results, so they have not been maintained as the program evolved. However there are still sections of code and parameters in the parameter file which pertain to these obsolete methods, and thus have no (working) function.

Ivalan also has the capability to integrate the intensities of pixels which lie between any two intensity values, over the entire video frame. This is done by taking an intensity histogram of the image and then computing the integral from the histogram.

The program is executed from the command line:

```
ivalan paramfile filebase [options]
```

Paramfile is a text file which contains the parameters for the run. These include the reciprocal space coordinates of diffraction spots, integration window size, and many other details specifying how the operation will be done. *Filebase* is a string from which the filenames of the LEED diffraction image files are constructed. These should be `.img` / `.imp` files, saved by the Lvideo program in the file format described in Appendix B. The filenames are constructed by appending an integer, plus the extension `.img`, to the end of this string. For example if *filebase* were equal to `“d:\data\ivdata”`, then the first image file to be loaded would be `d:\data\ivdata1.img`. The `-s` option is used to cause this sequence to start from a number other than one. Note that the directory path should be provided as part of *filebase*, regardless of what the current directory is.

The program may be aborted at any time by hitting escape, although data extracted until then will not be saved. The "q" key causes the program to be aborted with saving of already-extracted data.

Options

- c filename** Causes the computer to load the coordinates for the tracking spots from a file. *Filename* need not contain the directory path if the file is in the current directory. This is a file containing $m+1$ lines of ASCII text, where m is the number of tracking spots. The first line contains only the integer m . The next m lines each contain six numbers separated by spaces: (1) the value of the first energy in eV, (2-3) the (x,y) pixel coordinates of the spot at that energy, (4) the second energy, and (5-6) the pixel coordinates of the spot at the second energy. This file may be generated automatically using the program gtrcd2, to be described later in this chapter under Selecting Spot Positions. Note: in an earlier version of the program this "option" was optional because the spots could be alternatively tracked by other means. However it is now required and is the only method of tracking spots.
- nfg** No frame grabber present (this mode has not been tested). In this case memory to load the video frames is allocated from system memory.
- s n** When constructing the image filenames, start with the integer n , rather than one.
- t s** This causes the computer to delay s milliseconds after drawing the rectangle around each integration window. The purpose of this is to keep it there long enough to see it; if no delay is used the window will often be drawn and erased before the frame grabber is able to update the video monitor.

Parameter File

The parameter file is a text file which contains all the information (besides that supplied in the options above) to determine how and what $I(E)$ data will be extracted. Information is supplied by the parameter file by a series of identifiers, each followed (usually on the next line) by the value of the datum identified. The identifiers do not have to be supplied in any particular order, except in a few cases where data supplied by one identifier is needed for a later identifier to determine how many data fields to read. The identifiers, which are case sensitive, must appear in exactly the form given, starting with the first character of a line. In most cases if the identifier is not followed by the expected type of information, a run-time error will result. Other information, including blank lines or comments, may be inserted into the file between identifiers, provided that none of the comments start with one of the identifier strings. This section will list each identifier in the order in which they usually appear in the file, and provide a description of each. Each identifier will be shown in bold, while the data which follows it will be shown

in italics and the description will be shown below it in plain type. The identifier and data will be shown in the exact form it should appear -- including whether or not the data appears on the same line as the identifier. Many of the identifiers are optional. If an optional identifier is not present, then the data specified by that identifier takes on a default value. If an identifier is optional, this will be indicated in brackets after the identifier. A few identifiers, which appear in existing parameter files as of this writing, will not be included here because they are no longer used.

hexagonal [optional: default = true]

true / false

Specifies whether a hexagonal or square coordinate system is to be used for the reciprocal-space coordinates. If hexagonal, the y axis is 60° counter-clockwise from the x axis.

convert fstop [optional: default = false]

true / false

If true, the intensities of each video frame are corrected for the aperture setting of the camera. This is done by reading the aperture setting from each video .imp file, loading the appropriate fstop LUT file, and performing a LUT feedback operation on the image. Note: this function has not been used for a long time and may not work correctly.

map pixel values [optional]

n

i1 i2

.....

..... [*n* lines]

Changes the intensities of all pixels of intensity *i1* to *i2*. (These values specify intensities on the 8-bit 0-255 scale.) This is done after each video frame is loaded but before any other operations are done, and is done for *n* such pairs. Up to 100 to and from values may be specified.

num hist [optional]

nhist

If this is specified, the computer will generate a histogram of each video frame and create one or more curves whose y values contain the number of pixels of a certain energy in each video frame. (Note: the entire histogram is not saved; only the number of pixels at a certain intensity or set of intensities.) If this identifier is used, it must be followed by the identifiers **hist value** and **use hist fname** or **hist fname**. *nhist* is an integer (up to 10) which specifies the number of curves (corresponding to different intensity values) to create.

hist value [used only if histogram curves are to be generated]

i1

i2

...

... [*nhist* integers]

The specifies the intensity values used in generating the histograms.

hist fname [used only if histogram curves are to be generated]

fname1

...

... [*nhist* filenames]

Specifies the filename under which each of the above curves is to be saved.

use hist fname [used only if histogram curves are to be generated]

fname i

This option is mutually exclusive with the previous one – only one of the two may be used. If this one is used, the histogram filenames are generated by appending integers to *fname*, starting with *i*. The exception to this behavior is that if *fname* is equal to “default”, then the video frame filebase is used. In either case the filenames use the extension “.his”.

num integration curves [optional]

nint

This option causes intensity integration curves over all pixels within a certain intensity range to be generated. It is performed in a similar manner to the histogram curves above, except that the intensity values are integrated from a lower limit to an upper limit, using the histogram. This option, if it is used, must be followed by the identifiers *int curve range* and *use int fname* or *int fname*. *nint* is the number of integration curves to be generated (up to 10).

int curve range [used only if above identifier is true]

i1 i2

.....

..... [*nint pairs*]

Specifies the endpoints of the integration described above. The integration includes the endpoints.

int fname [used only if integration curves are used]

Same as *hist fname*, except specifies filenames for integration curves.

use int fname [used only if integration curves are used]

See above.

frame backsubtract [optional: default = false]

true / false

If this is true, then the intensity values of a background video frame will be subtracted from each video frame, before the analysis is done. If this is true, it must be followed by *frame background*.

frame background [only used if above identifier is true]

fname

Specifies the filename (including complete path) of the background video frame.

smooth frames [optional: default = 0]

n

Causes each video frame to be smoothed using an $n \times n$ box before the analysis is done. Each pixel is replaced by the average intensity of pixels in a box around it.

correct channel efficiency [optional]

a

s

Corrects pixel intensities for the nonuniform gain due to the changing angle of the electron beam incident to the channel plate (discussed in Chapter Three). The intensity is corrected after integration, and is based on the beam energy and the reciprocal space coordinates of the spot. *a*

is the real-space distance corresponding to the (1, 0) position in reciprocal space. Because of the flat electron suppresser grid, non-normal angle of incidence of the electrons to the channel plate will be enhanced (see Figure 3.18). This effect is also included, and so *s*, the electron suppresser value, must be provided. *s* represents the fraction of the suppresser voltage to the beam voltage, and should be a number between zero and one.

Each of the rest of the identifiers listed should be preceded by either an "s" or "d", depending on whether information about the tracking spots or the data spots is being provided, respectively. There should be one space between the "s" or "d" and each identifier listed below.

verify [optional: default = false]

true / false

If this is true, the user will have to manually verify each diffraction spot position. For each spot, after placing the box on the screen, the computer will wait for input from the user. Hitting return will cause the position to be accepted. Hitting any other key (besides "~", "q", or escape) will cause the computer to wait for the user to click on the desired position at which to center the integration window. Return must then be hit to verify that position. By hitting "~" the manual verify is turned off for the rest of the run.

extrap peaktops

true / false

This causes the computer to apply the compensation for saturated pixels at the center of a spot, discussed in Chapter Three (section 5.3.1.) It must be followed by the identifier **lock hwhm**.

lock hwhm

true / false

width

If **extrap peaktops** is true, this identifier specifies whether to lock the width of the peak when doing the fitting to determine the missing intensity. This is a good idea if the peak has a lot of saturated pixels (and therefore not much peak left on which to base the fit.) *width* is the value to lock the width at, given as a fraction of the average radius of the tracking spot positions. If *false* is used, it is not necessary to include *width*.

back subtract

true / false

If this is true, each integrated window intensity will be corrected by subtracting a planar background based on the intensity values at the perimeter of the window.

save background

true / false

Specifies whether to save the planar background intensities mentioned above. These may be saved in the same manner as the I(E) curves. If this background is saved, either **back fname** or **use back fname** must also be used. These identifiers behave in a similar fashion to **hist fname** and **use hist fname**.

no of spots

n

Number of I(E) curves to extract. *n* specifies the number, and may be as large as 30.

spots coords

x1 y1

x2 y2

.....

.....

xn yn

Specifies the reciprocal-space coordinates of the diffraction spots. These are not pixel positions, but coordinates in reciprocal space, using whatever units are convenient. Usually miller indices of the diffraction spots are used. The coordinate system may be hexagonal or Cartesian, depending on the value of the hexagonal identifier. If tracking spots are being specified (i. e. the identifier is *s* spot coords) then these (x, y) values define the units being used (that is, the scaling between pixel coordinates on the screen and these coordinates). If data spots are being specified, they specify the coordinates which will be used to calculate the positions for the integration window.

scale coords [optional: default = 1.0]

c

Divides all the reciprocal space positions defined in **spot coords** by the value of *c*. It is convenient to use this feature doing fractional order beams.

int rad

r

Specifies the radius of the (round) integration window. The radius, in pixels, is calculated by multiplying *r* by the average distance between the tracking spots and the screen center. Thus the integration radius will change with beam energy in such a way that the window covers a constant area in reciprocal space.

save curves

true / false

Specifies whether to save the I(E) curves. This is usually set to *true* for the data spots and *false* for the tracking spots.

filenames

fname1

fname2

.....

..... [entries equal to the number of spots]

Specifies the output filenames of the I(E) curves.

use fname

fname I

See the explanation under **use hist fname**. This identifier is mutually exclusive with the previous one. If this identifier is used, the filename extension will be ".ivd" if pertaining to data spots and ".iv" if pertaining to tracking spots.

Selecting Spot Positions

The program Gtcrd2 allows the user to select the pixel coordinates of the tracking spots using the mouse, and writes the coordinates and beam energies to a file for use with the -c option of Ival. Gtcrd2 runs from the command prompt and does not use any command-line parameters. When started, it shows the same graphical interface screen which is used by Lvideo. (Menu items and shortcut keys are not

available; this screen is shown by default.) After starting the program, the user may type "I" (lowercase ell) to load a video frame or increment / decrement frames in a series using "i" or "I", in order to find the frame to use for the first of the two energies. When the desired frame is found, the user should hit enter. A message on the screen will then ask the user for a filename under which to save the coordinate file and how many spots will be selected, after which the user will be directed to click on the spot positions. The arrow keys may also be used to move the cursor with finer precision. After selecting the desired number of spots, the process of loading a video frame is repeated (again using the "I", "I", and "i" keys), and a second set of spots is selected. This terminates the program, and the file is saved and ready for use with Ival.

C.2. Intensity Integration at a Single Energy

For some types of experiments it is necessary to measure the integrated intensity of an area of reciprocal space at a single energy, as a function of time, temperature, or some other variable. This can be done in live mode directly from the Lvideo program, or it can be done from stored video frames. Ival would be capable of performing such an operation, but this would make the task unnecessarily complicated. Therefore another program has been written to perform this task, Iplot.

Iplot Program

Iplot is run from the command line with a number of command line parameters to specify how the operation will be performed. The integration window positions may be provided in the command line, or they may be provided from a coordinate file as with Ival. As with Ival, Iplot has an additional special-purpose program, called Getcoord, which can be used to generate a coordinate file. The usage of Iplot is as follows:

```
iplot filename outfilename [options]
```

Filename is an actual image filename, or more often a wildcard specifying a set of images. For example, if the 10-13c series in the d:\data directory is to be operated upon, *filename* should be equal to d:\data\10-13c*.img. The frames are loaded in the order they are accessed on the disk, which is normally the order in which they were saved. *Outfilename* is a string from which output filenames are generated. This string should be in the form of a complete filename, with optional directory path, name, and extension. For each integration position, an output filename is generated by inserting an integer, beginning with zero, into *outfilename* before the extension, just before the period. The output will contain two columns of numbers:

the first will be the number of the image file (starting with one), and the second will be the integrated intensity.

The options are as follows:

- f name** Specifies the filename of the spot coordinates. This is a text file which may be generated using the Getcoord program, explained below.
- s n** Causes the program to construct the input video frame filenames in the same way that the output filenames are constructed – by inserting an integer, starting with *n*. Sequential frames are then loaded until a frame is not found. If this option is specified, filename should not contain a wildcard.
- n** Normalizes the extracted intensities for the total video frame illumination. This compensates for the normalizing to the full 8-bit range that is done when a video frame is acquired.
- fg** Use DT2851 frame grabber buffer for frame storage. If this is selected, the frames may be viewed on the video monitor while the operation is in progress.
- p** Causes a box to be drawn around each integration window. This option is useful for checking to see that the integration windows are in the correct positions.
- b** Subtracts a planar background from the edge pixels.
- e** Causes the program to apply the camera saturation correction (discussed previously).
- l w** Locks the peak width, used in fitting a profile through the spot in order to apply the camera saturation correction.
- o n** Causes the indices for the output files to begin with *n* rather than with zero.
- t** Plots x axis as time, rather than file number. This time is obtained from the .imp image files, and is the number of seconds after the acquisition of the first video frame loaded.
- d t** Delay *t* milliseconds between each spot measurement (so that the integration window boxes may be seen more easily.)
- x name** This causes the x axis values of the saved curves to be taken from a curve specified by the filename *name*. The first x value of the output curves will be the x value of the first data point of *name*, the second will be from the second data point of *name*, and so on.
- y name** Similar to the -x option, except that the x values for the output curves are taken from the y values in *name*.

Selecting Integration Positions

The file specified under the -f option for the Iplot program, which contains the pixel coordinates for the integration windows, may be generated by the program Getcoord. The usage is as follows:

Getcoord filename

Filename is the name of an image file which will be used for selecting the positions. The computer will prompt the user to supply an output filename, number of spots, position of each spot (by clicking with the mouse, or moving the cursor with the arrow keys and hitting enter), and the radius of the integration window. The radii of integration are given as a fraction of the average spot distance from the center of the screen.

Extracting Other Information from Video Frames

In cases where intensities are integrated at a single energy, the goal is usually to measure the intensities of a diffraction spot (or region of diffuse scattering) as a function of time, sample temperature, or pressure in the chamber. In these cases it is useful to be able to quickly extract such quantities (which have been saved in the .imp files) from a set of video frames. The program Frameq has been written for this purpose.

The usage of Frameq is as follows:

```
frameq infile outfile [options]
```

where *infile* is a .imp filename (or more likely, a wildcard specifying a set of filenames), and *outfile* is the name of the output file which will be created. The output file is a text file which will contain several columns, separated by spaces. The first will list the names of the input files. The following columns will list the quantities extracted from the video frames. The quantities to be extracted are determined by the options in the command line. The options are as follows:

- T** Extract the sample temperature.
- t** Extract the frame acquisition time. The first frame processed is assigned time zero, and the times for the following ones are calculated in seconds after this time.
- p** Extract the chamber pressure.
- e** Extract the electron beam energy.
- m** Extract the maximum frame illumination.
- c** Extract the 60-character comment saved with the frame.
- n** Put row number in first column rather than file name.

- s *n*** Look for sequentially named input files by appending integers, starting with *n*, to the *infile* string.

C.3. Extraction of One-Dimensional Intensity Profiles

Two programs have been written in order to extract a particular intensity profile from a set of video frames. The two programs are Lineprof and Azprof, and they extract linear and azimuthal profiles, respectively. In both cases they are run from the command line, and all parameters specifying the extraction are specified in the command line. The profiles are extracted in a manner described in Chapter Three.

Line Profiles

Usage of Lineprof is as follows:

```
lineprof filename x1 y1 x2 y2 [options]
```

Filename is name of the input video frame. This may contain wildcards, in which case the same profile is extracted from all video frames matching *filename*. For each video frame found matching *filename* a curve file is generated for the output. The filenames of the curve files are formed by using the video frame filenames and replacing the .img tag with a .lin tag. (*x1*, *y1*) and (*x2*, *y2*) specify the (integer) pixel coordinates of the endpoints of the line profile. The options are as follows:

- f *fname*** Save the output curve under an alternate *fname*. If this option is specified, the input *filename* cannot contain a wildcard.
- ft *tag*** Save output under filenames with an alternate extension.
- s *n*** Look for sequentially names files for the input video frames, rather than matching a wildcard. In this case the wildcard should be omitted, and integers, starting with *n*, are inserted into the *filename* string right before the period.
- w *width*** Width of profile, in pixels. The profile is formed by taking an average of the pixel intensities inside this path.
- ch** Correct the intensities for the channel plate gain dependence on the incident angle of the electrons to the channels. The angle is computed using the default values of the screen center and distance to screen which were last set by the Lvideo program.
- S *supp*** Specify the electron suppresser voltage, as a fraction of the incident beam energy. Should be a number between zero and one. Default is 0.76. This number is used by the procedure which corrects for the channel plate incident angle.

- n** Normalize pixel intensities for video frame illumination.
- fg** Use frame grabber buffer for storage of video frames.

Azimuthal Profiles

Usage of Azprof is as follows:

```
azprof filename cx cy rad  $\theta_1$   $\theta_2$  [options]
```

The *filename* parameter has the same function as for Lineprof. The center of the arc is specified by the (integer) pixel coordinates (*cx*, *cy*). *rad* is the radius of the arc. This is not specified in pixel widths, (since the video aspect ratio is non-unity) but in screen inches. θ_1 and θ_2 specify the beginning and ending angle of the arc, in degrees. The arc begins at an angle of θ_1 from the positive x axis, and goes counter clockwise to an angle of θ_2 . Thus θ_1 may be larger or smaller than θ_2 . The options are as follows:

- f *fname*** Same function as in Lineprof.
- ft *tag*** Same function as in Lineprof.
- s *n*** Same function as in Lineprof.
- w *width*** Same function as in Lineprof.
- ch** Same function as in Lineprof.
- S *supp*** Same function as in Lineprof.
- n** Same function as in Lineprof.
- fg** Same function as in Lineprof.
- x *ecc*** Specifies that the arc should have a non-unity eccentricity. This has the effect of turning the circle which defines the arc into an ellipse with major axes oriented parallel to the x and y axes.

Vita
Gerald S. Leatherman

Education

- The Pennsylvania State University, University Park, PA.
Ph.D. in Physics, December 1996.
- Goshen College, Goshen, IN.
B.A. in Physics, December 1990.

Publications

- G. S. Leatherman and R. D. Diehl, "Coadsorption of Rare Gases and Alkali Metals on Ag(111)", submitted to *Surface Science*.
- P. Kaukasoina, M. Lindroos, G. S. Leatherman and R. D. Diehl, "Adsorption Site Change for Cs, Rb or K Adsorption on Ag(111)", *Surf. Rev. Lett.*, accepted for publication.
- G. S. Leatherman, R. D. Diehl, P. Kaukasoina and M. Lindroos, "Unexpected Adsorption Sites for Potassium and Rubidium Adsorption on Ag(111)", *Phys. Rev. B*, **53**, 10254 (1996).
- G. S. Leatherman and R. D. Diehl, "The Phase Diagrams and Rotated Incommensurate Phases of K, Rb, and Cs Adsorbed on Ag(111)", *Phys. Rev. B* **53**, 4939 (1996).
- D. L. Adler, I. R. Collins, X. Liang, S. J. Murray, G. S. Leatherman, K. -D. Tsuei, E. E. Chaban, S. Chandavarkar, R. McGrath, R. D. Diehl, P. H. Citrin, "Top Site Adsorption for Potassium on Cu and Ni (111) Surfaces", *Phys. Rev. B* **48**, 17445 (1993).